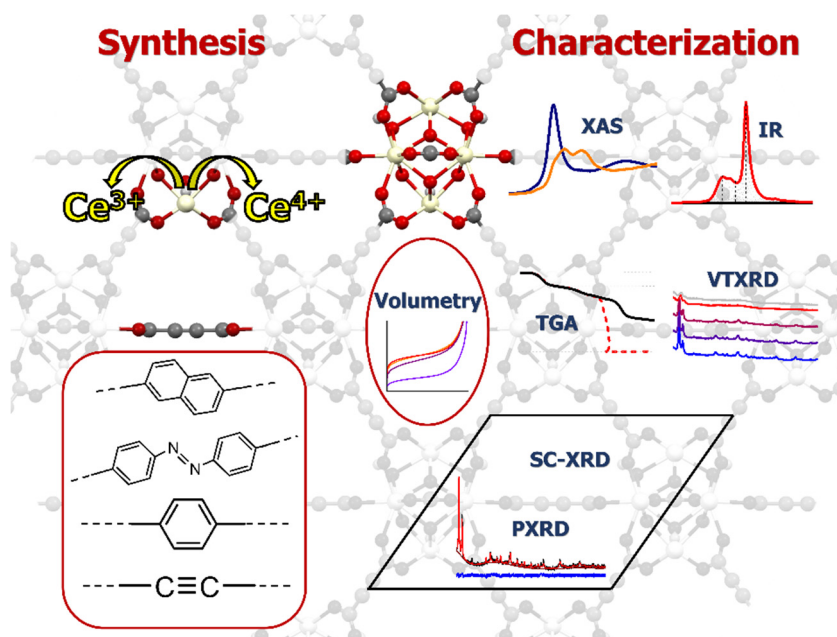




Università degli Studi di Torino

Doctoral School of Sciences and Innovative Technologies
PhD Programme in Chemical and Materials Sciences XXXI Cycle

Novel Ce^{3+} and Ce^{4+} Metal-Organic Frameworks: a multi-technique characterization



Cesare Atzori

Supervisor:

Dr. **Francesca Carla Bonino**



Università degli Studi di Torino

Doctoral School of Sciences and Innovative Technologies
PhD Programme in Chemical and Materials Sciences XXXI cycle

Novel Ce³⁺ and Ce⁴⁺ Metal-Organic Frameworks: a multi-technique characterization

Candidate: **Cesare Atzori**

Supervisor: Dr. **Francesca Carla Bonino**

Jury Members: Prof. **Bartolomeo Civaleri**
Università di Torino
Dipartimento di Chimica

Prof. **Claudio Gerbaldi**
Politecnico di Torino
Dipartimento Scienza Applicata e Tecnologia (DISAT)

Dr. **Kirill A. Lomachenko**
European Synchrotron Radiation Facility

Head of the Doctoral School: Prof. **Massimo Emilio Maffei**

PhD Programme Coordinator: Prof. **Mario Chiesa**

Torino, 2018

Index

Index

Preface.....	2
1. Introduction.....	4
1.1 Metal-organic Frameworks.....	4
1.1.1 Definition and nomenclature.....	4
1.1.2 History.....	5
1.1.3 Reticular chemistry.....	6
1.1.4 Ce-based MOFs.....	8
1.1.5 Mixed-metal MOFs.....	12
1.2 Synthesis.....	14
1.2.1 High-Throughput methods.....	16
1.2.2 Linker functionalization.....	17
1.2.3 Post-synthetic functionalization.....	17
1.3 Characterization.....	18
1.3.1 Structure determination.....	18
1.3.2 Solvent removal and thermal stability.....	19
1.3.3 Gas adsorption volumetry.....	19
1.3.4 X-Ray absorption spectroscopies in MOFs.....	19
1.4 Applications.....	21
1.4.1 Gas storage and separation.....	21
1.4.2 Catalysis.....	22
1.4.3 Energy applications.....	23
2. Experimental.....	24
2.1 Synthetic procedures for the MOFs.....	24
2.1.1 Synthesis of $\text{Ce}_2(\text{NDC})_3(\text{DMF})_2$	24
2.1.2 Synthesis of $\text{Ce}_2(\text{ADB})_3(\text{DMA})_{3.4}$	24

2.1.3	Synthesis of Ce/Zr-UiO-66.....	25
2.1.4	Synthesis of Ce-UiO-66-ADC.....	26
2.2	Experimental methods.....	27
2.2.1	X-Ray diffraction techniques.....	27
2.2.2	Thermal analysis techniques.....	28
2.2.3	X-ray absorption spectroscopy.....	29
2.2.4	Vibrational spectroscopy.....	30
2.2.5	Volumetric adsorption.....	30
3.	Results and discussion.....	32
3.1	Ce ₂ (NDC) ₃ (DMF) ₂	32
3.1.1	Thermal activation.....	33
3.1.2	Crystal structure.....	37
3.1.3	X-ray absorption spectroscopy.....	42
3.1.4	Adsorption properties.....	45
3.2	Ce ₂ (ADB) ₃ (DMA) _{3,4}	48
3.2.1	Crystal structure.....	49
3.2.2	Thermal activation.....	53
3.2.2	Adsorption properties.....	57
3.3	Ce/Zr-UiO-66.....	60
3.3.1	Crystal structure.....	60
3.3.2	Thermal activation.....	63
3.3.3	X-ray absorption spectroscopy.....	65
3.3.4	Vibrational spectroscopy.....	69
3.4	Ce-UiO-66-ADC.....	72
3.4.1	Crystal structure.....	72
3.4.2	Thermal activation.....	76
3.4.3	Adsorption properties.....	78
3.4.4	Vibrational spectroscopy.....	80
3.4.5	Linker decarboxylation.....	84

3.4.6 Defectivity hypothesis	85
4. Conclusions	88
Acknowledgements	92
List of abbreviations	94
Bibliography	96
Appendix I	111
Appendix II	172

Preface

The present thesis concerns the core activities of my three years of PhD studies: the synthesis of novel Metal-Organic Frameworks (MOFs) and their characterization using a multi-technique approach.

The activities of my laboratory (NIS center at the Università di Torino) are focused on the characterization of materials and their surfaces using a wide range of techniques, mainly spectroscopies. In order to develop the synthetic skills required for the present research I spent a period of 3 months abroad in the laboratory of Prof. Stock in Kiel (Germany), whose research interests are mainly devoted to synthesis of new MOFs. The skills acquired in that period were applied to the development of the synthetic procedure of each material reported in the present document.

The “trait d’union” of this thesis is the use of cerium cations in Metal-Organic Frameworks. This metal, albeit uncommon in the current MOF literature, is characterized by a high availability and a peculiar chemistry which permitted to obtain equally peculiar MOF compounds.

The following work is articulated into: 1) Introduction section, where MOFs will be described in general together with the main synthetic methods and characterization techniques used in the field and a fast survey on the main applications where MOFs play a role; 2) Synthetic procedures and Experimental methods; 3) Results presented in four different sections, each one devoted to a different material; 4) Conclusions.

1. Introduction

1.1 Metal-organic Frameworks

Metal-organic frameworks (MOFs) represent a class of hybrid porous solids formed by both organic and inorganic metal clusters connected together by coordination bonds.¹⁻⁶ They represent a versatile class of materials very often characterized by permanent porosity. They are made of discrete inorganic metal cations or small clusters that act as nodes in the framework and organic linker molecules that form together a specific crystalline structure when they establish a metal-ligand coordination bond. For this reason a lattice is generated by the ideal infinite repetition of this motif in the three dimensions. The very high structural diversity and chemical versatility of these materials can be attributed to the possibility to tune their properties by an opportune choice of both organic and inorganic building units. Thanks to this peculiarity, MOFs have opened access to a wide spectrum of functionalities not present in traditional porous materials. The exploration of structure-function relationships has attracted a tremendous amount of interest by the scientific community in the last two decades, mainly. These materials can be characterized by high specific surface areas, tunable pore size and specific chemical functionalities opening a wide landscape of potential applications in various fields like catalysis, gas storage and separation and energy-related usages, for example light-harvesting.

1.1.1 Definition and nomenclature

According to IUPAC,⁷ the term “Metal-Organic Framework” stands for a coordination compound which structure satisfies the following criteria:

- Extends in two or three dimensions through repeating coordination bonded entities
- Contains organic linkers
- Contains potential voids

These compounds must follow the classical rules for naming chemical compounds (e.g. sodium benzoate) but in the literature from the very beginning the name assigned to the MOF refers to the laboratory where the material was discovered, followed by a number. For example MIL- for the Materials Institute Lavoisier, UiO- for the University of Oslo, while the short name MOF- is used by the material synthesized in the laboratory of Prof. Yaghi in Berkeley who is, in fact,⁸ the inventor of the “Metal-Organic Framework” name.

1.1.2 History

Compounds falling in the definition of MOF proposed by IUPAC started to appear in the literature way back in 1959, where an early example of coordination network with potential voids based on copper and organic linkers is reported by Kinoshita et al.⁹ Some other compounds with those criteria appeared in the literature at the end of the '80's,^{10,11} and some other in the first years of the '90s principally due to Zaworotko,¹² Kitagawa,¹³ and Yaghi.¹⁴ After a couple of years MOF-2¹⁵ (1998), MOF-5¹⁶ (1999) and HKUST-1¹⁷ (1999) will be published by Yaghi and co-workers and the last by Williams et al.. These are the first published MOFs based on carboxylate building units. MOF-5, which is chemically a zinc terephthalate, is characterized by an extremely high porosity, which can be measured in the order of 3000 m²/g by nitrogen adsorption uptake experiments. This evidence was judged to be ground-breaking for the time of the discovery, being these specific surface areas totally unprecedented. This resulted in an enormous increase of effort by the scientific community in researching MOFs, which is still growing nowadays, as testified by the number of MOF structures¹⁸ published in the CSD (Cambridge Structural Database) crystallographic database (Figure 1).

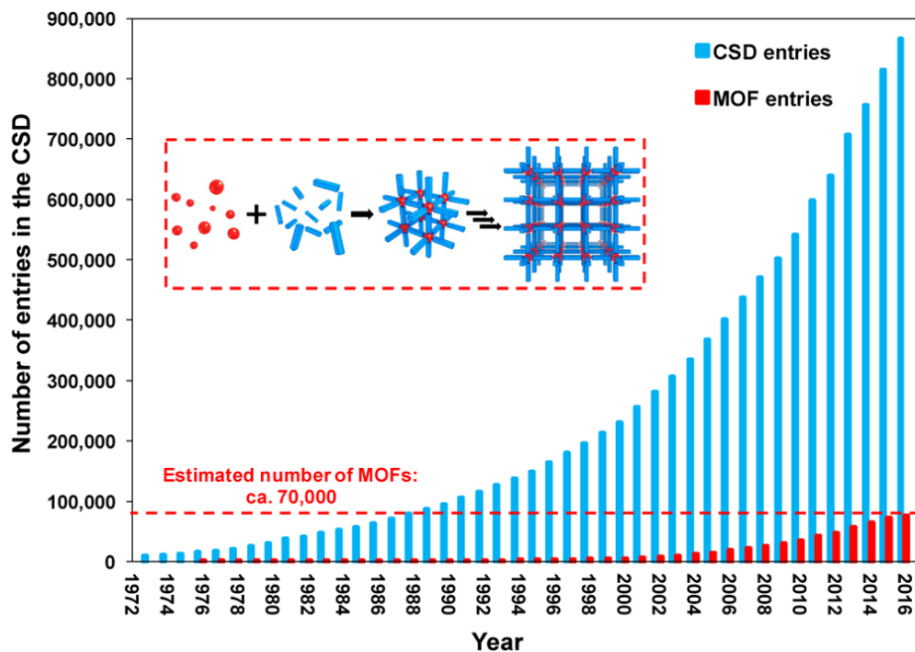


Figure 1 – Growth of the MOF entries published in the Cambridge Structural Database (CSD). Taken from ref. [18].

1.1.3 Reticular chemistry

Some authors, principally O’Keeffe, Yaghi and Eddaoudi¹⁹ rationalized MOFs structure on the basis of a network analysis: they considered the combination of the inorganic and the organic building units of the structure as Secondary Building Units (SBUs) which can be used to build the MOF structures.

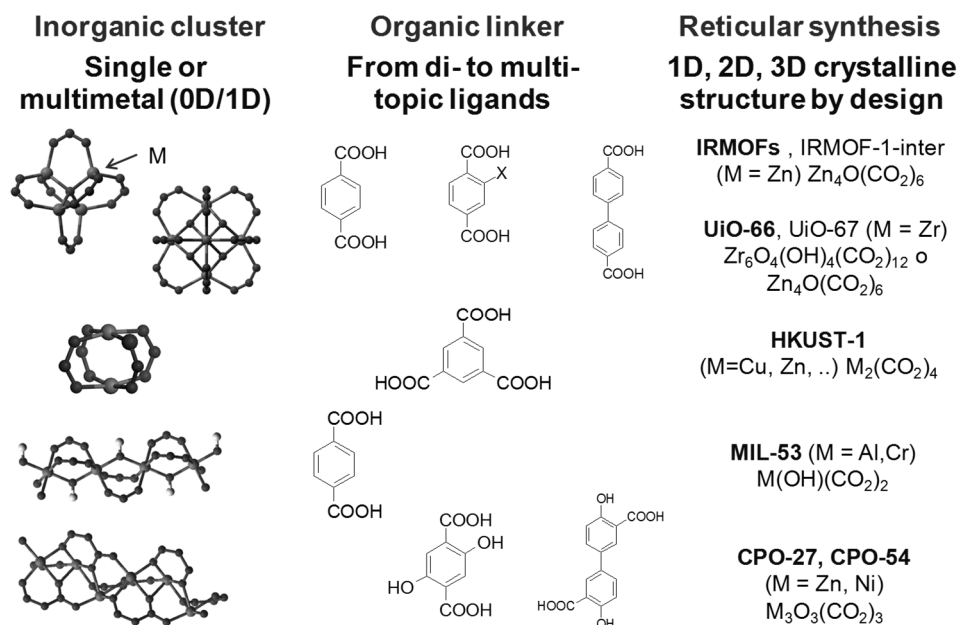


Figure 2 – Examples of inorganic and organic components of the most common MOFs. SBUs are highlighted in the left column. Taken from ref. [20]

The identification and the classification of the networks, done mainly with an *ab-initio* approach (i.e. without a knowledge on the chemistry of the materials, only relying on the connectivity of the SBUs), allowed the building of targeted networks by design. The Reticular Chemistry Structure Resource²¹ (RCSR) is a collection of thousands of different theoretical nets which all different combinations among different geometries of the metals and the linkers is explored: it reports also the crystallographic space group of the resulting materials.

An example of the so-called reticular chemistry is the series of UiO-66, 67 and 68 materials²² (Figure 3) where only varying the length of the organic linkers one obtain a series of materials with the same inorganic cluster and the same cubic topology.

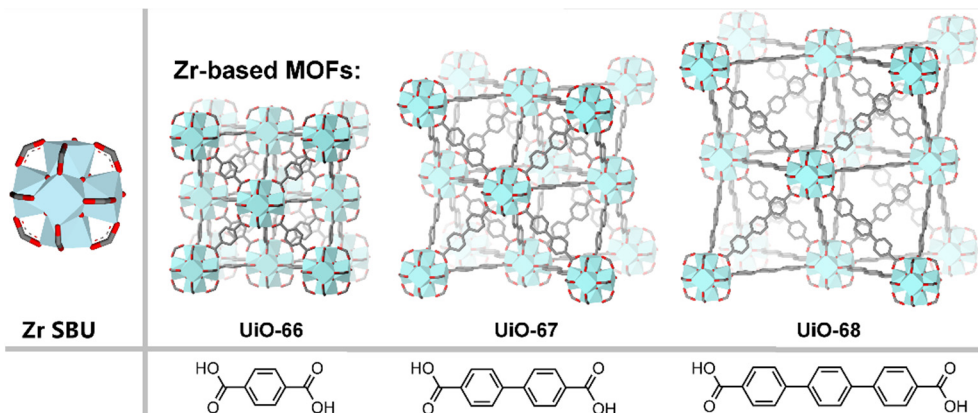


Figure 3 – Crystal structures of UiO-66, 67 and 68 materials as published by Cavka et al.²² Coordination spheres of Zr atoms are represented by polyhedrons, carbon and oxygen atoms are printed in black and red, respectively. Hydrogen atoms are omitted for the sake of clarity. Taken from ref. [23].

This approach permitted to modulate the final properties of the MOFs by a very high degree of control. For example the specific surface area for these materials is reported to be 1187 m²/g for UiO-66 and 3000 and 4170 m²/g for UiO-67 and UiO-68, respectively.

1.1.4 Ce-based MOFs

Cerium is the most abundant lanthanide element present in the earth crust^{24,25} (see Figure 4) and it is inherently cheap for this reason. The ores that are mined for the extraction of the more rare and precious rare earth elements (like Nd, Eu, Tm and Lu) are also rich in Ce and this causes a large introduction of this element in the market, which is the cause for its low price (6 US\$/kg for Ce metal and 2.6 US\$/kg for CeO₂ in 2018²⁶).

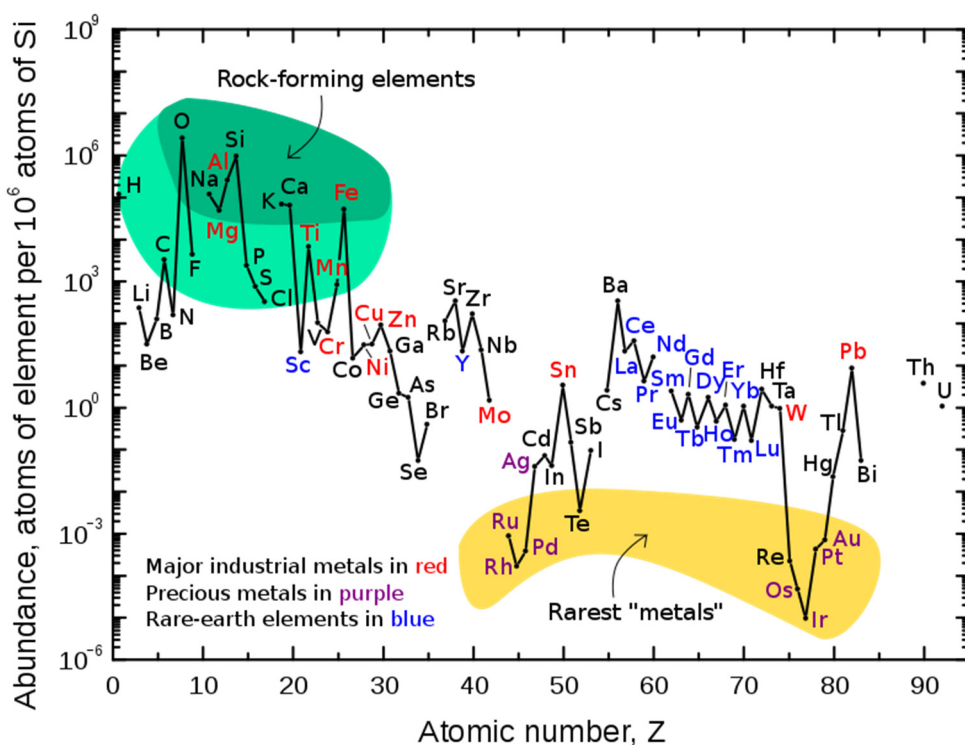


Figure 4 – Abundance (atomic fraction) of the chemical elements in the Earth’s upper continental crust as a function of the atomic number. Adapted from ref. [24]

Its oxide CeO₂, commonly named ceria, is particularly relevant for redox chemistry being a catalyst for oxidation and reduction reactions²⁷. The fact that Ce is stable in both oxidation states Ce³⁺ and Ce⁴⁺, a unique peculiarity for a lanthanide element, is exploited in applications like combustion catalysis,²⁸ reforming processes and photocatalysis.²⁷

Ce based MOFs have been more recently studied by the scientific community: general traits that can be drawn looking at the current literature published on Ce containing MOFs is the following:

- Both Ce³⁺ and Ce⁴⁺ oxidation states can be used in the synthesis of MOFs
- Synthetic conditions for Ce³⁺ containing MOFs tends to be harsher than Ce⁴⁺
- Usually Ce⁴⁺ starting reagents may be reducing to Ce³⁺ during the synthesis, the opposite was never observed, at the best of the knowledge of the author.
- Ce³⁺ materials have more frequently peculiar structures, while Ce⁴⁺ tends to give rise to MOFs having the same structure of other 4+ cations (e.g. Zr⁴⁺ or Hf⁴⁺). Their thermal stability is generally lower than their Zr⁴⁺ counterparts.

A list of reported Ce³⁺ containing MOFs is reported in Table 1 while the Ce⁴⁺ containing ones are reported in Table 2, respectively. Part of the reviewing of the literature has been already done by Lammert.²⁹

Table 1 – MOFs containing Ce³⁺ cations published in literature.

Formula	Linker molecule	Reference
[Ce ₂ (L) ₂ (DMF) ₄]	4,4',4''-{[(2,4,6-trimethylbenzene-1,3,5-triyl)tris-(methylene)]tris(oxy)}tribenzoic acid	30
[Ce(HTCPB)]·(EtOH) _{0.28} ·(H ₂ O) _{2.75}	1,2,4,5-Tetrakis(4-carboxyphenyl)benzene	31
[Ce(BTC)(DMF) ₂]	Trimesic acid	32
[Ce ₅ (BDC) _{7.5} (DMF) ₄]	Terephthalic acid	33
[Ce ₂ (ADC) ₃ (DMF) ₄]·DMF	9,10-Anthracenedicarboxylic acid	34
[Ce(ADC) _{1.5} (DMA) ₃]	9,10-Anthracenedicarboxylic acid	34
[Ce(BTC)(H ₂ O)]·DMF	Trimesic acid	35,36
[Ce ₂ (H ₂ O)(BPyDC) ₃ (DMF) ₂]·2(DMF)	2,2-Bipyridine-5,5'-dicarboxylic acid	37

[Ce ₄ (H ₂ O) ₅ (BPyDC) ₆ (DMF)] · x(DMF)	2,2-Bipyridine-5,5'-dicarboxylic acid	37
[Ce(TTTPC)(NO ₂) ₂ Cl] · H ₂ O ₁₀	1,1',1''-tris(2,4,6- trimethylbenzene-1,3,5- triyl)- tris(methylene)-tris(pyridine-4- carboxylic acid)}	38
[Ce ₂ (EBTC) _{1.5} (CH ₃ OH) ₄] · 6H ₂ O	1,1'-ethynebenzene-3,3',5,5'- tetracarboxylic acid	39
[Ce(HL)(DMA) ₂] · DMA · 2H ₂ O	5,5'-(2,3,5,6-tetramethyl-1,4- phenylene) bis(methylene) bis(azanediy) diisophthalic acid	40
[Ce ₂ (BPDA) ₃ (H ₂ O) ₄] · H ₂ O	Benzophenone-2,4'-dicarboxylic acid	41
[Ce ₂ (NDC) ₃ (DMF) ₄] · xH ₂ O	1,4-Naphthalenedicarboxylic acid	42
[Ce(NDC) _{1.5} (DMF)(H ₂ O) _{0.5}] · 0.5DMF	2,6-Naphthalenedicarboxylic acid	43
[Ce(PDC) _{1.5} (DMF)] · DMF	3,5-Pyridinedicarboxylic acid	44,45
[Ce ₂ (PDC) ₃ (H ₂ O) ₂]	3,5-Pyridinedicarboxylic acid	46
[CeCl(BPDC)(DMF)]	4,4'-Biphenyldicarboxylic acid	47
[Ce(BTPCA)(H ₂ O)] · 2DMF · 3H ₂ O	1,1',1''-(benzene-1,3,5- triyl)tripiperidine-4-carboxylic acid	48
[Ce ₂ (DHBDC) ₃ (DMF) ₄] · DMF	Benzene-2,5-dihydroxy-1,4- dicarboxylic acid	49
[Ce ₆ (BDC) ₉ (DMF) ₆ (H ₂ O) ₃] · 33DMF	Terephthalic acid	50
[Ce ₂ (ADB) ₃ (DMSO) ₄] · 6DMSO · 8H ₂ O	4,4'-Azodibenzoic acid	50

$[\text{Ce}_3(\text{ADB})_3(\text{HADB})_3] \cdot 33\text{DMSO} \cdot 29\text{H}_2\text{O}$	4,4'-Azodibenzoic acid	50
$[\text{Ce}_2(\text{ADB})_3(\text{H}_2\text{O})_3]$	4,4'-Azodibenzoic acid	50
$[\text{Ce}_2(\text{SDBA})_3(\text{DMF})_4]$	4,4'-Sulfonyldibenzoic acid	51
$[(\text{CH}_3)_2\text{NH}_2]_3[\text{Ce}_3(\text{SDBA})_6] \cdot 6\text{DMF}$	4,4'-Sulfonyldibenzoic acid	51
$[\text{Ce}(\text{BTB})(\text{H}_2\text{O})]$	1,3,5-Tris(4-carboxyphenyl)benzene	52
$[\text{Ce}_2(\text{PDA})_3(\text{H}_2\text{O})] \cdot 2\text{H}_2\text{O}$	1,4 Phenylendiacetic acid	53

Table 2 – MOFs containing Ce^{4+} cations published in literature.

Formula	Linker molecule	Reference
$[\text{Ce}_6\text{O}_4(\text{OH})_4(\text{Fum})_6]$	Fumaric acid	54
$[\text{Ce}_6\text{O}_4(\text{OH})_4(\text{BDC})_6]$	1,4-benzenedicarboxylic acid	54
$[\text{Ce}_6\text{O}_4(\text{OH})_4(\text{NDC})_6]$	2,6-naphthalenedicarboxylic acid	54
$[\text{Ce}_6\text{O}_4(\text{OH})_4(\text{BPDC})_6]$	4,4'-biphenyldicarboxylic acid	54
$[\text{Ce}_6(\mu_3\text{-O})_4(\mu_3\text{-OH})_4(\text{H}_2\text{O})_4(\text{TCPB})_2]$	1,2,4,5-tetrakis(4-carboxyphenyl)benzene	55
$[\text{Ce}_6\text{O}_4(\text{OH})_4(\text{FDC})_4(\text{OH})_4(\text{H}_2\text{O})_4]$	2,5-furandicarboxylic acid	56
$[\text{Ce}_6(\mu_3\text{-O})_4(\mu_3\text{-OH})_4(\text{BPyDC})_6]$	2,2'-bipyridine-5,5'-dicarboxylic acid	57
$\text{Ce}_6(\mu_3\text{-O})_4(\mu_3\text{-OH})_4(\text{PZDC})_4(\text{OH})_4(\text{H}_2\text{O})_4$	3,5-pyrazoledicarboxylic acid	57
$\text{Ce}_6(\mu_3\text{-O})_4(\mu_3\text{-OH})_4(\text{TDC})_4(\text{OH})_4(\text{H}_2\text{O})_4$	2,5-thiophenedicarboxylic acid	57
$\text{Ce}_6(\mu_3\text{-O})_4(\mu_3\text{-OH})_4(\text{BTC})_2(\text{OH})_6(\text{H}_2\text{O})_6$	benzene-1,3,5-tricarboxylic acid	57
$[\text{Ce}_6(\text{OH})_4(\text{O})_4(\text{PDC})_{6-x}(\text{Cl})_{2x}(\text{H}_2\text{O})_{2x}]$	2,5-pyridinedicarboxylic acid	58

$[\text{Ce}_6\text{O}_4(\text{OH})_4(\text{CCA})_6] \cdot 6\text{DMF} \cdot 16\text{H}_2\text{O}$	4-carboxycinnamic acid	59
$[\text{CeZr}_5(\mu_3\text{-O})_4(\mu_3\text{-OH})_4(\text{PZDC})_4(\text{OH})_2(\text{H}_2\text{O})_2]$	1-H-Pyrazole-3,5-dicarboxylic acid	60
$[\text{Ce}_6\text{O}_4(\text{OH})_4(\text{Muc})_6]$	Muconic acid	61
$[\text{Ce}_6\text{O}_4(\text{OH})_4(\text{CDC})_6]$	Trans-1,4-cyclohexanedicarboxylic acid	61
$[\text{Ce}_6(\text{OH})_4\text{O}_4(\text{BA})_4(\text{TBAPy})_2]$	1,3,6,8-tetrakis(p-benzoate)pyrenehexacarboxylic acid	61

As an example of successful employing of Ce MOFs as redox catalysts Smolders et al.⁶² reported in 2018 the catalytic activity of Ce-UiO-67 in the aerobic oxidation of benzylic alcohol to benzaldehyde mediated by TEMPO (2,2,6,6-tetramethyl-1-piperidinyloxy), as shown in Figure 5. The usage of X-Ray absorption spectroscopy permitted to unravel the role of the Ce cations in this catalytic cycle.

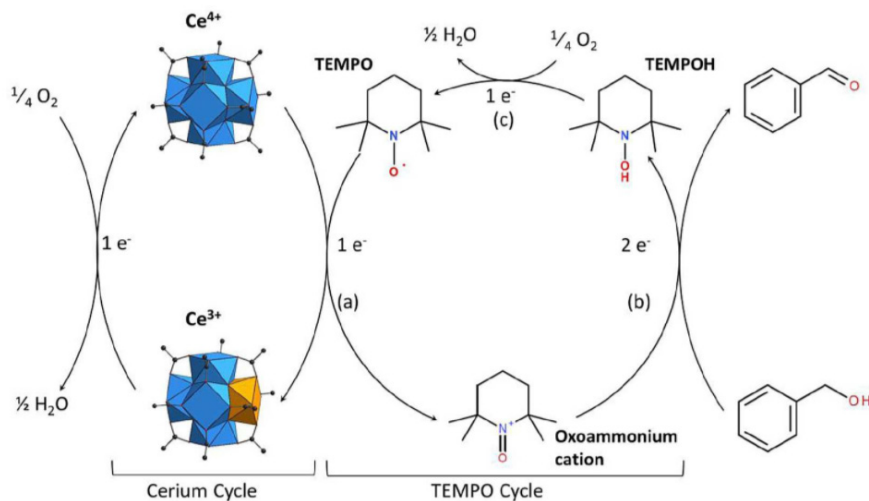


Figure 5 – Proposed reaction mechanism for the aerobic TEMPO-mediated oxidation of benzyl alcohol by Ce-UiO-67. Taken from ref.[62]

1.1.5 Mixed-metal MOFs

MOFs that present more than one metal (which can be named bimetallic or multi-metallic) were more recently introduced in the literature⁶³ as a way to impart those

materials the wanted properties (e.g. electronic, catalytic or sorption performances). They can be prepared by two main routes:

- One-step synthesis: this method involves the simultaneous reaction of the two metal precursors during the synthesis. This method often leads to fragile networks and unpredictable topologies. This method is then restricted to those metal whose reactivity is very similar. This is the method exploited by Lammert and co-workers⁶⁴ to synthesize Ce/Zr-UiO-66 bimetallic MOFs.
- Post-synthetic modifications: as an alternative way one can also firstly synthesize a mono-metallic MOF then exchange this metal with a different one with a process that is, in fact, a post-synthetic modification (see section 1.2.3). This method was used by Brozek et al.⁶⁵ to exchange Zn²⁺ cations in MOF-5 with Ti, V, Cr, Mn and Fe cations, also in different oxidation states. This approach permitted to obtain materials with peculiar catalytic properties⁶⁶

Some of the relevant MOFs that have been synthesized also with multiple metals are enlisted in Table 3.

Table 3 – Review of the mixed-metal MOFs published in literature.

MOF	Involved metals	Reference
UiO-66	Ce, Zr, Ti	60,64,67,68
MOF-5	Ti, V, Cr, Mn, Fe	65
HKUST-1	Cu, Zn, Ru	69,70
MOF-74	Ni, Co	71
DUT-67	Ce, Zr	60
CAU-38	Ce, Zr	60
(M ₃ O) ₂ (TCPP) ₃	Mn, Co, Ni, Fe	72
CPM-200	Fe, Mg, In, Ga, Co, Mn, Sc, Ni	73
PCN-224	Zr, Ti	74
MIL-88B	Fe, Ni	75

1.2 Synthesis

A great amount of effort was spent on the bottom-up synthesis of Metal-Organic Frameworks^{76,77}: tuning the performance of these materials for selected applications has in fact to pass through the sieve of a successful and reliable synthesis.

Generally speaking, the optimization a MOF synthesis is the act of finding the conditions that lead to a defined inorganic unit without decomposing the organic linker. Moreover, the material has to nucleate and grow with an appropriate kinetics in order to have a crystalline product. This self-assembly phenomenon is depicted in Figure 6.

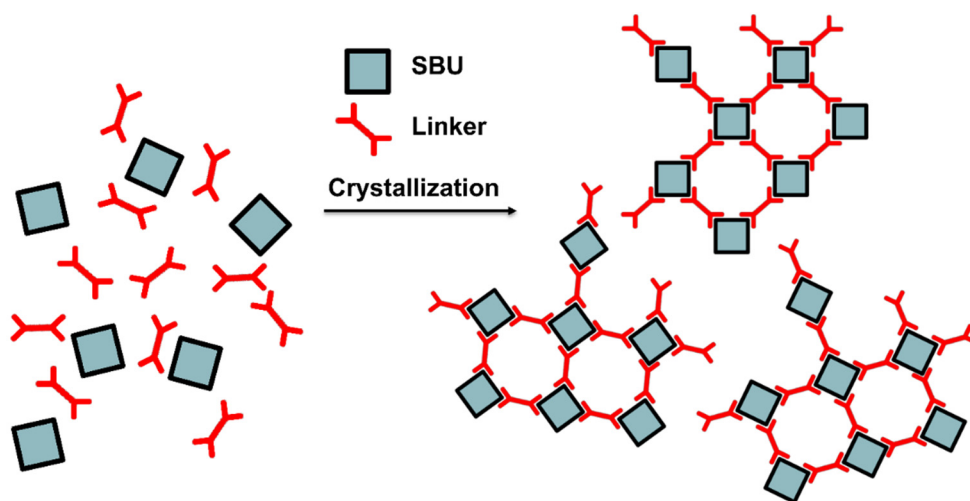


Figure 6 – Representation of the assembly phenomena of SBUs and linkers in MOF synthesis. Taken from ref. [78]

The most widely used method to synthesize MOFs is solvothermal synthesis, and in fact this is the way the materials discussed in the present thesis are made. This procedure is simply made by mixing a metal salt with the organic linker in a solvent (typically a high-boiling polar aprotic one, like DMF, DMA or DMSO) in a closed and robust vessel (like a Teflon-lined autoclave or a screw-top vial) and heat this using an oven for a fixed amount of time (that can be varying from minutes to days). The product then has to be retrieved (by filtering or centrifuging) and carefully washed from the solvent excess and the unreacted reagents.

To approach this problem several methods were employed and developed in the literature, some of these depicted in Figure 7 below. Not all of them are belonging to a solvothermal classification: for example solvent-free, mechanochemical or sonochemical methods were also exploited.

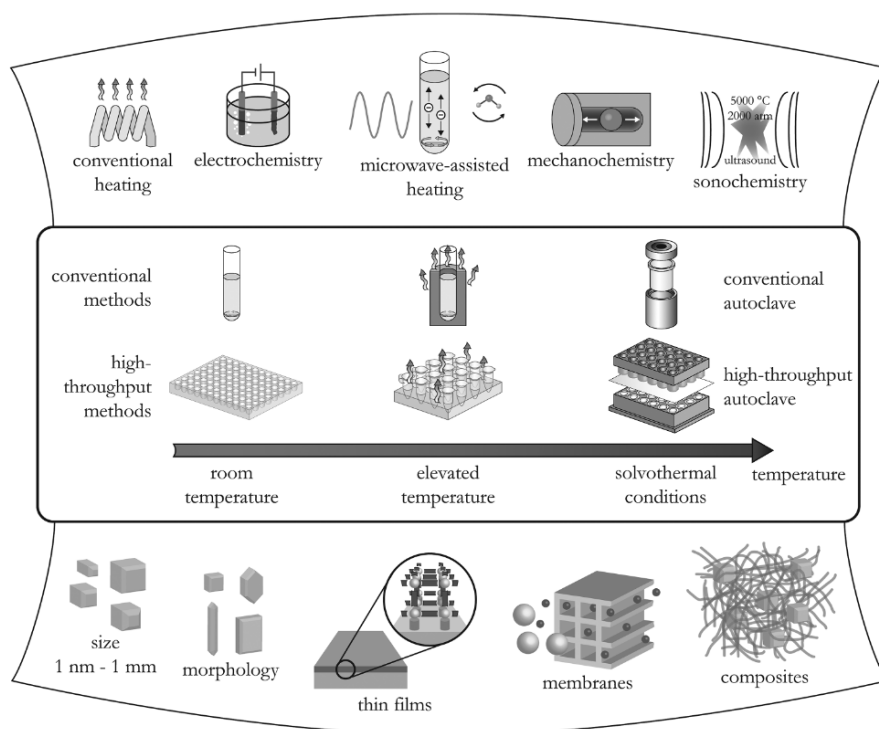


Figure 7 – Pictorial representation of some common synthetic methods for MOFs. Taken from ref. [76].

Apart from the correctness of the synthesized crystal phase and the yield of the reaction also the particle size and the morphology of the product must be optimized to suit the material for a specific application. Just to cite an example, a crystal of suitable dimensions ($>200 \mu\text{m}$, at laboratory instruments) is needed for the structural determination using the single-crystal X-Ray diffraction technique. Our synthetic procedure must be optimized in order to have such a crystal dimension if we want to do this experiment.

Controlled additions of reagents like modulators, Structure Directing Agents (SDAs) or mineralizers are widely used in MOF synthesis. Modulators are monodentate ligands having the same chemical functionality of the linker (which, for definition, must be multidentate) and is able to compete with the linker during the synthesis,

modifying thus the nucleation and growth kinetics and causing effects into the crystal size and the morphology of the product.⁷⁹ These have been used to modulate the dimensions of the crystals for example in UiO-66⁸⁰ and in the same material they demonstrated to have a great influence also on the defectivity.^{81–84} SDAs, on the other hand, are used to “fill” the pore space and thus to promote the formation of the network. An example of usage of a SDA can be the usage of DABCO (1,4-diazabicyclo[2.2.2]octane) in the synthesis of DUT-8,^{85,86} a Ni naphthalenate MOF. Mineralizing agents, finally, are added to help the dissolution of the reagents into the reaction mixture: commonly inorganic acids, bases or fluoride salts.

1.2.1 High-Throughput methods

Such a wide set of synthetic parameters (solvent, concentrations, temperature, residence time, addition of modulators, SDAs, mineralizers) must be optimized through exploratory synthesis and reasoned guess, as this field of synthetic chemistry is lacking the deep and mechanistic knowledge that is owned by the synthetic organic chemistry, for example. To overcome this time-consuming work a so called High-Throughput (HT) synthesis approach has been developed by Stock et al.^{76,87} in order to accelerate the discovery of new compounds and the optimization of the parameters. The key point of such an approach is the parallelization of the syntheses achieved using multi-welled reactors and the systematic variation of the parameters like the solvent, metal source, reagents concentration, the additions of modulators. The obtained products, after recovery by filtration or centrifugation, are characterized by a fast PXRD measurement and the diffractograms are compared with databases containing the known compounds and the diffractogram of the reagents used in the synthesis. Analyzing those datasets, relevant trends and crystallization fields can be found. The whole HT process is flowcharted in Figure 8 below.

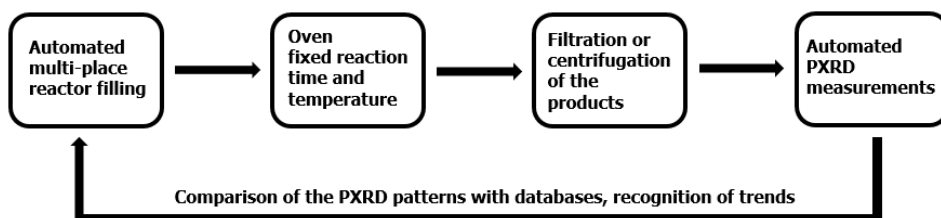


Figure 8 – A High-Throughput approach to MOF synthesis. Taken from ref. [20]

A nice example of HT investigation (Figure 9) of MOF compounds can be found in a work by Albat et al.⁸⁸ regarding the synthesis of compounds of Bi³⁺ and 4,8-disulfonyl-2,6-naphthalenedicarboxylic acid (H₄DSNDC). It is truly astonishing to

observe that with the systematic variation of the molar ratio, the pH, residence time and temperature (which was studied in more than 500 different reactions) six different compounds were isolated and the “recipe” for obtaining those pure compounds was obtained.

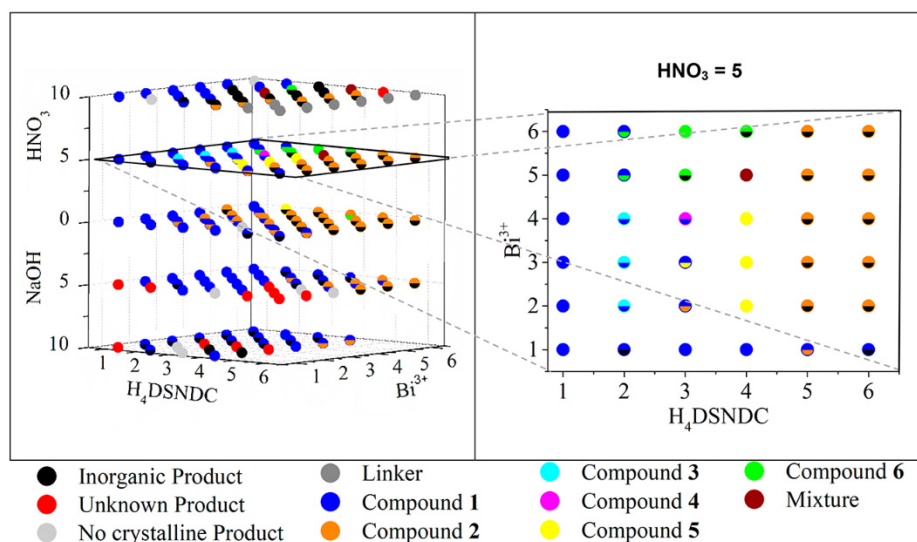


Figure 9 – Investigated parameter space for the synthesis of $\text{Bi}^{3+}/\text{H}_4\text{DSNDC}$ MOF compounds at 180°C and 48 h of reaction time. Taken from ref.[88]

1.2.2 Linker functionalization

Linkers with the same topicity and geometry but different chemical functionalities can be exploited in MOFs in order to synthesize isostructural material with tunable and desired properties. Nice examples are the usage of 2-aminoterephthalic acid instead or in conjunction with terephthalic acid in Fe-MIL-101⁸⁹ and UiO-66^{90,91} in order to insert $-\text{NH}_2$ dangling in the pores and thus control properties like the adsorption of carbon dioxide.

1.2.3 Post-synthetic functionalization

MOFs can be modified chemically after the synthesis in order to tune their properties^{92,93}. This has been achieved by exchanging the monodentate moieties dangling from the defects of the material by Shearer et al.^{82,94} in order to tune the adsorption properties of the materials for carbon dioxide. Another approach, followed by Øien et al.⁹⁵ and Braglia et al.⁹⁶, was to coordinate metallic species (respectively Pt and Cu) into bipyridine functionalized UiO-67s in order to synthesize potential heterogeneous catalysts.

1.3 Characterization

When the synthesis has been optimized at the point to produce the desired phase with sufficient purity and an acceptable yield, the characterization, as recently suggested by Howarth et al.⁹⁷, traditionally follows the following steps:

- Structure determination by X-ray diffraction techniques (i.e. Single-crystal or powder X-Ray diffraction, or SCXRD and PXRD)
- Assessment of the stability upon guest removal or thermal treatment by Thermogravimetry (TGA) or Variable-temperature powder X-Ray diffraction (VTXRD)
- Adsorption measurements by N₂ or Ar at low temperatures in order to measure the specific surface area and assess the porosity of the material.

1.3.1 Structure determination

Crystal structure determination is preferentially obtained through single-crystal X-Ray diffraction experiments, this technique being a very mature and reliable way to obtain crystallographic information.⁹⁸ In order to do so a crystal of sufficient dimensions (hundreds of μm , for laboratory diffractometers) has to be grown which is sometimes not compatible with the synthesis peculiarities (i.e. kinetics). The synthetic procedure can be adjusted in order to promote the formation of bigger crystals, also exploiting specific techniques like diffusion limited growth⁷⁶. It has to be kept in mind that a synthetic procedure optimized for the formation of big crystals may not be representative of the material synthesized in the “classical” way. Synchrotron sources may be exploited to overcome this problem as single-crystal diffraction beamlines typically require crystal of smaller dimensions⁹⁹ than laboratory diffractometers but the access to these facilities may be not easy or immediate. For those materials all the efforts have failed in this sense, the less straightforward task of solving the structure from a powder diffractogram may be tempted. In this case, having complementary information like a similar structure that can be adapted to fit the unknown one may be extremely helpful. Also chemical measurements like elemental analysis (by ICP-MS), oxidation state determination (by XPS, XAS or UV spectroscopy experiments) may be used. Nevertheless *ab-initio* modeling can be also exploited to drive the structural determination toward a correct structure.

1.3.2 Solvent removal and thermal stability

A crucial step in the characterization of MOFs is the possibility to remove the solvent from the pores of the system keeping a permanent porosity, a procedure very often called activation. After any solvothermal synthesis the pore of the material remain filled with the solvent used in the reaction. These molecules can be removed in most of the cases by a thermal treatment during dynamic outgassing or inert flow at temperatures mild enough to keep intact the crystal structure of the materials. In order to optimize the activation conditions TGA and VTXRD data are combined to observe the temperature at which the solvent is removed and simultaneously looking at the diffractogram of the material at that temperature. In the cases when the temperature required is so high to cause a structural collapse, an exchange of the solvent with a more volatile one (for example exchange DMF with methanol) may be helpful to use a lower activation temperature. The same TGA and VTXRD techniques are used to measure the thermal stability of the material and to assess if there are phase transformations associated with the solvent removal or the thermal treatment itself. New crystal phases deriving from the thermal treatment may be solved using the same techniques described in the previous section.

1.3.3 Gas adsorption volumetry

Porous materials, as MOFs are, may have their porosity evaluated measuring adsorption isotherms of probe molecules like N₂, Ar or CO₂ that adsorbs into the internal surface of these frameworks. A nice review of what can be done with those kind of experiments has been published by Thommes et al.¹⁰⁰. As this technique evidences directly the porosity, which may be overlooked by structural diffraction or thermal analysis techniques, the presence of specific surface area observed after activation is the most recognized proof for the successful removal of the solvent from the pores of the system.

1.3.4 X-Ray absorption spectroscopies in MOFs

X-Ray absorption spectroscopy (XAS)^{101,102} techniques may be used in the characterization of MOF materials: information about the oxidation state and the local geometry of the metal cations can be extracted from the XANES spectra. EXAFS spectroscopy can be exploited in challenging case where single-crystal data is not available or there are motifs that are not following the symmetry of the whole structure (and thus, are “invisible” from diffraction) like defects or cluster geometries. The element-selectivity and the local structure information available from the EXAFS data analysis can be very helpful.

EXAFS can be relevant in confirming the structure obtained from diffraction experiments, as in the case of $\text{Ce}_2(\text{NDC})_3$ (section 3.1) or in highlighting that the inorganic cornerstone has a lower symmetry with respect to that of the organic framework, as in the case of Ce/Zr UiO-66 (section 3.3). Such a synergic approach with X-Ray diffraction already shown its potentialities in disclosing the structures of solvated and desolvated UiO-66,^{22,103} UiO-67,¹⁰⁴ Hf-UiO-66,¹⁰⁵ (see Figure 10) desolvated HKUST-1,¹⁰⁶ MOF-76-Ce,³⁶ and Ni-cubane MOFs.¹⁰⁷

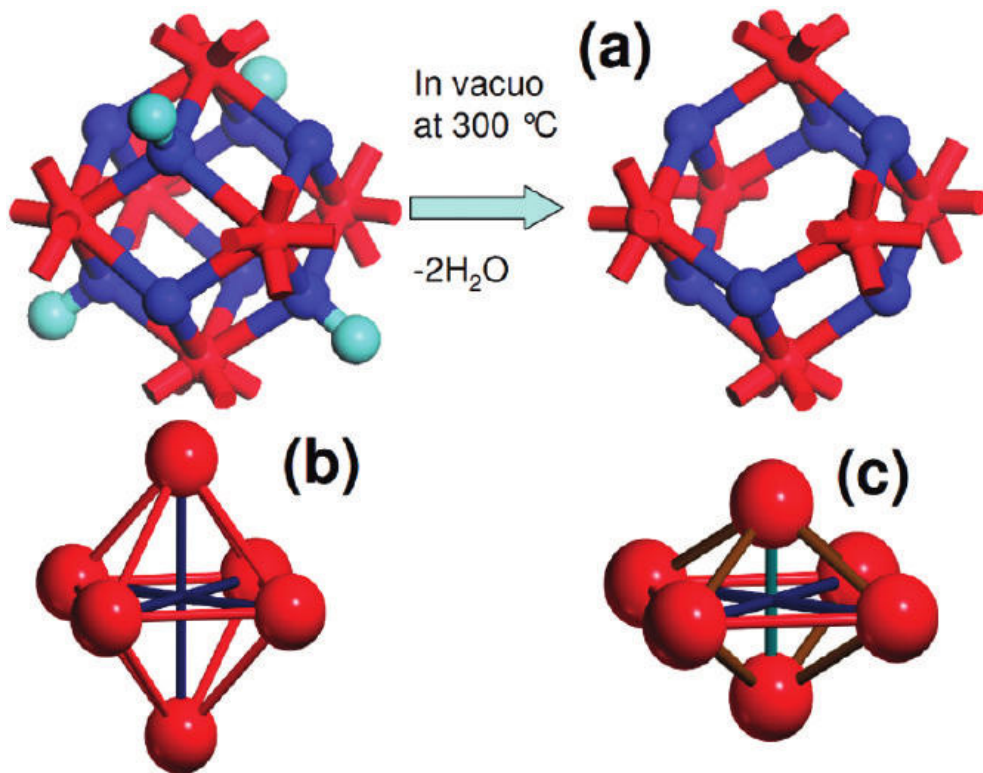


Figure 10 – Representation of the dehydroxylation undergone by the $\text{Zr}_6\text{O}_4(\text{OH})_4$ cluster upon thermal treatment at 300°C in vacuo resulting in a disordered Zr_6O_6 cluster. Such transformation is “invisible” by diffraction and only EXAFS was able to see it. Red, blue and cyan color refer to Zr, O and H atoms respectively. Taken from ref. [103]

1.4 Applications

Among the variety of the applications in which the usage of MOFs was proposed in literature, the following three paragraphs are concerning three of them, being according the author the most prominent ones.

1.4.1 Gas storage and separation

The high porosity and specific surface areas of MOFs, sometimes combined with the presence of active species on the surfaces (i.e. open-metal sites), confers these materials the ability to store considerable amount of gases inside their pores. For this reason perhaps the most researched application of MOFs is their usage in gas storage¹⁰⁸⁻¹¹⁰ and separation^{109,111}. Being really important for our economy the most studied gases in this respect are H₂ and CH₄ as energy vectors and CO₂ to CCUS (carbon capture, utilization and storage) applications. Patel and co-workers¹¹² recently published a series of guidelines (Table 4) which are to be followed if a technology based on a solid sorbent (like a MOF) has to compete with a classical carbon dioxide capture technology (i.e. aqueous solution of monoethanolamine).

Table 4 – Benchmark checkpoints for an effective CO₂ sorbent. Adapted from ref. [112]

Checkpoint	Desired
Capacity	> 2 mmol CO ₂ per g of sorbent
Recyclability	> 1000 cycles
Selectivity	> 100 (CO ₂ /other gases)
Stability	> 150 °C, boiling water, H ₂ S, SO _x , NO _x , HCl, NaOH, mechanical strength with low attrition index (AI)
Cost	< \$50 kg ⁻¹ (sorbent cost < \$10 kg ⁻¹)
Kinetics	> 1 mmol(g×min) ⁻¹

1.4.2 Catalysis

The usage of MOFs as heterogeneous catalysts has received extensively attention by the scientific community^{113–115}. They are promising because the pore dimensions and the catalytic site can be designed at an unmatched degree if compared to previous catalysts. Their first results were essentially proof of concepts, as, in comparison to the most known inorganic catalysts (e.g. zeolites), MOFs are indeed fragile materials. Gascon and co-workers shown in a pictorial way (Figure 11) the possibilities to host a catalytic site inside MOFs, they can be inserted by both in-synthesis and post-synthesis modes and they rely on modifications of both inorganic and organic component of MOFs.

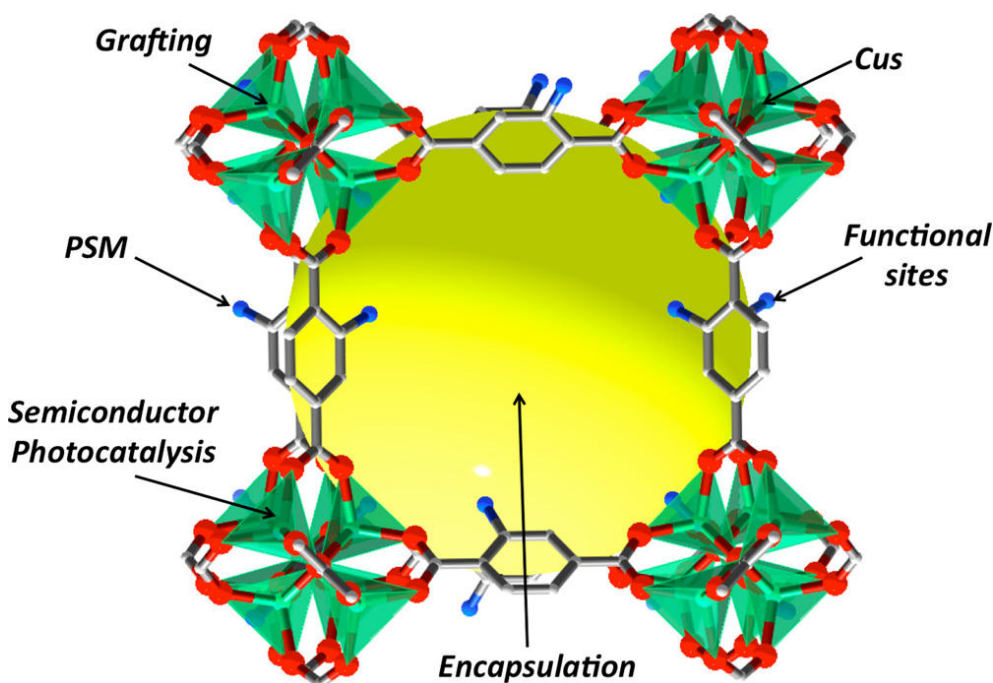


Figure 11 – Pictorial representation of the catalytic opportunities offered by MOFs. Taken from ref. [114].

Farrusseng et al.¹¹⁶ classified the catalytic activities of MOFs in different mechanisms: (i) Lewis acidity, shown for example by open-metal sites. (ii) Brønsted acidity (iii) Basic functionality (iv) Enantioselectivity (enhanced by the chirality of the pore system) (v) C-C bond formation and polymerization (vi) Nanosized metal nanoparticles trapped inside the pores (vii) Organometallic complexes supported on MOFs.

1.4.3 Energy applications

Being MOFs extremely versatile, due to the unique possibility to tune their properties by a careful choice of the linker and the metal, a significant amount of research has been devoted in MOFs for energy related applications.^{117,118} Recent examples of usage of MOFs in light harvesting,^{119–121} energy storage,¹²² conductive properties¹²³ have been recently published in the literature.

Exploiting the enormous structural tunability of MOFs, researchers explored a large numbers of structures in order to obtain photoactive materials, either using luminescent/chromophoric linkers or metal nodes^{124,125} or inserting photoactive guest molecules in the MOF pores, using the ordered nanostructure to optimize the exciton migration.¹²⁶ Porphyrin-containing¹²⁴ MOFs, as well as Ruthenium based framework¹²⁵ have been explored for a possible use in hybrid photovoltaics such as Dye-Sensitized Solar Cells,¹²⁷ and their role as interfacial active agents at semiconductor interface or in the electrolyte^{128,129} has been investigated.¹²⁶

Until now, power conversion efficiencies in working devices are still very low, especially respect to the state of the art of these systems, but the first results are encouraging.

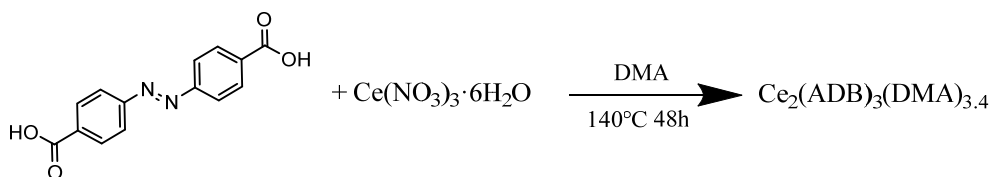
2. Experimental

2.1 Synthetic procedures for the MOFs

2.1.1 Synthesis of $\text{Ce}_2(\text{NDC})_3(\text{DMF})_2$

Chemicals were obtained from Alfa Aesar ($\text{Ce}(\text{NO}_3)_3 \cdot 6\text{H}_2\text{O}$, 99,5% purity), TCI (H_2NDC , 98 % purity) and Grüssing (DMF, 99 % purity) were used without further purification. Synthesis conditions were optimized by means of high-throughput methods (see section 1.2.1) To this purpose, reactors containing 24 Teflon liners with a maximum volume of 2 mL were filled with the reaction mixtures and then heated at the set temperature for a fixed time. After recovery of the solid product by filtration automated PXRD measurements permitted to identify the conditions where yield and crystallinity of the product were optimal. Once these optimal conditions were established, for the scaled-up synthesis of $\text{Ce}_2(\text{NDC})_3(\text{DMF})_2$ 778.3 mg (3.6 mmol) of 2,6-naphthalenedicarboxylic acid (H_2NDC), 13.2 mL (170 mmol) of DMF and 6 mL of a 130 g/L $\text{Ce}(\text{NO}_3)_3 \cdot 6\text{H}_2\text{O}$ solution in DMF (0.3 M and thus 1.8 mmol of Ce) were combined in a 25 mL Teflon lined autoclave. This vessel was closed and heated to 160°C in 3 h, kept at this temperature for 72 h and cooled down to RT in 12 h. The product was filtered off, washed with fresh DMF in the funnel for three times and dried on the filter paper under air flow. The yield of the reaction using the formula $\text{Ce}_2(\text{NDC})_3(\text{DMF})_2$ is 89% (based on the metal source). The product appears in the form of pale yellow needle-like crystals in the half-millimeter range of dimensions along the “long” axis of the crystal (see optical image in Figure 1).

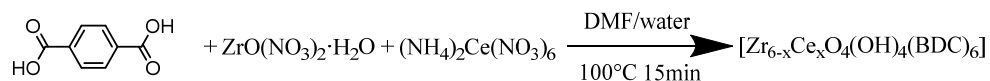
2.1.2 Synthesis of $\text{Ce}_2(\text{ADB})_3(\text{DMA})_{3,4}$



The synthesis of $\text{Ce}_2(\text{ADB})_3(\text{DMA})_{3,4}$ MOF was optimized by means of high-throughput methods (see section 1.2.1 and) under solvothermal conditions, details about the explored synthetic parameters are reported elsewhere.¹³⁰ Thus, 1.5 mmol (0.41 g) of azobenzene-4,4'-dicarboxylic acid (H_2ADB 95.0%, TCI) and 0.75 mmol (2.5 mL of a 0.3 M concentrated DMA solution) of $\text{Ce}(\text{NO}_3)_3 \cdot 6\text{H}_2\text{O}$ (99.0%, Sigma-Aldrich) were dissolved in 7.5 mL DMA (N,N-dimethylacetamide, 99.5%, Sigma-Aldrich). Then, the mixture was sealed in a 100 mL Teflon-lined stainless steel

autoclave and heated at 140 °C for 48 h. After cooling to RT (cool down rate: 0.4 °C/min), the product was centrifuged to remove the supernatant. Then it was washed with fresh DMA (2 mL) to remove unreacted linker and impurities. Finally, the product was dried at RT with a dry N₂ flow. The final yield was 0.59 g (57%, based on the metal source and the Ce₂(ADB)₃(DMA)_{3,4} formula).

2.1.3 Synthesis of Ce/Zr-UiO-66



Cerium (IV) ammonium nitrate (98 %, (NH₄)₂Ce(NO₃)₆, Alfa Aesar), 1,4-benzenedicarboxylic acid (98 %, H₂BDC, Sigma Aldrich), zirconyl nitrate monohydrate (ZrO(NO₃)₂·H₂O, ABCR), zirconium(IV) chloride (99 %, ZrCl₄, Sigma Aldrich), N,N-dimethylformamide (99 %, DMF, Grüssing) and formic acid (100 %, HCOOH, BASF) were used as obtained. The synthesis of the mixed-metal Ce/Zr-UiO-66 compounds was previously reported by Lammert et al.^{54,64} and this procedure was also used in the current study. The Ce/Zr-UiO-66 compounds were synthesized using Pyrex glass reaction tubes (maximum volume 14 mL). The linker 1,4-benzenedicarboxylic acid (H₂BDC, 127.6 mg) was dissolved in N,N-dimethylformamide (DMF, 3.6 mL) and transferred into the glass reactor. Subsequently the formic acid (HCOOH, 100 %, 1.03 mL) and finally the aqueous solutions of (NH₄)₂Ce(NO₃)₆ (0.533 M) and ZrO(NO₃)₂·H₂O (0.533 M) were added in the desired stoichiometry (Table 5). The total volume of the two metal salt solutions was always 1.2 mL.

Table 5 – Parameters for the synthesis of pure Ce-UiO-66 and mixed-metal Ce/Zr-UiO-66 samples. Ce, Zr, H₂BDC and HCOOH values are intended as mutual molar ratios.

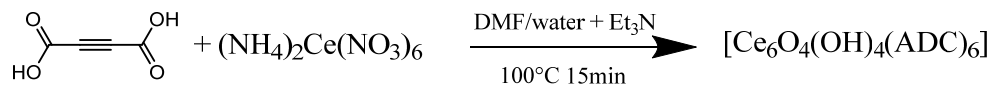
Sample	Ce	Zr	H ₂ BDC	HCOOH	Ce [μL]	Zr [μL]
Ce5	0.3	5.7	7.2	256	60	1140
Ce10	0.6	5.4	7.2	256	120	1080
Ce15	0.9	5.1	7.2	256	180	1020
Ce22	2.0	4.0	7.2	256	400	800
Ce45	4.0	2.0	7.2	256	800	400
Ce84	5.5	0.5	7.2	256	1100	100
Ce-UiO-66	6.0	0.0	7.2	256	1200	0

The glass reactors were heated under stirring for 15 min at 100 °C using an aluminum heating block. After the synthesis the glass reactor was cooled down to room temperature and the precipitate was isolated by centrifugation. The mother liquor was decanted off and the MOF were re-dispersed and centrifuged two times in DMF (2

mL) and three times in acetone (2 mL). Finally, the MOF was dried in air at 70 °C. The addition of formic acid to the synthesis mixture worked as a modulator, slowing down the kinetics of the reaction and thus improving the crystallinity of the product. The nomenclature of the samples, Cexx, stands for the percentage of Ce metal in respect of the total metal content of the MOF.

Zr-UiO-66 was synthesized following the procedure reported by Cavka et al.²² Zirconium(IV) chloride (530 mg) and 1,4-benzenedicarboxylic acid (H₂BDC, 340 mg) were dissolved in N,N-dimethylformamide (DMF, 20 mL). This mixture was sealed in a steel autoclave and placed in an oven at 120 °C for 24 h. After the synthesis the solvothermal reactor was cooled down to room temperature and the precipitate was centrifuged. The mother liquor was decanted off and the product was re-dispersed and centrifuged two times in DMF (5 mL) and three times in acetone (5 mL). Finally, the MOF was dried in air at 70 °C.

2.1.4 Synthesis of Ce-UiO-66-ADC



Cerium (IV) ammonium nitrate (98 %, (NH₄)₂Ce(NO₃)₆, Sigma-Aldrich), acetylenedicarboxylic acid (95 %, H₂ADC, TCI Chemicals), N,N-dimethylformamide (99 %, DMF, Sigma-Aldrich) and triethylamine (99 %, Et₃N, Sigma-Aldrich) were used as obtained. The synthesis procedure was optimized using high-throughput methods (section 1.2.1) starting from the one reported by Lammert et al.⁵⁴ in 2015 using different ditopic linkers, details about the optimization of the synthesis can be found elsewhere.^{131,132} 644 mg of H₂ADC, 32 mL of DMF, 790 μL of triethylamine and 10.66 mL of 0.0533 M of Cerium(IV) Ammonium Nitrate (CAN) aqueous solution were added to a thick-walled glass tube with a screw cap which was closed and inserted into a pre-heated oven and kept at 100°C for 15 minutes. Product was then centrifuged and briefly washed with fresh acetone to let it dry at room temperature. The final yield was 32% based on the metal source and using the formula [Ce₆O₄(OH)₄(ADC)₆]. The addition of triethylamine to the synthesis mixture worked as a deprotonating agent to the linker, speeding up the reaction by a high degree. This is needed to improve the yield of the reaction and to avoid the linker decarboxylation (see section 3.4.5).

2.2 Experimental methods

2.2.1 X-Ray diffraction techniques

Single-crystal X-ray diffraction (SCXRD) data for the $\text{Ce}_2(\text{NDC})_3(\text{DMF})_2$ MOF were recorded on a Stoe IPDS diffractometer equipped with an image-plate detector using MoK_α radiation; a crystal was glued to the tip of a glass capillary and cooled down to about 153 K with a cold nitrogen blower. Direct methods implemented in the SHELXS-2013 code were used in order to solve the structure, while crystal structure refinement, using full-matrix least-squares algorithms, was done using SHELXL-2013.¹³³ All non-hydrogen atoms were refined with anisotropic displacement parameters while C-H atoms were positioned via a riding model and refined isotropically. Numerical absorption correction was carried out by using X-Shape and X-Red from the X-Area package.¹³⁴ Diffraction data of the $\text{Ce}_2(\text{NDC})_3$, after desolvation, were acquired at 100 K using a Bruker D8 Venture diffractometer equipped with a Photon100 CMOS detector and using MoK_α radiation. Several crystals were screened for diffraction due to poor diffraction. The crystals showed signs of degradation, with visible cracks and opacity. The diffraction frames show very broad reflections and diffuse scattering. The Material Studio software package from Accelrys was used during the crystal structure pictures making.

The crystal structure of the $\text{Ce}_2(\text{ADB})_3(\text{DMA})_{3.4}$ was solved with single-crystal diffraction data collected using an Oxford Xcalibur CCD area detector diffractometer. Structure solution was performed by SIR2011¹³⁵ and refinement with full-matrix least-squares by SHELXL-2013.¹³³ Mercury was used for crystal structure drawing.¹³⁶

Powder X-ray diffraction (PXRD) patterns of $\text{Ce}_2(\text{NDC})_3(\text{DMF})_2$, $\text{Ce}_2(\text{ADB})_3(\text{DMA})_{3.4}$ and Ce-UiO-66-ADC were taken with a Panalytical X'Pert PRO MPD diffractometer equipped with a CuK_α source operating in Debye-Scherrer geometry. Borosilicate glass capillaries with inner diameter of 0.5 mm were used as sample holders. Scattered photons were collected by a X'Celerator detector equipped with a Ni filter in order to attenuate K_β radiation. High-resolution diffractograms of pure Ce, pure Zr and $\text{Zr}_{3.54}\text{Ce}_{2.46}$ -UiO-66 samples after desolvation at 180°C were conducted at the high-resolution powder diffraction beamline of the European Synchrotron Radiation Facility (ID22, ESRF, Grenoble, France).

Pawley and Rietveld refinements were carried out using the TOPAS-Academic¹³⁷ V5 software. Peaks were fitted using a Pseudo Voigt profile and all the diffractometers were modeled using a simple axial model.

2.2.2 Thermal analysis techniques

Variable temperature PXRD (VTXRD) measurements on $\text{Ce}_2(\text{NDC})_3(\text{DMF})_2$ were collected on a STOE Stadi P combi with CuK_α radiation in transmission geometry and equipped with a furnace; open quartz capillaries with an inner diameter of 0.5 mm were used as sample holders. The temperature program was set to measure a diffractogram every 25°C from RT to 600°C, waiting at each step 15 min at the setpoint before collecting data. The sample was heated at a rate of 3°C/min. Diffraction patterns of $\text{Ce}_2(\text{ADB})_3(\text{DMA})_{3.4}$ and Ce-UiO-66-ADC, instead, have been collected with a PW3050/60 X'Pert PRO MPD diffractometer from PANalytical working in Bragg-Brentano geometry, using as source a ceramic tube with a Cu anode. Scattered photons were collected by a X'Celerator detector equipped with Ni filter to attenuate K_β . Non-ambient chamber Anton Paar XRK900 with Be windows was used to collect the PXRD data in dynamic vacuum with a ramp rate of 3°C/min and the sample was held in an isothermal temperature for 25 min prior to every 2 θ scan.

Thermogravimetric analysis (TGA) data were recorded with a TA instruments Q600 thermobalance in a dry air or N_2 flow (100 mL/min) with a ramp of 3°C/min from RT to 700°C working with about 10 mg of sample in an open alumina crucible for all the samples reported in the present document.

2.2.3 X-ray absorption spectroscopy

All XAS measurements except for those for Ce10 sample were performed at BM31 beamline¹³⁸ of European Synchrotron Radiation Facility (ESRF, Grenoble, France). The ring was operating in 7/8 multibunch mode with the current between 160 and 200 mA. All the measurements at BM31 were conducted in transmission mode using Si (111) double-crystal monochromator. Three ionization chambers were used for photon detection (30 cm long, 1 bar filling, 1 kV voltage), the third one being used for energy calibration with CeO₂ reference. Gas mixtures used for filling the ionization chambers and resulting absorption values are given in Table 6.

Table 6 – Filling of the ionization chambers for the XAS experiments.

Edge	Edge energy, eV	I₀ mixture	I₁ and I₂ mixture
Ce L ₃ edge	5723	30% N ₂ in He	10% Ar in He
Zr K edge	17998	30% Ar in He	10 % Kr in Ar
Ce K edge	40443	15% Kr in Ar	100% Kr

XAS spectra for Ce10 sample were collected at BM23 beamline of the ESRF. The experimental setup was similar to the one at BM31, except for the use of Si (311) monochromator for the measurements at Ce K-edge.

All MOFs were measured in the form of self-supporting pellets of 5 mm diameter, packed using the power achievable pressure. The mass of MOF powder for sample preparation was optimized by XAFSmass software.¹³⁹

XAS data analysis was performed using Athena program for averaging and normalizing data and Artemis code for EXAFS fitting, both codes coming from Demeter package.¹⁴⁰ Scattering amplitudes and phase shifts were calculated by FEFF6¹⁴¹ code bundled with Artemis.

2.2.4 Vibrational spectroscopy

Vibrational infrared spectra (FTIR) were collected in transmission mode using a Thermo Scientific Nicolet 6700 spectrometer equipped with a liquid N₂ cooled MCT detector on thin self-supporting pellets. Samples of Ce₂(NDC)₃(DMF)₂ and Ce-UiO-66-ADC were outgassed in dynamic high vacuum ($5 \cdot 10^{-4}$ mbar) at the reported temperature for in a homemade quartz cell equipped with KBr windows that allows also controlled dosages of gaseous probes (i.e. CD₃CN) in an *in-situ* manner.

Raman spectra were collected on a sample of Ce-UiO-66-ADC that was prepared and pretreated in the same manner as for the transmission FTIR measurements, albeit using another type of locally constructed airtight cell featuring a suprasil quartz cuvette in place of KBr windows. Raman spectra were recorded over a wavenumber range of 3200-100 cm⁻¹ on a Renishaw inVia Raman microscope spectrometer in backscattering mode. A 785 nm diode laser was used for the excitation, and the scattered photons by were dispersed by a 1200 lines/mm grating monochromator and collected on a CCD camera whose collection optic was set at 20X objective summing up 20 scans with an exposition time of 20 s per step working at the 10% of the total laser power and using a rotating sample holder of local construction¹⁴² to overcome the degradation of the sample under the beam.

2.2.5 Volumetric adsorption

A Micromeritics ASAP 2020 apparatus was used to measure both N₂ and CO₂ adsorption isotherms for all the materials studied in the present thesis. While for the measure at -196°C a classical liquid nitrogen dewar was used as isothermal bath, the data at -78°C was measured using a dry ice / acetone cold bath whose temperature was accurately measured with a Pt100 thermometer and then used to obtain the saturation pressure looking at the published phase diagram for carbon dioxide. For the CO₂ measurement in the 0°C-60°C range the temperature was kept stable by means of an isothermal water bath (Julabo F25). A local construction setup was employed which permitted us to thermally activate Ce₂(NDC)₃(DMF)₂ and Ce₂(ADB)₃(DMA)_{3,4} materials (ramping at 5°C/min to the target temperature and keeping this temperature for 2 h) in dynamic vacuum and then measure the isotherms without exposing the sample to air.

3. Results and discussion

3.1 $\text{Ce}_2(\text{NDC})_3(\text{DMF})_2$

The synthesis procedure of $\text{Ce}_2(\text{NDC})_3(\text{DMF})_2$ described in section 2.1.1 was optimized by the means of high-throughput methods, also described earlier in the introduction in section 1.2.1. An optical micrograph of the as-synthesized compound is shown in Figure 12 below.



Figure 12 – Optical micrograph of $\text{Ce}_2(\text{NDC})_3(\text{DMF})_2$ crystals.

3.1.1 Thermal activation

$\text{Ce}_2(\text{NDC})_3(\text{DMF})_2$ was studied upon thermal treatment by means of TGA, VT-XRD and in-situ FTIR spectroscopy. The data resulting from these experiments are enlisted below.

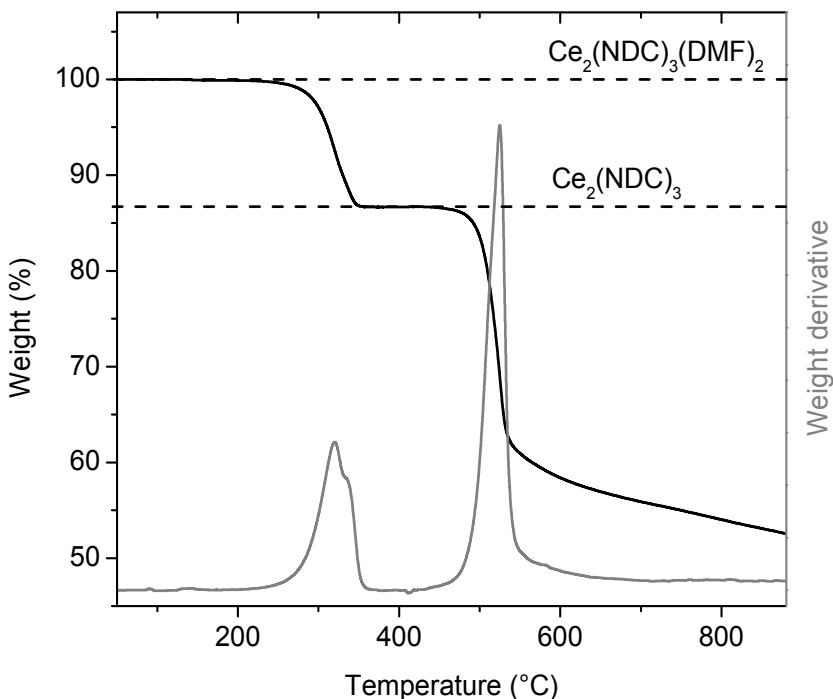


Figure 13 – TGA curve of $\text{Ce}_2(\text{NDC})_3(\text{DMF})_2$ in a dry nitrogen atmosphere (black), its derivative (DTA) is reported in grey color.

The TGA curve collected on $\text{Ce}_2(\text{NDC})_3(\text{DMF})_2$ is characterized by the presence of a steep weight loss at an onset temperature of 293°C that can be well assigned to the desorption of all the structural DMF molecules present to give $\text{Ce}_2(\text{NDC})_3$. Such assignation is strongly suggested by a calculation made on the stoichiometry of the pristine compound: calculating the amount of weight that must change during the desorption of those DMF molecules one obtains a good agreement with the experiment (dashed lines in Figure 13). For this reason, a static temperature of 300°C was adopted to desolvate the pristine material and obtain $\text{Ce}_2(\text{NDC})_3$ when needed for the other experiments (FTIR, SCXRD, XAS, adsorption measurements). At

higher temperatures the weight does not change till about 440°C. At an onset temperature of 502°C the material is decomposing (pyrolysis) yielding CeO₂ and coke-like species, as expected for the thermal decomposition of a Ce-MOF in an inert atmosphere.³⁶

The FTIR spectrum collected on a thin self-supporting pellet of Ce₂(NDC)₃(DMF)₂ is reported in Figure 14. The same pellet was thermally activated at 300°C for 2 h under dynamic vacuum with a setup of local construction: this treatment leads to the desolvation into Ce₂(NDC)₃ as hypothesized from TGA data. The resulting spectrum is also shown in Figure 14.

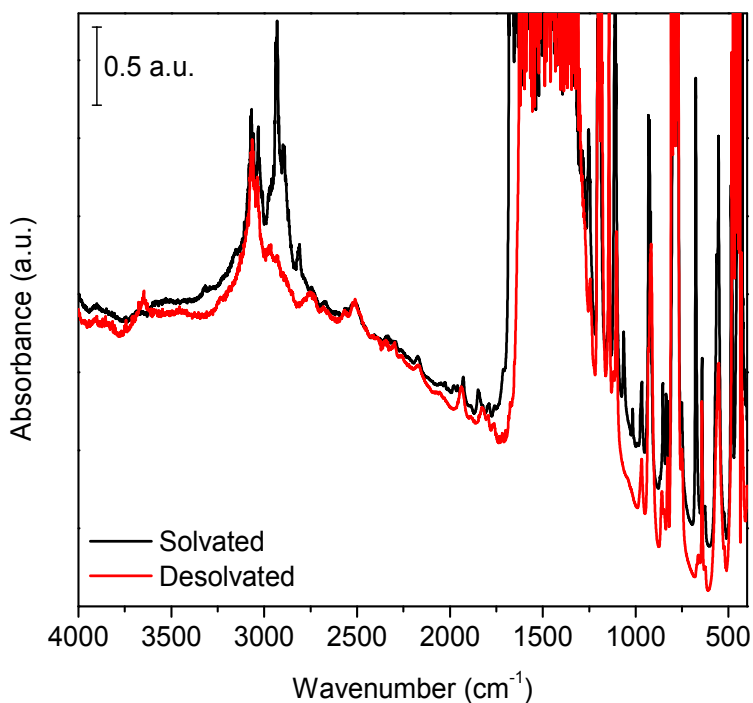


Figure 14 – FTIR spectra of Ce₂(NDC)₃(DMF)₂ (black line) and Ce₂(NDC)₃ (red line).

Very intense bands coming from the symmetric and asymmetric stretching of carboxylates are clearly visible in the 1630-1300 cm⁻¹ range, as expected for a MOF. In the region below these signals, also called fingerprint region, a great number of bands is present due to complex vibrational modes involving mainly the naphthalenic

aromatic rings. Around 3000 cm^{-1} an absorption due to C-H stretching is clearly visible: while the band at 3070 cm^{-1} can be undoubtedly assigned to the naphthalenic hydrogens, the one at 2930 cm^{-1} is due to aliphatic CHs coming from DMF.¹⁴³ This band is vanishing with thermal activation confirming the hypothesis drawn from the TGA data together with the diminishing of the shoulder at 1670 cm^{-1} due to the carbonyl stretching in DMF molecules. The fact that only signals coming from DMF are changing upon thermal activation is again suggesting the hypothesis for which the MOF can be successfully desolvated by such a treatment.

VTXRD data (Figure 15), complementarily to TGA and *in-situ* FTIR, are showing a similar behavior. Three different phases can be recognized from the patterns, which are enlisted below.

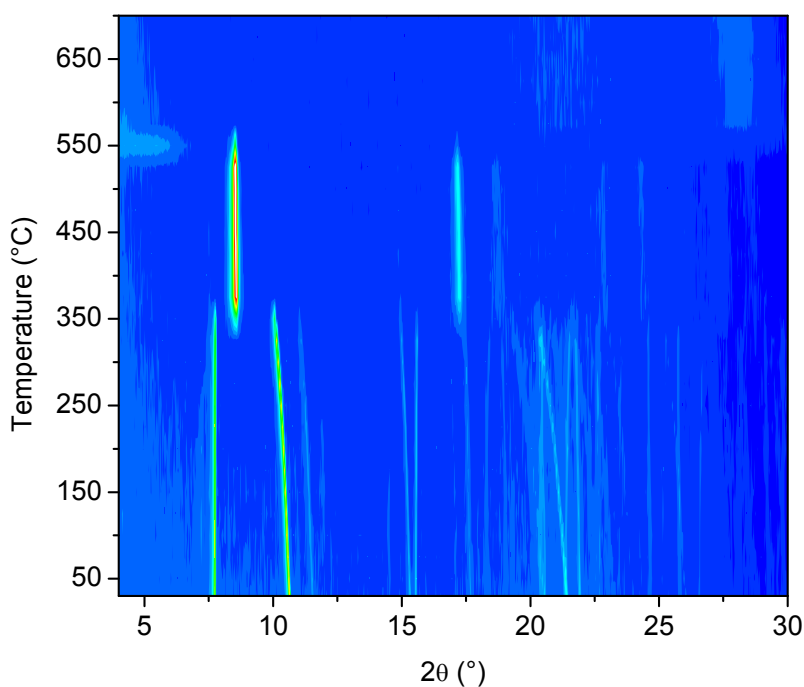


Figure 15 – VTXRD data collected on $\text{Ce}_2(\text{NDC})_3(\text{DMF})_2$ visualized as a contour plot. ($\lambda = 1.5406\text{ \AA}$)

- From RT to 360°C : $\text{Ce}_2(\text{NDC})_3(\text{DMF})_2$
- From 360°C to 550°C : $\text{Ce}_2(\text{NDC})_3$, as supported by TGA and FTIR data.

- Above 550°C: Ce₂(NDC)₃ pyrolysis to nano-sized CeO₂³⁶ and coke-like species.

PXRD Reflections clearly undergo a shift upon heating (before phase transformation associated to the loss of DMF molecules) that is caused by thermal expansion effects (the higher the temperature, the larger the cell parameter, the lower the angle of the diffraction signal). The Ce₂(NDC)₃ phase is probably crystallizing in a less symmetric space group, as the number of peaks that are visible is lower; for this phase no thermal effect on the cell parameters is visible till the MOF collapses. The difference in temperature between the phase transformation observed in TGA and FTIR experiments (at about 300°C) and the one happening here (360°C) is probably due to the different atmospheres used in these experiments i.e. a stream of inert gas for TGA and dynamic vacuum for TGA and FTIR, respectively, and static conditions for the VTXRD experiment. The crystalline structure of these compounds will be discussed in the following section.

3.1.2 Crystal structure

The crystal structures of the as-synthesized $\text{Ce}_2(\text{NDC})_3(\text{DMF})_2$ and fully desolvated $\text{Ce}_2(\text{NDC})_3$ compounds, were determined from SC-XRD data and taking also into account the input coming from the EXAFS data about the atoms surrounding Ce cations. Table 7 reports the crystallographic data of both compounds.

Table 7 – Crystal data for $\text{Ce}_2(\text{NDC})_3(\text{DMF})_2$ and $\text{Ce}_2(\text{NDC})_3$.

	$\text{Ce}_2(\text{NDC})_3(\text{DMF})_2$	$\text{Ce}_2(\text{NDC})_3$
Formula	$\text{C}_{84}\text{H}_{64}\text{Ce}_4\text{N}_4\text{O}_{28}$	$\text{C}_{36}\text{H}_{18}\text{Ce}_2\text{O}_{12}$
Formula weight ($\text{g}\cdot\text{mol}^{-1}$)	2137.88	922.76
Crystal system	<i>Orthorhombic</i>	<i>Trigonal</i>
Space group	$Pca2_1$	$P\bar{3}c1$
a (Å)	19.836(4)	11.845(5)
b (Å)	8.7339(17)	11.845(5)
c (Å)	45.451(9)	7.698(3)
$\alpha = \beta$ (°)	90	90
γ (°)	90	120
Cell volume (Å ³)	7874(3)	935.3(8)
Temperature (K)	153(2)	100(2)
Abs. coefficient (mm^{-1})	2.357	2.460
Calc. density ($\text{g}\cdot\text{cm}^{-3}$)	1.803	1.606
Z	4	2
Measured reflections	11957	108
R_{int}	0.0519	0.0727
No. of parameters	1082	29
R_1	0.0519	0.0729
wR (all data)	0.1317	0.1205
Largest. diff. peak ($\text{e}\cdot\text{Å}^{-3}$)	-1.920 / 2.677	-0.555 / 0.450

The solvated compound, $\text{Ce}_2(\text{NDC})_3(\text{DMF})_2$, crystallizes in an orthorhombic space group with a structure that consists of distorted pentagonal bipyramidal Ce(III) cations coordinated by carboxylates coming from different linkers and one oxygen atom coming from an adsorbed DMF molecule (see Figure 16 for a structure representation).

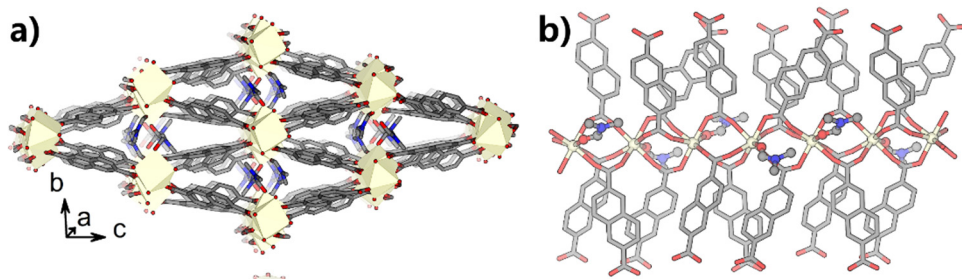


Figure 16 – Pictorial representation of the crystal structure $\text{Ce}_2(\text{NDC})_3(\text{DMF})_2$, Color code: Ce (dark yellow), O (red), C (gray), N (blue), H (omitted)

Every Ce(III) cation is sharing three different carboxylate groups, coming from the naphthalenic moieties, to form extended chains parallel to the a-axis. The same linker molecules are forming inter-chain bridges to give a network structure with diamond-shaped channels parallel to the Ce(III) chains (Figure 16b).

Upon desolvation by thermal treatment in dynamic vacuum (300°C for 2 h), see VTXRD and TGA data reported below, the crystal structure of $\text{Ce}_2(\text{NDC})_3(\text{DMF})_2$ undergoes a phase transition characterized by the loss of the DMF molecules and thus becomes $\text{Ce}_2(\text{NDC})_3$. The quality of the diffraction data collected on a single-crystal of $\text{Ce}_2(\text{NDC})_3$ is significantly worsened from the one collected on $\text{Ce}_2(\text{NDC})_3(\text{DMF})_2$ and consists of very diffuse diffraction peaks (see also Figure 19). These signals are also broadening with the scattering angle, giving readable diffraction data only to 1.3 Å. Nevertheless data reduction with the hexagonal space group P-3c1 (see Table 7 for details) proceeded without issues giving a structure depicted in Figure 17 below.

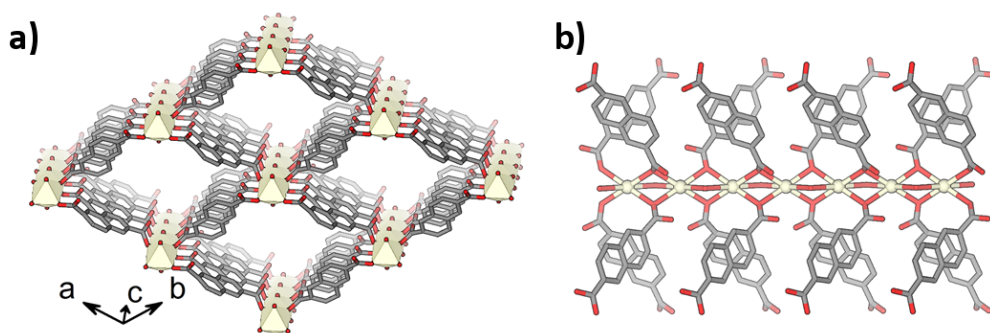


Figure 17 – Pictorial representation of the crystal structure $\text{Ce}_2(\text{NDC})_3$, Color code: Ce (dark yellow), O (red), C (gray), N (blue), H (omitted).

The solved structure for $\text{Ce}_2(\text{NDC})_3$ shows a hexagonal crystal structure consisting of linear chains of Ce cations, as for the solvated structure, aligned to the crystal c-axis. As there is disorder in the linker structure, that cannot be resolved directly, the

occupancies of the linker has been set to one half in order to accommodate also a linker that bridges two Ce chains in a way that “closes the pores” shown in Figure 17a. These occupancies factors are in accordance to the proposed stoichiometry of the compound, $\text{Ce}_2(\text{NDC})_3$, that is also confirmed by TGA measurements (see Figure 13) Figure 18 represents the structure of the desolvated compound plotting all linker atoms, even with non-integer occupancies.

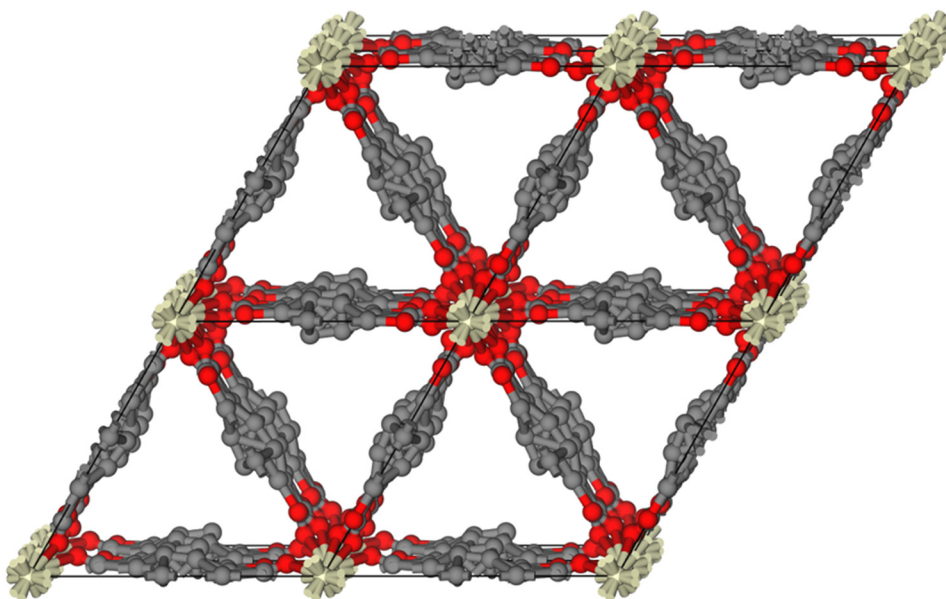


Figure 18 – Pictorial representation of the crystal structure of $\text{Ce}_2(\text{NDC})_3$ viewed along the c-axis, showing all possible positions of the atoms.

Considering the disorder associated to the linker positions, the presence of diamond-shaped channels, as present in the solvated structure, must be declined and instead triangular channels (as shown in Figure 18) must be considered. It has to be noticed what other MOFs characterized by a flexible structure, such as MIL-53^{144,145}, upon adsorption of gas molecules are not showing such rearrangement of its constituents upon thermal activation.

With the aim to demonstrate that the proposed structures found by SCXRD are the only crystalline phases present in the bulk samples Pawley PXRD refinements were done on the diffractograms using the unit cells coming from Table 7. The results are enlisted in Figure 19 and Table 8 below.

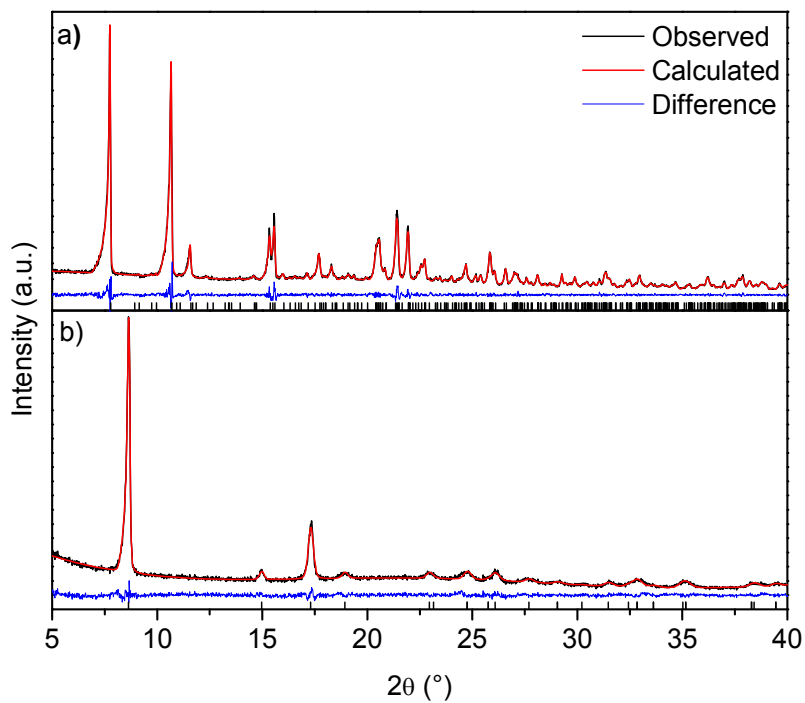


Figure 19 – Pawley fits on PXRD patterns of Ce₂(NDC)₃(DMF)₂ (a) and Ce₂(NDC)₃ (b). Observed, calculated and residuals are drawn respectively in black, red and blue lines, allowed reflections are reported by black ticks. ($\lambda = 1.5406 \text{ \AA}$).

Table 8 – Comparison between cell parameters obtained by SC-XRD and Pawley refinements on $\text{Ce}_2(\text{NDC})_3(\text{DMF})_2$ and $\text{Ce}_2(\text{NDC})_3$ PXRD patterns

$\text{Ce}_2(\text{NDC})_3(\text{DMF})_2$	Pawley	SC-XRD
a (Å)	19.791(3)	19.836(4)
b (Å)	8.865(11)	8.7339(17)
c (Å)	45.392(6)	45.451(9)
Volume (Å ³)	7964(2)	7874(3)
$\text{Ce}_2(\text{NDC})_3$	Pawley	SC-XRD
a (Å)	11.823(2)	11.845(5)
b (Å)	11.823(2)	11.845(5)
c (Å)	7.675(4)	7.698(3)
Volume (Å ³)	929.1(5)	935.3(8)

As it is evident from the fit results, the cell parameters coming from the powder diffraction data are in accordance with those of single-crystal data refinements. It is relevant to notice also that while single-crystal data is collected at low temperatures (100-150 K), the powder one is measured at room temperature: for this reason such differences in cell lengths have to be accounted to a thermal expansion effect. No new crystalline phase can be recognized looking at the fits in Figure 19 confirming the purity of the synthesized compounds.

3.1.3 X-ray absorption spectroscopy

X-ray absorption spectroscopy (XAS) was exploited in studying this material as i) a method to determine the oxidation state of Ce before by means of XANES spectroscopy before and after thermal activation and, more importantly, ii) confirm the structural results coming from SC-XRD through EXAFS fitting analysis. Figure 20 shows XANES spectra of both $\text{Ce}_2(\text{NDC})_3(\text{DMF})_2$ and $\text{Ce}_2(\text{NDC})_3$ and their comparison with Ce(III) and Ce(IV) standards.

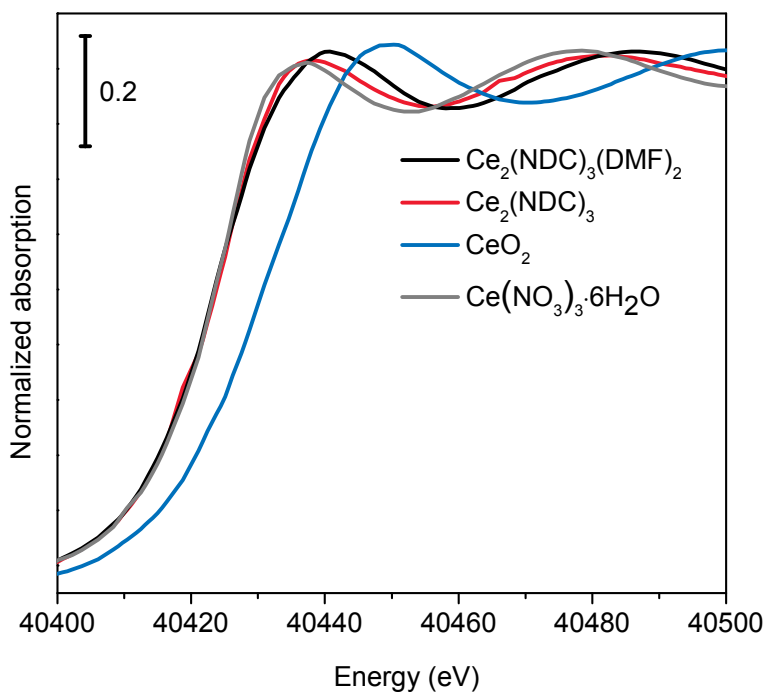


Figure 20 – Ce K-edge XANES spectra of $\text{Ce}_2(\text{NDC})_3(\text{DMF})_2$ (black line) and $\text{Ce}_2(\text{NDC})_3$ (red line) compared to those of Ce(IV) oxide and Ce(III) nitrate hexahydrate (respectively blue and grey curves).

The absorption edges of both $\text{Ce}_2(\text{NDC})_3(\text{DMF})_2$ and $\text{Ce}_2(\text{NDC})_3$ correspond to the one of Ce(III) comparing it with the Ce(III) nitrate hexahydrate standard. This indicates the conservation of the 3+ oxidation state during the desolvation of the material, despite the phase transition.

As a complement to the long-range structural analysis done with SC-XRD (and its limitations due to inherent disorder) Ce K-edge EXAFS spectra were collected for the solvated and desolvated materials. As starting point for the structural EXAFS fitting of the atoms surrounding Ce, the crystal structure coming from X-ray diffraction was used. To increase the reliability of the fit the scattering paths from Ce atoms to light atoms were grouped in three O and three C shells reducing the number of parameters used in the fitting process. Being Ce-Ce a significant scattering path (due to the high Z of Ce), this path has been included in the model for $\text{Ce}_2(\text{NDC})_3$. EXAFS fitting results are shown in Figure 21 and in Table 9 below.

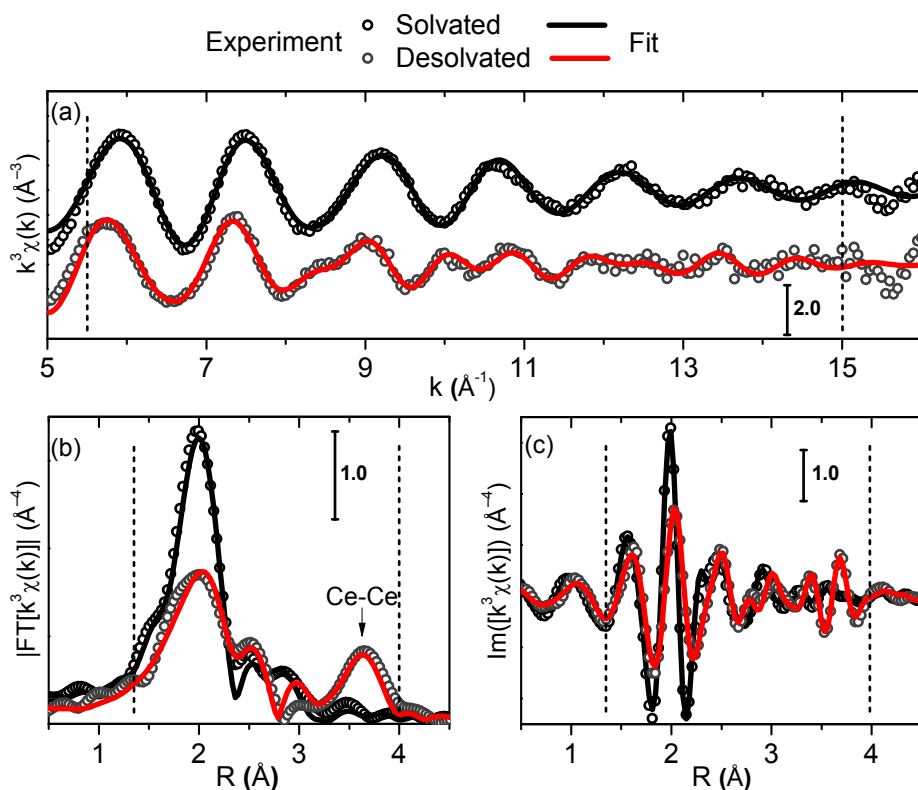


Figure 21 – Ce K-edge EXAFS spectra of $\text{Ce}_2(\text{NDC})_3(\text{DMF})_2$ and $\text{Ce}_2(\text{NDC})_3$ (dots). The fit results, spectra (a), magnitude (b) and imaginary part (c) are shown by black and red lines for the solvated and the desolvated compounds, respectively.

Table 9 – Fitting results of the Ce K-edge EXAFS spectra for Ce₂(NDC)₃(DMF)₂ and Ce₂(NDC)₃.

Parameter	Ce ₂ (NDC) ₃ (DMF) ₂	Ce ₂ (NDC) ₃
R-factor	0.02	0.03
Fitting range in k, Å ⁻¹		5.5 – 15
Fitting range in R, Å		1.35 – 4
N _{ind}		15.7
N _{par}	5	9
S ₀ ²	1.0	1.0
ΔE	-0.3(1.7)	2.3(2.8)
N _{O1}	2.33	3
R _{O1} , Å	2.40(1)	2.44(1)
σ ² _{O1} , Å ²	0.006(1)	0.009(1)
N _{O2}	2.33	3
R _{O2} , Å	2.43(1)	2.49(1)
σ ² _{O2} , Å ²	0.006(1)	0.010(1)
N _{O3}	2.33	3
R _{O3} , Å	2.46(1)	2.53(1)
σ ² _{O3} , Å ²	0.006(1)	0.010(1)
N _{C1}	2.33	3
R _{C1} , Å	3.28(2)	2.98(2)
σ ² _{C1} , Å ²	0.004(2)	0.005(1)
N _{C2}	2.33	3
R _{C2} , Å	3.36(2)	3.46(3)
σ ² _{C2} , Å ²	0.004(2)	0.006(1)
N _{C3}	2.33	3
R _{C3} , Å	3.43(2)	4.15(9)
σ ² _{C3} , Å ²	0.004(2)	0.006(1)
N _{Ce}	-	2
R _{Ce} , Å	-	3.87(2)
σ ² _{Ce} , Å ²	-	0.009(1)

The EXAFS fitting confirmed the structural features observed by SC-XRD with good R-factors and reasonable parameters for both Ce₂(NDC)₃(DMF)₂ and Ce₂(NDC)₃. The Ce-Ce (Figure 21) distance can be observed only for Ce₂(NDC)₃ as with thermal activation they become closer (3.87(2) Å by EXAFS vs. 3.849(2) Å from SC-XRD). As concerns Ce-O and Ce-C distances a general disordering (i.e. broadening of the range span of those bonds) is observed upon desolvation. This can be correlated with the strain associated to the removal of the solvent from the pores and the subsequent rearrangement of the crystal structure.

3.1.4 Adsorption properties

In order to measure the surface area and the porosity of $\text{Ce}_2(\text{NDC})_3$, N_2 was dosed at -196°C with an automatic volumetric apparatus in order to measure an adsorption isotherm. The results (reported in Figure 22) show a nearly negligible adsorption in the whole pressure range (0-1 p/p_0 range) indicating nil surface area or porosity whatever the model used to reduce this data (e.g. Langmuir or BET models).

CO_2 was dosed at a temperature of -78°C as an alternative probe to N_2 in order to address the end of measuring a specific surface area on $\text{Ce}_2(\text{NDC})_3$ giving isotherms reported in Figure 22.

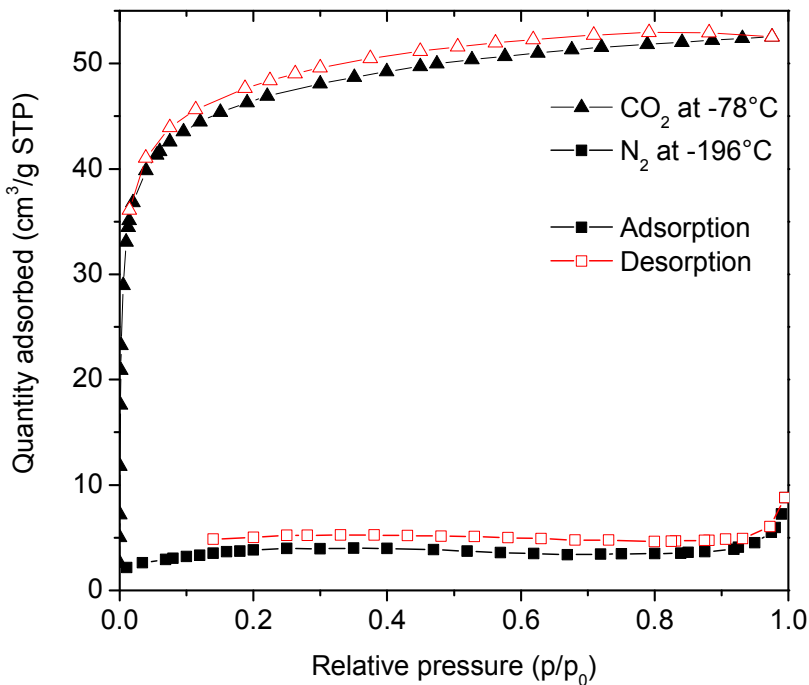


Figure 22 – $\text{Ce}_2(\text{NDC})_3$ adsorption isotherms of N_2 at -196°C and CO_2 at -78°C .

The two molecules are represented by squares and triangles, respectively. Adsorption branches is reported by solid black symbols while the desorption one is represented by open red symbols.

The adsorption isotherm of CO_2 can be assigned to a Type I^{100} , typical of microporous materials.

Such results indicate that $\text{Ce}_2(\text{NDC})_3$ is characterized by a kind of porosity that cannot be traditionally determined by N_2 adsorption at -196°C . The application of BET and Langmuir models in order to extract a specific surface area gave results enlisted in Table 10 .

Table 10 – Specific surface area values measured on $\text{Ce}_2(\text{NDC})_3$.

Probe	BET (m^2/g)	Langmuir (m^2/g)
N_2 at -196°C	–	–
CO_2 at -78°C	170(3)	222(1)

It must be considered that the application of CO_2 in the determination of specific surface area and porosity of polar materials, like MOFs and siliceous porous materials (e.g. mesoporous silica like SBA-15 or MCM-41 or zeolites) is not recommended^{100,146,147} as the type of interaction that is established between the probe and the surface of the material is too specific, principally due to the high quadrupolar moment of CO_2 .

A series of hypotheses for which the surface area was zero for N_2 and not for CO_2 can be drawn:

- The kinetic diameter of CO_2 is smaller than the one of N_2 : in case of ultra-microporous material carbon dioxide can enter in pores where nitrogen cannot.
- The experiment with CO_2 is done at a temperature which is substantially higher than the one of liquid nitrogen, being 118 K higher. For this reason the diffusion kinetics of carbon dioxide can improve significantly. In this case the nitrogen isotherm must be considered not at equilibrium.
- This particular material, $\text{Ce}_2(\text{NDC})_3$, is characterized by a phase transformation that occurs at the temperature of -196°C which converts it into a non-porous one. In order to catch this an X-ray diffraction experiment must be carried out at the temperature of liquid nitrogen. Such an experiment cannot be performed with the equipment currently available.

Apart from the specific surface area and porosity measurements the uptake performances were measured by volumetric CO₂ adsorption measurements, reported below in Figure 23.

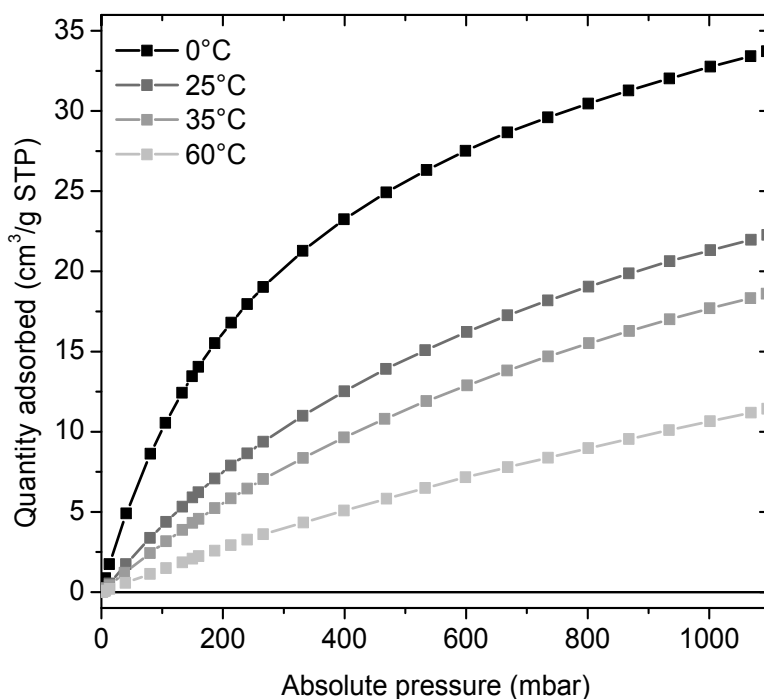


Figure 23 – CO₂ adsorption isotherms of Ce₂(NDC)₃ collected at different temperatures. Desorption branches (superimposable to adsorption ones) are omitted for the sake of clarity.

Ce₂(NDC)₃ adsorbs a not negligible amount of CO₂ at around room temperature. As these uptakes are not in the same order of magnitude of those ones measured on the best candidate for CO₂ storage and capture porous materials (i.e. UTSA-16¹⁴⁸ or Mg-MOF-74¹⁰⁹), this material cannot be unfortunately proposed for such applications.

3.2 $\text{Ce}_2(\text{ADB})_3(\text{DMA})_{3.4}$

The synthesis procedure of $\text{Ce}_2(\text{ADB})_3(\text{DMA})_{3.4}$ described in section 2.1.2 was optimized by the means of high-throughput methods, also described earlier in the introduction in section 1.2.1. An optical image of the product is shown in Figure 24.

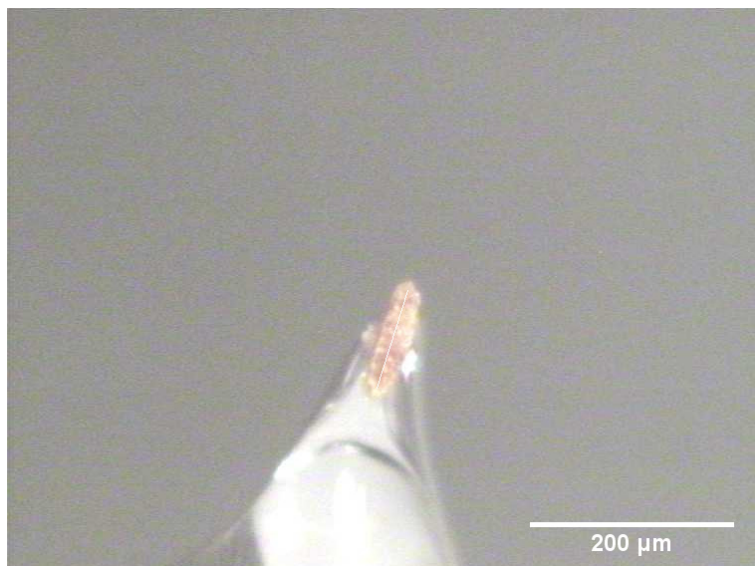


Figure 24 – Optical image of the crystal of $\text{Ce}_2(\text{ADB})_3(\text{DMA})_{3.4}$ selected for the SCXRD experiment.

3.2.1 Crystal structure

By looking at the solved crystal structure (Table 11 and Figure 25) the materials shows a typical coordination polymer structure with bonds between carboxylates and Ce cations. Such atoms build Ce-O-Ce chains aligned to the c-axis of the crystal structure. Linker molecules, instead, work as a bridge from those chains forming a 3D structure with one-dimensional long channels aligned in the same direction of the Ce chains (Figure 25)

Table 11 – Crystal data for $\text{Ce}_2(\text{ADB})_3(\text{DMA})_{3.4}$

	$\text{Ce}_2(\text{ADB})_3(\text{DMA})_{3.4}$
Formula	$\text{C}_{21}\text{H}_{12}\text{CeN}_3\text{O}_6$
Formula weight ($\text{g}\cdot\text{mol}^{-1}$)	542.46
Crystal system	<i>Monoclinic</i>
Space group	$P2_1/n$
a (Å)	16.238(3)
b (Å)	8.858(3)
c (Å)	21.124(5)
$\alpha = \gamma$ (°)	90
β (°)	96.47(2)
Cell volume (Å ³)	3019.0(13)
Temperature (K)	293(2)
Abs. coefficient (mm^{-1})	1.537
Calc. density ($\text{g}\cdot\text{cm}^{-3}$)	1.193
Z	4
Measured reflections	9577
R_{int}	0.2170
No. of parameters	304
R_1	0.2170
wR (all data)	0.1378
Largest. diff. peak ($\text{e}\cdot\text{Å}^{-3}$)	-1.937 / 3.530

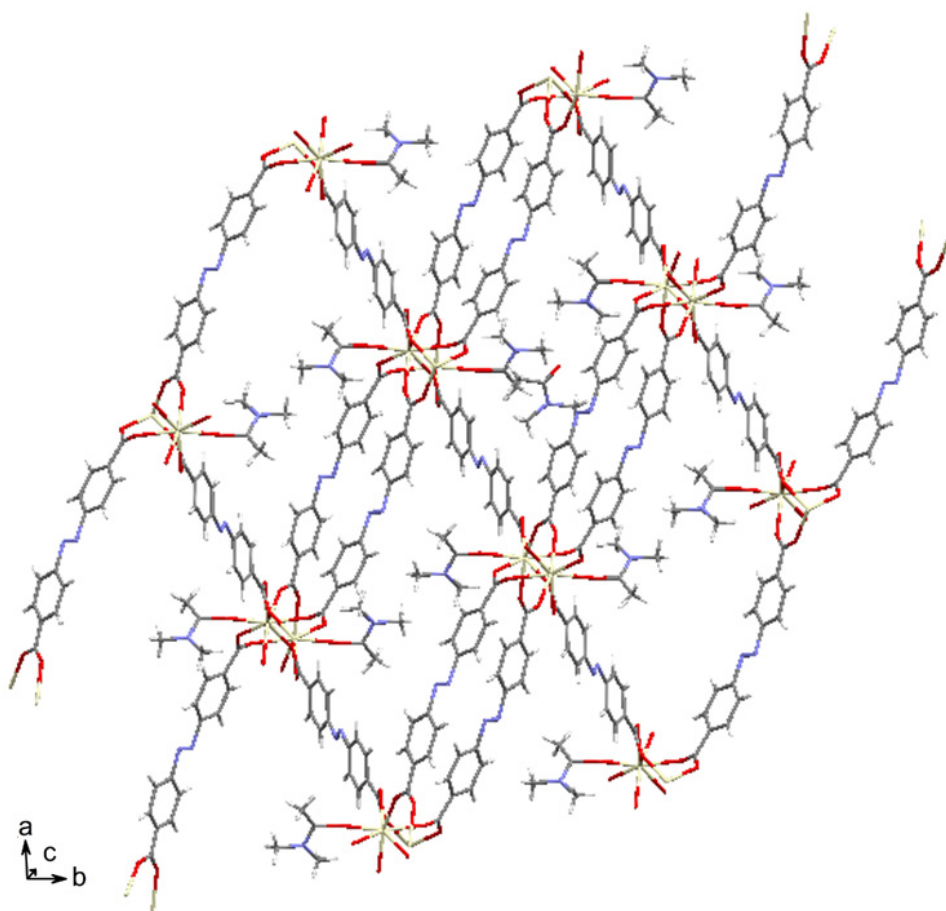


Figure 25 – Structural representation of $\text{Ce}_2(\text{ADB})_3(\text{DMA})_{3.4}$. c-axis is perpendicular to the figure. Cerium, carbon, nitrogen, oxygen and hydrogen atoms are depicted respectively in yellow, black, blue, red and white.

Two crystallographic independent DMA molecules are present in the structure: one directly coordinated to Ce atoms through a dative bond and one in the middle of the pore. While the occupancy factor of the latter DMA molecule has been refined to 1, the one directly coordinated to the metal site has been refined only to 0.7, explaining the 3.4 stoichiometric factor associated to DMA molecules observed in the structural formula.

Looking at the Pawley refinement done on the powder diffraction pattern in Figure 26 no new further crystalline phase different from the monoclinic one can be observed. Beside the purity of the synthesized compound such data is indicating also that the single crystal used for the structure solution is representative of the whole powder.

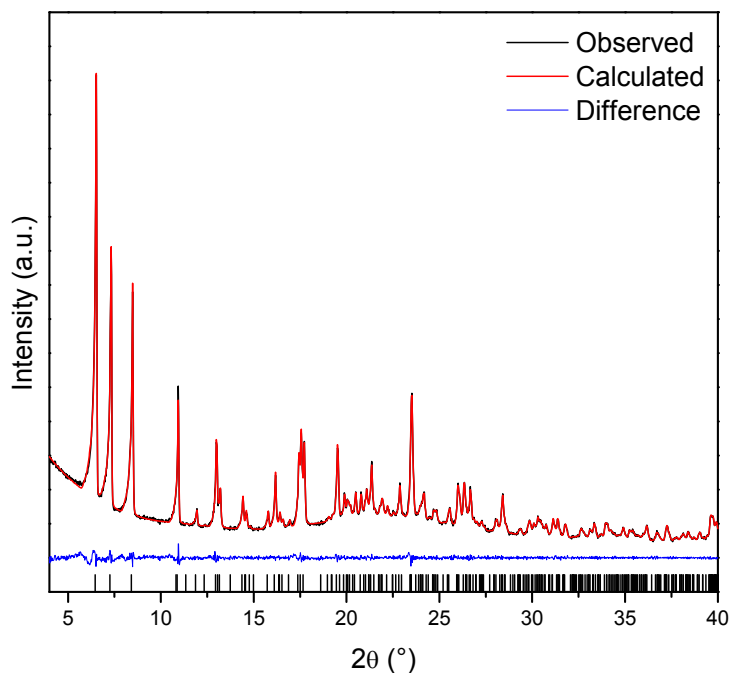


Figure 26 – Pawley fit on PXRD pattern of $\text{Ce}_2(\text{ADB})_3(\text{DMA})_{3.4}$. Observed, calculated and residuals are drawn respectively in black, red and blue lines, allowed reflections are reported by black ticks. ($\lambda = 1.5406 \text{ \AA}$).

Table 12 – Comparison between cell parameters obtained by SC-XRD and Pawley refinements on Ce₂(ADB)₃(DMA)₃. PXRD pattern.

Ce ₂ (ADB) ₃ (DMA) _{3,4}	Pawley	SC-XRD
<i>a</i> (Å)	16.371(2)	16.238(3)
<i>b</i> (Å)	8.875(2)	8.858(3)
<i>c</i> (Å)	21.142(3)	21.124(5)
<i>β</i> (°)	96.911(2)	96.47(2)
Volume (Å ³)	3049.51(8)	3019.0(13)

The slight discrepancy between the cell volume measured by SCXRD and Pawley refinement may be due to the small dimensions of the measured crystal (especially along one crystal axis) which is causing a low accuracy in the determination of one of the parameters. The data coming out from the Pawley refinement has to be considered as the most accurate, as in powder diffraction a virtually infinite number of different crystals contributes to the statistics of the measured values.

3.2.2 Thermal activation

The behavior of $\text{Ce}_2(\text{ADB})_3(\text{DMA})_{3.4}$ upon thermal treatment was studied by the means of TGA (in a flow of nitrogen or dry air) and VTXRD (in dynamic vacuum). Figure 27 reports the TGA curves obtained on $\text{Ce}_2(\text{ADB})_3(\text{DMA})_{3.4}$.

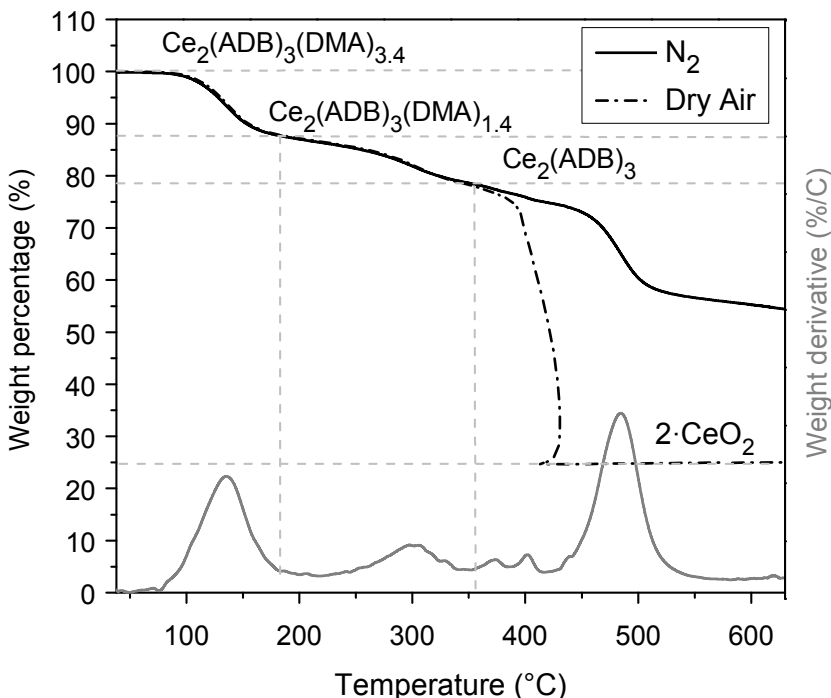
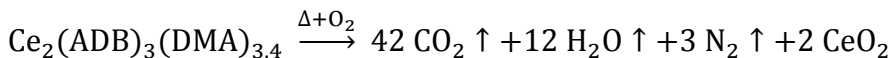


Figure 27 – TGA curve collected on $\text{Ce}_2(\text{ADB})_3(\text{DMA})_{3.4}$ in a N_2 flow (solid line) and dry air flow (dashed line). Derivative of TGA data for the N_2 flow is reported as a grey line. Dashed grey lines represents the relative formula weights of the written compounds.

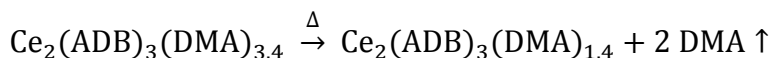
TGA curves collected in different atmospheres (nitrogen and dry air) are superimposable up to 350°C. Above this temperature, they separate as the organic part of the MOF, in presence of dry air, burns to give carbon dioxide and water vapor yielding CeO_2 as observed for other Ce-based MOFs³⁶ and already observed for $\text{Ce}_2(\text{NDC})_3(\text{DMF})_2$. On the other hand, in nitrogen flow the MOF is decomposing into coke-like species and again CeO_2 . These hypotheses are supported by the color of the material after the TGA measurement: black for the nitrogen one, and pale yellow for the one made in presence of oxygen.

Starting from this hypothesis, one can consider the ratio between the formula weights of the pristine compound and the cerium dioxide to be linked by the following combustion reaction:



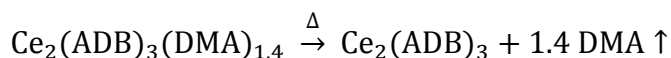
Considering the relative mass of the sample after 450°C in air being only CeO₂ (plateau at 24.9%) it is possible to calculate the relative weight of the MOF that has reacted to give the oxide. By means of such calculation one obtain a value of about 100%, extremely close to the experimental one. This evidence strongly supports the correctness of the proposed unit formula coming from the SCXRD structure solution.

Working a similar way it is possible to assign the weight losses observed in the region between room temperature and the combustion temperature (395°C). The first weight loss, appearing in a temperature range between 110°C and 180°C can be modeled by means of the following equation:



The accordance between the experimental value of the weight (87.8%) and the calculated one (87.4%) is good and permits to assign this weight loss to the desorption of the DMA molecules present inside the pores.

The other DMA molecules are desorbed at a higher temperature, between 250°C and 350°C, as modeled by the following chemical equation:



Again a good agreement between the observed value (78.4%) and the theoretical value (78.1%) permits to assign this weight loss to the desorption of the DMA molecules directly coordinated to Ce cations. It is relevant to notice that these TGA data are confirming very strongly the stoichiometric number of DMA molecules refined by SCXRD method (which is a weaker datum, in this sense, mainly for being such a refinement linked to the idiosyncrasies of the crystallographer who is running the calculations) and also their speciation in two different families: a weakly and a strongly adsorbed one.

Such desolvation reactions were also studied by means of variable-temperature powder diffraction (VTXRD) in dynamic vacuum, giving results reported in Figure 28.

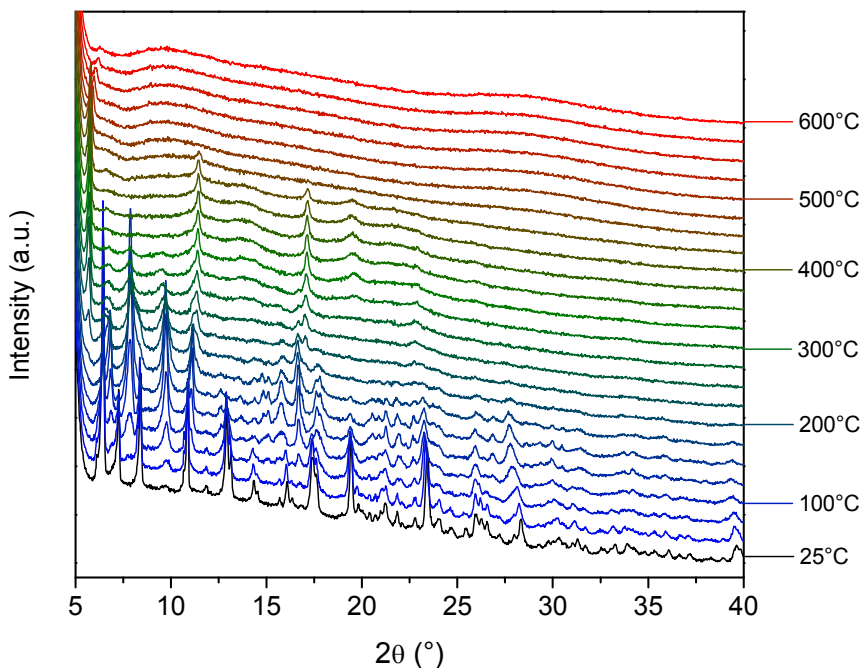


Figure 28 – VTXRD data collected on $\text{Ce}_2(\text{ADB})_3(\text{DMA})_3$. ($\lambda = 1.5406 \text{ \AA}$)

The black curve reported in Figure 28, recorded at room temperature, is superimposable to the one reported in Figure 26 indicating that no phase transformation is happening at room temperature due to the dynamic evacuation. Upon heating up to 600°C three different phase transformations are visible in the patterns. The first one, starting at 50°C (see the peak at 9.8°) and being completed at 150°C can be linked to the first weight loss observed in TGA and assigned to the desorption of the first 2 DMA molecules loosely adsorbed in the pore system. A second phase transformation starting at 225°C and ending at 300°C can be similarly reconducted to the loss of the DMA molecules directly coordinated to the Ce metal sites. Above this temperature a collapse of the crystal structure is observed to give rise to amorphous (or nanocrystalline) solids. At temperatures above this amorphization a broad halo around 28° can be seen: this signal, being the most intense diffraction peak of crystalline CeO_2 ,²⁷ can be assigned to nanocrystalline cerium

dioxide coming from the pyrolysis of the MOF. In order to look at the relevant diffractograms collected in the variable-temperature PXRD experiments only five curves are shown in Figure 29 below:

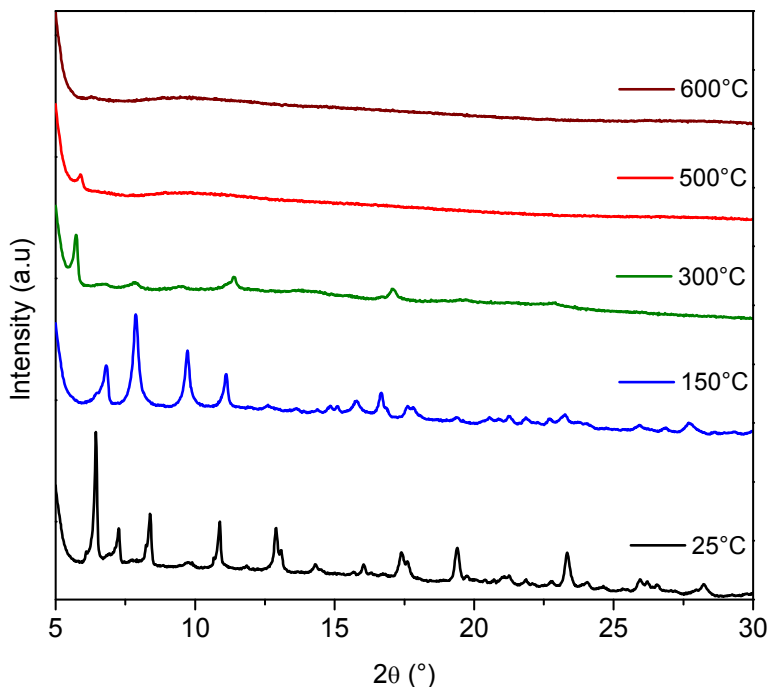


Figure 29 – Selection of five different diffractograms on Ce₂(ADB)₃(DMA)_{3.4} from the VT-XRD experiment at the temperatures of 25°C (black), 150°C (blue), 300°C (green), 500°C (red) and 600°C (brown) ($\lambda = 1.5406 \text{ \AA}$).

As noticeable from the curves in Figure 29 two new different crystalline phases are formed during the heating of Ce₂(ADB)₃(DMA)_{3.4} in dynamic vacuum: as for their diffraction peaks in the low-angle region of the diffractogram they have crystalline cells with dimensions probably similar to those of Ce₂(ADB)₃(DMA)_{3.4} which has been solved with single-crystal diffraction techniques. The one formed at 150°C having a number of peaks comparable to the pristine one is probably characterized by a similar space group (i.e. with a similar number of symmetry elements). The crystalline phase formed at temperatures above 300°C, having a substantially lower number of reflections, is probably belonging to a higher-symmetry space group. As the overall intensity of the diffraction signal is severely lowered in this final phase the general crystallinity of the sample is probably lost in the final phase

transformation. Despite many attempts the solution, of the crystal phases formed at high temperatures by single-crystal diffraction was not successful for the moment. This can be due to many reasons: i) after thermal activation the crystals become extremely sensitive to air moisture, decomposing in the time scale of minutes in air; ii) a general lower crystallinity that broadens and weakens the diffraction signals; iii) the disordering of the structure. A session of single-crystal diffraction measurements at a synchrotron source is scheduled in order to try to solve those crystal structures.

3.2.2 Adsorption properties

In order to measure the surface area and the porosity of $\text{Ce}_2(\text{ADB})_3(\text{DMA})_{3.4}$ a series of adsorption isotherms of N_2 at 77K (Figure 30) and of CO_2 (Figure 31) at 0°C were collected after a thermal activation in dynamic vacuum (for a duration of 3 h each) at different temperatures. For each adsorptive a different aliquot of powder was activated at increasing temperatures in a consecutive way.

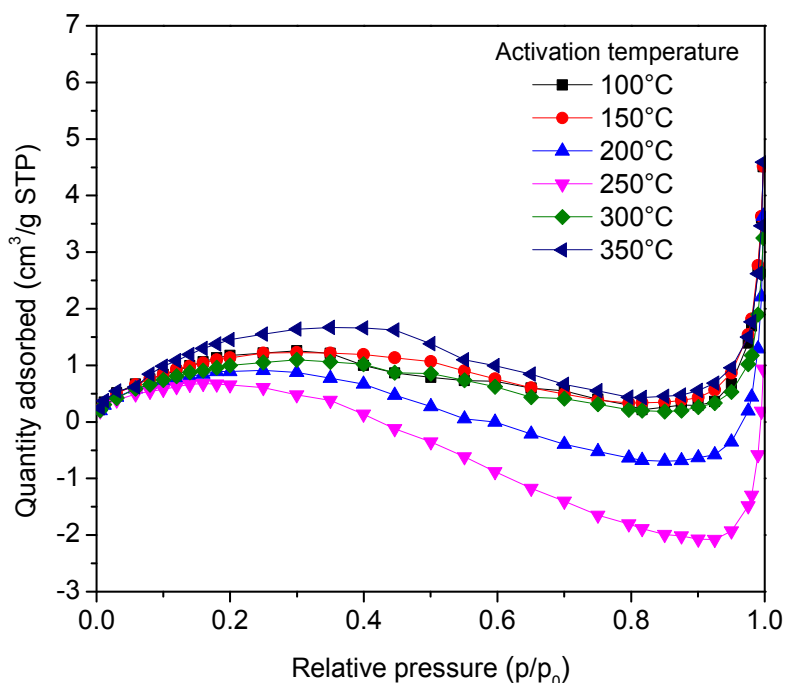


Figure 30 – -196°C N_2 adsorption isotherms collected on $\text{Ce}_2(\text{ADB})_3(\text{DMA})_{3.4}$. Desorption branches are omitted for the sake of clarity.

As the amount of adsorbed nitrogen is quite negligible for the all isotherms, $\text{Ce}_2(\text{ADB})_3(\text{DMA})_{3,4}$ cannot be considered porous for nitrogen at -196°C . The adsorbed amount is so little that the isotherms are dominated by the error and this causes them to be not strictly increasing (as expected for every adsorption isotherm) and even becoming negative. It has to be noticed that as a microporosity (and thus a Type I isotherm) is expected, the amount of sample admitted in the cell (about 20 mg) was optimized for a material with a typical figure of hundreds of m^2/g . This increases the error on the specific amount of adsorbed gas, which is normalized to the mass of the sample. With these considerations in mind, the analysis of those data with a BET or Langmuir model in order to extract a specific surface area measurement has to be considered meaningless and is not reported for this reason.

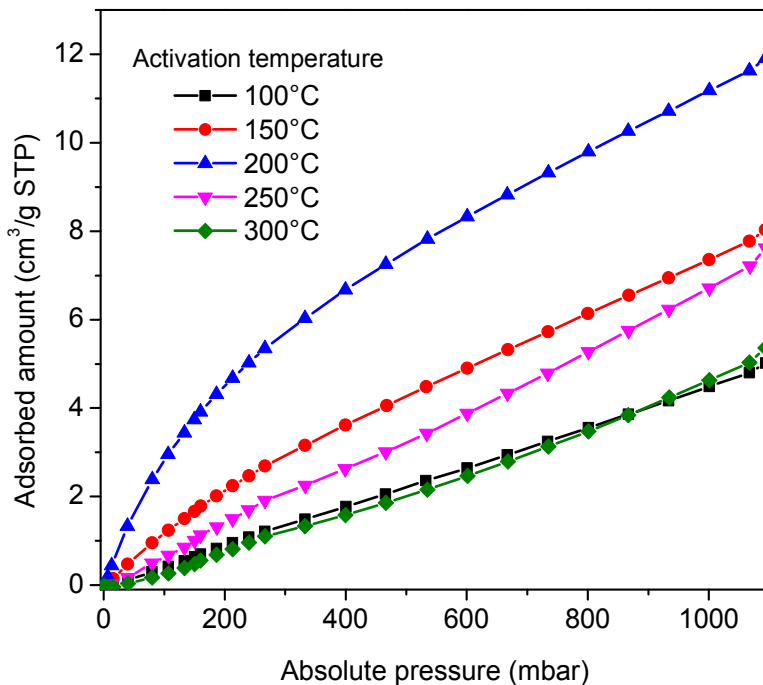


Figure 31 – 0°C CO_2 adsorption isotherms collected on $\text{Ce}_2(\text{ADB})_3(\text{DMA})_{3,4}$ after thermal activation at various temperatures. Desorption isotherms (still totally superimposable to adsorption ones) are omitted for the sake of clarity.

As an alternative method to characterize the porosity in this system CO_2 adsorption were measured in similar conditions to the nitrogen ones but at a temperature of 0°C . This time the isotherms are “well-behaving” as the material is capturing a not

negligible amount of gas: nevertheless this time the amount of sample used for the experiment was about ten times larger. The amount of carbon dioxide reaches a maximum at an activation temperature of 200°C then diminishes to go back at the one measured after the treatment at 100°C. The uptakes at a pressure of 1000 mbar are reported in the Table 13 below.

Table 13 – CO₂ uptakes of Ce₂(ADB)₃(DMA)_{3.4}. Isotherms measured at 0°C

Activation temperature	CO₂ uptake (wt%) at 1000 mbar
100°C	0.98
150°C	1.55
200°C	2.28
250°C	1.48
300°C	1.05

This material adsorbs a not negligible amount of CO₂ at 0°C. As these uptakes are not in the same order of magnitude of those measured on the best candidate for CO₂ storage and capture porous materials (i.e. UTSA-16¹⁴⁸ or Mg-MOF-74¹⁰⁹) this material cannot be proposed for such applications. It must be considered that a kind of porosity, invisible for nitrogen, is present upon activation of Ce₂(ADB)₃(DMA)_{3.4}.

3.3 Ce/Zr-UiO-66

The synthesis of pure Zr, pure Ce and Ce-Zr mixed metal UiO-66 samples is described in section 2.1.3. The recipe for Ce containing samples is following what previously published by Lammert et al.^{29,54,64}. For the synthesis of the pure Zr UiO-66, instead, the recipe published by Cavka et al.²² was followed.

3.3.1 Crystal structure

The crystal structure of UiO-66, as thoroughly described in literature,^{22,54,64,78,103,149} consists of a densely packed cubic face-centered lattice made from cubooctahedral $Zr_6O_4(OH)_4(CO_2)_{12}$ inorganic clusters connected by linear terephthalate linkers (see Figure 32). The carboxylates are bonding Zr^{4+} cations in a bidentate manner, above the edges of the hexanuclear octahedron. The three dimensional buildup of the structure forms a continuous face-centered cubic structure in which every cluster is linked to the 12 next neighbors.

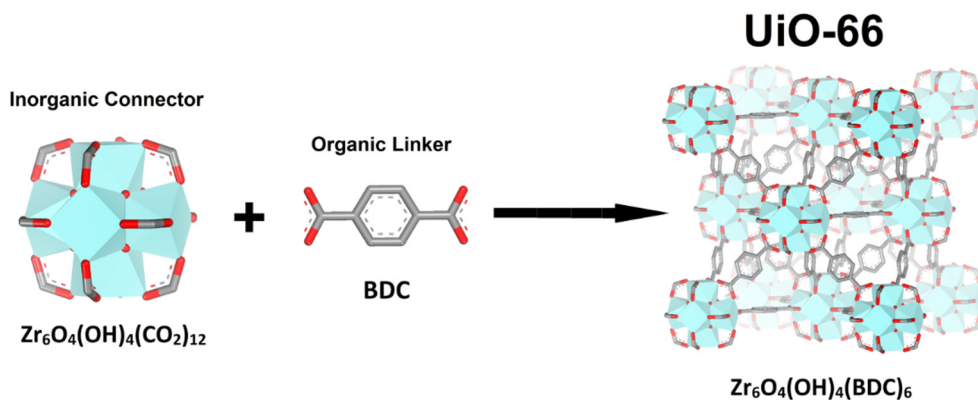


Figure 32 – Pictorial representation of the building of UiO-66: inorganic hexanuclear Zr_6 clusters and terephthalates assembling in a tightly packed cubic structure. Taken from ref. [78].

The pure Zr, pure Ce and the $Zr_{3.54}Ce_{2.46}$ samples were measured at the ID22 high-resolution powder diffraction beamline after being desolvated at 180°C in dynamic vacuum for 16 hours each. The results are shown in Figure 33, and results are summarized in Table 14.

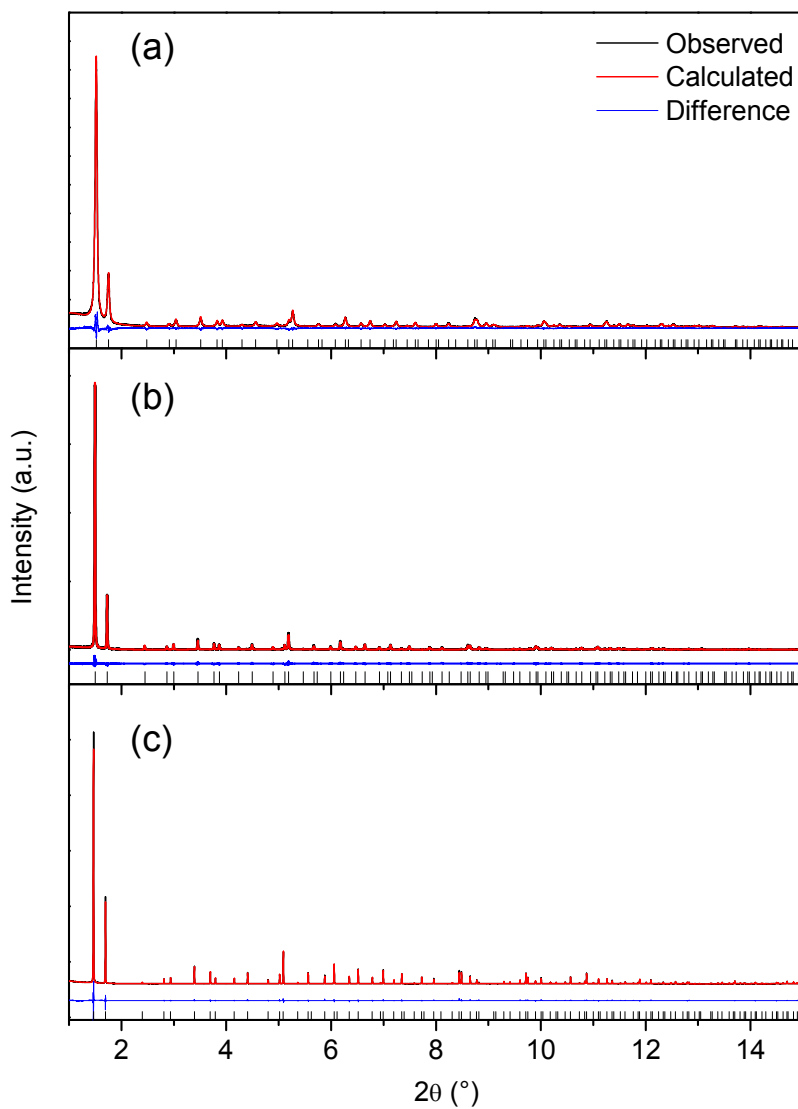


Figure 33 – PXR D pattern obtained on Zr UiO-66 (a), $Zr_{3.54}Ce_{2.46}$ UiO-66 (b) and Ce UiO-66 (c). The result for the Rietveld refinement is shown in red, and the residuals in blue. Vertical bars mark the allowed peak positions. ($\lambda = 0.31783 \text{ \AA}$).

Table 14 – Results and relevant information for the Rietveld refinement of the pure Ce, the pure Zr and one Ce/Zr-UiO-66 sample, the Ce45.

	Zr-UiO-66	Zr _{3.54} -Ce _{2.46} UiO-66 (Ce45)	Ce-UiO-66
Formula	12 · [Zr ₆ O ₆ BDC ₆]	12 · [Zr _{3.54} Ce _{2.46} O ₆ BDC ₆]	12 · [Ce ₆ O ₆ BDC ₆]
Crystal system	<i>Cubic</i>	<i>Cubic</i>	<i>Cubic</i>
Space group	<i>Fm3m</i>	<i>Fm3m</i>	<i>Fm3m</i>
a (Å)	20.7535(2)	21.0652(1)	21.48825(2)
b (Å)	20.7535(2)	21.0652(1)	21.48825(2)
c (Å)	20.7535(2)	21.0652(1)	21.48825(2)
α = β = γ (°)	90	90	90
Cell volume (Å ³)	8938.75(26)	9347.52(14)	9922.09(2)
Temperature (K)	293(2)	293(2)	293(2)
R _{wp}	0.073	0.087	0.085
R _{Bragg}	0.027	0.03	0.024

All Rietveld refinements, performed up to $2\theta = 32^\circ$ ($d_{\min} = 0.577 \text{ \AA}$), started from the published structure of Zr-UiO-66^{22,103} and Ce-UiO-66⁵⁴ and proceeded without any issue. For the mixed metal sample the cations were refined independently of each other and their summed occupancy was fixed to one. As a general finding the cell parameter of the mixed-metal material seem to be linearly varying with the relative concentration of the metals. This behavior, already reported by Lammert et al. in 2017,⁶⁴ can be ascribed to the Vegard's law, which has been found to be working also for MOFs. As all Bragg peaks observed in the three samples belong to the UiO-66 phase no crystalline impurity could be detected. The peak width decreases with the amount of Ce: this indicates the progressive increase of crystallite size with the rise of Ce content.

As a general consideration from diffraction data, where only what is ordered can be observed¹⁵⁰, the fact that Ce and Zr are not forming any sort of superlattice or new crystal phase is a strong sign for the mutual disorder of Zr and Ce atoms in the lattice, even at the atomic level or at the cluster level. This results in a diffraction data that cannot discriminate between these two metals inside the crystal cell.

The different width of the PXRD peaks from the three samples (Figure 33) is due to the different dimensions of the crystallites, as reported by Lammert et al.⁶⁴.

3.3.2 Thermal activation

For the thermal properties of pure Zr, pure Ce and mixed-metal UiO-66 material the present thesis refer totally to the works by Cavka et al.²² for the Zr-UiO-66 and two papers from Lammert et al.^{54,64} published in 2015 and 2017 for Ce-UiO-66 and the mixed-metal materials.

Remarkable thermal stability is one of the most important features of Zr-UiO-66: in fact this material shown to be still porous and crystalline up to 500°C in inert atmosphere. This has been shown by both TGA and VTXRD measurements.

Ce-UiO-66, on the other hand, showed a greatly reduced thermal stability when compared to the Zr counterpart losing totally its crystallinity at the temperature of 240°C, as shown by VTXRD measures.

The mixed-metal Ce/Zr-UiO-66 materials showed to have an intermediate behavior between the two pure compounds: as thoroughly shown by Lammert et al.⁶⁴ the thermal stability, determinated again by TGA and VTXRD measurements, showed to be greatly influenced by relative small amounts of Ce (Figure 34).

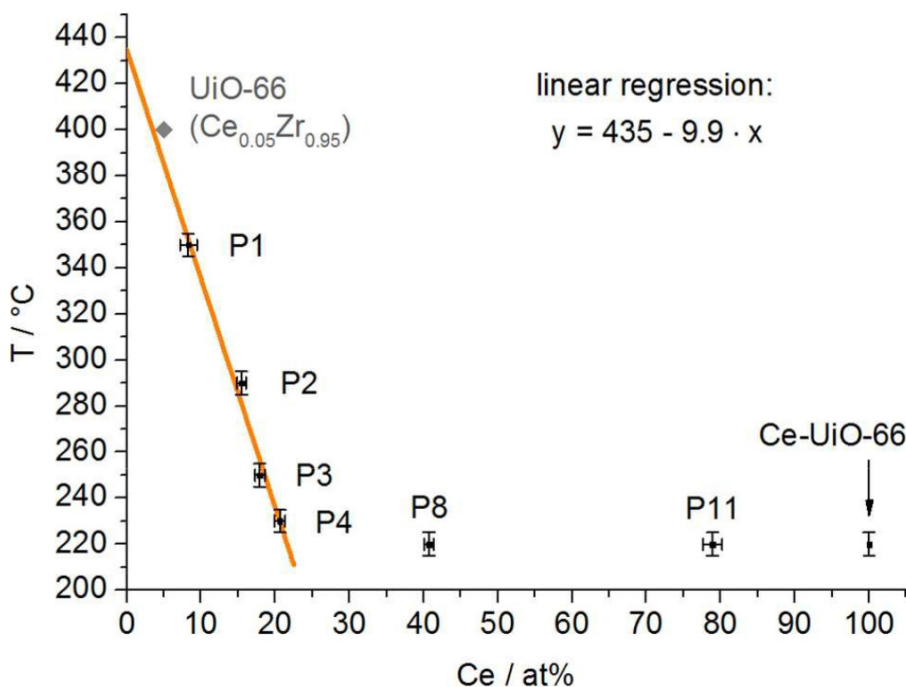


Figure 34 – Thermal stabilities of Ce/Zr-UiO-66 MOFs plotted against the amount of Ce. Taken from ref. [64].

As the samples studied in the paper by Lammert et al. are spanning the whole composition range from the pure Zr to the pure Ce materials, this data is perfectly compatible also with the samples studied in the present work.

3.3.3 X-ray absorption spectroscopy

As powder diffraction data gave no any new information about the spatial arrangement of Ce and Zr atoms the usage of XAS techniques (see section 1.3.2), being local techniques, shed light on this system.

XANES data collected on Ce L-edge, (Figure 35) demonstrate that Ce in all studied samples of MOFs is predominantly in the 4+ oxidation state. Zr is assumed to be also in the 4+ oxidation state, as already shown by Valenzano et al.¹⁰³.

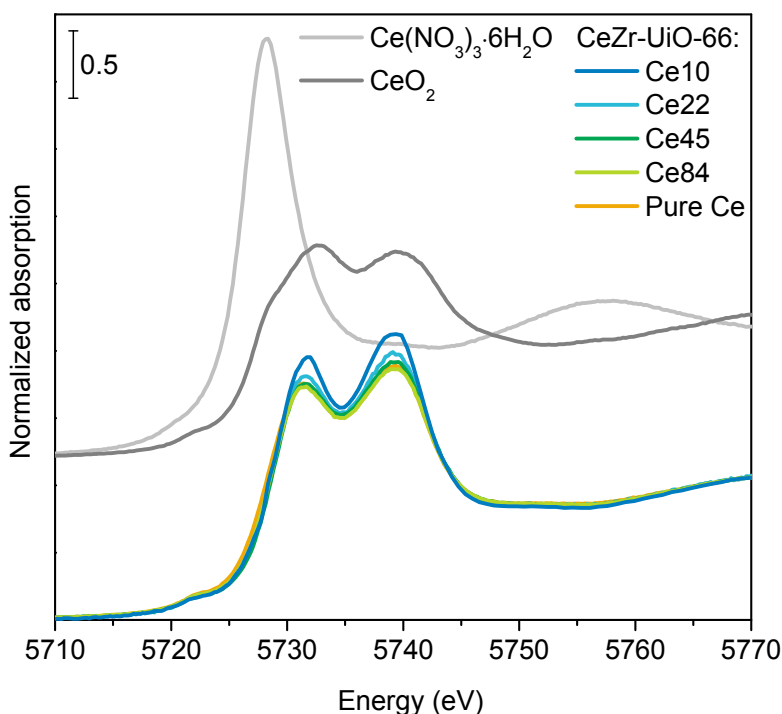


Figure 35 – Ce L₃-edge XANES spectra of bimetallic Ce/Zr-UiO-66 samples and pure Ce-UiO-66 compared to references for Ce(III) and Ce(IV) oxidation states.

XANES spectra of all Ce containing samples are very similar to each other, which confirms the similarity of the local geometry and electronic structure of both Ce and Zr cations also varying the Ce Zr ratio. This indicates that we are dealing with an isomorphous substitution of Ce in Zr sites (or vice-versa). These observations confirm the conclusions drawn from the PXRD Rietveld refinement.

The EXAFS region of the K-edges of both Ce and Zr is shown below in Figure 36.

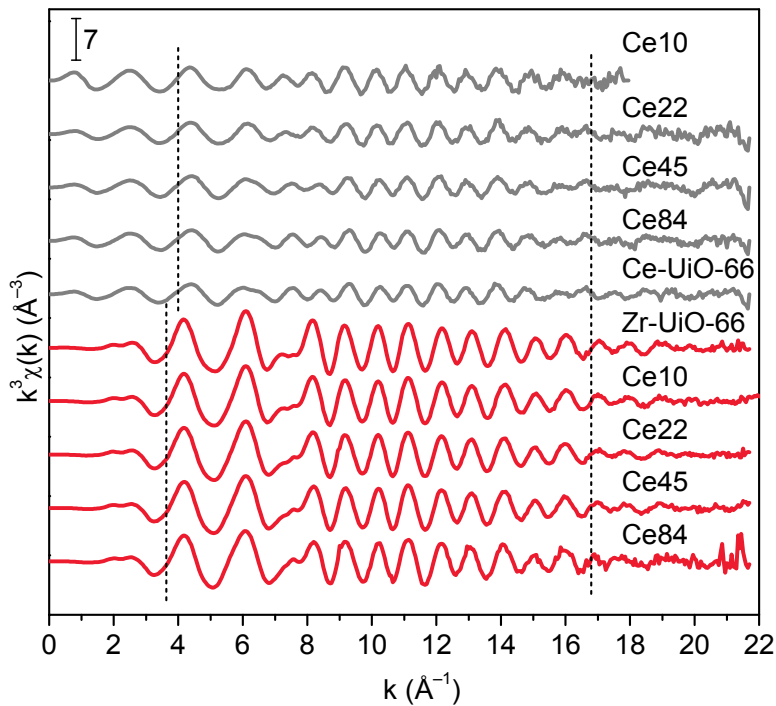


Figure 36 – EXAFS data at Ce (gray) and Zr K-edges (red) for all pure and bimetallic Ce/Zr-UiO-66 samples studied by XAS. Dashed lines indicate the regions used for the Fourier transform.

Fourier transformed Zr K-edge and Ce K-edge EXAFS data for five of the samples are shown in Figure 37 and Figure 38, respectively.

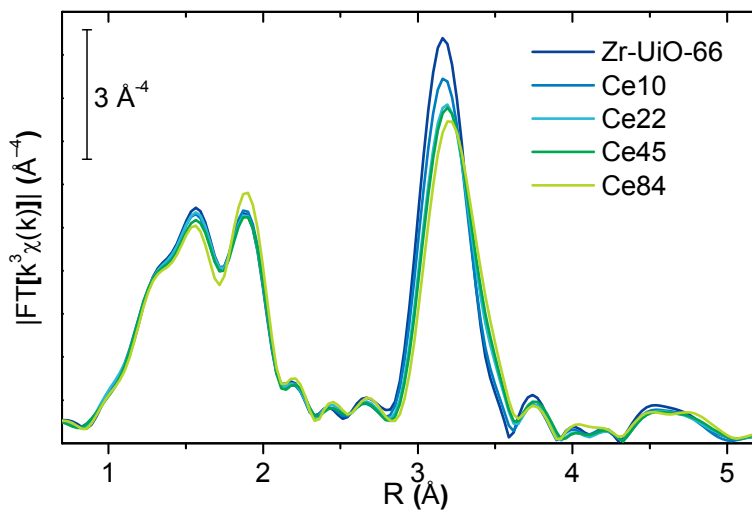


Figure 37 – Moduli of the phase-uncorrected Fourier transforms of k^3 -weighted EXAFS data collected at the Zr K-edge for Ce/Zr-UiO-66 MOFs.

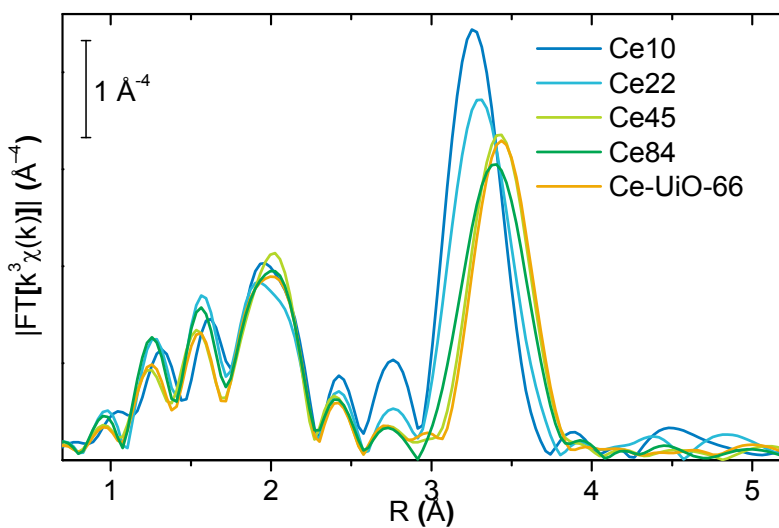


Figure 38 – Moduli of the phase-uncorrected Fourier transforms of k^3 -weighted EXAFS data collected at the Ce K-edge for Ce/Zr-UiO-66 MOFs.

Qualitatively all the Fourier transformed spectra are in agreement with those already reported for UiO-66.¹⁰³ The shape of the peaks in the 1.2-2.5 Å, originating from the so-called first shell, and assignable to metal-oxygen scattering does not change in a significant way with the increase of Ce content: this evidences rather small variations in oxygen coordination of both Zr and Ce cations. The 2.8-3.8 Å peak, belonging to the second-shell of neighbors, is assigned to the metal-metal scattering from the members of the hexanuclear clusters present in the structure. The fact that the average value of the metal-metal distance depends on the ratio between the two metals confirms the formation of mixed-metal Ce_xZr_{6-x} cornerstones. It should be noticed that in this case, having a high-quality dataset (i.e. with a low signal to noise ratio), also the presence of a peak at 4.5-5 Å in the Zr edge data (Figure 37) can be observed. This signal is due to the scattering between the absorber atom and another one situated in the opposite vertex of the octahedron.

The changes that are taking place in the EXAFS spectra even upon addition of small amounts of Ce (Figure 38) can be explained hypothesizing the preferential formation of $CeZr_5$ clusters. This implies that only for Ce loadings lower than 17% one should have the contemporary presence of Zr_6 and $CeZr_5$ clusters. This is due to the simple consideration that there are six metallic cations per cluster and a material made only with $CeZr_5$ clusters would have a 17% Ce loading. In the case that any number of Zr atoms in a pristine Ce_6 cluster should be the same of a number of Ce atoms in a Zr_6 cluster the Zr and Ce EXAFS spectra should be looking pretty similar. As this is not the case (Ce additions to Zr-UiO-66 are not causing the same effect as Zr additions to Ce-UiO-66) some preferential cluster composition should be hypothesized. By similar considerations, the presence of hexanuclear Ce_6 clusters should be considered when dealing with samples with a Ce content higher than 17%, as the differences between Zr K-edge spectra of Ce22, Ce45 and Ce84 samples are minor. A detailed description about also the fitting of the EXAFS curves can be found in the paper in Appendix I.

The preferential formation of $CeZr_5$ cornerstones is also explaining the trend in the thermal stability already observed by Lammert et al.⁶⁴ (Figure 34): in fact, once the Ce concentration has reached around 20% the thermal stability of the bimetallic MOF is constant and it is the same value observed for Ce-UiO-66. This is consistent with the hypothesis for which above the Ce concentration of 20% there is the formation of hexanuclear Ce_6 clusters, whose thermal stability is indeed the one of Ce-UiO-66.

3.3.4 Vibrational spectroscopy

With the aim to characterize only mixed metal Ce/Zr-UiO-66 samples having CeZr₅ clusters and Zr₆ clusters, a series of low-containing samples (<17%, under the hypothesis advanced in the last chapter) was synthesized and characterized by dosing a probe molecule in an *in-situ* FTIR experiment. Aiming to probe the Lewis acidic sites present inside the pores CD₃CN was dosed after a prolonged thermal activation in dynamic vacuum at the temperature of 160°C. The activation conditions were optimized in order to get rid of almost all the solvent present in the pores of the material without collapsing it. The spectra of Ce5, Ce10 and Ce15 samples after thermal activation and after dosing the vapor pressure of CD₃CN are shown in Figure 39 below.

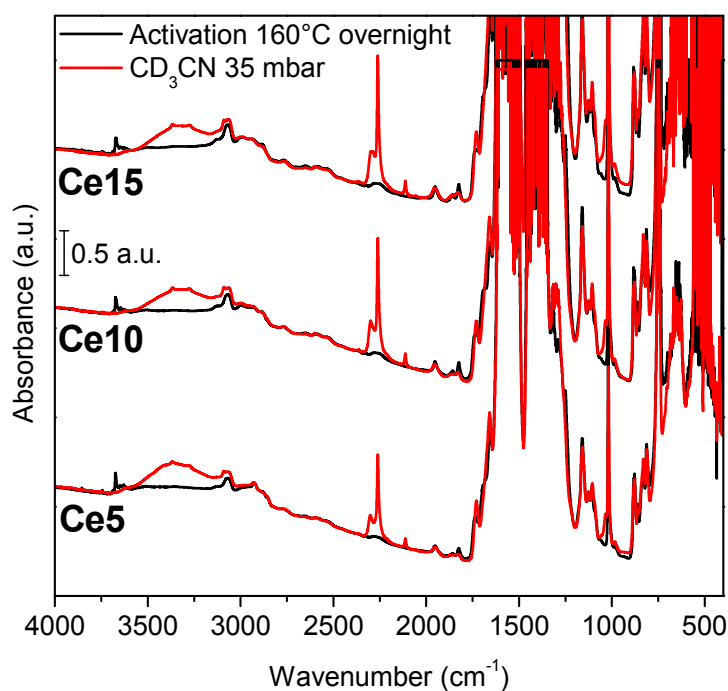


Figure 39 – FTIR transmission spectra of Ce5, Ce10 and Ce15 Ce/Zr mixed-metal UiO-66 samples after activation at 160°C (black). Spectra after dosing CD₃CN are reported in red.

All the spectra from the three samples are quite similar and the bands typical of MOFs are quite visible: the carboxylate symmetric and asymmetric stretching in the 1700-1250 cm^{-1} are evident. A complete assignation of all the vibrational bands, aided by computational simulations of the vibrational modes, can be found in the paper by Valenzano et al.¹⁰³. Upon interaction with deuterated acetonitrile vapors, the sharp signal from OHs at 3670 cm^{-1} shifts into a broad band centered at 3300 cm^{-1} because of hydrogen bond formation. At the same time a sharp signal coming from the stretching of the $\text{C}\equiv\text{N}$ bond is visible in the region around 2275 cm^{-1} . A magnified look at this spectral region for the Ce15 sample is reported in Figure 41 below, while the data collected on all three samples are reported in Figure 41.

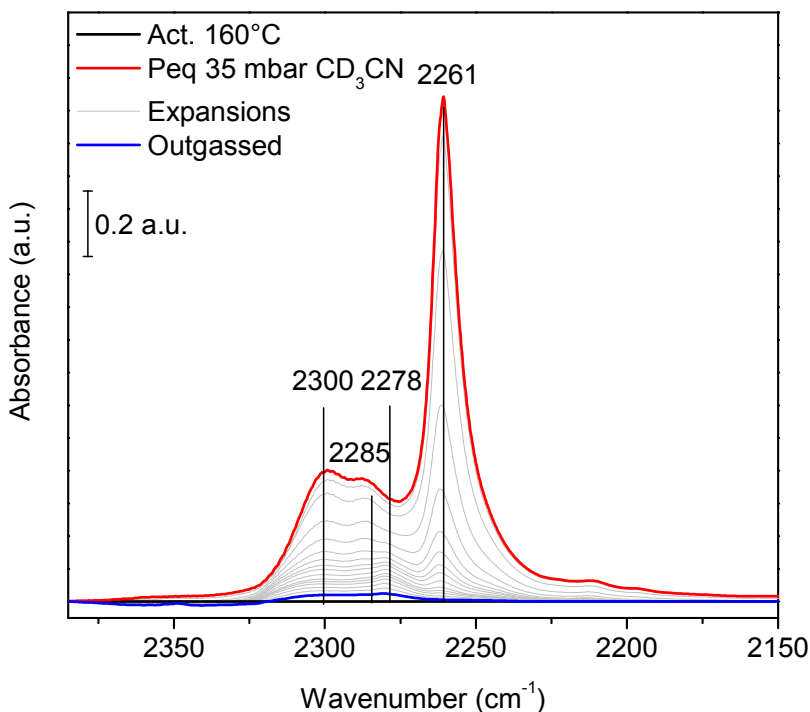


Figure 40 – Background subtracted FTIR spectra of the $\text{C}\equiv\text{N}$ stretching region collected on Ce15 Ce/Zr-UiO-66 sample. Maximum coverage is reported in red, progressive outgassing in grey and prolonged outgassing in blue.

The C≡N stretching region is characterized by four bands in all three samples, assignable in the following way:

- 2261 cm⁻¹: Liquid-like CD₃CN, characteristic of porous systems.¹⁵¹
- 2278 cm⁻¹: CD₃CN interacting with OHs from the cornerstones: the growth of this band is correlated with the one at 3300 cm⁻¹ (Figure 39) that is restored upon outgassing
- 2285 cm⁻¹: CD₃CN interacting with Ce⁴⁺ Lewis acidic sites¹⁵²
- 2300 cm⁻¹: CD₃CN interacting with Zr⁴⁺ Lewis acidic sites as reported by Nouar et al.¹⁵³

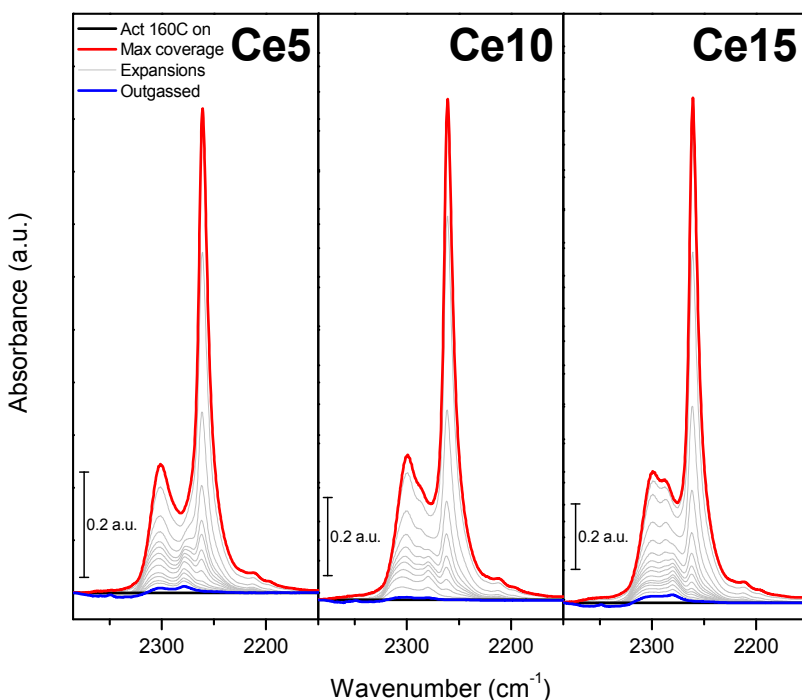


Figure 41 – Background subtracted FTIR spectra of the C≡N stretching region collected on Ce5, Ce10 and Ce15 Ce/Zr-UiO-66 samples. Maximum coverage is reported in red, progressive outgassing in grey and prolonged outgassing in blue.

The shape and the relative intensity of those bands is related to the Ce/Zr ratio (Figure 41): the higher the Ce content, stronger the band related to CD₃CN interacting with Ce sites.

3.4 Ce-UiO-66-ADC

The synthesis procedure of Ce-UiO-66-ADC described in section 2.1.4 was optimized by the means of high-throughput methods, also described earlier in the introduction in section 1.2.1. A SEM image of the product is printed in Figure 42. Only aggregates are visible as the crystal size is too small for being observed by SEM.

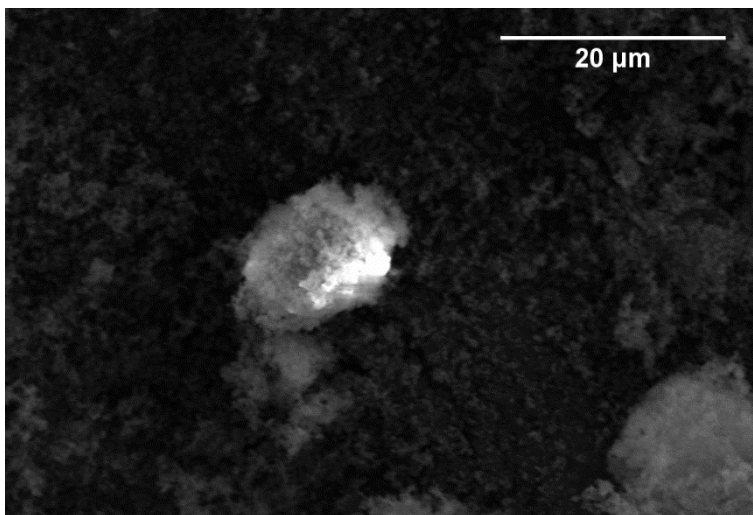


Figure 42 – SEM image of Ce-UiO-66-ADC.

3.4.1 Crystal structure

As in this case the synthesized product presents crystallites in the sub-micrometer dimension range the application of a single-crystal x-ray diffraction method to solve the structure was impossible as a crystal of suitable dimensions ($>200\ \mu\text{m}$) is needed. To overcome this, a structural refinement on the powder x-ray diffraction pattern was done in order to obtain a suitable crystal structure for the material using the Rietveld method¹⁵⁰ (Figure 43). As a starting point for the refinement a structural model for Ce-UiO-66-ADC was built in Materials Studio (Figure 44) starting from the structure of UiO-66^{22,103}, substituting the terephthalate moieties with acetylenedicarboxylates and optimizing geometrically the structure using the Forcite program module.

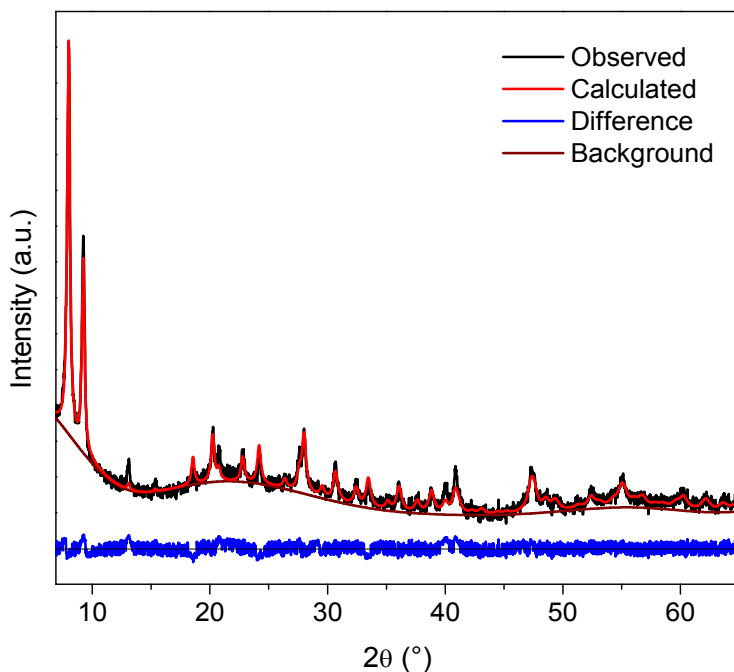


Figure 43 – PXRD pattern obtained on Ce-UiO-66-ADC (black curve). The result for the Rietveld refinement is shown in red, and the residuals in blue. ($\lambda = 1.5406 \text{ \AA}$)

Position of Ce atoms was refined freely while acetylenedicarboxylates were treated as rigid bodies in order to increase the stability of the fit and reduce the number of parameters refined. The refined parameters along with relevant crystallographic data are reported in Table 15 below.

It is relevant to notice that even the refinement was done on a dehydroxylated structure, as the presence of OH groups is very difficult to be observed by x-ray diffraction techniques. The presence of OH groups in the structure of UiO-66 is a well-known fact in literature¹⁰³ and for this reason their presence can be also hypothesized here. For this reason, the proposed structure would be $[\text{Ce}_6\text{O}_4(\text{OH})_4(\text{ADC})_6]$ while the refined one is slightly different.

Table 15 – Results and relevant information for the Rietveld refinement of Ce-UiO-66-ADC.

	Ce-UiO-66-ADC
Formula	$12 \cdot [Ce_6O_6ADC_6]$
Formula weight ($\text{g}\cdot\text{mol}^{-1}$)	6563.73
Crystal system	<i>Cubic</i>
Space group	<i>Fm3m</i>
a (Å)	19.1101(2)
b (Å)	19.1101(2)
c (Å)	19.1101(2)
$\alpha = \beta = \gamma$ (°)	90
Cell volume (Å ³)	6979.9(2)
Temperature (K)	293(2)
Abs. coefficient (cm^{-1})	300.58
Calc. density ($\text{g}\cdot\text{cm}^{-3}$)	1.559
Z	1
Measured reflections	24
No. of structural parameters	14
R _{wp}	0.097
R _{Bragg}	0.074

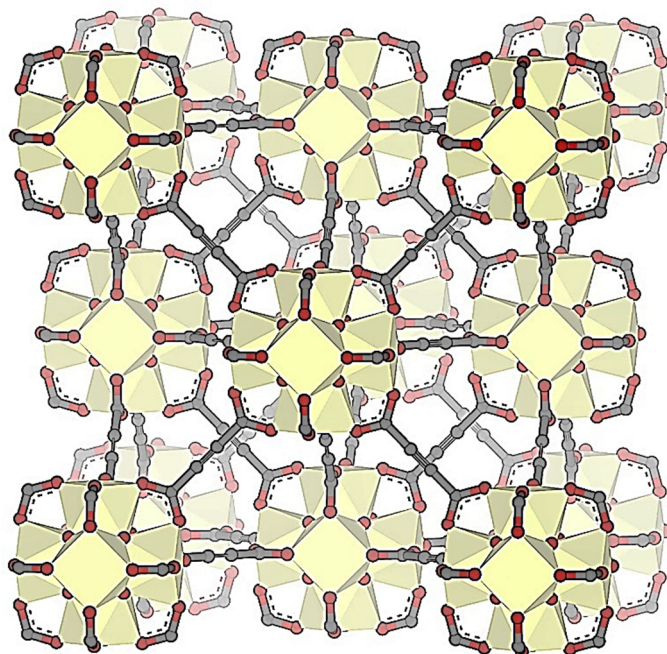


Figure 44 – Pictorial representation of the crystal structure of Ce-UiO-66-ADC. Cerium, oxygen and carbon atoms are printed respectively in yellow, red and black.

The crystal structure of Ce-UiO-66-ADC is characterized by the presence of hexanuclear Ce clusters (that can be considered as SBU) connected 12-fold with the neighboring ones to form a tightly packed face-centered cubic structure. This makes the material perfectly isostructural with the one of the pristine UiO-66^{22,103} making this material an example of reticular chemistry, as described by Yaghi et al.¹⁹. Being acetylenedicarboxylates shorter than their terephthalate counterparts, the cell parameter is indeed smaller than UiO-66, nevertheless it has to be noticed that Ce-based MOFs have cell parameters slightly larger than their Zr materials made with the same linker, as shown by Lammert et al.^{54,64}.

3.4.2 Thermal activation

The behavior of Ce-UiO-66-ADC upon thermal treatment was studied by the means of TGA (Figure 45) and VTXRD (Figure 46) techniques giving results shown below.

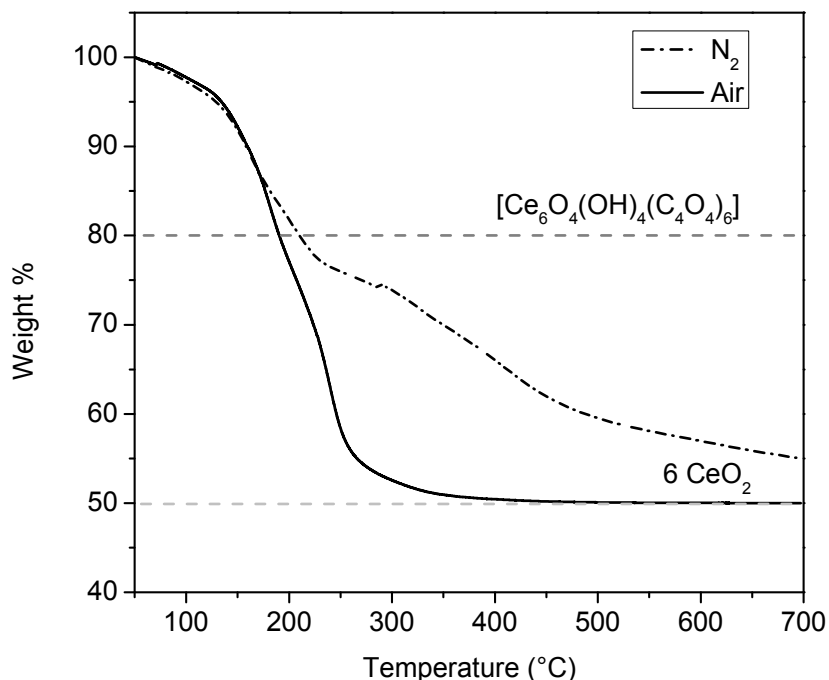


Figure 45 – TGA data collected on Ce-UiO-66-ADC in dry air (solid curve) and nitrogen (dashed curve) atmospheres.

The TGA curves show a very steep weight loss starting below 100°C in both atmospheres. They begin to diverge at about 200°C indicating that oxygen is playing a role in the weight loss of the materials and an oxidative process can be inferred from this data as the “classical” combustion of the organic moieties is expected to happen at higher temperatures (about 400°C). Considering the final mass of the sample after total combustion in air to be merely cerium dioxide one can use the formula unit of the crystal structure to calculate what would be the mass of sample that has to react to have this amount of oxide. This calculation is represented by the dashed horizontal grey lines in Figure 45. The residual 20% of the mass can be attributed to solvent (DMF or water) adsorbed within the pores of the material.

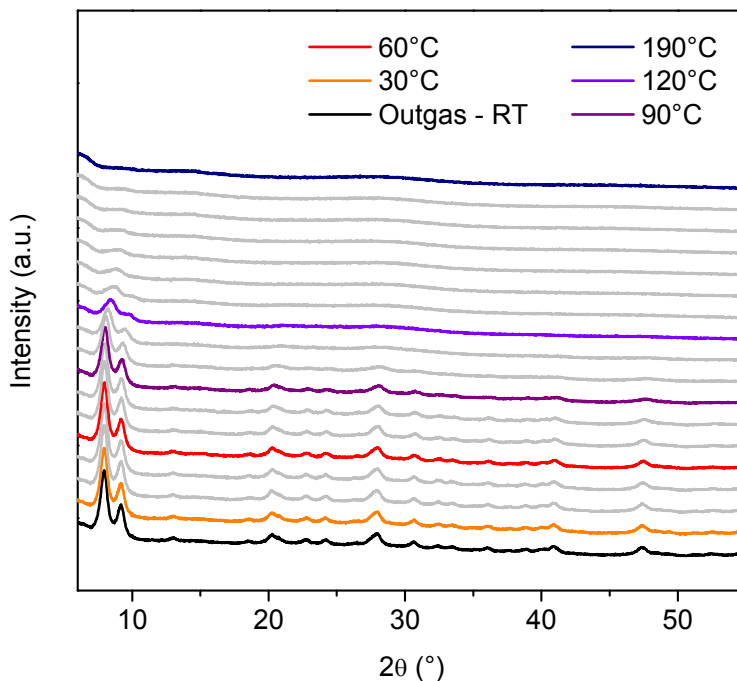


Figure 46 – VTXRD data collected on Ce-UiO-66-ADC in dynamic vacuum conditions. ($\lambda = 1.5406 \text{ \AA}$). Some relevant temperatures are highlighted for the sake of clarity.

As it is evident from the VTXRD data Ce-UiO-66-ADC retains its crystal structure upon heating in dynamic vacuum only up to 90°C. Above this temperature the main PXRD reflexes positioned above 10° in 2θ are vanishing totally together with all other signals. An extremely broad signal around 28° can be assigned to the formation of extremely small CeO₂ nanocrystals.

Comparing TGA with VTXRD (even considering that TGA data was collected in nitrogen flow, while the diffraction was carried out in dynamic vacuum for technical limitations) it is evident that the solvent cannot be outgassed during a thermal treatment keeping the MOF crystalline, as the amorphization temperature is much lower than the onset temperature of the first weight loss of the TGA curve, assigned to the desorption of solvent from the pore system of the material.

3.4.3 Adsorption properties

In order to highlight porosity and specific surface area of Ce-UiO-66-ADC, N₂ adsorption isotherms at -196°C were measured after thermal treatments in dynamic vacuum at increasing temperatures giving isotherms shown in Figure 47.

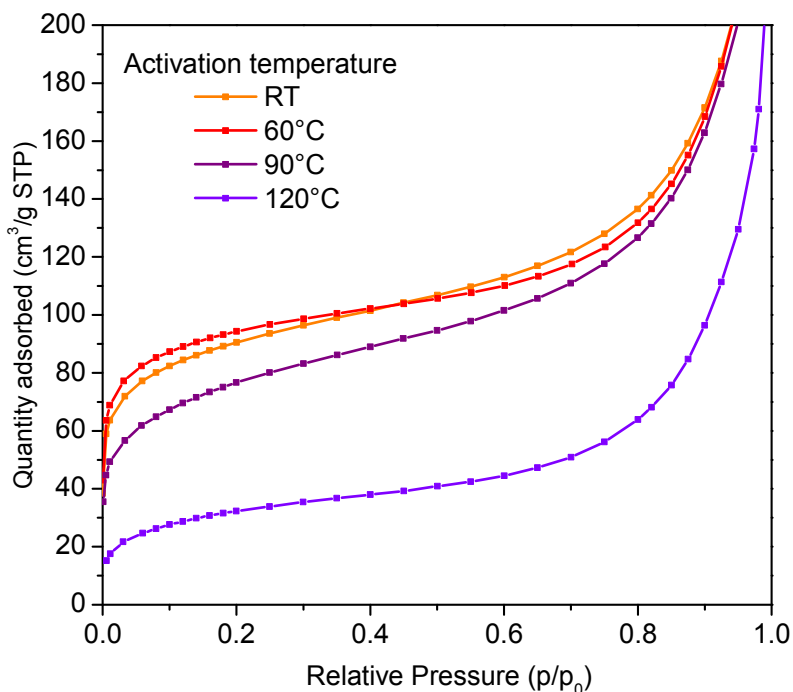


Figure 47 – -196°C N₂ adsorption isotherms collected on Ce-UiO-66-ADC. Activation temperature is highlighted by the color of the curve: RT (orange), 60°C (red), 90°C (purple) and 120°C (violet). Desorption branches (superimposable to adsorption branches) are omitted for the sake of clarity.

The activation temperatures for the thermal activation procedure were chosen looking at the results of the VT-XRD experiment (Figure 46) in order to observe a correlation between uptake (and thus, porosity and surface area) with structural changes due to heating. All isotherms belong to the Type I classification according to IUPAC guidelines¹⁰⁰ as typical of microporous materials and expected for a UiO-66 isostructural material²².

The analysis of the N₂ adsorption isotherms reported in Figure 47 with both Langmuir and BET models for the calculation of the specific surface area leads to values reported in Table 16 below. All activation procedures were 3 h long.

Table 16 – Specific surface area values measured on Ce-UiO-66-ADC.

Activation temperature	Langmuir area (m²/g)	BET area (m²/g)
RT	425(5)	316(3)
60°C	437(4)	327(4)
90°C	371(6)	273(2)
120°C	163(3)	118(1)

Despite the small weight loss observed in TGA in this temperature range (RT-120°C) the material is showing a remarkable specific surface area (up to about 430 m²/g after activation at 60°C). Those values decrease at higher activation temperatures as suggested by VT-XRD data which is pointing out a collapse of the crystal structure at temperatures above 90°C.

It is relevant to notice that a geometrical calculation made with the Materials Studio code of the specific surface area, made from the crystal structure found by Rietveld refinement, indicates a value of about 1200 m²/g. The discrepancy between the simulated and the experimental values can be explained by the presence of adsorbed solvent (DMF or water) inside the pores of the material at those activation temperatures, as shown by TGA data (Figure 45). With those experimental result it is reasonable to consider that DMF cannot be desorbed by dynamic outgassing during heating because the material itself is collapsing before. Regular UiO-66, instead, being stable up to 500°C can be desolvated by this method without losing crystallinity^{22,103,154}.

3.4.4 Vibrational spectroscopy

Vibrational spectroscopies (FTIR and Raman) were employed to characterize Ce-UiO-66-ADC in order to obtain information about the chemical nature of the material. Those spectroscopies were also used to follow in an *ex-situ* manner the thermal activation procedure made before the nitrogen adsorption isotherms and the VTXRD experiments. Results are shown below in Figure 48 and Figure 49, respectively.

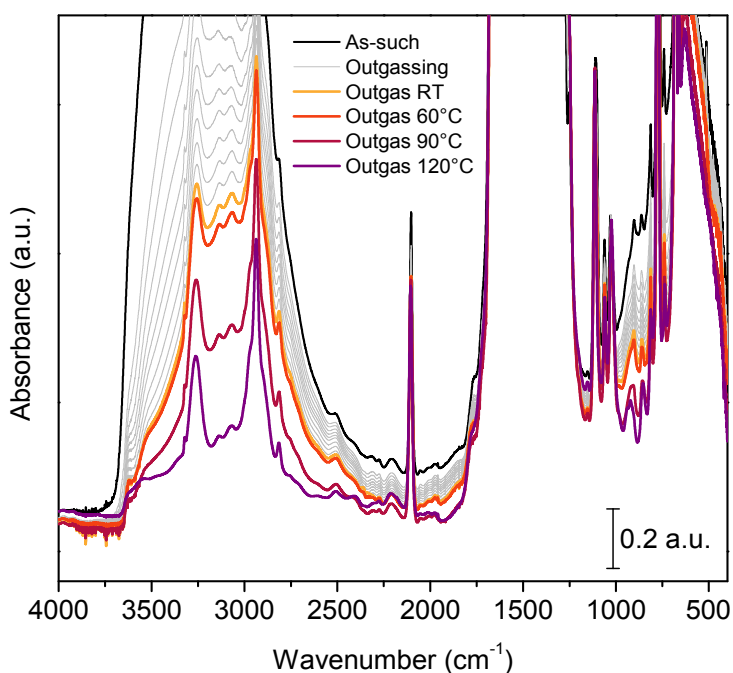


Figure 48 – Transmission FTIR spectra collected on Ce-UiO-66-ADC as such (black), after an overnight outgassing (orange) and thermal activations in dynamic vacuum (3 h long) at 60°C (red) 90°C (purple) and 120°C (violet).

The high-wavenumber region of the FTIR spectra is dominated by a very intense broad band in the 3400-2800 cm⁻¹ range that can be assigned to OH groups of adsorbed solvent molecules (DMF and water, supposedly) interacting via H-bonds mutually within the pores of the MOF. This band is weakening but not vanishing after an overnight outgassing at room temperature (orange curve).

An assignment¹⁴³ of some relevant vibrational bands of the spectra reported in Figure 48 is the following:

- 3260 cm⁻¹ $\nu(\text{CH})$ of terminal alkyne
- 2935 cm⁻¹ $\nu(\text{CH})_{\text{sym}}$ of aliphatic CH groups from DMF
- 2810 cm⁻¹ $\nu(\text{CH})_{\text{asym}}$ of aliphatic CH groups from DMF
- 2107 cm⁻¹ $\nu(\text{C}\equiv\text{C})$ of asymmetrically substituted alkyne
- 1770 cm⁻¹ $\nu(\text{C}=\text{O})$ (shoulder) of carbonyl from DMF
- 1690-1280 cm⁻¹ $\nu(\text{COO}^-)$ symmetric and asymmetric stretching of carboxylates

The region under 1000 cm⁻¹, the fingerprint region, is full of bands due to both linker moieties and Ce-O vibrational modes. For a complete assignment of the bands in this region a computational modelling is mandatory as successfully applied in similar cases^{83,103}.

The effect of thermal treatment at increasingly higher temperatures (up to 120°C, violet curve in Figure 48) is causing the progressive decrease of the intensity of the broad band centered at 3100 cm⁻¹ as the solvent adsorbed in the pores is being outgassed. As demonstrated by VT-XRD and N₂ adsorption measurements at temperatures above 90°C the material collapses losing its crystallinity and porosity: this spectroscopic data demonstrate that it's not possible to outgas totally the MOF from the adsorbed solvents without collapsing it. It is however interesting to notice that the collapse is not testified by the comparison of the vanishing of a vibrational band, testifying a substantial chemical similarity between the crystalline pristine product and the collapsed one after treatment at temperatures above 90°C. The faint shoulder observable at 3620 cm⁻¹ can be tentatively assigned to the presence of dangling OH groups from the Ce₆ clusters, as thoroughly known for UiO-66¹⁰³ but still engaged in H-bond interaction with solvent molecules adsorbed in the pores.

The color of the pellet during the thermal treatments changes from the pale yellow of the as-synthesized compound to a dark yellow at 90°C and a brown color at 120°C indicating the comparison of visible light absorbing species during the heat treatment.

The bands at 3260 and 2107 cm⁻¹ characteristic of terminal alkynes are extremely informative and unexpected, as the linker used is, in fact a symmetrical substituted alkyne and the stretching of the triple bond is not active in IR spectroscopy¹⁴³. Their intensity, however, it is not changing during outgassing and thermal treatments. Being the stretching of symmetric triple bonds a vibrational mode active in Raman spectroscopy the study continued with the measurement of such a spectra.

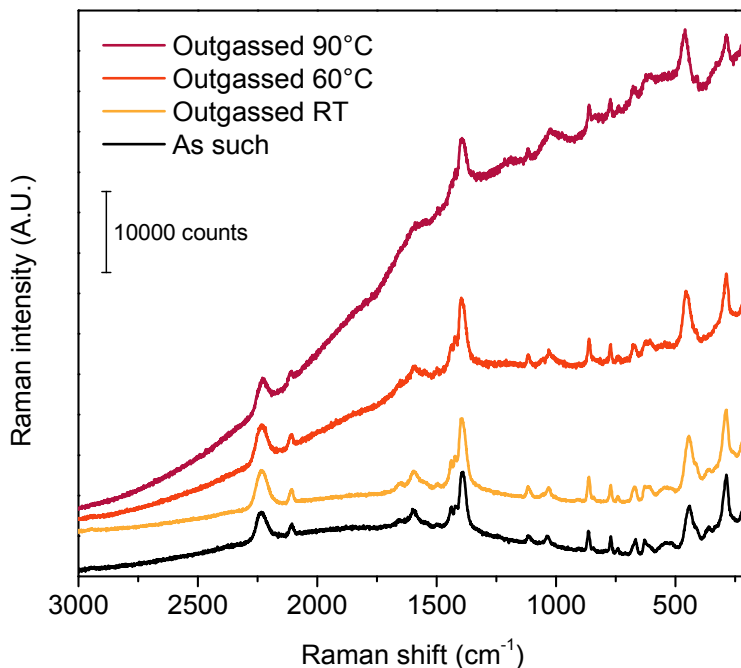


Figure 49 – Raman spectra collected on Ce-UiO-66-ADC as-such (black) after an overnight outgassing (orange) and after thermal activations in dynamic vacuum (3 h long) at 60°C (red) and 90°C (purple). ($\lambda_i = 785$ nm). The 120°C curve is omitted for too high fluorescence.

The same *ex-situ* experiment done by means of FTIR spectroscopy was replicated in the case of Raman technique (Figure 49). A general trend that can be correlated with increasingly high activation temperatures is the growing of the baseline due to concomitant fluorescence. The principal and most informative Raman bands were assigned¹⁴³ as the following:

- 2234 cm^{-1} $\nu(\text{C}\equiv\text{C})$ of symmetrically substituted alkynes
- 2107 cm^{-1} $\nu(\text{C}\equiv\text{C})$ of asymmetrically substituted alkynes
- 1584 cm^{-1} $\nu(\text{C}=\text{O})$ of carbonyl from DMF
- 1475-1350 cm^{-1} $\nu(\text{COO}^-)_{\text{sym}}$ of carboxylates

The contemporary presence of symmetrically and unsymmetrically substituted alkynes can be inferred by the presence of both vibrational bands in the Raman spectra.

To undoubtedly assign those unexpected vibrational bands typical of triple bonds the vibrational spectra of Ce-UiO-66-ADC was compared with the spectra of acetylenedicarboxylate and propiolate anions, as in Figure 51, (the common name for the propynoate anion) in water solution as prepared from commercial starting materials. The standard solutions were prepared titrating with an excess of aqueous 5M KOH solution a suitable amount of commercial acetylenedicarboxylic acid (the linker used in the MOF synthesis) and propiolic acid.

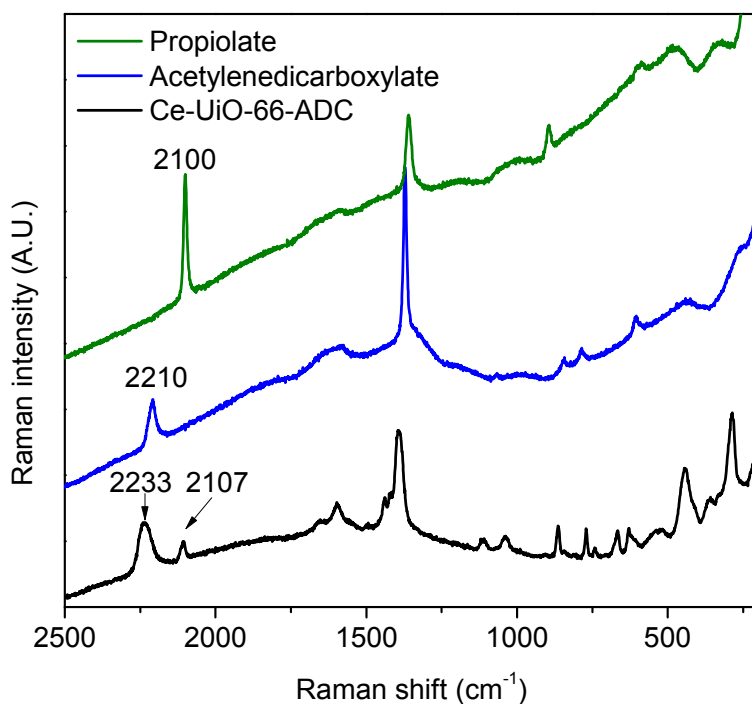


Figure 50 – Comparison of the Raman spectra of Ce-UiO-66-ADC (black) with basic water solutions of acetylenedicarboxylate (blue) and propiolate (green). ($\lambda_i = 785$ nm).

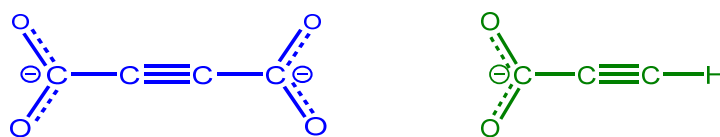


Figure 51 – Acetylenedicarboxylate (blue) and propiolate (green) anions.

3.4.5 Linker decarboxylation

As prompted out by the unexpected and serendipitous presence of vibrational bands typical of terminal alkynes they must be synthesized during the synthesis of the MOF, which is done solvothermally in water/DMF mixture at 100°C. No any relevant impurity of propiolic acid in the commercial acetylenedicarboxylic acid is highlighted by Raman spectroscopy. As previously reported by Tranchemontagne et al.¹⁵⁵ H₂ADC is thermally sensitive and it decomposes during synthesis if this is done at a sufficiently high temperature.

Li et al. reported in 2002¹⁵⁶ a detailed study about the kinetics of the decarboxylation reaction of acetylenedicarboxylic acid in water medium in function of the temperature (Figure 52).

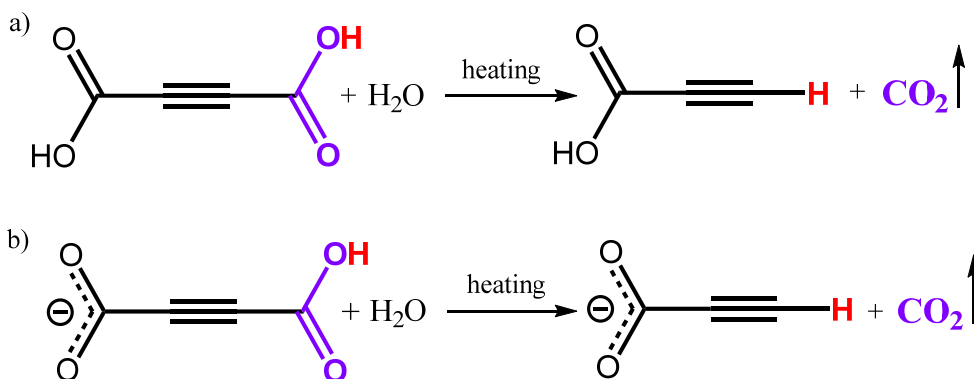


Figure 52 – Water-mediated decarboxylation reaction of H₂ADC (a) and HADC⁻ (b).

What emerges from the paper is that the speed of this reaction is strongly dependent from the starting species i.e. the mono and the double deprotonated HADC⁻ and ADC²⁻ as reported below in Figure 53.

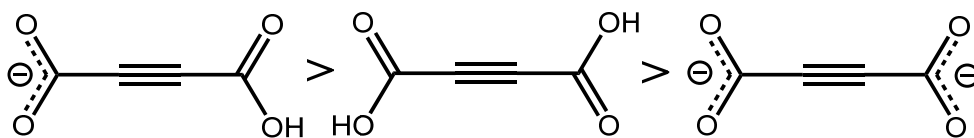


Figure 53 – Order of the decarboxylation speed for acetylenedicarboxylate related conjugated acids and bases.

This is also reasoning the finding for which the yield of the synthesis reaction for Ce-UiO-66-ADC is greatly improved if triethylamine is added to the synthesis mixture, as noticed during the optimization of the synthesis procedure of this compound¹³².

The addition of a base pushes the equilibrium towards the double deprotonated species, which is more resistant to decarboxylation.

3.4.6 Defectivity hypothesis

The presence of defects in the crystal structure of UiO-66 is well-known in literature^{157–159}. They can be related to both inorganic and organic components and, in the case of UiO-66, two main point defects types were characterized: missing cluster and missing linker defects. The first one corresponding to the absence of a hexanuclear metal cluster and the latter related to the lack of a linker molecule bridging two different SBUs. Both defects require some compensating anions in order to achieve the electrical neutrality: frequently they have been identified as monocarboxylate moieties (e.g. formate, acetate). The deliberate addition of monocarboxylic acids in the synthesis mixture of UiO-66 permitted to modulate the presence and concentration of defects in such material doing an effective “defect-engineering”^{81,83,94,160}. Defectivity in UiO-66 is testified by the following experimental evidences, as reported by Shearer et al.¹⁵⁷: reduced thermal stability, the occurrence of forbidden PXRD reflections, stoichiometric incongruencies from TGA data and deviations from the theoretical surface area. As reported in the paper⁸³ reported in Appendix II if the monocarboxylic moieties have a definite vibrational fingerprint, i.e. benzoate anions, the presence of defects can be correlated also with the appearance of unexpected vibrational bands.

In the case of Ce-UiO-66-ADC the *in-situ* production of the monocarboxylic derivative of the linker propiolic acid through a decarboxylation reaction was demonstrated by vibrational spectroscopy. For this reason the presence of defects decorated by propiolate moieties can be hypothesized looking at the current multi-technique dataset. Such proposed defective structure is visualized in Figure 54.

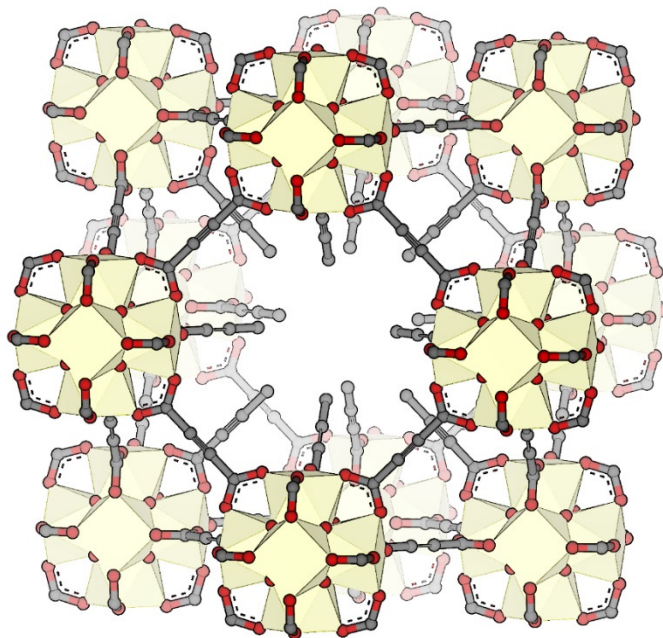


Figure 54 – Hypothesized missing-cluster defect decorated by propiolates for Ce-UiO-66-ADC.

As the current dataset does not permit to recognize unambiguously the presence of this defect into Ce-UiO-66-ADC such sentence is not anything more than a hypothesis. New experimental data as dissolution ^1H and ^{13}C NMR quantitative spectroscopy is needed in order to strengthen this hypothesis.

4. Conclusions

This thesis presented the successful synthesis of four novel Ce-based MOFs and their characterization with a selection of techniques specifically selected to disclose the properties of each material. The following paragraphs will concern singular conclusions that can be drawn from each material.

Ce₂(NDC)₃(DMF)₂

A novel MOF based on Ce³⁺ cations and a simple ditopic linker (2,6-naphthalenedicarboxylic acid) was synthesized with a solvothermal method. Its crystal structure solved by the means of a SCXRD technique, revealed its simple and rather unique structure formed by infinite Ce chains forming diamond-shaped channels. This material upon thermal treatment loses its crystallization DMF molecules and transforms into a different phase characterized by a high amount of crystalline disorder, as demonstrated by TGA and VTNRD data. The crystal structure of the desolvated MOF was solved from a synergic use of both SCXRD and EXAFS techniques that revealed a disordered structure with triangular channels. Despite the absence of a surface area by the means of N₂ volumetry at -196°C the material showed a decent porosity by CO₂ at -78°C evidencing a kind of porosity traditionally overlooked by classical characterization methods.

As this material is selectively adsorbing CO₂ over N₂, applications in separation of CO₂/N₂ mixtures can be proposed exploiting this characteristic of Ce₂(NDC)₃.

Ce₂(ADB)₃(DMA)_{3,4}

In a tight comparison with the above mentioned material, another novel Ce³⁺-based material has been synthesized with solvothermal methods. The optimization of the synthesis procedure, with the help of the so-called High-Throughput methods, permitted to find the optimal conditions: the usage of DMA instead of DMF revealed to be necessary for the success of the synthesis. The material revealed a series of phase transitions upon heating accompanied by the loss of the crystallization solvent. These crystalline phases are characterized by a high degree of inherent disorder that prevented their solution by single-crystal x-ray diffraction. The study of the porosity of these compounds and their crystal structures may be completed by exploiting the same techniques that revealed to be useful in the study of Ce₂(NDC)₃(DMF)₂: synchrotron-based techniques (i.e. EXAFS spectroscopy) and CO₂ volumetry at -78°C.

Being the linker used in the building of the $Ce_2(ADB)_3(DMA)_{3.4}$ able to absorb visible light (i.e. colored) a possible application for this material may be inside optical devices as a light harvester.

Ce/Zr-UiO-66

Mixed metal Ce/Zr-UiO-66 was recently introduced in the literature as a way to improve the reactivity of UiO-66 using a redox-active metal like cerium. The resulting material revealed a diminished thermal stability than its pure Zr counterpart even at low Ce contents. In order to highlight the composition of the metal clusters, synchrotron high-resolution powder diffraction and the *in-situ* dosage of CD_3CN as a probe molecule in FTIR spectroscopy experiments were employed: the results highlighted the presence of Ce cations inside the material but without a specific information about the composition of the clusters. Thanks to a multi-wavelength EXAFS analysis on both Zr and Ce K-edges, the composition of the metallic cornerstones was finally identified to be truly bimetallic. The same technique highlighted also the preferential formation of $CeZr_5$ hexanuclear clusters instead of any other type of stoichiometry. By a result of this, a Ce/Zr-UiO-66 material would have a mixture of Zr_6 and $CeZr_5$ clusters at Ce loadings lower than 17% (1/6 of the total atomic metallic content) and a mixture of $CeZr_5$ and Ce_6 clusters at higher concentrations. This result explains also the relationship between the Ce content and the thermal stability already observed by Lammert et al.⁶⁴

In respect to their Zr counterparts Ce-based UiO-type materials are suffering a general decreasing of the thermal and chemical stability. As Ce is known to be a redox-active metal (its oxide, CeO_2 , is widely exploited as redox catalyst) Ce/Zr mixed UiO-66 MOFs may bridge the gap between the thermally delicate Ce-UiO-66 and the redox-inactive Zr-UiO-66 and they can be exploited as redox catalysts.

Ce-UiO-66-ADC

Since the discovery of UiO-66 a number of works by the scientific community was devoted to this material: iso-reticular material with ditopic linkers, defect engineering, post-synthetic modifications, just to cite few of these. None of these papers is devoted to the insertion of acetylenedicarboxylate as linker in UiO-66, probably because of its extreme thermolability, thus its non-decomposition being difficult during the synthetic conditions of UiO-66. This thesis presented the first successful synthesis of an acetylenedicarboxylate-containing UiO-66 derivative with Ce^{4+} cations. The crystalline structure of this compound was determined via a Rietveld refinement which resulted in an isostructurality with UiO-66. This MOF revealed a poor thermal stability collapsing totally already at $90^\circ C$ but even at after a

thermal activation at lower temperature it showed a decent porosity by the means of N₂ adsorption measurement at -196°C in the order of 400 m²/g. Vibrational spectroscopies, IR and Raman, showed serendipitously the presence of a band assignable to the presence of propiolates, coming from the decarboxylation of the linker during the synthesis. As UiO-66 is known to incorporate monodentate moieties in the form of defects this allowed us to hypothesize the presence of such defective structures decorated by propiolate moieties inside the MOF.

Ce-UiO-66-ADC is one of the very few MOFs (looking at the literature) containing the carbon triple bond. In this respect, the specific reactivity of this moiety may be exploited in various applications: for example the addition of a gaseous species (e.g. HCl) to the triple bond can be used to build an adsorber for this gas.

In conclusion, the present work demonstrates how it is possible to design and synthesize novel Ce-based MOFs. Till now, cerium was not commonly adopted in MOF synthesis, but, being, among rare earth metals, one of the most abundant, I thought its adoption would have been interesting. Finally, the explored field revealed to be very rich and malleable, also considering the possible imaginable applications.

Acknowledgements

I would like to thank my supervisor, Dr. Francesca Bonino, for her constant and irreplaceable guidance over these three years (and not only...) of PhD. Prof. Claudia Barolo and Prof. Silvia Bordiga are acknowledged for their supervision under some specific topics. I owe all of you my personal growth into scientific research during these years of PhD.

Professor Norbert Stock, from the University of Kiel, and his research group are acknowledged for having kindly welcome me in its laboratory in Kiel and for his precious supervision that introduced me into the realm of the MOF synthesis.

Prof. Karl Petter Lillerud and Dr. Sigurd Øien-Ødegaard, from the University of Oslo, are acknowledged for the fruitful discussions and for having done part of the crystallographic work reported in the present thesis.

I am grateful to Dr. Kirill Lomachenko and Prof. Carlo Lamberti for their work with X-Ray Absorption spectroscopies and all the scientists who helped us at the ID22 and the BM31 beamlines at the ESRF facility.

Concerning $\text{Ce}_2(\text{ADB})_3(\text{DMA})_{3,4}$ my acknowledgements are due to Gioele Giordanengo (MSc thesis student) for having done part of the experiments. The whole work-group about this activity is also acknowledged: Prof. Marco Milanese, Prof. Bartolomeo Civalleri, Dr. Luca Palin and Dr. Nadia Barbero.

With regard to Ce-UiO-66-ADC topic, I am grateful to Alessia Airi (MSc thesis student) for her help with a relevant fraction of the experimental work.

H2020 project ProDIA (Project No. 685727) is acknowledged for having partially granted my PhD.

List of abbreviations

ASAP	Accelerated Surface Area and Porosimetry system
CAN	Cerium Ammonium Nitrate
CCD	Charge Coupled Device
CCDC	Cambridge Crystallographic Data Centre
CCUS	Carbon Capture, Utilization and Storage
CMOS	Complementary Metal-Oxide Semiconductor
CSD	Cambridge Structural Database
DABCO	1,4-diazabicyclo[2.2.2]octane
DMA	N,N-dimethylacetamide
DMF	N,N-dimethylformamide
DMSO	Dimethyl sulfoxide
EXAFS	Extended X-ray Absorption Fine Structure
FTIR	Fourier Transform Infrared Spectroscopy
H ₂ ADB	4,4'-azodibenzoic acid or 4,4'-(E)-diazene-1,2-diylidibenzoic acid
H ₂ ADC	Acetylenedicarboxylic acid or Butynedioic acid
H ₂ BDC	Terephthalic acid or Benzene-1,4-dicarboxylic acid
H ₂ NDC	2,6-Naphthalenedicarboxylic acid
H ₄ DSNDC	4,8-Disulfonyl-2,6-Naphthalenedicarboxylic acid
HKUST	Hong Kong University of Science and Technology
HT	High Throughput
ICP-MS	Inductively Coupled Plasma – Mass Spectrometry
IUPAC	International Union of Pure and Applied Chemistry

MCM	Mobil Composition of Matter
MIL	Matériaux de l'Institut Lavoisier
MOF	Metal-Organic Framework
PXRD	Powder X-Ray Diffraction
RCSR	Reticular Chemistry Structure Resource
SBA	Santa Barbara Amorphous
SBU	Structure Building Unit
SCXRD	Single-Crystal X-Ray Diffraction
SDA	Structure Directing Agent
SEM	Scanning Electron Microscopy
TCI	Tokyo Chemical Industry
TGA	Thermogravimetry Analysis
UiO	Universitetet i Oslo (University of Oslo)
UTSA	University of Texas at San Antonio
UV-Vis	Ultraviolet-Visible
VTXRD	Variable-Temperature X-Ray Diffraction
XAFS	X-Ray Absorption Fine Structure
XANES	X-Ray Absorption Near Edge Structure
XAS	X-Ray Absorption Spectroscopy
XPS	X-Ray Photoelectron Spectroscopy

Bibliography

- (1) Kaskel, S. *The Chemistry of Metal-Organic Frameworks: Synthesis, Characterization, and Applications*; Kaskel, S., Ed.; John Wiley & Sons: Weinheim, 2016.
- (2) Zhou, H.-C.; Long, J. R.; Yaghi, O. M. Introduction to Metal–Organic Frameworks. *Chem. Rev.* **2012**, *112*, 673–674.
- (3) Long, J. R.; Yaghi, O. M. The Pervasive Chemistry of Metal-Organic Frameworks. *Chem. Soc. Rev.* **2009**, *38*, 1213–1214.
- (4) Zhou, H. C. J.; Kitagawa, S. Metal-Organic Frameworks (MOFs). *Chem. Soc. Rev.* **2014**, *43*, 5415–5418.
- (5) Furukawa, H.; Cordova, K. E. E.; O’Keeffe, M.; Yaghi, O. M. O. M.; O’Keeffe, M.; Yaghi, O. M. O. M. The Chemistry and Applications of Metal-Organic Frameworks. *Science* **2013**, *341*, 1230444.
- (6) Butova, V. V; Soldatov, M. A.; Guda, A. A.; Lomachenko, K. A.; Lamberti, C. Metal-Organic Frameworks: Structure, Properties, Methods of Synthesis and Characterization. *Russ. Chem. Rev.* **2016**, *85*, 280–307.
- (7) Batten, S. R.; Champness, N. R.; Chen, X.-M.; Garcia-Martinez, J.; Kitagawa, S.; Öhrström, L.; O’Keeffe, M.; Paik Suh, M.; Reedijk, J. Terminology of Metal–organic Frameworks and Coordination Polymers (IUPAC Recommendations 2013). *Pure Appl. Chem.* **2013**, *85*, 1715–1724.
- (8) Yaghi, O. M.; Li, H. Hydrothermal Synthesis of a Metal-Organic Framework Containing Large Rectangular Channels. *J. Am. Chem. Soc.* **1995**, *117*, 10401–10402.
- (9) Kinoshita, Y.; Matsubara, I.; Saito, Y. The Crystal Structure of Bis(Succinonitrilo)Copper(I) Nitrate. *Bull. Chem. Soc. Jpn.* **1959**, *32*, 741–747.
- (10) Hoskins, B. F.; Robson, R. Infinite Polymeric Frameworks Consisting of Three Dimensionally Linked Rod-like Segments. *J. Am. Chem. Soc.* **1989**, *111*, 5962–5964.
- (11) Kato, R.; Kobayashi, H.; Kobayashi, A. Crystal and Electronic Structures of Conductive Anion-Radical Salts, (2, 5-R1, R2-DCNQI)2Cu (DCNQI = N, N’-Dicyanoquinonediimide; R1, R2= CH3, CH3O, Cl, Br). *J. Am. Chem. Soc.* **1989**, *111*, 5224–5232.
- (12) MacGillivray, L. R.; Subramanian, S.; Zaworotko, M. J. Interwoven Two-

- and Three-Dimensional Coordination Polymers through Self-Assembly of CuI cations with Linear Bidentate Ligands. *J. Chem. Soc. Chem. Commun.* **1994**, No. 11, 1325–1326.
- (13) Kitagawa, S.; Munakata, M.; Tanimura, T. Synthesis of the Novel Infinite-Sheet and -Chain Copper(I) Complex Polymers $\{[\text{Cu}(\text{C}_4\text{H}_4\text{N}_2)_3/2(\text{CH}_3\text{CN})](\text{PF}_6)_0.5\text{C}_3\text{H}_6\text{O}\}_\infty$ and $[\text{Cu}_2(\text{C}_8\text{H}_{12}\text{N}_2)_3](\text{ClO}_4)_2)_\infty$ and Their X-Ray Crystal Structures. *Inorg. Chem.* **1992**, *31*, 1714–1717.
- (14) Yaghi, O. M.; Li, H. T-Shaped Molecular Building Units in the Porous Structure of $\text{Ag}(4,4'\text{-Bpy})\cdot\text{NO}_3$. *J. Am. Chem. Soc.* **1996**, *118*, 295–296.
- (15) Li, H.; Eddaoudi, M.; Groy, T. L.; Yaghi, O. M. Establishing Microporosity in Open Metal–Organic Frameworks: Gas Sorption Isotherms for Zn(BDC) (BDC = 1,4-Benzenedicarboxylate). *J. Am. Chem. Soc.* **1998**, *120*, 8571–8572.
- (16) Li, H.; Eddaoudi, M.; O’Keeffe, M.; Yaghi, O. M. Design and Synthesis of an Exceptionally Stable and Highly Porous Metal–Organic Framework. *Nature* **1999**, *402*, 276–279.
- (17) Chui, S. S. Y.; Lo, S. M. F.; Charmant, J. P. H.; Orpen, A. G.; Williams, I. D. A Chemically Functionalizable Nanoporous Material $[\text{Cu}_3(\text{TMA})_2(\text{H}_2\text{O})_3](\text{N})$. *Science* **1999**, *283*, 1148–1150.
- (18) Moghadam, P. Z.; Li, A.; Wiggin, S. B.; Tao, A.; Maloney, A. G. P.; Wood, P. A.; Ward, S. C.; Fairen-Jimenez, D. Development of a Cambridge Structural Database Subset: A Collection of Metal–Organic Frameworks for Past, Present, and Future. *Chem. Mater.* **2017**, *29*, 2618–2625.
- (19) Yaghi, O. M.; O’Keeffe, M.; Ockwig, N. W.; Chae, H. K.; Eddaoudi, M.; Kim, J. Reticular Synthesis and the Design of New Materials. *Nature* **2003**, *423*, 705–714.
- (20) Vitillo, J. G.; Atzori, C.; Civalieri, B.; Barbero, N.; Barolo, C.; Bonino, F. Design and Characterization of MOFs (Metal–Organic Frameworks) for Innovative Applications. In *Hybrid Organic–Inorganic Interfaces*; Wiley-VCH Verlag GmbH & Co. KGaA: Weinheim, Germany, 2017; pp 459–495.
- (21) O’Keeffe, M.; Peskov, M. A.; Ramsden, S. J.; Yaghi, O. M. The Reticular Chemistry Structure Resource (RCSR) Database of, and Symbols for, Crystal Nets. *Acc. Chem. Res.* **2008**, *41*, 1782–1789.
- (22) Cavka, J. H.; Jakobsen, S.; Olsbye, U.; Guillou, N.; Lamberti, C.; Bordiga, S.; Lillerud, K. P. A New Zirconium Inorganic Building Brick Forming Metal Organic Frameworks with Exceptional Stability. *J. Am. Chem. Soc.*

2008, 130, 13850–13851.

- (23) Research topics - Department of chemistry UiO
<https://www.mn.uio.no/kjemi/english/research/groups/catalysis/research/>.
- (24) Haxel, G. B.; Hedrick, J. B.; Orris, G. J. *Rare Earth Elements—Critical Resources for High Technology SUPPORTING SOUND MANAGEMENT OF OUR MINERAL RESOURCES*; 2002.
- (25) Long, K. R.; Van Gosen, B. S.; Foley, N. K.; Cordier, D. *The Principal Rare Earth Elements Deposits of the United States: A Summary of Domestic Deposits and a Global Perspective*; 2012.
- (26) Institut für Seltene Erden und Metalle (ISE, Germany) <http://www.institut-seltene-erden.org/>.
- (27) Montini, T.; Melchionna, M.; Monai, M.; Fornasiero, P. Fundamentals and Catalytic Applications of CeO₂-Based Materials. *Chem. Rev.* **2016**, *116*, 5987–6041.
- (28) Kašpar, J.; Fornasiero, P.; Graziani, M. Use of CeO₂-Based Oxides in the Three-Way Catalysis. *Catal. Today* **1999**, *50*, 285–298.
- (29) Lammert, M. PhD Thesis, Christian-Albrechts-University, Kiel, 2017.
- (30) Liang, L. L.; Xu, L.; Xue, H. B.; Tao, Z. L.; Chen, F. J. Two Metal-Organic Frameworks with Different Configurations Constructed from a Flexible Tripodal Triaromatic Acid. *J. Mol. Struct.* **2016**, *1125*, 656–661.
- (31) Warren, J. E.; Perkins, C. G.; Jelfs, K. E.; Boldrin, P.; Chater, P. A.; Miller, G. J.; Manning, T. D.; Briggs, M. E.; Stylianou, K. C.; Claridge, J. B.; et al. Shape Selectivity by Guest-Driven Restructuring of a Porous Material. *Angew. Chemie - Int. Ed.* **2014**, *53*, 4592–4596.
- (32) Li, Z.; Liu, K. Poly[(μ(4)-Benzene-1,3,5-Tricarboxyl-Ato)Bis-(N,N-Dimethyl-Formamide)-Cerium(III)]. *Acta Crystallogr. Sect. E. Struct. Rep. Online* **2011**, *67*, m1020.
- (33) D'Arras, L.; Sassoie, C.; Rozes, L.; Sanchez, C.; Marrot, J.; Marre, S.; Aymonier, C. Fast and Continuous Processing of a New Sub-Micronic Lanthanide-Based Metal–organic Framework. *New J. Chem.* **2014**, *38*, 1477.
- (34) Quah, H. S.; Ng, L. T.; Donnadiou, B.; Tan, G. K.; Vittal, J. J. Molecular Scissoring: Facile 3D to 2D Conversion of Lanthanide Metal Organic Frameworks Via Solvent Exfoliation. *Inorg. Chem.* **2016**, *55*, 10851–10854.
- (35) Almáši, M.; Zeleňák, V.; Opanasenko, M.; Čísařová, I. Ce(III) and Lu(III) Metal-Organic Frameworks with Lewis Acid Metal Sites: Preparation,

- Sorption Properties and Catalytic Activity in Knoevenagel Condensation. *Catal. Today* **2015**, *243*, 3098–3114.
- (36) Ethiraj, J.; Bonino, F.; Vitillo, J. G.; Lomachenko, K. A.; Lamberti, C.; Reinsch, H.; Lillerud, K. P.; Bordiga, S. Solvent-Driven Gate Opening in MOF-76-Ce: Effect on CO₂ Adsorption. *ChemSusChem* **2016**, *9*, 713–719.
- (37) Ayhan, O.; Malaestean, I. L.; Ellern, A.; Van Leusen, J.; Baca, S. G.; Kögerler, P. Assembly of Cerium(III) 2,2'-Bipyridine-5,5'-Dicarboxylate-Based Metal-Organic Frameworks by Solvent Tuning. *Cryst. Growth Des.* **2014**, *14*, 3541–3548.
- (38) Bag, P. P.; Wang, X. S.; Cao, R. Microwave-Assisted Large Scale Synthesis of Lanthanide Metal-Organic Frameworks (Ln-MOFs), Having a Preferred Conformation and Photoluminescence Properties. *Dalton Trans.* **2015**, *44*, 11954–11962.
- (39) Zhai, L.; Zhang, W. W.; Ren, X. M.; Zuo, J. L. Luminescent Lanthanide MOFs Based on Conjugated 1,1'-Ethynebenzene-3,3',5,5'-Tetracarboxylate Ligand: Syntheses, Structures and Photoluminescent Properties. *Dalton Trans.* **2015**, *44*, 5746–5754.
- (40) Wang, C.; Li, L.; Bell, J. G.; Lv, X.; Tang, S.; Zhao, X.; Thomas, K. M. Hysteretic Gas and Vapor Sorption in Flexible Interpenetrated Lanthanide-Based Metal-Organic Frameworks with Coordinated Molecular Gating via Reversible Single-Crystal-to-Single-Crystal Transformation for Enhanced Selectivity. *Chem. Mater.* **2015**, *27*, 1502–1516.
- (41) Wu, Y. P.; Li, D. S.; Xia, W.; Guo, S. S.; Dong, W. W. Three Novel Lanthanide Metal-Organic Frameworks (Ln-MOFs) Constructed by Unsymmetrical Aromatic Dicarboxylate Tectonics: Synthesis, Crystal Structures and Luminescent Properties. *Molecules* **2014**, *19*, 14352–14365.
- (42) Das, S. K.; Chatterjee, S.; Bhunia, S.; Mondal, A.; Mitra, P.; Kumari, V.; Pradhan, A.; Bhaumik, A. A New Strongly Paramagnetic Cerium-Containing Microporous MOF for CO₂ Fixation under Ambient Conditions. *Dalton Trans.* **2017**, *46*, 13783–13792.
- (43) Liu, Y. H.; Chien, P. H. A Series of Lanthanide-Organic Frameworks Possessing Arrays of 2D Intersecting Channels within a 3D Pillar-Supported Packed Double-Decker Network and Co²⁺-Induced Luminescence Modulation. *CrystEngComm* **2014**, *16*, 8852–8862.
- (44) Nandi, G.; Thakuria, R.; Titi, H. M.; Patra, R.; Goldberg, I. Synthesis, Structure, Topology and Magnetic Properties of New Coordination Polymers Based on 5(-Br/-COOH)-Substituted Nicotinic Acid. *CrystEngComm* **2014**, *16*, 5244–5256.

- (45) Nandi, G.; Titi, H. M.; Thakuria, R.; Goldberg, I. Solvent Dependent Formation of Metallogels and Single-Crystal MOFs by La(III) and Ce(III) Connectors and 3,5-Pyridinedicarboxylate. *Cryst. Growth Des.* **2014**, *14*, 2714–2719.
- (46) Silva, P.; Ananias, D.; Bruno, S. M.; Valente, A. A.; Carlos, L. D.; Rocha, J.; Almeida Paz, F. A. Photoluminescent Metal-Organic Frameworks - Rapid Preparation, Catalytic Activity, and Framework Relationships. *Eur. J. Inorg. Chem.* **2013**, *2013*, 5576–5591.
- (47) Jia, L. N.; Hou, L.; Wei, L.; Jing, X. J.; Liu, B.; Wang, Y. Y.; Shi, Q. Z. Five Sra Topological Ln(III)-MOFs Based on Novel Metal-Carboxylate/Cl Chain: Structure, near-Infrared Luminescence and Magnetic Properties. *Cryst. Growth Des.* **2013**, *13*, 1570–1576.
- (48) Tang, Q.; Liu, S.; Liu, Y.; Miao, J.; Li, S.; Zhang, L.; Shi, Z.; Zheng, Z. Cation Sensing by a Luminescent Metal-Organic Framework with Multiple Lewis Basic Sites. *Inorg. Chem.* **2013**, *52*, 2799–2801.
- (49) Nayak, S.; Nayek, H. P.; Pietzonka, C.; Novitchi, G.; Dehnen, S. A Series of Three-Dimensional Lanthanide MOFs: Observation of Reversible Structural Changes Controlled by Solvent Desorption-Adsorption, and Magnetic Properties. *J. Mol. Struct.* **2011**, *1004*, 82–87.
- (50) Han, Y.; Li, X.; Li, L.; Ma, C.; Shen, Z.; Song, Y.; You, X. Structures and Properties of Porous Coordination Polymers Based on Lanthanide Carboxylate Building Units. *Inorg. Chem.* **2010**, *49*, 10781–10787.
- (51) Neofotistou, E.; Malliakas, C. D.; Trikalitis, P. N. Remarkable Structural Diversity and Single-Crystal-to-Single-Crystal Transformations in Sulfone Functionalized Lanthanide MOFs. *CrystEngComm* **2010**, *12*, 1034–1037.
- (52) Devic, T.; Wagner, V.; Guillou, N.; Vimont, A.; Haouas, M.; Pascolini, M.; Serre, C.; Marrot, J.; Daturi, M.; Taulelle, F.; et al. Synthesis and Characterization of a Series of Porous Lanthanide Tricarboxylates. *Microporous Mesoporous Mater.* **2011**, *140*, 25–33.
- (53) Pan, L.; Adams, K. M.; Hernandez, H. E.; Wang, X.; Zheng, C.; Hattori, Y.; Kaneko, K. Porous Lanthanide-Organic Frameworks: Synthesis, Characterization, and Unprecedented Gas Adsorption Properties. *J. Am. Chem. Soc.* **2003**, *125*, 3062–3067.
- (54) Lammert, M.; Wharmby, M. T.; Smolders, S.; Bueken, B.; Lieb, A.; Lomachenko, K. A.; Vos, D. De; Stock, N. Cerium-Based Metal Organic Frameworks with UiO-66 Architecture: Synthesis, Properties and Redox Catalytic Activity. *Chem. Commun.* **2015**, *51*, 12578–12581.

- (55) Lammert, M.; Reinsch, H.; Murray, C. A.; Wharmby, M. T.; Terraschke, H.; Stock, N. Synthesis and Structure of Zr(IV)- and Ce(IV)-Based CAU-24 with 1,2,4,5-Tetrakis(4-Carboxyphenyl)Benzene. *Dalton Trans.* **2016**, *45*, 18822–18826.
- (56) Dreischarf, A. C.; Lammert, M.; Stock, N.; Reinsch, H. Green Synthesis of Zr-CAU-28: Structure and Properties of the First Zr-MOF Based on 2,5-Furandicarboxylic Acid. *Inorg. Chem.* **2017**, *56*, 2270–2277.
- (57) Lammert, M.; Glißmann, C.; Reinsch, H.; Stock, N. Synthesis and Characterization of New Ce(IV)-MOFs Exhibiting Various Framework Topologies. *Cryst. Growth Des.* **2017**, *17*, 1125–1131.
- (58) Waitschat, S.; Fröhlich, D.; Reinsch, H.; Terraschke, H.; Lomachenko, K. A.; Lamberti, C.; Kummer, H.; Helling, T.; Baumgartner, M.; Henninger, S.; et al. Synthesis of M-UiO-66 (M = Zr, Ce or Hf) Employing 2,5-Pyridinedicarboxylic Acid as a Linker: Defect Chemistry, Framework Hydrophilisation and Sorption Properties. *Dalton Trans.* **2018**, *47*, 1062–1070.
- (59) SK, M.; Grzywa, M.; Volkmer, D.; Biswas, S. Zr(IV) and Ce(IV)-Based Metal-Organic Frameworks Incorporating 4-Carboxycinnamic Acid as Ligand: Synthesis and Properties. *Microporous Mesoporous Mater.* **2017**, *237*, 275–281.
- (60) Jacobsen, J.; Reinsch, H.; Stock, N. Systematic Investigations of the Transition between Framework Topologies in Ce/Zr-MOFs. *Inorg. Chem.* **2018**, *57*, acs.inorgchem.8b02019.
- (61) Smolders, S.; Struyf, A.; Reinsch, H.; Bueken, B.; Rhauderwiek, T.; Mintrop, L.; Kurz, P.; Stock, N.; De Vos, D. E. A Precursor Method for the Synthesis of New Ce(IV) MOFs with ReactiVe Tetracarboxylate Linkers. *Chem. Commun.* **2018**, *54*, 876–879.
- (62) Smolders, S.; Lomachenko, K. A.; Bueken, B.; Struyf, A.; Bugaev, A. L.; Atzori, C.; Stock, N.; Lamberti, C.; Roeffaers, M. B. J.; De Vos, D. E. Unravelling the Redox-Catalytic Behavior of Ce⁴⁺ Metal–Organic Frameworks by X-Ray Absorption Spectroscopy. *ChemPhysChem* **2018**, *19*.
- (63) Yang, X.; Xu, Q. Bimetallic Metal-Organic Frameworks for Gas Storage and Separation. *Cryst. Growth Des.* **2017**, *17*, 1450–1455.
- (64) Lammert, M.; Glißmann, C.; Stock, N. Tuning the Stability of Bimetallic Ce(IV)/Zr(IV)-Based MOFs with UiO-66 and MOF-808 Structures. *Dalton Trans.* **2017**, *46*, 2425–2429.
- (65) Brozek, C. K.; Dincă, M. Ti³⁺-, V^{2+/3+}-, Cr^{2+/3+}-, Mn²⁺-, and Fe²⁺-Substituted

- MOF-5 and Redox Reactivity in Cr- and Fe-MOF-5. *J. Am. Chem. Soc.* **2013**, *135*, 12886–12891.
- (66) Stubbs, A. W.; Braglia, L.; Borfecchia, E.; Meyer, R. J.; Román-Leshkov, Y.; Lamberti, C.; Dincă, M. Selective Catalytic Olefin Epoxidation with Mn(II)-Exchanged MOF-5. *ACS Catal.* **2018**, *8*, 596–601.
- (67) Marshall, R. J.; Forgan, R. S. Postsynthetic Modification of Zirconium Metal-Organic Frameworks. *Eur. J. Inorg. Chem.* **2016**, *2016*, 4310–4331.
- (68) Kim, M.; Cahill, J. F.; Fei, H.; Prather, K. A.; Cohen, S. M. Postsynthetic Ligand and Cation Exchange in Robust Metal–Organic Frameworks. *J. Am. Chem. Soc.* **2012**, *134*, 18082–18088.
- (69) Gul-E-Noor, F.; Jee, B.; Mendt, M.; Himsl, D.; Pöpll, A.; Hartmann, M.; Haase, J.; Krautscheid, H.; Bertmer, M. Formation of Mixed Metal Cu₃-_xZn_x(Btc)₂ frameworks with Different Zinc Contents: Incorporation of Zn²⁺ into the Metal-Organic Framework Structure as Studied by Solid-State NMR. *J. Phys. Chem. C* **2012**, *116*, 20866–20873.
- (70) Gotthardt, M. A.; Schoch, R.; Wolf, S.; Bauer, M.; Kleist, W. Synthesis and Characterization of Bimetallic Metal-Organic Framework Cu-Ru-BTC with HKUST-1 Structure. *Dalton Trans.* **2015**, *44*, 2052–2056.
- (71) Sun, D.; Sun, F.; Deng, X.; Li, Z. Mixed-Metal Strategy on Metal-Organic Frameworks (MOFs) for Functionalities Expansion: Co Substitution Induces Aerobic Oxidation of Cyclohexene over Inactive Ni-MOF-74. *Inorg. Chem.* **2015**, *54*, 8639–8643.
- (72) Liu, Q.; Cong, H.; Deng, H. Deciphering the Spatial Arrangement of Metals and Correlation to Reactivity in Multivariate Metal-Organic Frameworks. *J. Am. Chem. Soc.* **2016**, *138*, 13822–13825.
- (73) Zhai, Q. G.; Bu, X.; Mao, C.; Zhao, X.; Feng, P. Systematic and Dramatic Tuning on Gas Sorption Performance in Heterometallic Metal-Organic Frameworks. *J. Am. Chem. Soc.* **2016**, *138*, 2524–2527.
- (74) He, J.; Zhang, Y.; He, J.; Zeng, X.; Hou, X.; Long, Z. Enhancement of Photoredox Catalytic Properties of Porphyrinic Metal-Organic Frameworks Based on Titanium Incorporation via Post-Synthetic Modification. *Chem. Commun.* **2018**, *54*, 8610–8613.
- (75) Vuong, G. T.; Pham, M. H.; Do, T. O. Synthesis and Engineering Porosity of a Mixed Metal Fe₂Ni MIL-88B Metal-Organic Framework. *Dalton Trans.* **2013**, *42*, 550–557.
- (76) Stock, N.; Biswas, S. Synthesis of Metal-Organic Frameworks (MOFs):

- Routes to Various MOF Topologies, Morphologies, and Composites. *Chem. Rev.* **2012**, *112*, 933–969.
- (77) Allendorf, M. D.; Stavila, V. Crystal Engineering, Structure–function Relationships, and the Future of Metal–organic Frameworks. *CrystEngComm* **2015**, *17*, 229–246.
- (78) Øien-Ødegaard, S.; Shearer, G. C.; Lillerud, K. P.; Bordiga, S. Metal–Organic Framework Sponges; In press, 2018.
- (79) Hermes, S.; Witte, T.; Hikov, T.; Zacher, D.; Bahnmeier, S.; Langstein, G.; Huber, K.; Fischer, R. A. Trapping Metal–Organic Framework Nanocrystals: An in-Situ Time-Resolved Light Scattering Study on the Crystal Growth of MOF-5 in Solution. *J. Am. Chem. Soc.* **2007**, *129*, 5324–5325.
- (80) Schaate, A.; Roy, P.; Godt, A.; Lippke, J.; Waltz, F.; Wiebcke, M.; Behrens, P. Modulated Synthesis of Zr-Based Metal–Organic Frameworks: From Nano to Single Crystals. *Chem. Eur. J.* **2011**, *17*, 6643–6651.
- (81) Shearer, G. C.; Chavan, S.; Bordiga, S.; Svelle, S.; Olsbye, U.; Lillerud, K. P. Defect Engineering: Tuning the Porosity and Composition of the Metal–Organic Framework UiO-66 via Modulated Synthesis. *Chem. Mater.* **2016**, *28*, 3749–3761.
- (82) Shearer, G. C. On the Defect Chemistry of the Metal–Organic Framework UiO-66, University of Oslo, 2015.
- (83) Atzori, C.; Shearer, G. C.; Maschio, L.; Civalleri, B.; Bonino, F.; Lamberti, C.; Svelle, S.; Lillerud, K. P.; Bordiga, S. Effect of Benzoic Acid as a Modulator in the Structure of UiO-66: An Experimental and Computational Study. *J. Phys. Chem. C* **2017**, *121*.
- (84) Butova, V. V.; Budnyk, A. P.; Guda, A. A.; Lomachenko, K. A.; Bugaev, A. L.; Soldatov, A. V.; Chavan, S. M.; Øien-Ødegaard, S.; Olsbye, U.; Lillerud, K. P.; et al. Modulator Effect in UiO-66-NDC (1,4-Naphthalenedicarboxylic Acid) Synthesis and Comparison with UiO-67-NDC Isorecticular Metal–Organic Frameworks. *Cryst. Growth Des.* **2017**, *acs.cgd.7b00892*.
- (85) Klein, N.; Herzog, C.; Sabo, M.; Senkovska, I.; Getzschmann, J.; Paasch, S.; Lohe, M. R.; Brunner, E.; Kaskel, S. Monitoring Adsorption-Induced Switching by ^{129}Xe NMR Spectroscopy in a New Metal–Organic Framework $\text{Ni}_2(2,6\text{-Ndc})_2(\text{Dabco})$. *Phys. Chem. Chem. Phys.* **2010**, *12*, 11778–11784.
- (86) Bon, V.; Kavooosi, N.; Senkovska, I.; Kaskel, S. Tolerance of Flexible MOFs toward Repeated Adsorption Stress. *ACS Appl. Mater. Interfaces* **2015**, *7*, 22292–22300.

- (87) Stock, N. High-Throughput Investigations Employing Solvothermal Syntheses. *Microporous Mesoporous Mater.* **2010**, *129*, 287–295.
- (88) Albat, M.; Stock, N. Multiparameter High-Throughput and in Situ X-Ray Diffraction Study of Six New Bismuth Sulfonatocarboxylates: Discovery, Phase Transformation, and Reaction Trends. *Inorg. Chem.* **2018**, *57*, 10352–10363.
- (89) Horcajada, P.; Chalati, T.; Serre, C.; Gillet, B.; Sebrie, C.; Baati, T.; Eubank, J. F.; Heurtaux, D.; Clayette, P.; Kreuz, C.; et al. Porous Metal–organic-Framework Nanoscale Carriers as a Potential Platform for Drug Delivery and Imaging. *Nat. Mater.* **2010**, *9*, 172–178.
- (90) Kandiah, M.; Nilsen, M. H.; Usseglio, S.; Jakobsen, S.; Olsbye, U.; Tilset, M.; Larabi, C.; Quadrelli, E. A.; Bonino, F.; Lillerud, K. P. Synthesis and Stability of Tagged UiO-66 Zr-MOFs. *Chem. Mater.* **2010**, *22*, 6632–6640.
- (91) Chavan, S. M.; Shearer, G. C.; Svelle, S.; Olsbye, U.; Bonino, F.; Ethiraj, J.; Lillerud, K. P.; Bordiga, S. Synthesis and Characterization of Amine-Functionalized Mixed-Ligand Metal – Organic Frameworks of UiO-66 Topology. *Inorg. Chem.* **2014**, *53*, 9509–9515.
- (92) Tanabe, K. K.; Cohen, S. M. Postsynthetic Modification of Metal-Organic Frameworks - A Progress Report. *Chem. Soc. Rev.* **2011**, *40*, 498–519.
- (93) Deria, P.; Mondloch, J. E.; Karagiari, O.; Bury, W.; Hupp, J. T.; Farha, O. K. Beyond Post-Synthesis Modification: Evolution of Metal-Organic Frameworks via Building Block Replacement. Royal Society of Chemistry 2014, pp 5896–5912.
- (94) Shearer, G. C.; Vitillo, J. G.; Bordiga, S.; Svelle, S.; Olsbye, U.; Lillerud, K. P. Functionalizing the Defects: Postsynthetic Ligand Exchange in the Metal Organic Framework UiO-66. *Chem. Mater.* **2016**, *28*, 7190–7193.
- (95) Øien, S.; Agostini, G.; Svelle, S.; Borfecchia, E.; Lomachenko, K. A.; Mino, L.; Gallo, E.; Bordiga, S.; Olsbye, U.; Lillerud, K. P.; et al. Probing Reactive Platinum Sites in UiO-67 Zirconium Metal-Organic Frameworks. *Chem. Mater.* **2015**, *27*, 1042–1056.
- (96) Braglia, L.; Borfecchia, E.; Maddalena, L.; Øien, S.; Lomachenko, K. A.; Bugaev, A. L.; Bordiga, S.; Soldatov, A. V.; Lillerud, K. P.; Lamberti, C. Exploring Structure and Reactivity of Cu Sites in Functionalized UiO-67 MOFs. Elsevier 2015.
- (97) Howarth, A. J.; Peters, A. W.; Vermeulen, N. A.; Wang, T. C.; Hupp, J. T.; Farha, O. K. Best Practices for the Synthesis, Activation, and Characterization of Metal–organic Frameworks. *Chem. Mater.* **2017**, *29*,

26–39.

- (98) Giacobozzo, C.; Monaco, H. L.; Artioli, G.; Viterbo, D.; Milanesio, M.; Gilli, G.; Gilli, P.; Zanotti, G.; Ferraris, G.; Catti, M. *Fundamentals of Crystallography*; International Union of Crystallography Texts on Crystallography; OUP Oxford, 2011.
- (99) Dyadkin, V.; Pattison, P.; Dmitriev, V.; Chernyshov, D. A New Multipurpose Diffractometer PILATUS@SNBL. *J. Synchrotron Radiat.* **2016**, *23*, 825–829.
- (100) Thommes, M.; Kaneko, K.; Neimark, A. V.; Olivier, J. P.; Rodriguez-Reinoso, F.; Rouquerol, J.; Sing, K. S. W. Physisorption of Gases, with Special Reference to the Evaluation of Surface Area and Pore Size Distribution (IUPAC Technical Report). **2015**, *87*, 1051–1069.
- (101) Bokhoven, J. A. van; Lamberti, C. *X-Ray Absorption and X-Ray Emission Spectroscopy: Theory and Applications*; Wiley, 2016.
- (102) Soldatov, M. A.; Martini, A.; Bugaev, A. L.; Pankin, I.; Medvedev, P. V.; Guda, A. A.; Aboraia, A. M.; Podkovyrina, Y. S.; Budnyk, A. P.; Soldatov, A. A.; et al. The Insights from X-Ray Absorption Spectroscopy into the Local Atomic Structure and Chemical Bonding of Metal–organic Frameworks. *Polyhedron* **2018**, *155*, 232–253.
- (103) Valenzano, L.; Civalieri, B.; Chavan, S.; Bordiga, S.; Nilsen, M. H.; Jakobsen, S.; Lillerud, K. P.; Lamberti, C. Disclosing the Complex Structure of UiO-66 Metal Organic Framework: A Synergic Combination of Experiment and Theory. *Chem. Mater.* **2011**, *23*, 1700–1718.
- (104) Chavan, S.; Vitillo, J. G.; Gianolio, D.; Zavorotynska, O.; Civalieri, B.; Jakobsen, S.; Nilsen, M. H.; Valenzano, L.; Lamberti, C.; Lillerud, K. P.; et al. H₂ Storage in Isostructural UiO-67 and UiO-66 MOFs. *Phys. Chem. Chem. Phys.* **2012**, *14*, 1614–1626.
- (105) Jakobsen, S.; Gianolio, D.; Wragg, D. S.; Nilsen, M. H.; Emerich, H.; Bordiga, S.; Lamberti, C.; Olsbye, U.; Tilset, M.; Lillerud, K. P. Structural Determination of a Highly Stable Metal–Organic Framework with Possible Application to Interim Radioactive Waste Scavenging: Hf–UiO-66. *Phys. Rev. B - Condens. Matter Mater. Phys.* **2012**, *86*, 125429.
- (106) Prestipino, C.; Regli, L.; Vitillo, J. G.; Bonino, F.; Damin, A.; Lamberti, C.; Zecchina, A.; Solari, P. L.; Kongshaug, K. O.; Bordiga, S. Local Structure of Framework Cu(II) in HKUST-1 Metallorganic Framework: Spectroscopic Characterization upon Activation and Interaction with Adsorbates. *Chem. Mater.* **2006**, *18*, 1337–1346.

- (107) Masciocchi, N.; Galli, S.; Colombo, V.; Maspero, A.; Palmisano, G.; Seyyedi, B.; Lamberti, C.; Bordiga, S. Cubic Octanuclear Ni(II) Clusters in Highly Porous Polypyrazolyl-Based Materials. *J. Am. Chem. Soc.* **2010**, *132*, 7902–7904.
- (108) Millward, A. R.; Yaghi, O. M. Metal-Organic Frameworks with Exceptionally High Capacity for Storage of Carbon Dioxide at Room Temperature. *J. Am. Chem. Soc.* **2005**, *127*, 17998–17999.
- (109) Sumida, K.; Rogow, D. L.; Mason, J. A.; McDonald, T. M.; Bloch, E. D.; Herm, Z. R.; Bae, T.-H.; Long, J. R. Carbon Dioxide Capture in Metal–Organic Frameworks. *Chem. Rev.* **2012**, *112*, 724–781.
- (110) Peng, Y.; Krungleviciute, V.; Eryazici, I.; Hupp, J. T.; Farha, O. K.; Yildirim, T. Methane Storage in Metal-Organic Frameworks: Current Records, Surprise Findings, and Challenges. *J. Am. Chem. Soc.* **2013**, *135*, 11887–11894.
- (111) Bae, Y. S.; Snurr, R. Q. Development and Evaluation of Porous Materials for Carbon Dioxide Separation and Capture. *Angew. Chemie - Int. Ed.* **2011**, *50*, 11586–11596.
- (112) Patel, H. A.; Byun, J.; Yavuz, C. T. Carbon Dioxide Capture Adsorbents: Chemistry and Methods. *ChemSusChem* **2017**, *10*, 1303–1317.
- (113) Llabres i Xamena, F.; Gascon, J. *Metal Organic Frameworks as Heterogeneous Catalysts*; Llabres i Xamena, F., Gascon, J., Eds.; Catalysis Series; Royal Society of Chemistry: Cambridge, 2013.
- (114) Gascon, J.; Corma, A.; Kapteijn, F.; Llabrés I Xamena, F. X. Metal Organic Framework Catalysis: Quo Vadis? *ACS Catal.* **2014**, *4*, 361–378.
- (115) Rogge, S. M. J.; Bavykina, A.; Hajek, J.; Garcia, H.; Olivos-Suarez, A. I.; Sepúlveda-Escribano, A.; Vimont, A.; Clet, G.; Bazin, P.; Kapteijn, F.; et al. Metal–organic and Covalent Organic Frameworks as Single-Site Catalysts. *Chem. Soc. Rev.* **2017**, *46*, 3134–3184.
- (116) Farrusseng, D.; Aguado, S.; Pinel, C. Metal-Organic Frameworks: Opportunities for Catalysis. *Angew. Chemie - Int. Ed.* **2009**, *48*, 7502–7513.
- (117) Ullman, A. M.; Brown, J. W.; Foster, M. E.; Léonard, F.; Leong, K.; Stavila, V.; Allendorf, M. D. Transforming MOFs for Energy Applications Using the Guest@MOF Concept. *Inorg. Chem.* **2016**, *55*, 7233–7249.
- (118) Han, Y.; Liu, M.; Li, K.; Zuo, Y.; Wei, Y.; Xu, S.; Zhang, G.; Song, C.; Zhang, Z. C.; Guo, X. Facile Synthesis of Morphology- and Size-Controlled Zirconium Metal-Organic Framework UiO-66: The Role of Hydrofluoric

- Acid in Crystallization. *CrystEngComm* **2015**, *17*, 1–9.
- (119) So, M. C.; Wiederrecht, G. P.; Mondloch, J. E.; Hupp, J. T.; Farha, O. K. Metal-Organic Framework Materials for Light-Harvesting and Energy Transfer. *Chem. Commun.* **2015**, *51*, 3501–3510.
- (120) Zhang, T.; Lin, W. Metal-Organic Frameworks for Artificial Photosynthesis and Photocatalysis. *Chem. Soc. Rev.* **2014**, *43*, 5982–5993.
- (121) Lee, C. Y.; Farha, O. K.; Hong, B. J.; Sarjeant, A. A.; Nguyen, S. T.; Hupp, J. T. Light-Harvesting Metal-Organic Frameworks (MOFs): Efficient Struto-Strut Energy Transfer in Bodipy and Porphyrin-Based MOFs. *J. Am. Chem. Soc.* **2011**, *133*, 15858–15861.
- (122) Wang, L.; Han, Y.; Feng, X.; Zhou, J.; Qi, P.; Wang, B. Metal-Organic Frameworks for Energy Storage: Batteries and Supercapacitors. *Coord. Chem. Rev.* **2016**, *307*, 361–381.
- (123) Sun, L.; Campbell, M. G.; Dinca, M. Electrically Conductive Porous Metal-Organic Frameworks. *Angew. Chemie - Int. Ed.* **2016**, *55*, 3566–3579.
- (124) Son, H.-J.; Jin, S.; Patwardhan, S.; Wezenberg, S. J.; Jeong, N. C.; So, M.; Wilmer, C. E.; Sarjeant, A. A.; Schatz, G. C.; Snurr, R. Q.; et al. Light-Harvesting and Ultrafast Energy Migration in Porphyrin-Based Metal-Organic Frameworks. *J. Am. Chem. Soc.* **2013**, *135*, 862–869.
- (125) Lee, D. Y.; Kim, E. K.; Shin, C. Y.; Shinde, D. V.; Lee, W.; Shrestha, N. K.; Lee, J. K.; Han, S. H. Layer-by-Layer Deposition and Photovoltaic Property of Ru-Based Metal-Organic Frameworks. *RSC Adv.* **2014**, *4*, 12037–12042.
- (126) Leong, K.; Foster, M.; Wong, B.; Spoerker, E.; Van Gough, D.; Deaton, J.; Allendorf, M. Energy and Charge Transfer by Donor–acceptor Pairs Confined in a Metal–organic Framework: A Spectroscopic and Computational Investigation. *J. Mater. Chem. A* **2014**, *2*, 3389–3398.
- (127) Li, Y.; Chen, C.; Sun, X.; Dou, J.; Wei, M. Metal–Organic Frameworks at Interfaces in Dye-Sensitized Solar Cells. *ChemSusChem* **2014**, *7*, 2469–2472.
- (128) Lee, D. Y.; Lim, I.; Shin, C. Y.; Patil, S. A.; Lee, W.; Shrestha, N. K.; Lee, J. K.; Han, S. H. Facile Interfacial Charge Transfer across Hole Doped Cobalt-Based MOFs/TiO₂ Nano-Hybrids Making MOFs Light Harvesting Active Layers in Solar Cells. *J. Mater. Chem. A* **2015**, *3*, 22669–22676.
- (129) Bella, F.; Bongiovanni, R.; Kumar, R. S.; Kulandainathan, M. A.; Stephan, A. M. Light Cured Networks Containing Metal Organic Frameworks as Efficient and Durable Polymer Electrolytes for Dye-Sensitized Solar Cells.

- J. Mater. Chem. A* **2013**, *1*, 9033–9036.
- (130) Giordanengo, G. Sintesi e Caratterizzazione Di Un Nuovo Polimero Di Coordinazione Metallo-Organico a Base Di Cerio Con Legante Azoico, Università di Torino, 2017.
- (131) Boghici, A. R. Sintesi Del MOF Ce-UiO-66-ADC, Università di Torino, 2017.
- (132) Airi, A. A Tough MOF with a Fragile Linker: Ce-UiO-66-ADC, Università di Torino, 2018.
- (133) Sheldrick, G. M. Crystal Structure Refinement with SHELXL. *Acta Crystallogr. Sect. C Struct. Chem.* **2015**, *71*, 3–8.
- (134) Stoe & Cie. X-Shape, X-Area and X-Red. Stoe & Cie: Darmstadt, Germany 2002.
- (135) Burla, M. C.; Caliandro, R.; Carrozzini, B.; Cascarano, G. L.; Cuocci, C.; Giacovazzo, C.; Mallamo, M.; Mazzone, A.; Polidori, G. Crystal Structure Determination and Refinement via SIR2014. *J. Appl. Crystallogr.* **2015**, *48*, 306–309.
- (136) Macrae, C. F.; Bruno, I. J.; Chisholm, J. A.; Edgington, P. R.; McCabe, P.; Pidcock, E.; Rodriguez-Monge, L.; Taylor, R.; Van De Streek, J.; Wood, P. A. Mercury CSD 2.0 - New Features for the Visualization and Investigation of Crystal Structures. *Journal of Applied Crystallography*. International Union of Crystallography April 1, 2008, pp 466–470.
- (137) Coelho, A. A. TOPAS and TOPAS-Academic: An Optimization Program Integrating Computer Algebra and Crystallographic Objects Written in C++: *An. J. Appl. Crystallogr.* **2018**, *51*, 210–218.
- (138) Abdala, P. M.; Safonova, O. V.; Wiker, G.; van Beek, W.; Emerich, H.; van Bokhoven, J. A.; Sá, J.; Szlachetko, J.; Nachttegaal, M. Scientific Opportunities for Heterogeneous Catalysis Research at the SuperXAS and SNBL Beam Lines. *Chim. Int. J. Chem.* **2012**, *66*, 699–705.
- (139) Klementiev, K.; Chernikov, R. XAFSmass: A Program for Calculating the Optimal Mass of XAFS Samples. *J. Phys. Conf. Ser.* **2016**, *712*, 012008.
- (140) Ravel, B.; Newville, M. ATHENA, ARTEMIS, HEPHAESTUS: Data Analysis for X-Ray Absorption Spectroscopy Using IFEFFIT. *J. Synchrotron Radiat.* **2005**, *12*, 537–541.
- (141) Rehr, J. J.; Albers, R. C. Theoretical Approaches to X-Ray Absorption Fine Structure. *Rev. Mod. Phys.* **2000**, *72*, 621–654.

- (142) Signorile, M.; Bonino, F.; Damin, A.; Bordiga, S. A Novel Raman Setup Based on Magnetic-Driven Rotation of Sample. *Top. Catal.* **2018**, *61*, 1491–1498.
- (143) Colthup, N. B.; Daly, L. H.; Wiberley, S. E. *Introduction to Infrared and Raman Spectroscopy*; Academic Press, 1990.
- (144) Schneemann, A.; Bon, V.; Schwedler, I.; Senkovska, I.; Kaskel, S.; Fischer, R. A. Flexible Metal-Organic Frameworks. *Chem. Soc. Rev.* **2014**, *43*, 6062–6096.
- (145) Serre, C.; Bourrelly, S.; Vimont, A.; Ramsahye, N. A.; Maurin, G.; Llewellyn, P. L.; Daturi, M.; Filinchuk, Y.; Leynaud, O.; Barnes, P.; et al. An Explanation for the Very Large Breathing Effect of a Metal–Organic Framework during CO₂ Adsorption. *Adv. Mater.* **2007**, *19*, 2246–2251.
- (146) Gregg, S. J.; Sing, K. S. W. *Adsorption, Surface Area and Porosity*; Academic Press, 1982.
- (147) Rouquerol, J. *Adsorption by Powders and Porous Solids : Principles, Methodology and Applications*.
- (148) Masala, A.; Vitillo, J. G.; Mondino, G.; Grande, C. A.; Blom, R.; Manzoli, M.; Marshall, M.; Bordiga, S. CO₂ Capture in Dry and Wet Conditions in UTSA-16 Metal–Organic Framework. *ACS Appl. Mater. Interfaces* **2017**, *9*, 455–463.
- (149) Øien, S.; Wragg, D.; Reinsch, H.; Svelle, S.; Bordiga, S.; Lamberti, C.; Lillerud, K. P. Detailed Structure Analysis of Atomic Positions and Defects in Zirconium Metal-Organic Frameworks. *Cryst. Growth Des.* **2014**, *14*, 5370–5372.
- (150) Pecharsky Vitalij, Z. P. *Fundamentals of Powder Diffraction and Structural Characterization of Materials*, second.; Springer US, 2009.
- (151) Bonino, F.; Damin, A.; Bordiga, S.; Lamberti, C.; Zecchina, A. Interaction of CD₃CN and Pyridine with the Ti(IV) Centers of TS-1 Catalysts: A Spectroscopic and Computational Study. *Langmuir* **2003**, *19*, 2155–2161.
- (152) Proust, B. *Synthesis and Characterization of Cerium(IV)-Based MOF*, ENSICAEN, Università di Torino, 2015.
- (153) Nouar, F.; Breeze, M. I.; Campo, B. C.; Vimont, A.; Clet, G.; Daturi, M.; Devic, T.; Walton, R. I.; Serre, C. Tuning the Properties of the UiO-66 Metal Organic Framework by Ce Substitution. *Chem. Commun.* **2015**, *51*, 14458–14461.
- (154) Shearer, G. C.; Forselv, S.; Chavan, S.; Bordiga, S.; Mathisen, K.; Bjorgen,

- M.; Svelle, S.; Lillerud, K. P. In Situ Infrared Spectroscopic and Gravimetric Characterisation of the Solvent Removal and Dehydroxylation of the Metal Organic Frameworks UiO-66 and UiO-67. *Top. Catal.* **2013**, *56*, 770–782.
- (155) Tranchemontagne, D. J.; Hunt, J. R.; Yaghi, O. M. Room Temperature Synthesis of Metal-Organic Frameworks: MOF-5, MOF-74, MOF-177, MOF-199, and IRMOF-0. *Tetrahedron* **2008**, *64*, 8553–8557.
- (156) Li, J.; Brill, T. B. Spectroscopy of Hydrothermal Reactions 20: Experimental and DFT Computational Comparison of Decarboxylation of Dicarboxylic Acids Connected by Single, Double, and Triple Bonds. *J. Phys. Chem. A* **2002**, *106*, 9491–9498.
- (157) Shearer, G. C.; Chavan, S.; Ethiraj, J.; Vitillo, J. G.; Svelle, S.; Olsbye, U.; Lamberti, C.; Bordiga, S.; Lillerud, K. P. Tuned to Perfection: Ironing Out the Defects in Metal–Organic Framework UiO-66. *Chem. Mater.* **2014**, *26*, 4068–4071.
- (158) Taddei, M. When Defects Turn into Virtues: The Curious Case of Zirconium-Based Metal-Organic Frameworks. *Coord. Chem. Rev.* **2017**, *343*, 1–24.
- (159) Dissegna, S.; Epp, K.; Heinz, W. R.; Kieslich, G.; Fischer, R. A. Defective Metal-Organic Frameworks. *Adv. Mater.* **2018**, *30*, 1704501.
- (160) Fang, Z.; Bueken, B.; De Vos, D. E.; Fischer, R. A. Defect-Engineered Metal-Organic Frameworks. *Angew. Chemie Int. Ed.* **2015**, *54*, 7234–7254.

Appendix I

This appendix containing two papers:

Atzori C., Lomachenko K.A., Øien-Ødegaard S., Stock N., Lamberti C., Barolo C., Bonino F. “Disclosing the properties of a new Ce(III)-based MOF: $\text{Ce}_2(\text{NDC})_3(\text{DMF})_2$ ”, *Submitted to Crystal Growth & Design in September 2018*.

Lomachenko K.A., Jacobsen J., Bugaev A.L., **Atzori C.**, Bonino F., Bordiga S., Stock N., Lamberti C. “Exact stoichiometry of $\text{Ce}_x\text{Zr}_{6-x}$ cornerstones in mixed-metal UiO-66 MOFs revealed by EXAFS spectroscopy”, *Accepted for publishing in JACS in November 2018*.

These papers concern activities discussed in the present thesis.

Disclosing the properties of a new Ce(III)-based MOF: $\text{Ce}_2(\text{NDC})_3(\text{DMF})_2$

Cesare Atzori^a, Kirill A. Lomachenko^b, Sigurd Øien-Ødegaard^c, Carlo Lamberti^{d,e}, Norbert Stock^f, Claudia Barolo^a,

Francesca Bonino^{a*}

^a Department of Chemistry, NIS and INSTM Reference Centre, Università di Torino, Via G. Quarello 15, I-10135 and Via P. Giuria 7, I-10125 Torino, Italy

^b European Synchrotron Radiation Facility, 71 Avenue des Martyrs, CS 40220, 38043 Grenoble Cedex 9, France

^c Department of Chemistry, University of Oslo, P.O. Box 1033, N-0315 Oslo, Norway

^d Department of Physics, INSTM Reference Center and CrisDi Interdepartmental Centre for Crystallography, Università di Torino, Via P. Giuria 1, I-10125 Torino, Italy

^e The Smart Materials Research Institute, Southern Federal University, A. Sladkova str. 178/24, 344090 Rostov-on-Don, Russia

^f Institut für Anorganische Chemie, Christian-Albrechts-Universität zu Kiel, Max-Eyth-Straße 2, 24118 Kiel, Germany

*Corresponding author e-mail: francesca.bonino@unito.it

Abstract

The new Ce(III) based metal-organic framework $\text{Ce}_2(\text{NDC})_3(\text{DMF})_2$, containing the simple ditopic linker naphthalenedicarboxylate (NDC^{2-}), has been synthesized under solvothermal reaction conditions with high purity and yield. Its crystal structure was determined with SC-XRD techniques and further confirmed by Ce K-edge XAS. Upon thermal activation the compound revealed a phase transformation at about 300°C involving the removal of the solvent molecules which has been investigated in detail by TGA, VT-PXRD and FTIR spectroscopy techniques. The crystal structure of the compound after desolvation ($\text{Ce}_2(\text{NDC})_3$) becomes severely disordered, but a synergic use of both SC-XRD and Ce K-edge EXAFS allowed us to reveal its crystal structure. Porosity and adsorption properties were studied by the means of volumetric adsorption measurements. $\text{Ce}_2(\text{NDC})_3$ is non-porous towards nitrogen at 77K but exhibits an uptake of CO_2 at 1 bar and 25°C of about 4% by weight.

Keywords

Metal-organic frameworks, cerium, lanthanides, XAS, XRD, FTIR

1. Introduction

Among porous materials, metal-organic frameworks (MOFs) have been extensively studied during the last two decades by a constantly increasing number of scientists.¹⁻⁴ These modular materials are built from organic linkers and inorganic metal-containing units whose careful choice allows to tune their chemical and physical properties. Nowadays, their use in applications like capture, storage, separation and conversion of gases,¹ (photo-) catalysis,⁵ drug delivery,⁶ optoelectronic (e.g. low-k dielectric materials),⁷ sensors,⁸ magnetism and ferroelectricity⁹ and light harvesting and energy transfer¹⁰ are actively researched.

Cerium is the most abundant in the earth crust among rare-earth metals and inherently cheap for this reason.¹¹ CeO₂ is known for its redox chemistry involving cycling between Ce(III) and Ce(IV) oxidation states which is exploited in a wide range of catalytic applications.¹²⁻¹⁴ Ce based MOFs have been more recently studied by the MOF community and a list of reported cerium carboxylate MOFs is given in the SI in Table S1. Thus, Lammert et al.¹⁵ published in 2015 the successful synthesis of four Ce(IV) based UiO-66 type materials, having formula [Ce₆O₄(OH)₄(L)₆], using the four ditopic linkers “L”: fumaric acid (H₂Fum), 1,4-benzenedicarboxylic acid (H₂BDC), 2,6-naphthalenedicarboxylic acid (H₂NDC) and 4,4'-diphenyldicarboxylic acid (H₂BPDC). The same group synthesized also other Ce based MOFs with various multi-topic linkers and topologies, all based on Ce(IV) cations.¹⁶⁻²² All these Ce(IV)-based materials are characterized by the same reticular chemistry and a general lower thermal and chemical stability in respect to their Zr(IV) counterparts. Using X-ray absorption spectroscopy, Smolders et al.²³ recently demonstrated the use of a MOF as a redox catalyst using Ce(IV) analogues of UiO-66 and UiO-67 to catalyze the aerobic oxidation of benzylic alcohol to benzaldehyde using these materials and TEMPO (2,2,6,6-tetramethyl-1-piperidinyloxy) as redox shuttle confirming the switch between Ce(III) and Ce(IV) during the catalytic cycle.

MOFs containing Ce(III) have been also reported.²⁴⁻²⁷ Thus a synthesis giving a Ce(III) MOF with the linker 4-tetracarboxyphenylporphyrin (H₆TCPP) was reported, although a Ce(IV) precursor was used during the synthesis.²⁴ Some of us also explored the possibility to adopt trimesic acid (1,3,5-benzenetricarboxylic acid) as a linker and a compound isorecticular to MOF-76 was obtained, which showed high performances in the capture of carbon dioxide.²⁵ Other authors obtained a material of composition Ce₅(BDC)_{7.5}(DMF)₄ characterized by a

complex triclinic crystal structure and Ce-O chains using the ditopic linker H₂BDC.²⁶ The linker 1,4-H₂NDC has been more recently used to synthesize the new Ce(III) MOF Ce₂(1,4-NDC)₃(DMF)₄·xH₂O whose synthesis was carried out in the presence of azoles acting as modulators.²⁷

In the present work, with the aim to study Ce(III) and ditopic carboxylic linkers, a new MOF, made from Ce(NO₃)₃·6H₂O and 2,6-naphthalenedicarboxylic acid (H₂NDC), was synthesized using DMF as the solvent. The synthesis was optimized by means of high-throughput methods and it resulted in a material with the composition Ce₂(NDC)₃(DMF)₂ whose crystal structure was determined from single-crystal X-ray diffraction (SC-XRD) data. The crystal structure of the activated MOF, with Ce₂(NDC)₃ composition, was determined by a synergic approach based on SC-XRD and synchrotron X-ray absorption spectroscopy (XAS), where the output structure of the XRD refinement was used as input for the EXAFS fit in order to validate or to discard the model; in the latter case a new XRD refinement was performed taking into consideration the first shell metal distances obtained from EXAFS. Such a synergic approach was already shown its potentialities in disclosing the structures of solvated and desolvated UiO-66,^{28,29} UiO-67,³⁰ Hf-UiO-66,³¹ desolvated HKUST-1,³² MOF-76-Ce,²⁵ and Ni-cubane MOFs.³³ The behavior of this material upon thermal activation was studied by means of VT-PXRD, TGA, in-situ FTIR and CO₂/N₂ adsorption measurements.

2. Experimental Section

2.1 Synthesis

Chemicals were obtained from Alfa Aesar ($\text{Ce}(\text{NO}_3)_3 \cdot 6\text{H}_2\text{O}$, 99,5% purity), TCI (H_2NDC , 98 % purity) and Grüssing (DMF, 99 % purity) and were used without further purification. Synthesis conditions were optimized by means of high-throughput methods³⁴ where a large number of different syntheses are carried out at small scale varying systematically reaction conditions like reaction temperature, reaction time, solvents and linker to metal ratio. To this end reactors containing 24 Teflon liners with a maximum volume of 2 mL were filled with the reaction mixtures and then heated at the set temperature for a fixed time. After recovery of the solid product by filtration automated PXRD measurements allowed us to identify the conditions where yield and crystallinity of the product were optimal.

Once these optimal conditions were established for the scaled-up synthesis $\text{Ce}_2(\text{NDC})_3(\text{DMF})_2$ 778.3 mg (3.6 mmol) of 2,6-naphthalenedicarboxylic acid (H_2NDC), 13.2 mL (170 mmol) of DMF and 6 mL of a 130 g/L $\text{Ce}(\text{NO}_3)_3 \cdot 6\text{H}_2\text{O}$ solution in DMF (0.3 M and thus 1.8 mmol of Ce) were combined in a 25 mL Teflon lined autoclave. This vessel was closed and heated to 160°C in 3 h, kept at this temperature for 72 h and cooled down to RT in 12 h. The product was filtered off, washed with fresh DMF in the funnel for three times and dried on the filter paper under air flow. The yield of the reaction using the formula $\text{Ce}_2(\text{NDC})_3(\text{DMF})_2$ is 89% (based on the metal source). The product appears in the form of pale yellow needle-like crystals in the half-millimeter range of dimensions along the “long” axis of the crystal (see optical image in Figure 1).



Figure 1 – Optical micrograph of Ce₂(NDC)₃(DMF)₂ crystals.

2.2 Experimental methods

Single-crystal XRD

Single-crystal X-ray diffraction (SC-XRD) data for the solvated MOF were measured on a Stoe IPDS diffractometer equipped with an image-plate detector using MoK α radiation; a crystal was glued to the tip of a glass capillary and cooled down to about 153 K with a cold nitrogen blower. Direct methods implemented in the SHELXS-2013 code were used in order to solve the structure, while crystal structure refinement, using full-matrix least-squares algorithms, was done using SHELXL-2013.³⁵ All non-hydrogen atoms were refined with anisotropic displacement parameters while C-H atoms were positioned via a riding model and refined isotropically. Numerical absorption correction was carried out by using X-Shape and X-Red from the X-Area package.³⁶ Structural illustrations have been drawn with CCDC Mercury, which was also used to calculate the powder diffractogram from single-crystal structural data (CCDC repository number 1847910).

Diffraction data of the activated MOF were acquired at 100 K using a Bruker D8 Venture diffractometer equipped with a Photon100 CMOS detector and using MoK α radiation. Several crystals were screened for diffraction due to poor diffraction. The crystals showed signs of degradation, with visible cracks and opacity. The diffraction

frames show very broad reflections and diffuse scattering (see figures S1 to S4). Still, satisfactory figures of merit were obtained in the structure refinement of the presented structure (CCDC repository number 1847909).

Powder XRD

Powder X-ray diffraction (PXRD) patterns were taken with a Panalytical X'Pert PRO MPD diffractometer equipped with a CuK α source operating in Debye-Scherrer geometry, scattered photons were collected by a X'Celerator detector equipped with a Ni filter in order to attenuate K β radiation. Pawley fits were carried out using TOPAS-Academic V5.³⁷

Variable temperature powder diffraction

Variable temperature PXRD (VT-PXRD) measurements were collected on a STOE Stadi P combi with CuK α radiation in transmission geometry and equipped with a furnace; open quartz capillaries were used as sample holders. The temperature program was set to measure a diffractogram every 25°C from RT to 600°C, waiting at each step 15 min at the setpoint before collecting data. The sample was heated at a rate of 3°C/min.

XAS spectroscopy

Ce K-edge XAS measurements were performed at BM31 beamline³⁸ of the European Synchrotron Radiation Facility (ESRF, Grenoble, France). The storage ring was operating in the multibunch regime, the electron current being between 160 and 200 mA. The measurements were conducted in transmission mode using a Si (111) double-crystal monochromator. Three ionization chambers (30 cm, 1 kV, 1 bar) were employed for photon detection, the third one being used for energy calibration with CeO₂ reference. The I₀ chamber was filled with a 15% Kr/Ar mixture, while pure Kr was used for I₁ and I₂, yielding the absorption of 15% and 57% at 41 keV for I₀ and I₁, I₂ respectively, this set-up allows a direct angle/energy calibration for each spectrum.^{39,40} Samples were measured at room temperature in the form of pellets. The mass of the pellets was calculated by XAFSmass code⁴¹ aiming to optimize the signal-to-noise ratio. EXAFS data analysis was carried out using the Demeter package,⁴² Athena for

normalization and averaging of the raw data and Artemis for fitting of the EXAFS spectra. Scattering amplitudes and phase shifts were calculated by FEFF6 code⁴³ bundled with Artemis.

Thermogravimetric measurements

Thermogravimetric analysis (TGA) data were recorded with a TA instruments Q600 thermobalance in dry N₂ flow (100 mL/min) with a ramp of 3°C/min from RT to 700°C working with about 10 mg of sample in an alumina crucible.

FTIR spectroscopy

Vibrational IR spectra were collected in transmission mode using a Thermo Scientific Nicolet 6700 spectrometer equipped with a liquid N₂ cooled MCT detector on thin self-supporting pellets. The MOF sample was activated in dynamic high vacuum ($5 \cdot 10^{-4}$ mbar) at 300°C for 2 h in a homemade jacketed quartz cell that allows also controlled dosages of gaseous probes (i.e. CO) and cooling of the pellet to about 100K using liquid nitrogen.

CO₂ and N₂ adsorption volumetry

A Micromeritics ASAP 2020 apparatus was used to measure both N₂ and CO₂ adsorption isotherms. For the CO₂ measurement the temperature was kept stable by means of an isothermal water bath (Julabo F25). A local construction setup was employed which permitted us to thermally activate Ce₂(NDC)₃(DMF)₂ (ramping at 5°C/min to 300°C and keeping this temperature for 2 h) in dynamic vacuum and then measure the isotherms without exposing the sample to air.

3. Results and Discussion

3.1 Crystal structures

The crystal structures of the as-synthesized and the fully desolvated compounds $\text{Ce}_2(\text{NDC})_3(\text{DMF})_2$ and $\text{Ce}_2(\text{NDC})_3$ were determined from SC-XRD data, taking into account the local structural motives suggested by EXAFS. Table 1 reports the main crystallographic data.

Table 1 – Crystal data for $\text{Ce}_2(\text{NDC})_3(\text{DMF})_2$ and $\text{Ce}_2(\text{NDC})_3$.

	$\text{Ce}_2(\text{NDC})_3(\text{DMF})_2$	$\text{Ce}_2(\text{NDC})_3$
Formula	$\text{C}_{84}\text{H}_{64}\text{Ce}_4\text{N}_4\text{O}_{28}$	$\text{C}_{36}\text{H}_{18}\text{Ce}_2\text{O}_{12}$
Formula weight ($\text{g}\cdot\text{mol}^{-1}$)	2137.88	922.76
Crystal system	<i>Orthorhombic</i>	<i>Trigonal</i>
Space group	<i>Pca2₁</i>	<i>P$\bar{3}$c1</i>
a (Å)	19.836(4)	11.845(5)
b (Å)	8.7339(17)	11.845(5)
c (Å)	45.451(9)	7.698(3)
$\alpha = \beta$ (°)	90	90
γ (°)	90	120
Cell volume (Å ³)	7874(3)	935.3(8)
Temperature (K)	153(2)	100(2)
Abs. coefficient (mm^{-1})	2.357	2.460
Calc. density ($\text{g}\cdot\text{cm}^{-3}$)	1.803	1.606
Z	4	2
Measured reflections	11957	108
R_{int}	0.0519	0.0727
No. of parameters	1082	29
R_1	0.0519	0.0729
wR (all data)	0.1317	0.1205
Largest. diff. peak ($\text{e}\cdot\text{Å}^{-3}$)	-1.920 / 2.677	-0.555 / 0.450

The as synthesized $\text{Ce}_2(\text{NDC})_3(\text{DMF})_2$ crystallizes in an orthorhombic space group, and the structure consists of slightly distorted pentagonal bipyramidal Ce(III) species coordinated by six carboxylate groups of different linkers and one DMF oxygen (Figure 2). Each Ce(III) shares three carboxylate ligands with each of its two neighboring Ce(III) species to form extended chains parallel to the *a* axis (Figure 2). The NDC^{2-} linker molecules form inter-chain bridges to give a network structure with diamond-shaped channels parallel to the Ce(III) chains (Figure 2a and 2b). The structural DMF molecules are aligned with neighboring naphthyl linkers with distances in the range of 3.7 – 4.0 Å, indicating π -stacking.

Upon desolvation at 300°C for 2 h in dynamic vacuum (see TGA data reported below), the crystal structure of $\text{Ce}_2(\text{NDC})_3(\text{DMF})_2$ undergoes a phase transition. The diffraction data from this activated sample consist of very diffuse diffraction peaks, and an apparent primitive hexagonal lattice was found when indexing. The reflections broaden as the scattering angle increases, giving readable diffraction only to 1.3 Å (see the SI, Section 2).

Data reduction using the hexagonal space group $P-3c1$ proceeded without issues. Structure solution with SHELXT and subsequent refinement with SHELXL produced a hexagonal crystal structure consisting of linear chains of Ce atoms along the c -axis at the cell vertices, and NDC^{2-} ligands form inter-chain bridges, where the O atoms of the carboxylate groups coordinate to Ce. The resulting pore structure is thus triangular channels running parallel to the c -axis. There is significant disorder in the ligand structure that could not be resolved. The occupancies of the light atoms have been determined by an iterative approach, and are in good agreement with the formula of the as-synthesized MOF and mass ratios obtained by TGA.

Concerning the local symmetry of the structure, the presence of triangular channels substantially shows structural changes from the diamond-shaped channels found in the as-synthesized structure. Other MOFs that exhibit a flexible structure, such as MIL-53, do not show such rearrangement of its constituents. Due to the partial occupancy of the light linker atoms, it is possible that the crystal after activation still contains diamond-shaped channels, but in high disorder (a detailed figure about these channels is reported in Figure S5).

An apparently primitive hexagonal lattice may in this case be a triply twinned C-centered orthorhombic lattice where the lattice parameters of the orthorhombic cell has the special relationship $a = \sqrt{3} * b$.⁴⁴ Using this unit cell, and three-fold twinning about the c -axis, where the domains are related by a 60 and 120 degree rotation, the structure can also be solved in several orthorhombic space groups (one of these possible solutions is supplied as supporting material). The structure is close to identical to the hexagonal structure, albeit with diamond-shaped channels instead of triangular. However, due to the poor data to parameter ratio of this structure, the hexagonal structure is used herein. Figure S6 illustrates how two of the twin domains are related to each other.

This type of twinning could also account for the surprisingly low N_2 adsorption. The stacking of twin domains could block the entrance to the diamond-shaped channels in the interior of the crystal. Similar blocking has been observed in the OFF-ERI zeolite which contains one-dimensional channels.⁴⁵

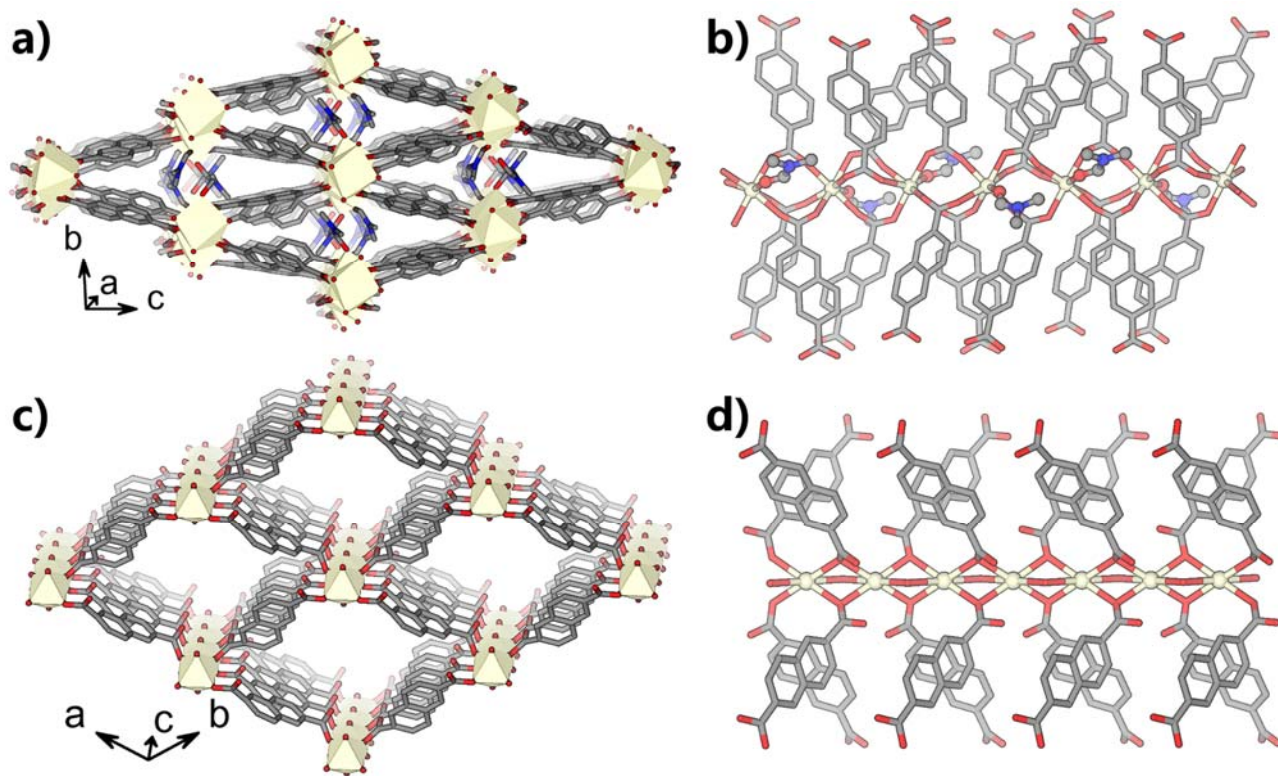


Figure 2 – Structural drawings of $\text{Ce}_2(\text{NDC})_3(\text{DMF})_2$ (a,b) and $\text{Ce}_2(\text{NDC})_3$ (c,d). Color code: Ce (dark yellow), O (red), C (gray), N (blue), H (omitted).

Pawley refinement of the PXRD patterns using the unit cells reported in Table 1 obtained from SC-XRD shows a good agreement, demonstrating that the structures found by SC-XRD are the only crystalline phases present in the bulk samples (see Figure 3 and Table 2).

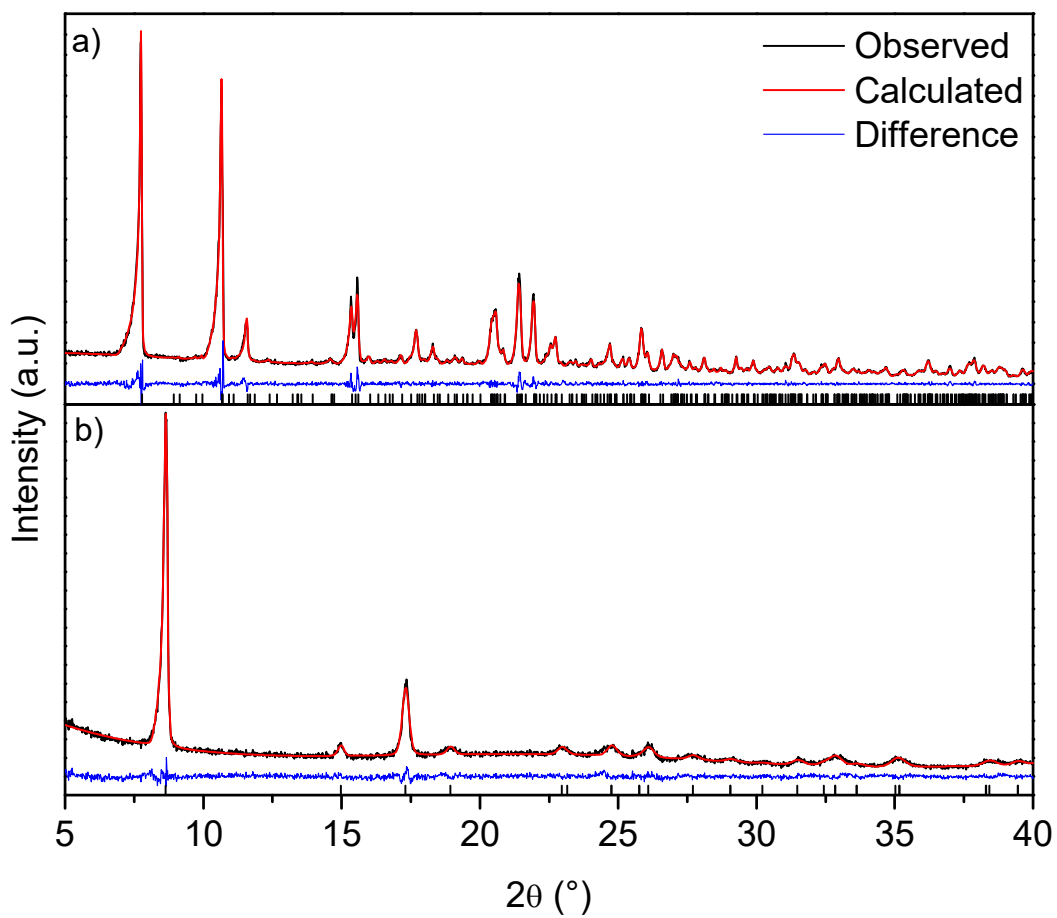


Figure 3 – Pawley fits on powder X-ray diffraction patterns of $\text{Ce}_2(\text{NDC})_3(\text{DMF})_2$ (a) and $\text{Ce}_2(\text{NDC})_3$ (b). Observed, calculated and residuals are drawn respectively in black, red and blue lines, allowed reflections are reported by black ticks. ($\lambda = 1.5406 \text{ \AA}$)

Table 2 – Comparison between cell parameters obtained by SC-XRD and Pawley refinements on $\text{Ce}_2(\text{NDC})_3(\text{DMF})_2$ and $\text{Ce}_2(\text{NDC})_3$ PXRD patterns.

Solvated	Pawley	SC-XRD	Desolvated	Pawley	SC-XRD
a (Å)	19.791(3)	19.836(4)	a (Å)	11.823(2)	11.845(5)
b (Å)	8.865(11)	8.7339(17)	b (Å)	11.823(2)	11.845(5)
c (Å)	45.392(6)	45.451(9)	c (Å)	7.675(4)	7.698(3)
Volume (Å ³)	7964(2)	7874(3)	Volume (Å ³)	929.1(5)	935.3(8)

The oxidation state of the Ce ions in $\text{Ce}_2(\text{NDC})_3(\text{DMF})_2$ was determined by Ce K- and Ce L₃-edge XANES spectroscopy in order to confirm the SC-XRD results. Energies of both absorption edges of the solvated material correspond to those of Ce(III) reference compound ($\text{Ce}(\text{NO}_3)_3 \cdot 6\text{H}_2\text{O}$) and are significantly different from those typical for Ce(IV) (Figure 4).^{15,20,23,24} Ce K-edge energy does not change upon activation of the material (Figure 4a), indicating the conservation of the 3+ oxidation state of Ce centers despite the concomitant structural rearrangements. These cations show also some accessibility to CO probe molecule (see FTIR spectra reported in Section 4 of SI).

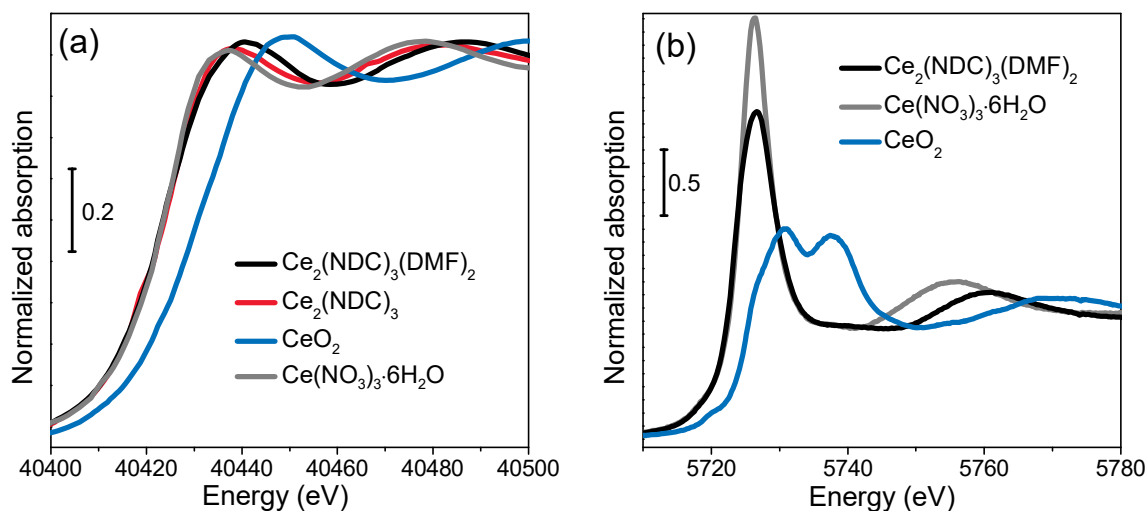


Figure 4. Ce K-edge (a) and Ce L₃-edge XANES spectra of Ce-MOFs compared to those of Ce(IV) oxide and Ce(III) nitrate hexahydrate.

To complement the long-range structural analysis carried out by XRD, Ce K-edge EXAFS spectra were collected for the solvated and the activated MOF, which allowed to probe the local environment of Ce centers. As already done to successfully optimize the metal K-edges of EXAFS signal for several MOFs,^{28,29,32,33,46} crystal structures obtained by the initial XRD refinements were used to develop the starting models for the EXAFS analysis. Then, several iterations of the EXAFS fitting were done, after each of which the XRD refinement was repeated implementing the structural modifications suggested by EXAFS. The resulting crystal structure was employed for the next run of EXAFS fitting and so on, until the qualitative convergence of the model. To increase the reliability of the fit, Ce–L scattering paths (L being a light neighbor, i.e. oxygen or carbon) were grouped in a way that three O and three C shells with different Ce–L distances were used to represent the nearest O- and C-coordination of Ce atoms. For the activated material the Ce–Ce scattering path was also included in the model. Further details of the EXAFS fitting procedure are provided in the Section 5 of the SI.

Overall, the EXAFS fitting confirmed the structural motives observed by XRD, resulting in low R-factors and reasonable parameter values for the solvated and activated MOF (Figure 5 and Table 3). While the Ce-Ce signal is absent in the EXAFS spectrum of solvated MOF due to too long Ce-Ce distance (around 4.9 Å according to the

XRD refinement), it is clearly observed in the spectrum of the activated material, contributing to EXAFS FT at 3.6 Å (phase-uncorrected), as shown in the Figure 5b. The Ce-Ce distance of 3.87(2) Å obtained as a result of the EXAFS fitting is in a close agreement to the 3.849(2) Å value from XRD. Concerning the nearest Ce coordination, EXAFS analysis indicates a general increase of Ce-O distances upon activation, coupled with a significant rearrangement of Ce-C ones. The latter is mostly expressed by broadening of the range of the Ce-C distances, from 3.28-3.43 Å in the solvated MOF to 2.98-4.15 Å in the activated material.

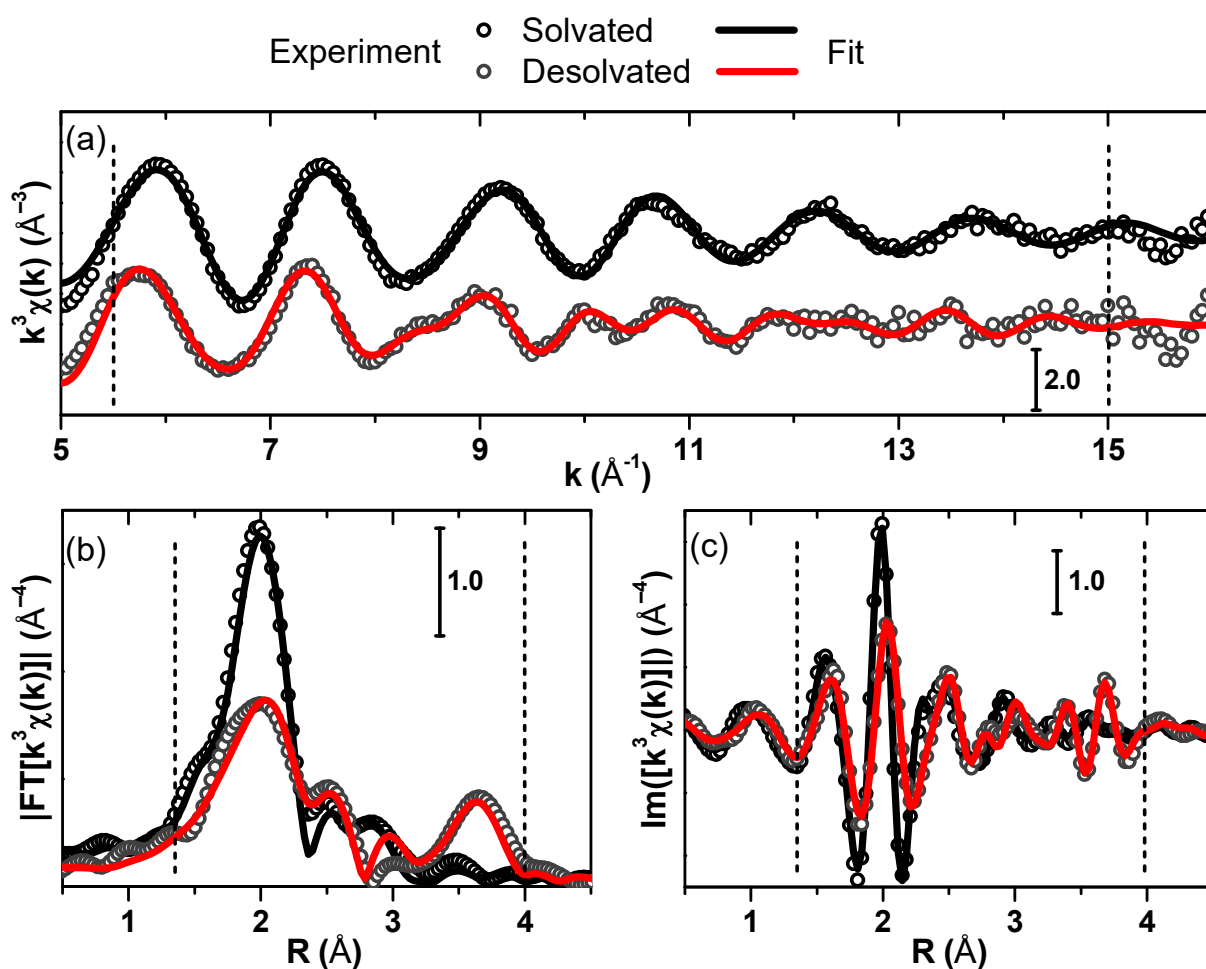


Figure 5. Experimental Ce K-edge EXAFS spectra of Ce₂(NDC)₃(DMF)₂ and Ce₂(NDC)₃, and the corresponding fits: $k^3\chi(k)$ spectra (a), the magnitude (b) and imaginary part of its phase-uncorrected Fourier transform. Experimental data are shown by open circles, fitted ones by the full lines.

Table 3. Fitting results for the Ce K-edge EXAFS spectra of the solvated and activated Ce-NDC MOF, $\text{Ce}_2(\text{NDC})_3(\text{DMF})_2$ and $\text{Ce}_2(\text{NDC})_3$. Parameters reported without error bars have been fixed in the optimization procedure.

Parameter	Solvated	Desolvated
R-factor	0.02	0.03
Fitting range in k , \AA^{-1}	5.5 – 15	
Fitting range in R , \AA	1.35 – 4	
N_{ind}	15.7	
N_{par}	5	9
S_0^2	1.0	1.0
ΔE	-0.3(1.7)	2.3(2.8)
N_{O1}	2.33	3
R_{O1} , \AA	2.40(1)	2.44(1)
σ_{O1}^2 , \AA^2	0.006(1)	0.009(1)
N_{O2}	2.33	3
R_{O2} , \AA	2.43(1)	2.49(1)
σ_{O2}^2 , \AA^2	0.006(1)	0.010(1)
N_{O3}	2.33	3
R_{O3} , \AA	2.46(1)	2.53(1)
σ_{O3}^2 , \AA^2	0.006(1)	0.010(1)
N_{C1}	2.33	3
R_{C1} , \AA	3.28(2)	2.98(2)
σ_{C1}^2 , \AA^2	0.004(2)	0.005(1)
N_{C2}	2.33	3
R_{C2} , \AA	3.36(2)	3.46(3)
σ_{C2}^2 , \AA^2	0.004(2)	0.006(1)
N_{C3}	2.33	3
R_{C3} , \AA	3.43(2)	4.15(9)
σ_{C3}^2 , \AA^2	0.004(2)	0.006(1)
N_{Ce}	-	2
R_{Ce} , \AA^2	-	3.87(2)
σ_{Ce}^2 , \AA^2	-	0.009(1)

3.2 Thermal activation

The behavior of $\text{Ce}_2(\text{NDC})_3(\text{DMF})_2$ upon thermal treatment was investigated by means of TGA, VT-PXRD and in-situ FTIR spectroscopy.

The TGA curve of $\text{Ce}_2(\text{NDC})_3(\text{DMF})_2$ (Figure 6) shows a steep weight loss at the onset temperature of 293°C due to the removal of all the structural DMF molecules giving rise to $\text{Ce}_2(\text{NDC})_3$. This can be inferred as there is a good agreement between the theoretical weight loss calculated removing the solvent from the formula unit (13.7%) and the experimental one (13.4%). Consequently, an activation temperature of 300°C was adopted when required (see SC-XRD, XAS, FTIR, adsorption measurements). The weight plateaus in the 360°C - 440°C temperature range. At higher temperatures (onset at 502°C) $\text{Ce}_2(\text{NDC})_3$ is decomposing at yielding CeO_2 and coke-like species, as expected for the thermal decomposition of a Ce-MOF in a nitrogen atmosphere.²⁵

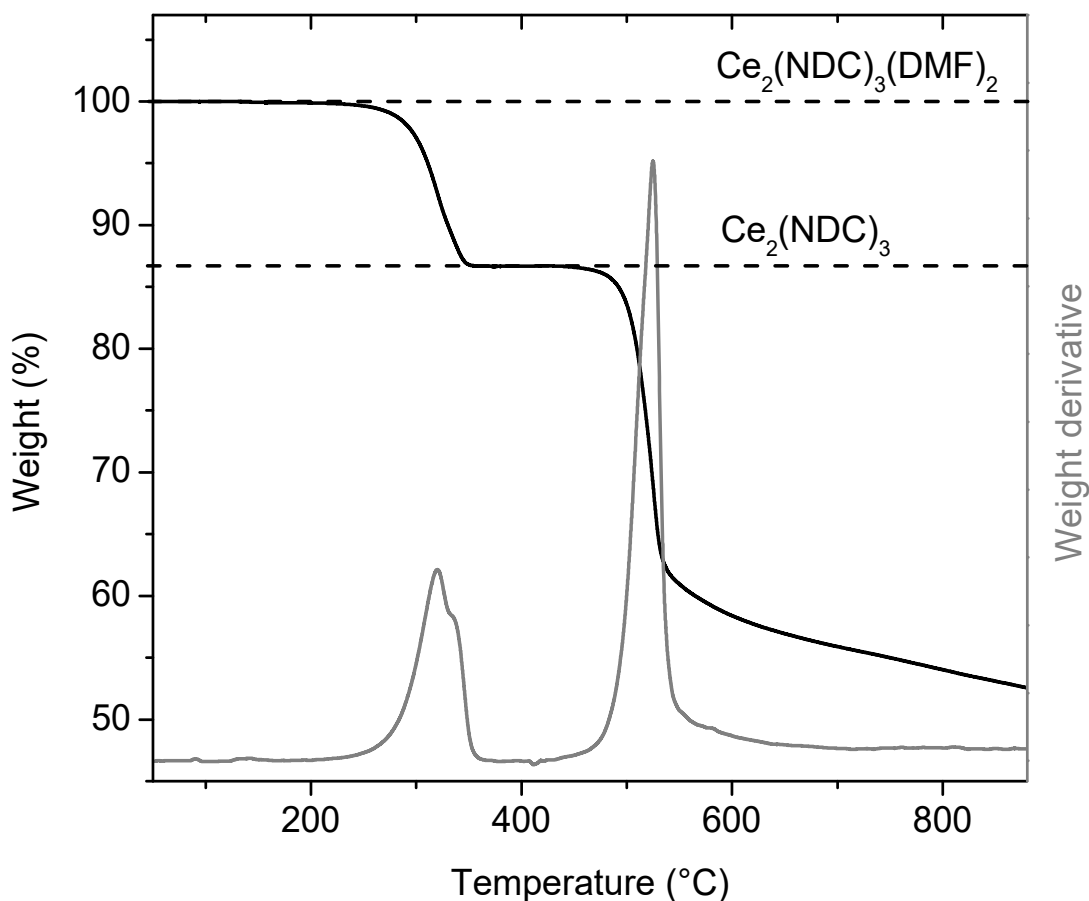


Figure 6 – TGA data of $\text{Ce}_2(\text{NDC})_3(\text{DMF})_2$ in a flow of dry nitrogen (black curve) and derivative of TGA curve (gray curve).

Figure 7 reports IR spectra collected on a thin pellet of the as-synthesized $\text{Ce}_2(\text{NDC})_3(\text{DMF})_2$ and the activated $\text{Ce}_2(\text{NDC})_3$ at 300°C for 2 h in dynamic vacuum (black and red curves, respectively). In both spectra, a series of typical fingerprints are well visible. Very intense bands due to carboxylate stretching modes (both symmetrical and antisymmetrical) can be observed in the 1630-1300 cm^{-1} range. At lower frequencies a very complex series of bands is present due to more complex vibrational modes involving mainly aromatic rings. At higher wavenumbers, O-H and/or C-H stretching modes are expected. In this case, a complex absorption around the C-H stretching

region (centered at 3000 cm^{-1}) is clearly visible in both spectra. The common bands found above 3000 cm^{-1} can be undoubtedly assigned to naphthalene C-H stretching modes. Comparing the two spectra some differences arise: upon thermal activation a very intense, out of scale, band centered at 1670 cm^{-1} together with the strong component below 3000 cm^{-1} vanishes. These two contributions can be easily assigned to DMF carbonyl and methyl group stretching modes, respectively. These findings strongly support the hypothesis, done previously by means of TGA measurements, whereby DMF, upon thermal treatment, is removed from the material leaving intact MOF typical vibrational modes.

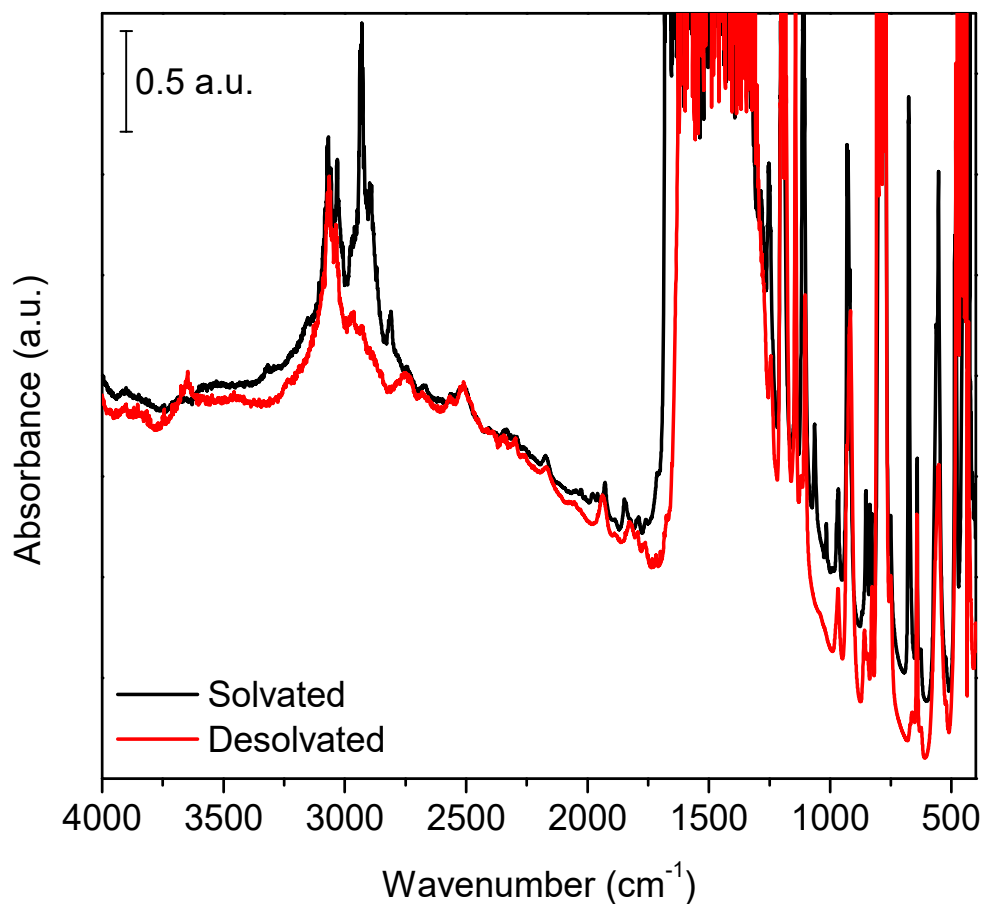


Figure 7 – Transmission FTIR spectra of as-synthesized $\text{Ce}_2(\text{NDC})_3(\text{DMF})_2$ (black curve) and after activation in dynamic vacuum at 300°C for 2 h (red curve).

A behavior similar to TGA can be noticed in the VT-PXRD data (Figure 8). Three different phases can be recognized from the patterns. The first one, stable from RT to 360°C, can be identified as the as-synthesized $\text{Ce}_2(\text{NDC})_3(\text{DMF})_2$ crystal structure as described above. In this case, the phase transition occurs probably at higher temperature (360°C vs. 300°C) as the measurement was performed in static conditions and not in dynamic ones (vacuum or inert gas flow). Reflections undergo a shift, most clearly seen for the one at 10.65°, which is progressively shifted to 10.10°, probably due to thermal expansion. Upon removal of the structural DMF molecules, the material undergoes a phase transformation into the new trigonal crystal structure of $\text{Ce}_2(\text{NDC})_3$ which is stable up to 550°C. Finally the third phase can be identified starting from 550°C and it is characterized by the presence of a weak and broad reflection at 28° ascribable to nano-sized CeO_2 particles²⁵ resulting from the pyrolysis of the framework. The thermal stability of $\text{Ce}_2(\text{NDC})_3(\text{DMF})_2$ is comparable with the one of other Ce based MOFs like MOF-76-Ce²⁵ and $[\text{Ce}_2(\text{NDC})_3(\text{DMF})_4] \cdot x\text{H}_2\text{O}$ ²⁷ which are based, respectively, on trimesic acid and 1,4-naphthalenedicarboxylic acid.

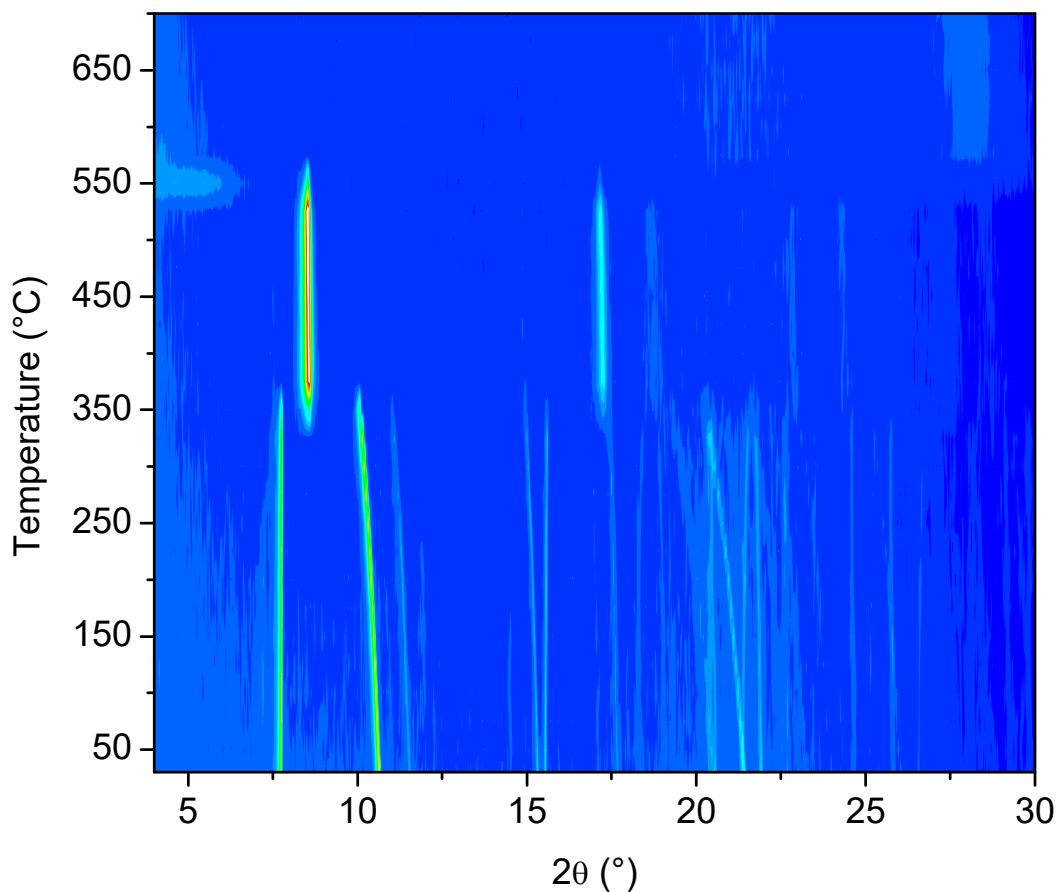


Figure 8 – Contour plot of the VT-PXRD measured on $\text{Ce}_2(\text{NDC})_3(\text{DMF})_2$. ($\lambda = 1.5406 \text{ \AA}$)

With the aim to measure porosity and surface area on $\text{Ce}_2(\text{NDC})_3$ N_2 was dosed at -196°C with an automatic volumetric apparatus giving a nearly negligible adsorption showing a very low surface area by adopting both BET and Langmuir models.

Volumetric N_2 and CO_2 adsorption isotherms recorded at 0°C , 25°C , 35°C and 60°C in the 0-1100 mbar pressure range are reported in Figure 9. As expected the carbon dioxide uptakes are much higher than the nitrogen ones at all temperatures and in all pressure ranges and it spans (at 1100 mbar) from a maximum of 1.5 mol/kg at 0°C to 0.5 mol/kg at 60°C . Even if the measured specific surface area measured by means of N_2 adsorption at -196°C is

negligible, the material shows a significant uptake of CO₂ at temperatures near the ambient one. The CO₂ uptake at 1000 mbar and 25°C for Ce₂(NDC)₃ amounts to 4 wt%, a value that is lower than those reported for other Ce based MOFs like MOF-76-Ce-hs and MOF-76-Ce-ds for which uptakes of 4.6% and 15%, respectively, are reported under the same conditions.²⁵ Comparing these data with the literature concerning CO₂ capture in MOFs one can find that these uptakes are easily overwhelmed by the majority of the materials proposed as CO₂ adsorbents like Mg-MOF-74⁴⁷ (26 wt%), HKUST-1⁴⁸ (18.4 wt%) and UTSA-16⁴⁹ (18.5 wt%).

However our material exhibits good CO₂/N₂ separation properties as indicated by the selectivity factor $S_{CO_2/N_2} = 17$ at 25°C. This value results from applying the following equation: $S_{CO_2/N_2} = (n_{CO_2} P_{N_2} / n_{N_2} P_{CO_2})$ in which p is the partial pressure of the gas and n is the adsorbed quantity at a pressure of CO₂ of 150 mbar and a pressure of N₂ of 750 mbar, relevant for a post-combustion capture process.⁵⁰ The reported result can be considered in line to what was published for MOFs proposed for CO₂ separation.⁴⁷

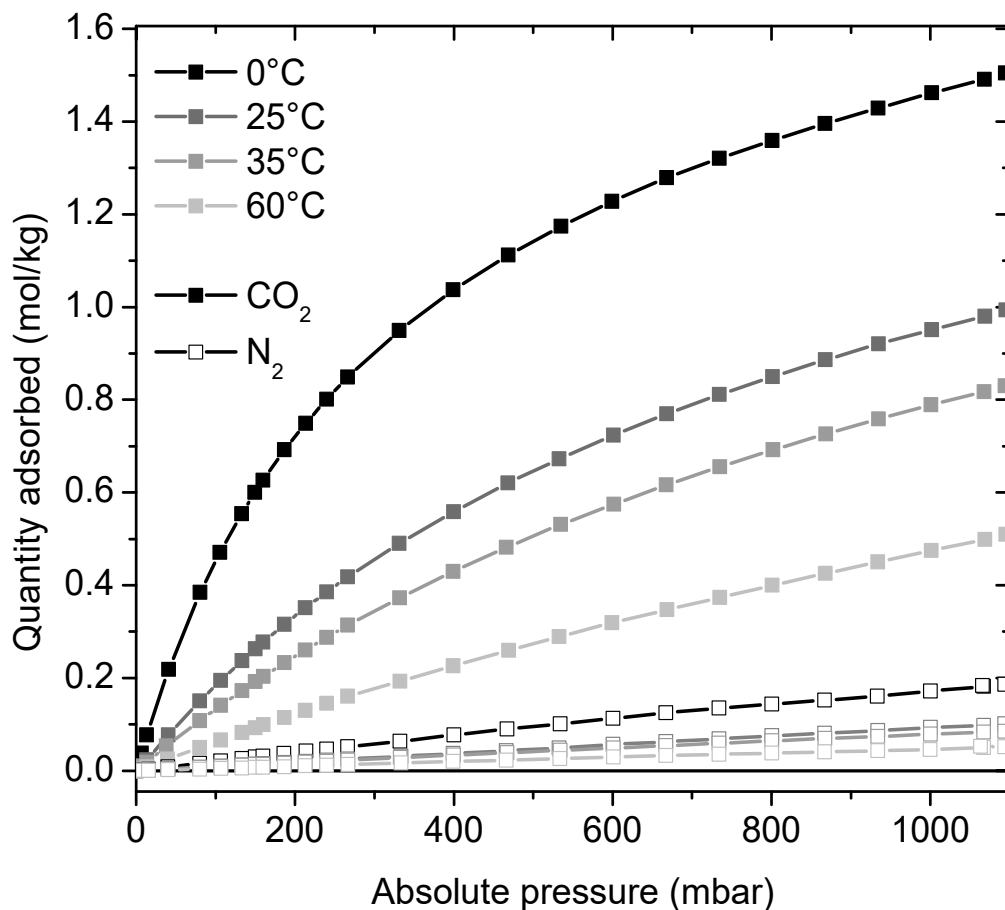


Figure 9 – Excess CO₂ (solid squares) and N₂ (hollow squares) adsorption isotherms at different temperatures (0, 25, 35 and 60°C, from black to light grey, respectively).

4. Conclusions

In the present work an unprecedented Ce(III)-based metal-organic framework containing a naphthalenedicarboxylate linker has been synthesized under solvothermal reaction conditions, using DMF as the solvent. The compound was obtained with a yield of 89% and high crystallinity. The crystal structure of the material was determined from SC-XRD obtaining a motif made of infinite Ce-O-C-O-Ce chains parallel to the *a*-axis surrounded by inter-chain linkers forming diamond-shaped channels. Each Ce(III) cation is coordinated by a

DMF molecule which is located inside the pore. These findings are further confirmed by XAS spectroscopy, evidencing pure Ce(III) oxidation state and FTIR spectroscopy, which points out the presence of DMF in the framework.

Upon thermal activation to about 300°C for 2 h in dynamic vacuum, the material undergoes a phase transformation from orthorhombic to trigonal which is accompanied by a large decline of crystallinity, due to the formation of disorder. Despite significant diffraction broadening and weakening, the crystal structure of the material after activation was determined exploiting a synergic approach using a synchrotron-based EXAFS method and SC-XRD which resulting structure consists of similar Ce chains as in the parent structure but with disordered linkers bridging from chain to chain. This phase is characterized by the loss of all DMF molecules and this hypothesis is further confirmed by TGA and in-situ FTIR spectroscopy. Pawley refinements on both phases show the absence of any crystalline impurity and confirms the reliability of the crystal data. Despite the presence of structural porosity, the desolvated MOF does not show any uptake for nitrogen at 77K; instead it shows a discrete adsorption for CO₂ at near-ambient temperatures evidencing a kind of porosity that cannot be traditionally characterized by low-temperature nitrogen adsorption volumetry.

Acknowledgements

The work received financial support from the Horizon 2020 ProDIA project (grant agreement No. 685727). C.L. acknowledges the Mega-grant of the Russian Federation Government (14.Y26.31.0001). Christian Näther and Milan Köppen from the University of Kiel are acknowledged, respectively, for their help in the collection of the SC-XRD data of the solvated material and of the VT-PXRD data. Prof. Silvia Bordiga and Prof. Karl Petter Lillerud are acknowledged for the fruitful discussion.

Supporting information description

The Supporting information contains a review of the Ce(III) based MOFs already published in literature; single-crystal diffraction frames and structural details about Ce₂(NDC)₃ (including one CIF file of an orthorhombic structure); an in-situ FTIR spectra of CO adsorbed on Ce₂(NDC)₃ at low temperature and EXAFS fitting details.

References

- (1) Furukawa, H.; Cordova, K. E. E.; O’Keeffe, M.; Yaghi, O. M.; O’Keeffe, M.; Yaghi, O. M. The Chemistry and Applications of Metal-Organic Frameworks. *Science* **2013**, *341*, 1230444.
- (2) Kaskel, S. *The Chemistry of Metal-Organic Frameworks: Synthesis, Characterization, and Applications*; Kaskel, S., Ed.; John Wiley & Sons: Weinheim, 2016.
- (3) Butova, V. V.; Soldatov, M. A.; Guda, A. A.; Lomachenko, K. A.; Lamberti, C. Metal-Organic Frameworks: Structure, Properties, Methods of Synthesis and Characterization. *Russ. Chem. Rev.* **2016**, *85*, 280–307.
- (4) Stock, N.; Biswas, S. Synthesis of Metal-Organic Frameworks (MOFs): Routes to Various MOF Topologies, Morphologies, and Composites. *Chem. Rev.* **2012**, *112*, 933–969.
- (5) Gascon, J.; Corma, A.; Kapteijn, F.; Llabrés I Xamena, F. X. Metal Organic Framework Catalysis: Quo Vadis? *ACS Catal.* **2014**, *4*, 361–378.
- (6) Horcajada, P.; Gref, R.; Baati, T.; Allan, P. K.; Maurin, G.; Couvreur, P. Metal À Organic Frameworks in Biomedicine. *Chem. Rev.* **2012**, *112*, 1232–1268.
- (7) Stavila, V.; Talin, A. A.; Allendorf, M. D. MOF-Based Electronic and Opto-Electronic Devices. *Chem. Soc. Rev.* **2014**, *43*, 5994–6010.
- (8) Kreno, L. E.; Leong, K.; Farha, O. K.; Allendorf, M.; Van Duyne, R. P.; Hupp, J. T. Metal-Organic Framework Materials as Chemical Sensors. *Chem. Rev.* **2012**, *112*, 1105–1125.
- (9) Zhang, Z.; Yates, J. T. Band Bending in Semiconductor Chemical and Physical Consequences at Surfaces and Interfaces. *Chem. Rev.* **2012**, *112*, 5520–5551.
- (10) So, M. C.; Wiederrecht, G. P.; Mondloch, J. E.; Hupp, J. T.; Farha, O. K. Metal-Organic Framework Materials for Light-Harvesting and Energy Transfer. *Chem. Commun.* **2015**, *51*, 3501–3510.
- (11) Long, K. R.; Van Gosen, B. S.; Foley, N. K.; Cordier, D. *The Principal Rare Earth Elements Deposits of the United States: A Summary of Domestic Deposits and a Global Perspective*; 2012.
- (12) Montini, T.; Melchionna, M.; Monai, M.; Fornasiero, P. Fundamentals and Catalytic Applications of CeO₂-Based Materials. *Chem. Rev.* **2016**, *116*, 5987–6041.

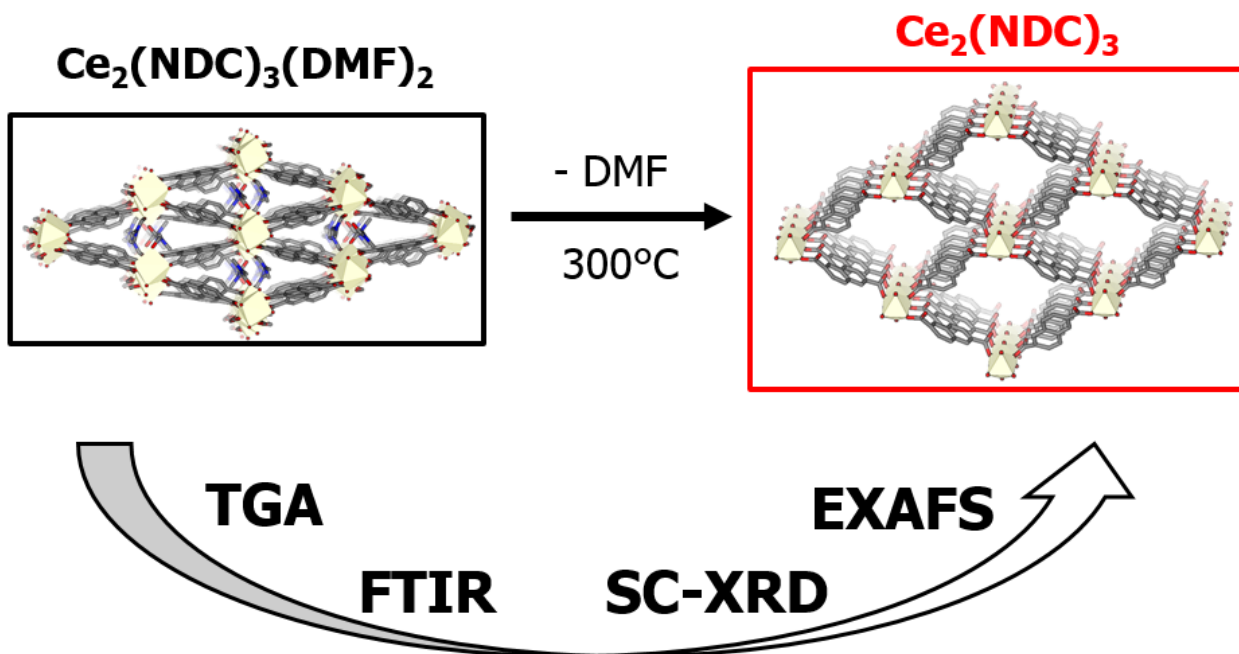
- (13) Kašpar, J.; Fornasiero, P.; Graziani, M. Use of CeO₂-Based Oxides in the Three-Way Catalysis. *Catal. Today* **1999**, *50*, 285–298.
- (14) Esch, F.; Fabris, S.; Zhou, L.; Montini, T.; Africh, C.; Fornasiero, P.; Comelli, G.; Rosei, R. Chemistry: Electron Localization Determines Defect Formation on Ceria Substrates. *Science* **2005**, *309*, 752–755.
- (15) Lammert, M.; Wharmby, M. T.; Smolders, S.; Bueken, B.; Lieb, A.; Lomachenko, K. A.; Vos, D. De; Stock, N. Cerium-Based Metal Organic Frameworks with UiO-66 Architecture: Synthesis, Properties and Redox Catalytic Activity. *Chem. Commun.* **2015**, *51*, 12578–12581.
- (16) Lammert, M.; Reinsch, H.; Murray, C. A.; Wharmby, M. T.; Terraschke, H.; Stock, N. Synthesis and Structure of Zr(IV)- and Ce(IV)-Based CAU-24 with 1,2,4,5-Tetrakis(4-Carboxyphenyl)Benzene. *Dalton Trans.* **2016**, *45*, 18822–18826.
- (17) Dreischarf, A. C.; Lammert, M.; Stock, N.; Reinsch, H. Green Synthesis of Zr-CAU-28: Structure and Properties of the First Zr-MOF Based on 2,5-Furandicarboxylic Acid. *Inorg. Chem.* **2017**, *56*, 2270–2277.
- (18) Lammert, M.; Glißmann, C.; Reinsch, H.; Stock, N. Synthesis and Characterization of New Ce(IV)-MOFs Exhibiting Various Framework Topologies. *Cryst. Growth Des.* **2017**, *17*, 1125–1131.
- (19) Smolders, S.; Struyf, A.; Reinsch, H.; Bueken, B.; Rhauderwiek, T.; Mintrop, L.; Kurz, P.; Stock, N.; De Vos, D. E. A Precursor Method for the Synthesis of New Ce(IV) MOFs with Reactive Tetracarboxylate Linkers. *Chem. Commun.* **2018**, *54*, 876–879.
- (20) Waitschat, S.; Fröhlich, D.; Reinsch, H.; Terraschke, H.; Lomachenko, K. A.; Lamberti, C.; Kummer, H.; Helling, T.; Baumgartner, M.; Henninger, S.; et al. Synthesis of M-UiO-66 (M = Zr, Ce or Hf) Employing 2,5-Pyridinedicarboxylic Acid as a Linker: Defect Chemistry, Framework Hydrophilisation and Sorption Properties. *Dalton Trans.* **2018**, *47*, 1062–1070.
- (21) Lammert, M.; Glißmann, C.; Stock, N. Tuning the Stability of Bimetallic Ce(IV)/Zr(IV)-Based MOFs with UiO-66 and MOF-808 Structures. *Dalton Trans.* **2017**, *46*, 2425–2429.
- (22) SK, M.; Grzywa, M.; Volkmer, D.; Biswas, S. Zr(IV) and Ce(IV)-Based Metal-Organic Frameworks

- Incorporating 4-Carboxycinnamic Acid as Ligand: Synthesis and Properties. *Microporous Mesoporous Mater.* **2017**, *237*, 275–281.
- (23) Smolders, S.; Lomachenko, K. A.; Bueken, B.; Struyf, A.; Bugaev, A. L.; Atzori, C.; Stock, N.; Lamberti, C.; Roeffaers, M. B. J.; De Vos, D. Unravelling the Redox-Catalytic Behavior of Ce⁴⁺-MOFs: A XAS Study. *ChemPhysChem* **2017**, *19*, 373–378.
- (24) Rhauderwiek, T.; Heidenreich, N.; Reinsch, H.; Øien-Ødegaard, S.; Lomachenko, K. A.; Rütt, U.; Soldatov, A. V.; Lillerud, K. P.; Stock, N. Co-Ligand Dependent Formation and Phase Transformation of Four Porphyrin-Based Cerium Metal-Organic Frameworks. *Cryst. Growth Des.* **2017**, *17*, 3462–3474.
- (25) Ethiraj, J.; Bonino, F.; Vitillo, J. G.; Lomachenko, K. A.; Lamberti, C.; Reinsch, H.; Lillerud, K. P.; Bordiga, S. Solvent-Driven Gate Opening in MOF-76-Ce: Effect on CO₂ Adsorption. *ChemSusChem* **2016**, *9*, 713–719.
- (26) D'Arras, L.; Sassoie, C.; Rozes, L.; Sanchez, C.; Marrot, J.; Marre, S.; Aymonier, C. Fast and Continuous Processing of a New Sub-Micronic Lanthanide-Based Metal–organic Framework. *New J. Chem.* **2014**, *38*, 1477.
- (27) Das, S. K.; Chatterjee, S.; Bhunia, S.; Mondal, A.; Mitra, P.; Kumari, V.; Pradhan, A.; Bhaumik, A. A New Strongly Paramagnetic Cerium-Containing Microporous MOF for CO₂ Fixation under Ambient Conditions. *Dalton Trans.* **2017**, *46*, 13783–13792.
- (28) Cavka, J. H.; Jakobsen, S.; Olsbye, U.; Guillou, N.; Lamberti, C.; Bordiga, S.; Lillerud, K. P. A New Zirconium Inorganic Building Brick Forming Metal Organic Frameworks with Exceptional Stability. *J. Am. Chem. Soc.* **2008**, *130*, 13850–13851.
- (29) Valenzano, L.; Civalleri, B.; Chavan, S.; Bordiga, S.; Nilsen, M. H.; Jakobsen, S.; Lillerud, K. P.; Lamberti, C. Disclosing the Complex Structure of UiO-66 Metal Organic Framework: A Synergic Combination of Experiment and Theory. *Chem. Mater.* **2011**, *23*, 1700–1718.
- (30) Chavan, S.; Vitillo, J. G.; Gianolio, D.; Zavorotynska, O.; Civalleri, B.; Jakobsen, S.; Nilsen, M. H.; Valenzano, L.; Lamberti, C.; Lillerud, K. P.; et al. H₂ Storage in Isostructural UiO-67 and UiO-66 MOFs. *Phys. Chem. Chem. Phys.* **2012**, *14*, 1614–1626.

- (31) Jakobsen, S.; Gianolio, D.; Wragg, D. S.; Nilsen, M. H.; Emerich, H.; Bordiga, S.; Lamberti, C.; Olsbye, U.; Tilset, M.; Lillerud, K. P. Structural Determination of a Highly Stable Metal-Organic Framework with Possible Application to Interim Radioactive Waste Scavenging: Hf-UiO-66. *Phys. Rev. B - Condens. Matter Mater. Phys.* **2012**, *86*, 125429.
- (32) Prestipino, C.; Regli, L.; Vitillo, J. G.; Bonino, F.; Damin, A.; Lamberti, C.; Zecchina, A.; Solari, P. L.; Kongshaug, K. O.; Bordiga, S. Local Structure of Framework Cu(II) in HKUST-1 Metallorganic Framework: Spectroscopic Characterization upon Activation and Interaction with Adsorbates. *Chem. Mater.* **2006**, *18*, 1337–1346.
- (33) Masciocchi, N.; Galli, S.; Colombo, V.; Maspero, A.; Palmisano, G.; Seyyedi, B.; Lamberti, C.; Bordiga, S. Cubic Octanuclear Ni(II) Clusters in Highly Porous Polypyrazolyl-Based Materials. *J. Am. Chem. Soc.* **2010**, *132*, 7902–7904.
- (34) Stock, N. High-Throughput Investigations Employing Solvothermal Syntheses. *Microporous Mesoporous Mater.* **2010**, *129*, 287–295.
- (35) Sheldrick, G. M. Crystal Structure Refinement with SHELXL. *Acta Crystallogr. Sect. C Struct. Chem.* **2015**, *71*, 3–8.
- (36) Stoe & Cie. X-Shape, X-Area and X-Red. Stoe & Cie: Darmstadt, Germany 2002.
- (37) Coelho, A. A. TOPAS and TOPAS-Academic: An Optimization Program Integrating Computer Algebra and Crystallographic Objects Written in C++. *An. J. Appl. Crystallogr.* **2018**, *51*, 210–218.
- (38) Van Beek, W.; Safonova, O. V.; Wiker, G.; Emerich, H. SNBL, a Dedicated Beamline for Combined in Situ X-Ray Diffraction, X-Ray Absorption and Raman Scattering Experiments. *Phase Transitions* **2011**, *84*, 726–732.
- (39) Lamberti, C.; Bordiga, S.; Bonino, F.; Prestipino, C.; Berlier, G.; Capello, L.; D’Acapito, F.; Llabrés I Xamena, F. X.; Zecchina, A. Determination of the Oxidation and Coordination State of Copper on Different Cu-Based Catalysts by XANES Spectroscopy in Situ or in Operando Conditions. *Phys. Chem. Chem. Phys.* **2003**, *5*, 4502–4509.
- (40) Bordiga, S.; Groppo, E.; Agostini, G.; Van Bokhoven, J. A.; Lamberti, C. Reactivity of Surface Species

- in Heterogeneous Catalysts Probed by in Situ X-Ray Absorption Techniques. *Chem. Rev.* **2013**, *113*, 1736–1850.
- (41) Klementiev, K.; Chernikov, R. XAFSmass: A Program for Calculating the Optimal Mass of XAFS Samples. *J. Phys. Conf. Ser.* **2016**, *712*, 012008.
- (42) Ravel, B.; Newville, M. ATHENA, ARTEMIS, HEPHAESTUS: Data Analysis for X-Ray Absorption Spectroscopy Using IFEFFIT. *J. Synchrotron Radiat.* **2005**, *12*, 537–541.
- (43) Rehr, J. J.; Albers, R. C. Theoretical Approaches to X-Ray Absorption Fine Structure. *Rev. Mod. Phys.* **2000**, *72*, 621–654.
- (44) Flack, H. D.; IUCr. Methods of Space-Group Determination – a Supplement Dealing with Twinned Crystals and Metric Specialization. *Acta Crystallogr. Sect. C Struct. Chem.* **2015**, *71*, 916–920.
- (45) Łukaszuk, K. A.; Rojo-Gama, D.; Øien-Ødegaard, S.; Lazzarini, A.; Berlier, G.; Bordiga, S.; Lillerud, K. P.; Olsbye, U.; Beato, P.; Lundegaard, L. F.; et al. Zeolite Morphology and Catalyst Performance: Conversion of Methanol to Hydrocarbons over Offretite. *Catal. Sci. Technol.* **2017**, *7*, 5435–5447.
- (46) Bordiga, S.; Bonino, F.; Lillerud, K. P.; Lamberti, C. X-Ray Absorption Spectroscopies: Useful Tools to Understand Metallorganic Frameworks Structure and Reactivity. *Chem. Soc. Rev.* **2010**, *39*, 4885–4927.
- (47) Sumida, K.; Rogow, D. L.; Mason, J. A.; McDonald, T. M.; Bloch, E. D.; Herm, Z. R.; Bae, T.-H.; Long, J. R. Carbon Dioxide Capture in Metal–Organic Frameworks. *Chem. Rev.* **2012**, *112*, 724–781.
- (48) Yazaydin, A. Ö.; Benin, A. I.; Faheem, S. A.; Jakubczak, P.; Low, J. J.; Richard, R. W.; Snurr, R. Q. Enhanced CO₂ Adsorption in Metal-Organic Frameworks via Occupation of Open-Metal Sites by Coordinated Water Molecules. *Chem. Mater.* **2009**, *21*, 1425–1430.
- (49) Masala, A.; Vitillo, J. G.; Mondino, G.; Grande, C. A.; Blom, R.; Manzoli, M.; Marshall, M.; Bordiga, S. CO₂ Capture in Dry and Wet Conditions in UTSA-16 Metal–Organic Framework. *ACS Appl. Mater. Interfaces* **2017**, *9*, 455–463.
- (50) Vitillo, J. G. Magnesium-Based Systems for Carbon Dioxide Capture, Storage and Recycling: From Leaves to Synthetic Nanostructured Materials. *RSC Adv.* **2015**, *5*, 36192–36239.

Table of Contents



Supporting information for:

Disclosing the properties of a new Ce(III)-based MOF: $\text{Ce}_2(\text{NDC})_3(\text{DMF})_2$

Cesare Atzori^a, Kirill A. Lomachenko^b, Sigurd Øien-Ødegaard^c, Carlo Lamberti^{d,e}, Norbert Stock^f, Claudia Barolo^a,
Francesca Bonino^{a*}

^a Department of Chemistry, NIS and INSTM Reference Centre, Università di Torino, Via G. Quarello 15, I-10135 and Via P. Giuria 7, I-10125 Torino, Italy

^b European Synchrotron Radiation Facility, 71 Avenue des Martyrs, CS 40220, 38043 Grenoble Cedex 9, France

^c Department of Chemistry, University of Oslo, P.O. Box 1033, N-0315 Oslo, Norway

^d Department of Physics, INSTM Reference Center and CrisDi Interdepartmental Centre for Crystallography, Università di Torino, Via P. Giuria 1, I-10125 Torino, Italy

^e The Smart Materials Research Institute, Southern Federal University, A. Sladkova str. 178/24, 344090 Rostov-on-Don, Russia

^f Institut für Anorganische Chemie, Christian-Albrechts-Universität zu Kiel, Max-Eyth-Straße 2, 24118 Kiel, Germany

*Corresponding author e-mail: francesca.bonino@unito.it

Outline:

1. Review of the Ce(III) based MOFs
2. $\text{Ce}_2(\text{NDC})_3$ single-crystal diffraction frames
3. $\text{Ce}_2(\text{NDC})_3$ structure details
4. In-situ FTIR spectra of CO adsorbed on $\text{Ce}_2(\text{NDC})_3$ at low temperature
5. EXAFS fitting details

References

1. Review of the Ce(III) based MOFs

Table S1 – MOFs with Ce(III) cations, a selection of what is reported in ref.¹

Formula	Linker molecule	Reference
[Ce ₂ (L) ₂ (DMF) ₄]	4,4',4''-{(2,4,6-trimethylbenzene-1,3,5-triyl)tris(methylene)tris(oxy)}tribenzoic acid	2
[Ce(HTCPB)] · (EtOH) _{0.28} · (H ₂ O) _{2.75}	1,2,4,5-Tetrakis(4-carboxyphenyl)benzene	3
[Ce(BTC)(DMF) ₂]	Trimesic acid	4
[Ce ₅ (BDC) _{7.5} (DMF) ₄]	Terephthalic acid	5
[Ce ₂ (ADC) ₃ (DMF) ₄] · DMF	9,10-Anthracenedicarboxylic acid	6
[Ce(ADC) _{1.5} (DMA) ₃]	9,10-Anthracenedicarboxylic acid	6
[Ce(BTC)(H ₂ O)] · DMF	Trimesic acid	7,8
[Ce ₂ (H ₂ O)(BPyDC) ₃ (DMF) ₂] · 2(DMF)	2,2-Bipyridine-5,5'-dicarboxylic acid	9
[Ce ₄ (H ₂ O) ₅ (BPyDC) ₆ (DMF)] · x(DMF)	2,2-Bipyridine-5,5'-dicarboxylic acid	9
[Ce(TTTPC)(NO ₂) ₂ Cl] · H ₂ O ₁₀	1,1',1''-tris(2,4,6-trimethylbenzene-1,3,5-triyl)-tris(methylene)-tris(pyridine-4-carboxylic acid)}	10
[Ce ₂ (EBTC) _{1.5} (CH ₃ OH) ₄] · 6H ₂ O	1,1'-ethynebenzene-3,3',5,5'-tetracarboxylic acid	11
[Ce(HL)(DMA) ₂] · DMA · 2H ₂ O	5,5'-(2,3,5,6-tetramethyl-1,4-phenylene)bis(methylene) bis(azanediy) diisophthalic acid	12
[Ce ₂ (BPDA) ₃ (H ₂ O) ₄] · H ₂ O	Benzophenone-2,4'-dicarboxylic acid	13
[Ce ₂ (NDC) ₃ (DMF) ₄] · xH ₂ O	1,4-Naphthalenedicarboxylic acid	14
[Ce(NDC) _{1.5} (DMF)(H ₂ O) _{0.5}] · 0.5DMF	2,6-Naphthalenedicarboxylic acid	15
[Ce(PDC) _{1.5} (DMF)] · DMF	3,5-Pyridinedicarboxylic acid	16,17
[Ce ₂ (PDC) ₃ (H ₂ O) ₂]	3,5-Pyridinedicarboxylic acid	18
[CeCl(BPDC)(DMF)]	4,4'-Biphenyldicarboxylic acid	19
[Ce(BTPCA)(H ₂ O)] · 2DMF · 3H ₂ O	1,1',1''-(benzene-1,3,5-triyl)tripiperidine-4-carboxylic acid	20
[Ce ₂ (DHBDC) ₃ (DMF) ₄] · DMF	Benzene-2,5-dihydroxy-1,4-dicarboxylic acid	21
[Ce ₆ (BDC) ₉ (DMF) ₆ (H ₂ O) ₃] · 33DMF	Terephthalic acid	22
[Ce ₂ (ADB) ₃ (DMSO) ₄] · 6DMSO · 8H ₂ O	4,4'-Azodibenzoic acid	22

$[\text{Ce}_3(\text{ADB})_3(\text{HADB})_3] \cdot 33\text{DMSO} \cdot 29\text{H}_2\text{O}$	4,4'-Azodibenzoic acid	22
$[\text{Ce}_2(\text{ADB})_3(\text{H}_2\text{O})_3]$	4,4'-Azodibenzoic acid	22
$[\text{Ce}_2(\text{SDBA})_3(\text{DMF})_4]$	4,4'-Sulfonyldibenzoic acid	23
$[(\text{CH}_3)_2\text{NH}_2]_3[\text{Ce}_3(\text{SDBA})_6] \cdot 6\text{DMF}$	4,4'-Sulfonyldibenzoic acid	23
$[\text{Ce}(\text{BTB})(\text{H}_2\text{O})]$	1,3,5-Tris(4-carboxyphenyl)benzene	24
$[\text{Ce}_2(\text{PDA})_3(\text{H}_2\text{O})] \cdot 2\text{H}_2\text{O}$	1,4 Phenylendiacetic acid	25

2. $\text{Ce}_2(\text{NDC})_3$ X-ray single-crystal diffraction

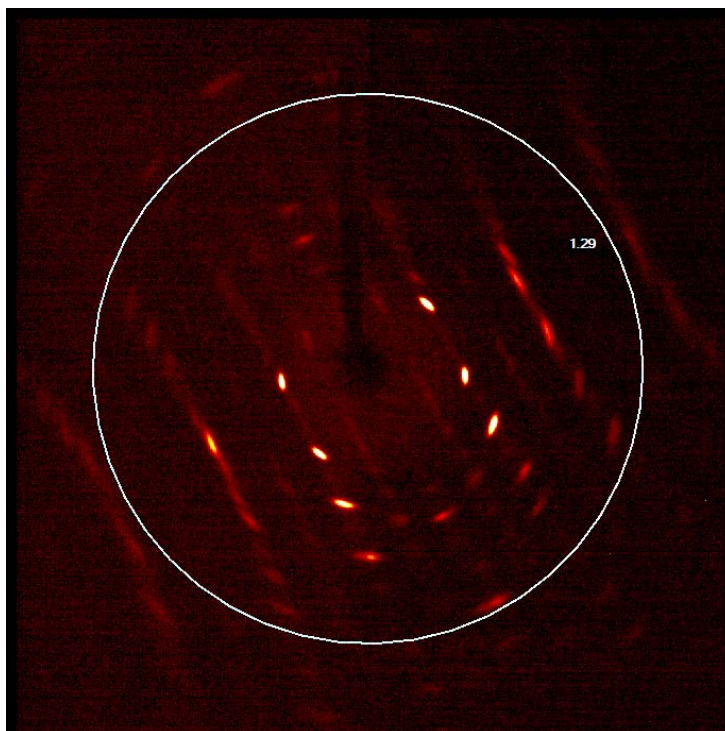


Figure S1 – Representative diffraction frame from $\text{Ce}_2(\text{NDC})_3$, with frame width 0.5° . The circle shows the data cut-off at 1.29 \AA , as the diffraction at higher angles could not be integrated.

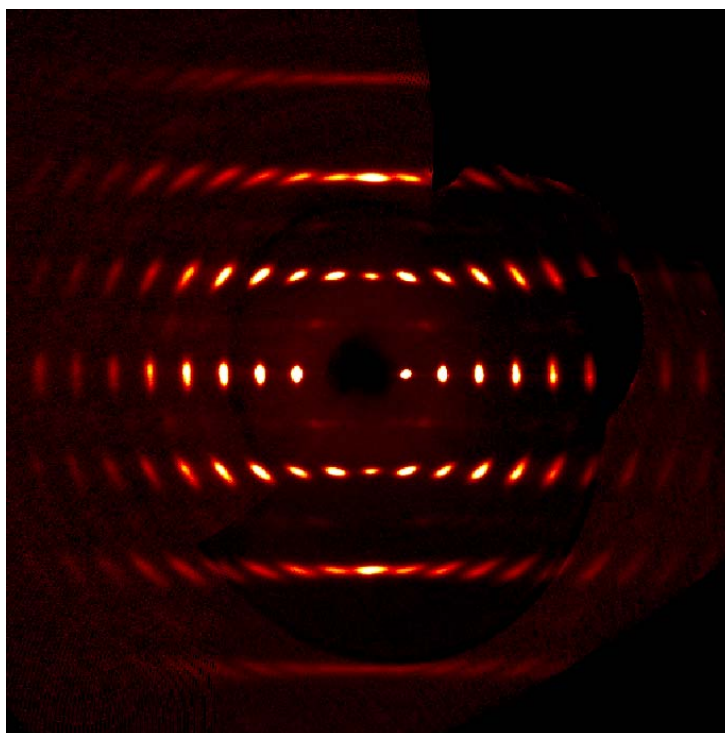


Figure S2 – Precession image of the diffraction from $\text{Ce}_2(\text{NDC})_3$ showing the $0kl$ plane.

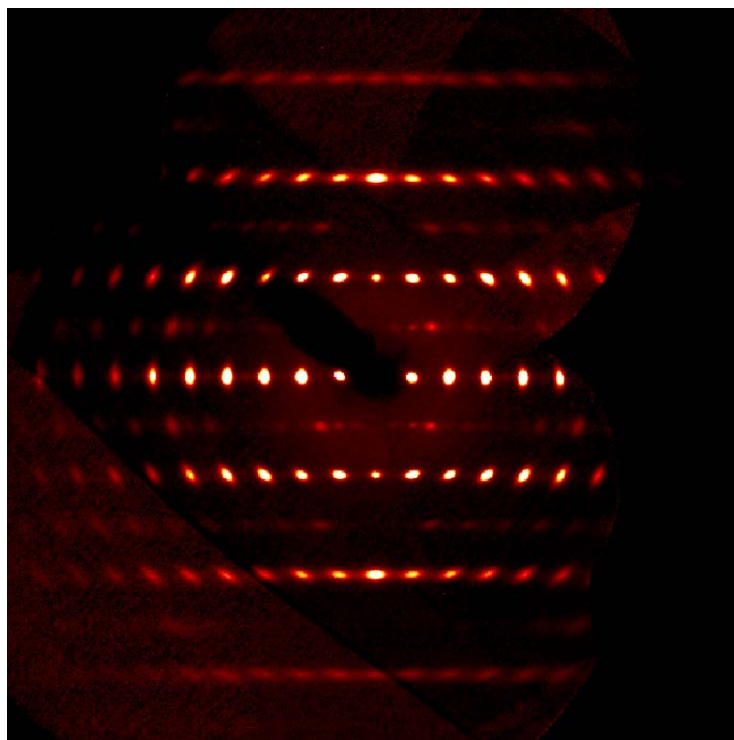


Figure S3 – Precession image of the diffraction from $\text{Ce}_2(\text{NDC})_3$ showing the $h0l$ plane.

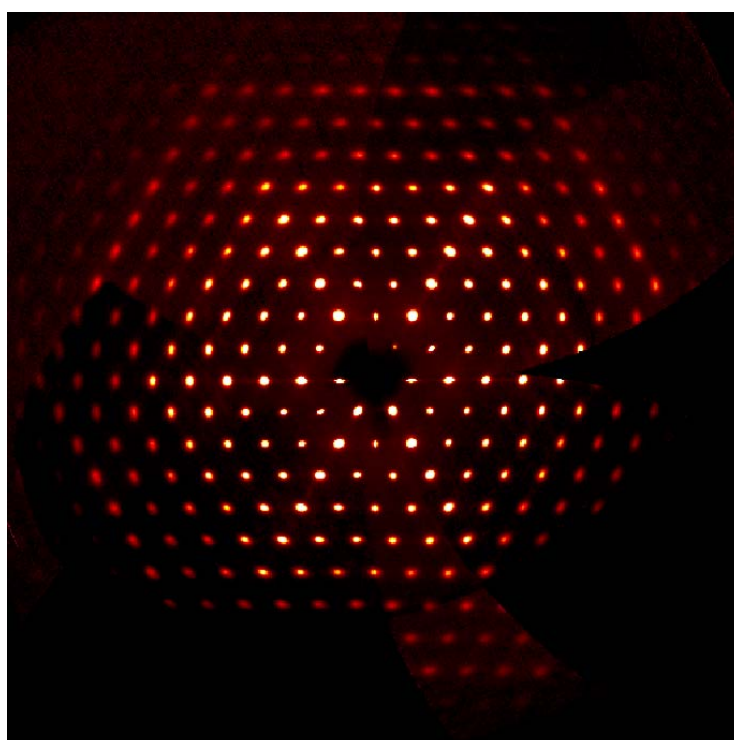


Figure S4 – Precession image of the diffraction from $\text{Ce}_2(\text{NDC})_3$ showing the $hk0$ plane.

3. $\text{Ce}_2(\text{NDC})_3$ structure details

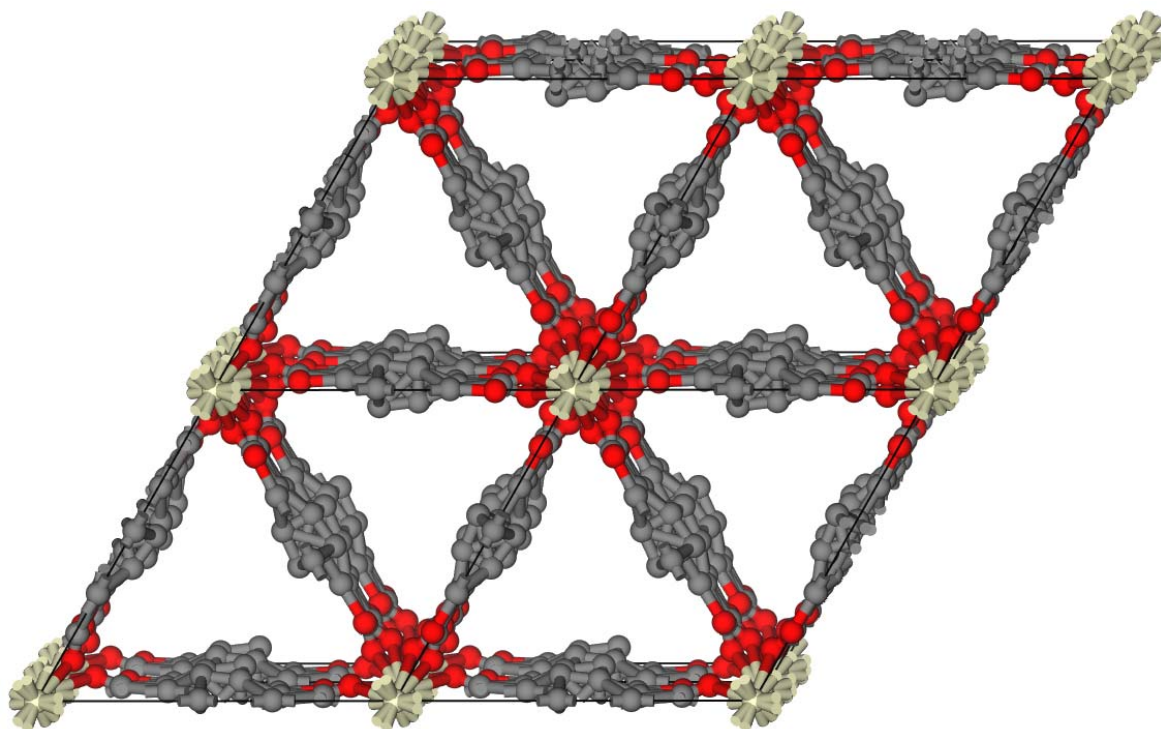


Figure S5 –Crystal structure of $\text{Ce}_2(\text{NDC})_3$ viewed along the c-axis, showing all possible positions of the atoms.

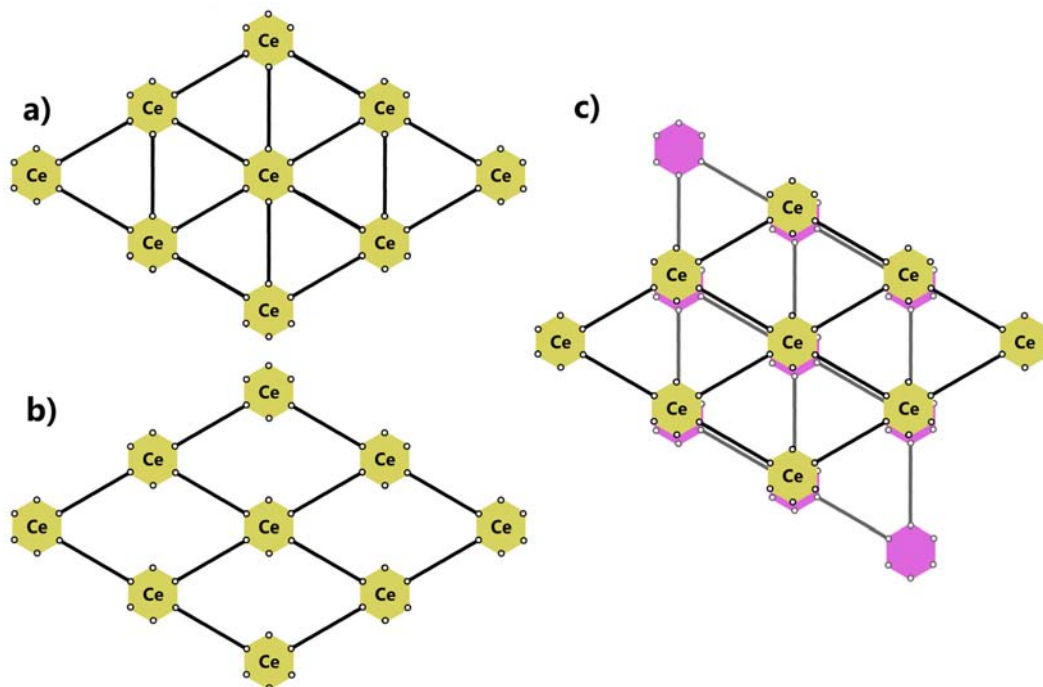


Figure S6 – Schematic representations of the structure of the activated MOF, viewed along the c-axis. a) Hexagonal unit cell. b) Orthorhombic cell. c) Two overlapping twin domains of the orthorhombic structure, showing the apparent hexagonal symmetry.

4. In-situ FTIR spectra of CO adsorbed on $\text{Ce}_2(\text{NDC})_3$ at low temperature

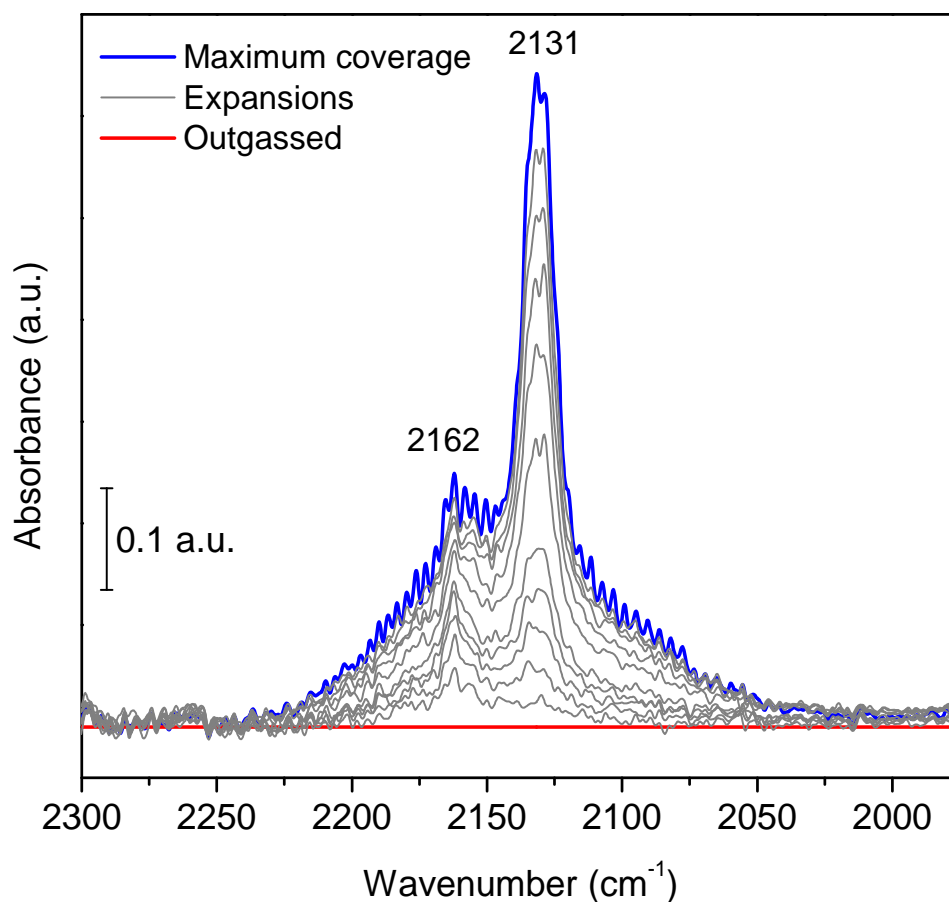


Figure S7 – Background subtracted FTIR spectra of CO adsorption at about 100K for $\text{Ce}_2(\text{NDC})_3$. Maximum and intermediate coverages are represented by the blue curve and the grey curves, respectively.

CO was dosed as a probe molecule during an in-situ FTIR spectroscopy²⁶ experiment performed on a self-supporting pellet of $\text{Ce}_2(\text{NDC})_3$. The temperature was then decreased to about 100K using a home made cell cooled down with liquid nitrogen. Figure S7 reports the spectra taken during the desorption procedure.

Under the typical roto-vibrational spectrum of gaseous CO ²⁷ which is clearly visible in the blue curve, two main signals of adsorbed CO are evident at 2162 and 2131 cm^{-1} , respectively. The latter (which is the first to be removed upon outgassing) is readily ascribable to physisorbed CO condensed in the pores while the other one can be assigned to CO interacting with acidic Ce^{3+} sites^{8,28}.

5. EXAFS fitting details

According to the XRD data, the sets of Ce-L distances (L being a light atom: O or C) of the nearest shells exhibit certain preferred values. Therefore, in order to decrease the amount of parameters for the EXAFS fitting and make the fit more robust, each of the four subsets of the scattering paths (Ce-O or Ce-C in both solvated and activated compounds) can be reasonably approximated by three groups with different Ce-L distance (Figure S7). The corresponding interatomic distances indicated in Figure S7 were used as initial values for three separate Ce-O and Ce-C shells during EXAFS fitting. Coordination numbers were set according to the XRD occupancies and kept fixed in the fitting procedures. Each of the three oxygen shells in the solvated material was parametrized with the same expansion/contraction parameter, scaled linearly with the corresponding Ce-O distance. Such approach was used also for the Ce-C and Ce-O shells in the hydrated and activated materials respectively. Conversely, each of the three Ce-C shells in the activated material were parametrized with a separate ΔR parameter. Four separate Debye-Waller (DW) parameters were used to parametrize the four above mentioned groups of shells, scaling within each group being as a square root of R. Finally, a separate ΔR and DW factor were assigned to Ce-Ce shell in the activated material. The amplitude reduction factor was fixed to $S_0^2 = 1$, which has proven to be a reasonable approximation for Ce K-edge EXAFS in porous material.²⁹

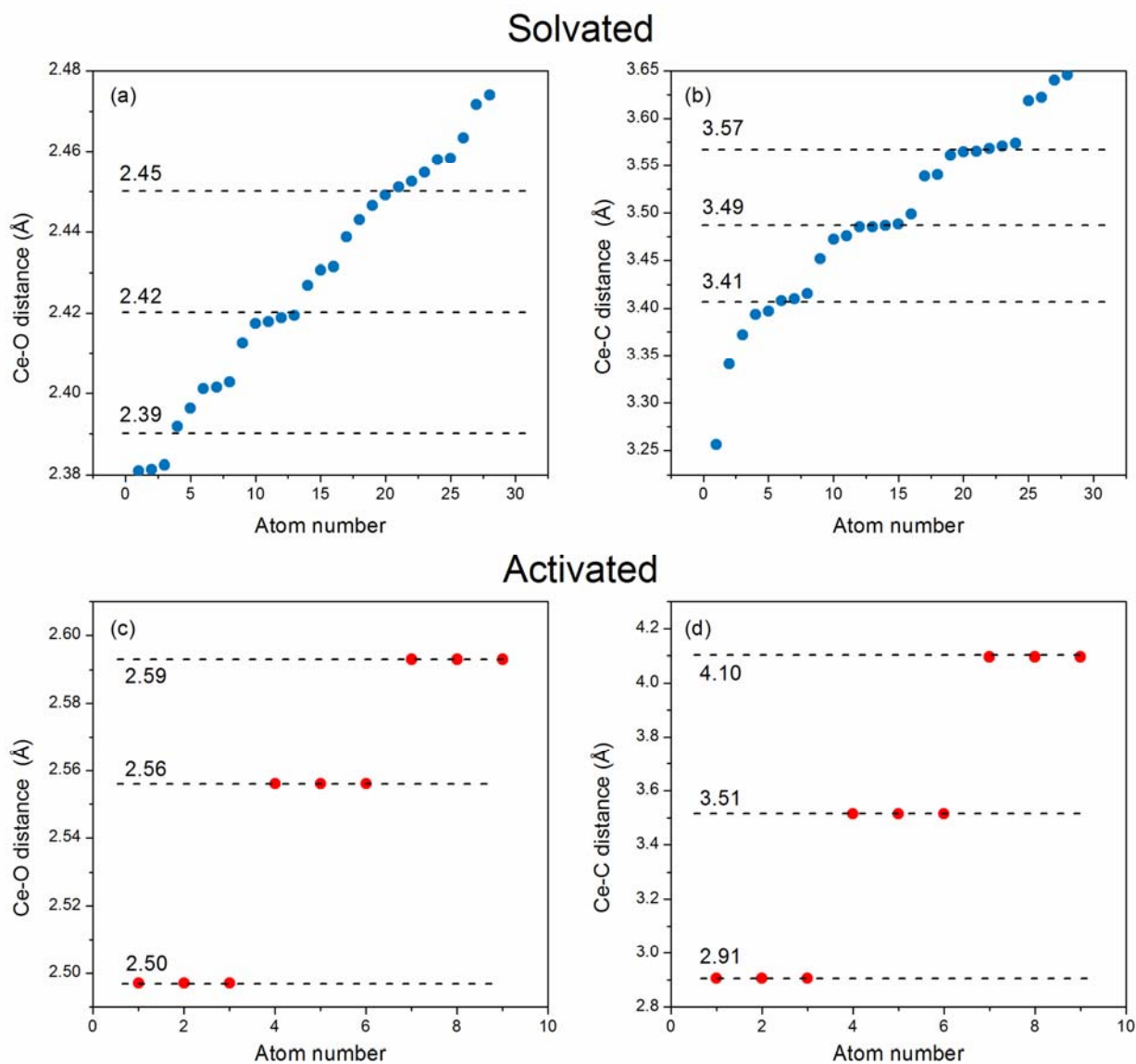


Figure S8 - Distances between Ce and the nearest O (left) and C (right) atoms in the solvated (top) and activated (bottom) materials obtained by XRD. Four and one non-equivalent Ce were considered for solvated and activated materials, respectively. Distances employed as initial values for EXAFS fitting are in the Figure by the dashed lines with the corresponding labels.

References

- (1) Lammert, M. PhD Thesis, Christian-Albrechts-University, Kiel, 2017.
- (2) Liang, L. L.; Xu, L.; Xue, H. B.; Tao, Z. L.; Chen, F. J. Two Metal-Organic Frameworks with Different Configurations Constructed from a Flexible Tripodal Triaromatic Acid. *J. Mol. Struct.* **2016**, *1125*, 656–661.
- (3) Warren, J. E.; Perkins, C. G.; Jelfs, K. E.; Boldrin, P.; Chater, P. A.; Miller, G. J.; Manning, T. D.; Briggs, M. E.; Stylianou, K. C.; Claridge, J. B.; et al. Shape Selectivity by Guest-Driven Restructuring of a Porous Material. *Angew. Chemie - Int. Ed.* **2014**, *53*, 4592–4596.
- (4) Li, Z.; Liu, K. Poly[(μ (4)-Benzene-1,3,5-Tricarboxyl-Ato)Bis-(N,N-Dimethyl-Formamide)-Cerium(III)]. *Acta Crystallogr. Sect. E. Struct. Rep. Online* **2011**, *67*, m1020.
- (5) D'Arras, L.; Sassoie, C.; Rozes, L.; Sanchez, C.; Marrot, J.; Marre, S.; Aymonier, C. Fast and Continuous Processing of a New Sub-Micronic Lanthanide-Based Metal–organic Framework. *New J. Chem.* **2014**, *38*, 1477.
- (6) Quah, H. S.; Ng, L. T.; Donnadiou, B.; Tan, G. K.; Vittal, J. J. Molecular Scissoring: Facile 3D to 2D Conversion of Lanthanide Metal Organic Frameworks Via Solvent Exfoliation. *Inorg. Chem.* **2016**, *55*, 10851–10854.
- (7) Almáši, M.; Zeleňák, V.; Opanasenko, M.; Císařová, I. Ce(III) and Lu(III) Metal-Organic Frameworks with Lewis Acid Metal Sites: Preparation, Sorption Properties and Catalytic Activity in Knoevenagel Condensation. *Catal. Today* **2015**, *243*, 3098–3114.
- (8) Ethiraj, J.; Bonino, F.; Vitillo, J. G.; Lomachenko, K. A.; Lamberti, C.; Reinsch, H.; Lillerud, K. P.; Bordiga, S. Solvent-Driven Gate Opening in MOF-76-Ce: Effect on CO₂ Adsorption. *ChemSusChem* **2016**, *9*, 713–719.
- (9) Ayhan, O.; Malaestean, I. L.; Ellern, A.; Van Leusen, J.; Baca, S. G.; Kögerler, P. Assembly of Cerium(III) 2,2'-Bipyridine-5,5'-Dicarboxylate- Based Metal-Organic Frameworks by Solvent Tuning. *Cryst. Growth Des.* **2014**, *14*, 3541–3548.
- (10) Bag, P. P.; Wang, X. S.; Cao, R. Microwave-Assisted Large Scale Synthesis of Lanthanide Metal-Organic Frameworks (Ln-MOFs), Having a Preferred Conformation and Photoluminescence Properties. *Dalton Trans.* **2015**, *44*, 11954–11962.
- (11) Zhai, L.; Zhang, W. W.; Ren, X. M.; Zuo, J. L. Luminescent Lanthanide MOFs Based on Conjugated 1,1'-Ethynebenzene-3,3',5,5'-Tetracarboxylate Ligand: Syntheses, Structures and Photoluminescent Properties. *Dalton Trans.* **2015**, *44*, 5746–5754.
- (12) Wang, C.; Li, L.; Bell, J. G.; Lv, X.; Tang, S.; Zhao, X.; Thomas, K. M. Hysteretic Gas and Vapor Sorption in Flexible Interpenetrated Lanthanide-Based Metal-Organic Frameworks with Coordinated Molecular Gating via Reversible Single-Crystal-to-Single-Crystal Transformation for Enhanced Selectivity. *Chem. Mater.* **2015**, *27*, 1502–1516.

- (13) Wu, Y. P.; Li, D. S.; Xia, W.; Guo, S. S.; Dong, W. W. Three Novel Lanthanide Metal-Organic Frameworks (Ln-MOFs) Constructed by Unsymmetrical Aromatic Dicarboxylate Tectonics: Synthesis, Crystal Structures and Luminescent Properties. *Molecules* **2014**, *19*, 14352–14365.
- (14) Das, S. K.; Chatterjee, S.; Bhunia, S.; Mondal, A.; Mitra, P.; Kumari, V.; Pradhan, A.; Bhaumik, A. A New Strongly Paramagnetic Cerium-Containing Microporous MOF for CO₂ Fixation under Ambient Conditions. *Dalton Trans.* **2017**, *46*, 13783–13792.
- (15) Liu, Y. H.; Chien, P. H. A Series of Lanthanide-Organic Frameworks Possessing Arrays of 2D Intersecting Channels within a 3D Pillar-Supported Packed Double-Decker Network and Co²⁺-Induced Luminescence Modulation. *CrystEngComm* **2014**, *16*, 8852–8862.
- (16) Nandi, G.; Thakuria, R.; Titi, H. M.; Patra, R.; Goldberg, I. Synthesis, Structure, Topology and Magnetic Properties of New Coordination Polymers Based on 5(-Br/-COOH)-Substituted Nicotinic Acid. *CrystEngComm* **2014**, *16*, 5244–5256.
- (17) Nandi, G.; Titi, H. M.; Thakuria, R.; Goldberg, I. Solvent Dependent Formation of Metallogels and Single-Crystal MOFs by La(III) and Ce(III) Connectors and 3,5-Pyridinedicarboxylate. *Cryst. Growth Des.* **2014**, *14*, 2714–2719.
- (18) Silva, P.; Ananias, D.; Bruno, S. M.; Valente, A. A.; Carlos, L. D.; Rocha, J.; Almeida Paz, F. A. Photoluminescent Metal-Organic Frameworks - Rapid Preparation, Catalytic Activity, and Framework Relationships. *Eur. J. Inorg. Chem.* **2013**, *2013*, 5576–5591.
- (19) Jia, L. N.; Hou, L.; Wei, L.; Jing, X. J.; Liu, B.; Wang, Y. Y.; Shi, Q. Z. Five Sra Topological Ln(III)-MOFs Based on Novel Metal-Carboxylate/Cl Chain: Structure, near-Infrared Luminescence and Magnetic Properties. *Cryst. Growth Des.* **2013**, *13*, 1570–1576.
- (20) Tang, Q.; Liu, S.; Liu, Y.; Miao, J.; Li, S.; Zhang, L.; Shi, Z.; Zheng, Z. Cation Sensing by a Luminescent Metal-Organic Framework with Multiple Lewis Basic Sites. *Inorg. Chem.* **2013**, *52*, 2799–2801.
- (21) Nayak, S.; Nayek, H. P.; Pietzonka, C.; Novitchi, G.; Dehnen, S. A Series of Three-Dimensional Lanthanide MOFs: Observation of Reversible Structural Changes Controlled by Solvent Desorption-Adsorption, and Magnetic Properties. *J. Mol. Struct.* **2011**, *1004*, 82–87.
- (22) Han, Y.; Li, X.; Li, L.; Ma, C.; Shen, Z.; Song, Y.; You, X. Structures and Properties of Porous Coordination Polymers Based on Lanthanide Carboxylate Building Units. *Inorg. Chem.* **2010**, *49*, 10781–10787.
- (23) Neofotistou, E.; Malliakas, C. D.; Trikalitis, P. N. Remarkable Structural Diversity and Single-Crystal-to-Single-Crystal Transformations in Sulfone Functionalized Lanthanide MOFs. *CrystEngComm* **2010**, *12*, 1034–1037.
- (24) Devic, T.; Wagner, V.; Guillou, N.; Vimont, A.; Haouas, M.; Pascolini, M.; Serre, C.; Marrot, J.; Daturi, M.; Taulelle, F.; et al. Synthesis and Characterization of a Series of Porous Lanthanide Tricarboxylates.

Microporous Mesoporous Mater. **2011**, *140*, 25–33.

- (25) Pan, L.; Adams, K. M.; Hernandez, H. E.; Wang, X.; Zheng, C.; Hattori, Y.; Kaneko, K. Porous Lanthanide-Organic Frameworks: Synthesis, Characterization, and Unprecedented Gas Adsorption Properties. *J. Am. Chem. Soc.* **2003**, *125*, 3062–3067.
- (26) Lamberti, C.; Zecchina, A.; Groppo, E.; Bordiga, S. Probing the Surfaces of Heterogeneous Catalysts by in Situ IR Spectroscopy. *Chem. Soc. Rev.* **2010**, *39*, 4951.
- (27) Bordiga, S.; Scarano, D.; Spoto, G.; Zecchina, A.; Lamberti, C.; Otero Areán, C. Infrared Study of Carbon Monoxide Adsorption at 77 K on Faujasites and ZSM-5 Zeolites. *Vib. Spectrosc.* **1993**, *5*, 69–74.
- (28) Vindigni, F.; Manzoli, M.; Tabakova, T.; Idakiev, V.; Boccuzzi, F.; Chiorino, A. Effect of Ceria Structural Properties on the Catalytic Activity of Au–CeO₂ Catalysts for WGS Reaction. *Phys. Chem. Chem. Phys.* **2013**, *15*, 13400.
- (29) Smolders, S.; Lomachenko, K. A.; Bueken, B.; Struyf, A.; Bugaev, A. L.; Atzori, C.; Stock, N.; Lamberti, C.; Roeffaers, M. B. J.; De Vos, D. Unravelling the Redox-Catalytic Behavior of Ce⁴⁺-MOFs: A XAS Study. *ChemPhysChem* **2017**, *19*, 373–378.

Exact stoichiometry of Ce_xZr_{6-x} cornerstones in mixed-metal UiO-66 MOFs revealed by EXAFS spectroscopy

Kirill A. Lomachenko,^{*1} Jannick Jacobsen,² Aram L. Bugaev,³ Cesare Atzori,⁴ Francesca Bonino,⁴ Silvia Bordiga,⁴ Norbert Stock² and Carlo Lamberti^{*3,5}

¹European Synchrotron Radiation Facility, 71 Avenue des Martyrs, CS 40220, 38043 Grenoble Cedex 9, France

²Institut für Anorganische Chemie, Christian-Albrechts-Universität, Max-Eyth-Straße 2, D 24118 Kiel, Germany

³Smart Materials Research Institute, Southern Federal University, Sladkova 178/24, 344090 Rostov-on-Don, Russia

⁴Department of Chemistry, NIS interdepartmental Center and INSTM Reference Center, University of Turin, Via Quarellone 15, 10135 Turin, Italy

⁵Department of Physics, INSTM Reference Center and CrisDi Interdepartmental Centre for Crystallography, University of Turin, Via P. Giuria 1, 10125 Turin Italy

Supporting Information Placeholder

ABSTRACT: Recently synthesized bimetallic Ce/Zr-UiO-66 MOFs proved to be a promising material for various catalytic redox applications, representing, together with other bimetallic MOFs, a new generation of porous materials. However, no direct proof for the presence of both metals in a single cornerstone of UiO-type MOFs was reported so far. Employing element-selective XAS techniques herein we demonstrate for the first time that our synthesis route allows obtaining Ce/Zr-UiO-66 MOFs with desired Ce content and bimetallic $CeZr_5$ cornerstones. Performing multiple-edge EXAFS analysis we determine the exact stoichiometry of the cornerstones, which explains the dependence of thermal and chemical stability of the materials on Ce content.

Metal-Organic Frameworks (MOFs) are porous compounds with high specific surface area, tuneable pore sizes and different chemical functionalities. They are formed by the connection of inorganic and organic building units through coordinative bonding.¹⁻² Zirconium-based MOFs have attracted substantial interest since the first Zr-MOF UiO-66, $[Zr_6(\mu_3-O)_4(\mu_3-OH)_4(BDC)_6]$ with $BDC^{2-} = 1,4$ -benzenedicarboxylate, has been reported (Figure 1a).³ The structure of most Zr-MOFs contain hexanuclear $[Zr_6(\mu_3-O)_4(\mu_3-OH)_4]^{12+}$ clusters which are connected by di-, tri- or tetra-carboxylate linker molecules to form two- or three-dimensional networks.³⁻⁷

Being exceptionally stable,^{3-4, 6} Zr clusters (Figure 1b) are not very active chemically due to the limited redox capabilities of Zr. In contrast, cerium is known for a wide range of catalytic applications.⁸ To combine the stability and porosity of UiO-66 structure with the redox properties of Ce metal, we have recently accomplished the first successful synthesis of pure Ce-UiO-66 employing linker molecules of various sizes and functional groups.⁹ Such MOFs have already been studied by us and other groups in various catalytical applications.⁹⁻¹² In a recent study, Smolders et al. demonstrated that one cerium atom per hexanuclear Ce_6 cluster in UiO-67 MOF is indeed redox-active and switches the oxidation state between Ce(III)/Ce(IV).¹³

To further improve the performance of Ce-UiO MOFs in terms of stability, which is still inferior to those of pure Zr-UiO-66,^{3-4, 6} we started to investigate the synthesis and properties of mixed-metal Ce/Zr-MOFs. As a result, an increased thermal and chemical stability compared to pure Ce-UiO-66 was observed for mixed-metal compounds containing low amounts of Ce(IV) ions (< 20% of total metal content), reaching up to 350 °C for the mixed-metal $Ce_{0.5}Zr_{5.5}$ UiO-66 MOF.¹⁴ Other groups have also reported the synthesis of Ce-containing Zr-UiO-66 MOF and successfully employed it in catalytic studies.¹⁵⁻¹⁶

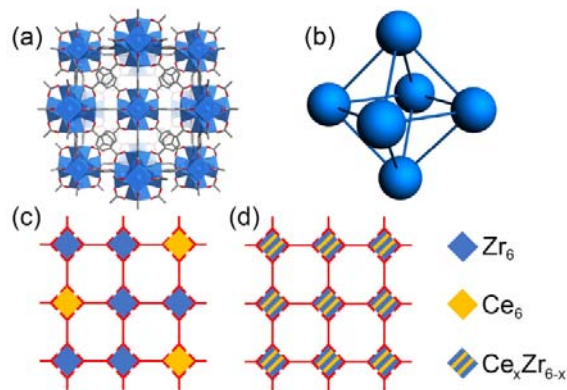


Figure 1 Fragment of crystal structure of UiO-66 MOF, showing BDC linkers and $Zr_6(\mu_3-O)_4(\mu_3-OH)_4$ cornerstones; (b) Closeup on UiO-66 cornerstone (M atoms only); (c-d) Schematic representation of mixed-metal Ce_xZr_{6-x} -UiO-66 structure with pure (c) and bimetallic cornerstones (d).

Although the metal substitution in different MOFs is widely discussed in the literature,¹⁷⁻²⁷ to the best of our knowledge, no direct proof for the existence of mixed-metal cornerstones in UiO-family MOFs have been presented so far. While extra-phases present in the framework pores may be detected by powder X-ray diffraction (PXRD)¹⁶ or N_2 physisorption,²⁸ in their absence the cornerstones in the mixed-metal compounds were only assumed to be either pure

(e.g. Zr/Ti- and Zr/Hf-UiO-66 MOFs)²⁹ or truly bimetallic (e.g. CeZr-UiO-66 MOF)¹⁵, as shown in panels c and d of Figure 1, respectively. However, no discussion regarding the discrimination of these chemically different cases was provided.

The key to the quantitative determination of the cornerstone composition is the use of element-selective techniques, since the fine non-periodic variations of local atomic structure can hardly be detected by non-selective scattering-based methods. In this study, we provide the first direct proof of the existence of mixed-metal Ce/Zr cornerstones in Ce_xZr_{6-x}-UiO-66 MOF, possible due to the combined analysis of Zr and Ce K-edge EXAFS data for the series of samples with different Ce content, coupled with complementary techniques.

The synthesis of the pure Ce-UiO-66 and mixed-metal Ce/Zr-UiO-66 compounds was performed following the procedure reported by Lammert et al.^{9,14}, whereas pure Zr-UiO-66 was prepared as described in the work of Cavka et al.³ (SI, Section 1). Ce content in all compounds was determined by energy-dispersive X-ray spectroscopy (SI, Section 2 and Table S2). The mixed-metal samples will be referred to as CeXX in the discussion of the EXAFS results, XX being the fraction of Ce in the total metal content of the MOF (in mol. %) determined by EDX.

Synchrotron PXRD measurements for desolvated pure Zr-, pure Ce- and bimetallic Zr_{3.54}Ce_{2.46}-UiO-66 MOFs were performed at ID22 beamline of the European Synchrotron Radiation Facility (ESRF) to determine with high precision their structural parameters, further used as the initial guess for the EXAFS refinement.

As a general tendency, the peak width decreases upon incorporation of Ce into the structure, thus the narrowest peaks were observed in the PXRD patterns of Ce-UiO-66 while Zr-UiO-66 exhibited the broadest ones, indicating the progressive increase of crystallite size with the rise of Ce content. The patterns indicate no symmetry-forbidden additional peaks due to nano-regions containing correlated lattice defects with reo topology³⁰ and are in perfect agreement with the *Fm-3m* space group (Figures S1-3 and Table S3). Hence, both Ce and Zr atoms, as well as the cluster and/or linker vacancies for all the investigated samples are randomly distributed throughout the crystal. The occurrence of large domains with lower crystalline symmetry, as well as the formation of crystalline extra-phases, is thus ruled out. Concomitantly, TGA and BET measurements reported by Lammert et al.¹⁴ for analogous CeZr-UiO-66 MOFs evidenced that substitution of Zr with Ce is not accompanied by a significant rise of missing linker defects, resulting in a maximum of 1 missing linker per cornerstone. Thus, it is not the defects, but the local composition of the clusters that has the major influence on the EXAFS data discussed below.

Ce and Zr K-edge EXAFS as well as Ce L₃ XANES spectra were collected at BM31³¹ (Ce22, Ce45 and Ce84 and pure Ce and Zr UiO-66 MOFs) and BM23³² (Ce10 MOF) beamlines of ESRF, measuring as-prepared compounds at room temperature. Ce L₃-edge XANES data for all Ce-containing samples show the pure Ce(IV) phase (indicatively more than 95% of Ce content), confirming the success of the synthesis (Figure S4a). Differences between the XANES spectra of all MOFs at the three edges were minor, indicating that the electronic structure of neither Ce nor Zr species was significantly altered at different Ce:Zr ratios and excluding the possibility to draw structural conclusions from the in-depth XANES analysis (Figure S4).

Fourier-transformed Zr and Ce K-edge EXAFS data for all MOFs are shown in the Figure S6. Qualitatively the spectra are in agreement with those reported previously for Zr-UiO-66 MOFs^{4,33} and for Ce complexes with the geometry similar to the UiO-type cornerstones.³⁴ The shape of the peaks in 1.2-2.5 Å range, originating mainly from M-O scattering (M being Zr or Ce), does not change significantly upon the increase of Ce content, which evi-

dences rather small variations in O-coordination of Zr and Ce atoms. However, very pronounced changes are observed in the position and intensity of the second peak (2.8-3.8 Å), which appears due to the M-M scattering from the members of M₆ cornerstones (Figure 1b). It clearly indicates that the average values of M-M interatomic distances, as well as the corresponding disorder, depend on Ce:Zr ratio, which confirms the formation of mixed-metal Ce_xZr_{6-x} cornerstones.

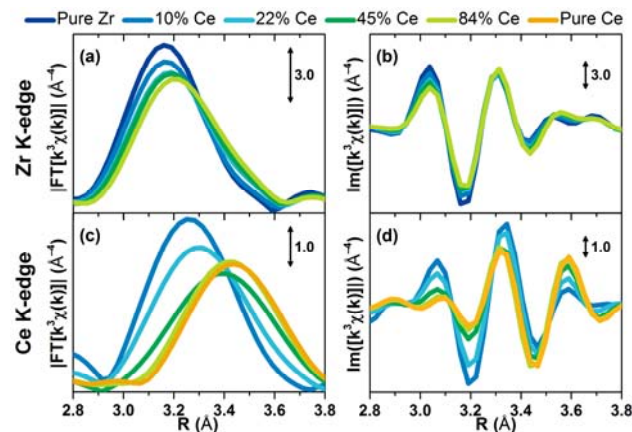


Figure 2 Closeup on the second shell peak in the modulus (a,c) and imaginary part (b,d) of phase-uncorrected Fourier transforms of k^3 -weighted EXAFS data collected at Zr (a,b) and Ce K-edges (c,d) for the pure and mixed-metal UiO-66 MOFs.

Figure 2a,c presents a closeup on the second EXAFS peak of all the studied MOFs, which simplifies a comparative rationalization of the data and allows to qualitatively explain the observed trends. Changes that take place upon introduction of Ce may be explained by assuming the preferential formation of CeZr₅ clusters, accompanied by pure Zr₆ or Ce₆ cornerstones in the proportion dictated by the total stoichiometry of the sample. This implies a coexistence of CeZr₅ and Zr₆ clusters for Ce contents lower than 17% (i.e. 1/6) and a mixture of CeZr₅ and Ce₆ for higher Ce loadings.

For the pure Zr MOF, the Zr-Zr distances in the cornerstones are highly homogeneous, leading to the maximum intensity of the Zr-Zr peak in the absence of static disorder. Upon the introduction of Ce, the formation of CeZr₅ clusters would cause progressive loss of intensity at Zr K-edge compared to the pure Zr MOF due to the splitting of the Zr-Zr coordination shell into Zr-Ce and Zr-Zr subshells with significantly different Zr-M distances, in agreement to the data for Ce10 and Ce22 samples (Figure 2a). The minimum should be reached at Ce content around 17%, when all of the cornerstones are represented by the CeZr₅ clusters. At the same time, at the Ce K-edge the intensity of the Ce-M peak would be at its maximum for low-Ce samples, since static and dynamic disorder of the Ce-Zr distances in the CeZr₅ clusters is expected to be quite low and comparable to the one of Zr-Zr in pure Zr clusters, while the Ce-Zr distance is likely to be shorter than the Ce-Ce one. For Ce loadings higher than 17%, the data evidence against the formation of mixed clusters with more than 1 Ce atom, but rather suggest that mainly pure Ce₆ cornerstones are formed from the excess of Ce, in addition to the CeZr₅ clusters. Indeed, that would explain the lack of major changes at the Zr K-edge between Ce22, Ce45 and Ce84 samples, since in such a case all the Zr atoms in the material would be present as a part of CeZr₅ cornerstones and it is only the abundance of such cornerstones that would change with the increase of Ce content, but not their composition. Concomitantly, pure Ce₆ clusters are expected to have longer and less homogenous Ce-Ce distances compared to Ce-Zr and Zr-Zr ones in Zr₆ and CeZr₅ clusters, resulting in a shift of the second EXAFS peak at Ce K-edge to higher R and a decrease of its intensity.

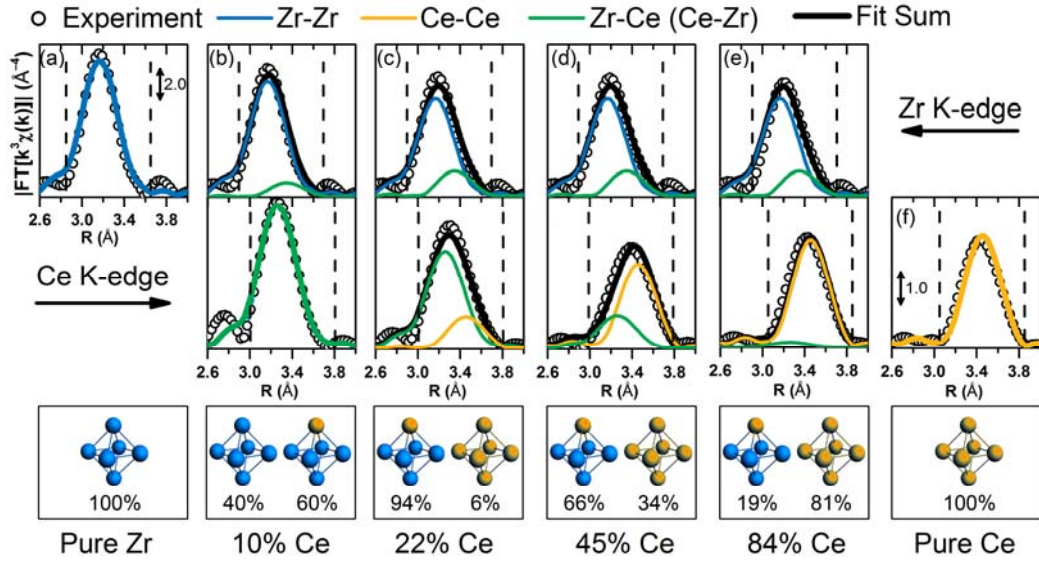


Figure 3 Results of the EXAFS fitting. Experimental data are shown as white circles, fitted curves are presented as full lines. Color code: Zr–Zr contribution – blue, Ce–Ce contribution – yellow, Zr–Ce and Ce–Zr contribution – green. For mixed-metal MOFs, the sum of the two contributions is shown in black. Bottom panels summarize the cornerstone composition employed for fitting the spectra of each sample.

Imaginary parts of the Ce K-edge EXAFS Fourier transforms (Figure 2d) indicate that it is the relative abundance of contributing Ce–Zr and Ce–Ce paths that changes at different Ce content rather than the lengths of these paths. Indeed, no shift of the oscillations is observed upon the increase of Ce content, but rather the redistribution of the intensity from $R = 3.1 \text{ \AA}$ region, where contribution of Ce–Zr scattering should be dominant, to $R = 3.6 \text{ \AA}$, where Ce–Ce signal is the strongest (given distances are not phase-corrected).

Table 1 Best-fit parameters obtained by combined EXAFS fitting of eight datasets at both Zr and Ce K-edges. M–M interatomic distances obtained from PXRD refinement are shown in parentheses.

Parameter	Value
R-factor	0.012
N_{ind}	63.1
N_{par}	11
S_0^2	1.0 ± 0.1
ΔE_{Ce} , eV	0.9 ± 1.1
ΔE_{Zr} , eV	0.6 ± 0.7
$R_{\text{Ce-Zr}}$, \AA	3.653 ± 0.004
$\sigma^2_{\text{Ce-Zr}}$, \AA^2	0.0050 ± 0.0002
$R_{\text{Ce-Ce}}$, \AA	3.784 ± 0.004 (3.78)
$\sigma^2_{\text{Ce-Ce}}$, \AA^2	0.0060 ± 0.0002
$R_{\text{Zr-Zr}}$, \AA	3.529 ± 0.003
$\sigma^2_{\text{Zr-Zr}}$, \AA^2	0.0050 ± 0.0002
R_{Zr6}	3.525 ± 0.003 (3.51)
σ^2_{Zr6} , \AA^2	0.0046 ± 0.0002

Hypothesis about the preferential formation of CeZr_5 cornerstones, put forward after the qualitative analysis of the EXAFS data was confirmed by quantitative EXAFS fitting at Zr and Ce K-edges. All ten EXAFS datasets (five at each edge) were fitted together, leading to the calculation of a global R-factor. Degeneracies of M–M paths for bimetallic MOFs were calculated from the ele-

mental composition data provided by EDX analysis assuming preferential formation of the CeZr_5 cornerstones (SI, Section 4.4). Results of the combined EXAFS fitting of ten independent datasets are shown in Figure 3, while the values of the obtained fitting parameters are reported in Table 1.

The fit shows excellent overall agreement with the experiment, especially given the large amount of data and a set of physical constraints applied during parametrization (see SI Section 4.4 for details). Obtained DW factors demonstrate that the extent of structural disorder depends on the composition of the cluster. The lowest DW factor $\sigma^2_{\text{Zr6}} = 0.0046 \text{ \AA}^2$ was obtained for the Zr-Zr path in pure Zr_6 cornerstones, which were expected to be the most rigid and ordered ones. Inclusion of one Ce atom in the cornerstone increases very slightly the inhomogeneity of the Zr–Zr and Zr–Ce distances, justifying the small rise of the corresponding DW factors to $\sigma^2_{\text{Zr-Zr}} = \sigma^2_{\text{Ce-Zr}} = 0.0050 \text{ \AA}^2$. Apart from the low values of the DW factors, rather low degree of disorder in metal-metal distances of both the Zr_6 and the CeZr_5 clusters is confirmed also by the presence of the peak at $R = 4.5\text{--}5 \text{ \AA}$ in the Zr K-edge EXAFS FT (see Figure S6a). This peak originates due to the scattering from the M atom, situated in the opposite vertex of the octahedron with respect to the absorbing atom (Figure 1b)^{45,35}. At the Ce K-edge EXAFS FT this peak is distinguishable from the noise only for Ce10 and Ce22 samples, where the majority of Ce atoms are part of CeZr_5 cornerstones, while in the MOFs with higher Ce content it is below the noise level, which implies higher disorder in Ce_6 clusters compared to Zr_6 and CeZr_5 ones. Concomitantly, the EXAFS fit results in DW factor $\sigma^2_{\text{Ce-Ce}} = 0.0060 \text{ \AA}^2$ for the Ce–Ce path, which is roughly 20 % higher compared to those for Zr–Zr and Zr–Ce pairs.

The preferential formation of CeZr_5 cornerstones explains the trends in the stability of bimetallic UiO-66 MOFs with different Ce content reported recently by Lammert et al.¹⁴ Indeed, while at low Ce loadings stability was decreasing linearly with the increase of Ce content, at around 20% it stabilized at the value observed for pure Ce–UiO-66 MOF. According to the current EXAFS analysis, this coincides with the disappearance of pure Zr_6 cornerstones, which, due to lower disorder and higher stability compared to Ce_6 and CeZr_5 cornerstones, increase the decomposition temperature of the material.

The preferential formation of CeZr_5 cornerstones over the other mixed-metal clusters is partially in line with the recent theoretical calculations of Trouselet et al.,³⁶ that show that as a general trend,

the mixing energy of the bimetallic cluster increases with the number of bimetallic edges. However, the mixing energy for all possible structure of Ce_xZr_{6-x} cornerstone was reported to be positive, suggesting that in principle the most favorable configuration for Ce/Zr-UiO-66 MOF would be the structure with only Zr_6 and Ce_6 cornerstones. Our DFT calculations also evidence that energetically the most favorable way to accommodate Ce atoms in the structure would be the formation of Ce_6 cornerstones (SI Section 5). In such case, though, the Ce and Zr K-edge EXAFS spectra at different Ce loadings would be identical, which is clearly not the case. Therefore, the formation of the MOF structure is likely to have more complex drivers, which might require the inclusion of additional factors (temperature, pressure, solvent effects) into the computational model to correctly account for them in the calculations. The high level of complexity of this challenging computational task highlights the value of the experimental methods for the determination of the composition of bimetallic MOFs.

To summarize, combined Ce and Zr K-edge EXAFS analysis demonstrates that in bimetallic Ce/Zr-UiO-66 MOFs mixed-metal $CeZr_5$ cornerstones coexist with pure Zr_6 (at Ce content lower than ca. 20%) and Ce_6 ones (at higher Ce content). The relative abundance of pure and bimetallic cornerstones is in both cases determined primarily by sample stoichiometry. Such observation serves as a first direct proof for the existence of mixed ZrCe cornerstones in the Ce/Zr-UiO-66 MOF and allows to explain the previously-reported non-trivial dependence of temperature stability of these MOFs on Ce content.

ASSOCIATED CONTENT

Supporting Information

The Supporting Information is available free of charge on the ACS Publications website.

Experimental and data analysis details (PDF)

AUTHOR INFORMATION

Corresponding Authors

*kirill.lomachenko@esrf.fr, carlo.lamberti@unito.it

Notes

The authors declare no competing financial interests.

ACKNOWLEDGMENT

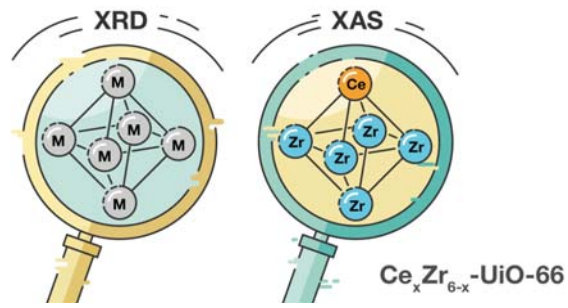
The authors are grateful to M. Brunelli, H. Emerich, W. van Beek, V. Dmitriev, O. Mathon and A. Fitch for the support during the experiments at BM31, BM23 and ID22 beamlines of the ESRF. We would like to thank B. Bueken, S. Smolders and A. Venier for the help with the XAS measurements, and H. Reinsch and N. Heidenreich for the assistance with PXRD experiment and data analysis. ALB acknowledges the grant of the Southern Federal University VnGr-07/2017-08.

REFERENCES

- (1) Yaghi, O. M.; O'Keeffe, M.; Ockwig, N. W.; Chae, H. K.; Eddaoudi, M.; Kim, J., *Nature* **2003**, *423*, 705.
- (2) Butova, V. V.; Soldatov, M. A.; Guda, A. A.; Lomachenko, K. A.; Lamberti, C., *Russ. Chem. Rev.* **2016**, *85*, 280-307.
- (3) Cavka, J. H.; Jakobsen, S.; Olsbye, U.; Guillou, N.; Lamberti, C.; Bordiga, S.; Lillerud, K. P., *J. Am. Chem. Soc.* **2008**, *130*, 13850-13851.
- (4) Valenzano, L.; Civalieri, B.; Chavan, S.; Bordiga, S.; Nilsen, M. H.; Jakobsen, S.; Lillerud, K. P.; Lamberti, C., *Chem. Mater.* **2011**, *23*, 1700-1718.
- (5) Chavan, S.; Vitillo, J. G.; Gianolio, D.; Zavorotynska, O.; Civalieri, B.; Jakobsen, S.; Nilsen, M. H.; Valenzano, L.; Lamberti, C.; Lillerud, K. P.; Bordiga, S., *Phys. Chem. Chem. Phys.* **2012**, *14*, 1614-1626.

- (6) Shearer, G. C.; Chavan, S.; Ethiraj, J.; Vitillo, J. G.; Svelle, S.; Olsbye, U.; Lamberti, C.; Bordiga, S.; Lillerud, K. P., *Chem. Mater.* **2014**, *26*, 4068-4071.
- (7) Øien, S.; Wragg, D.; Reinsch, H.; Svelle, S.; Bordiga, S.; Lamberti, C.; Lillerud, K. P., *Cryst. Growth Des.* **2014**, *14*, 5370-5372.
- (8) Montini, T.; Melchionna, M.; Monai, M.; Fornasiero, P., *Chem. Rev.* **2016**, *116*, 5987-6041.
- (9) Lammert, M.; Wharmby, M. T.; Smolders, S.; Bueken, B.; Lieb, A.; Lomachenko, K. A.; Vos, D. D.; Stock, N., *Chem. Commun.* **2015**, *51*, 12578-12581.
- (10) Dalapati, R.; Sakthivel, B.; Ghosalya, M. K.; Dhakshinamoorthy, A.; Biswas, S., *CrystEngComm* **2017**, *19*, 5915-5925.
- (11) Dalapati, R.; Sakthivel, B.; Dhakshinamoorthy, A.; Buragohain, A.; Bhunia, A.; Janiak, C.; Biswas, S., *CrystEngComm* **2016**, *18*, 7855-7864.
- (12) Buragohain, A.; Biswas, S., *CrystEngComm* **2016**, *18*, 4374-4381.
- (13) Smolders, S.; Lomachenko, K. A.; Bueken, B.; Struyf, A.; Bugaev, A. L.; Atzori, C.; Stock, N.; Lamberti, C.; Roefiaers, M. B. J.; De Vos, D. E., *ChemPhysChem* **2018**, *19*, 373-378.
- (14) Lammert, M.; Glibmann, C.; Stock, N., *Dalton Trans.* **2017**, *46*, 2425-2429.
- (15) Nouar, F.; Breeze, M. I.; Campo, B. C.; Vimont, A.; Clet, G.; Daturi, M.; Devic, T.; Walton, R. I.; Serre, C., *Chem. Commun.* **2015**, *51*, 14458-14461.
- (16) Ebrahim, A. M.; Bandoz, T. J., *ACS Appl. Mater. Interfaces* **2013**, *5*, 10565-10573.
- (17) Liu, Q.; Cong, H.; Deng, H., *J. Am. Chem. Soc.* **2016**, *138*, 13822-13825.
- (18) Lee, Y.; Kim, S.; Kang, J. K.; Cohen, S. M., *Chem. Commun.* **2015**, *51*, 5735-5738.
- (19) He, J.; Zhang, Y.; He, J.; Zeng, X.; Hou, X.; Long, Z., *Chem. Commun.* **2018**, *54*, 8610-8613.
- (20) Tu, J.; Zeng, X.; Xu, F.; Wu, X.; Tian, Y.; Hou, X.; Long, Z., *Chem. Commun.* **2017**, *53*, 3361-3364.
- (21) Szeto, K. C.; Lillerud, K. P.; Tilset, M.; Bjørgen, M.; Prestipino, C.; Zecchina, A.; Lamberti, C.; Bordiga, S., *J. Phys. Chem. B* **2006**, *110*, 21509-21520.
- (22) Szeto, K. C.; Prestipino, C.; Lamberti, C.; Zecchina, A.; Bordiga, S.; Bjørgen, M.; Tilset, M.; Lillerud, K. P., *Chem. Mater.* **2007**, *19*, 211-220.
- (23) Brozek, C. K.; Dincă, M., *J. Am. Chem. Soc.* **2013**, *135*, 12886-12891.
- (24) Brozek, C. K.; Dincă, M., *Chem. Soc. Rev.* **2014**, *43*, 5456-5467.
- (25) Vuong, G.-T.; Pham, M.-H.; Do, T.-O., *Dalton Trans.* **2013**, *42*, 550-557.
- (26) Stubbs, A. W.; Braglia, L.; Borfecchia, E.; Meyer, R. J.; Román-Leshkov, Y.; Lamberti, C.; Dincă, M., *ACS Catal.* **2018**, *8*, 596-601.
- (27) Butova, V. V.; Polyakov, V. A.; Budnyk, A. P.; Aboraia, A. M.; Bulanova, E. A.; Guda, A. A.; Reshetnikova, E. A.; Podkovyrina, Y. S.; Lamberti, C.; Soldatov, A. V., *Polyhedron* **2018**, *154*, 457-464.
- (28) Santaclara, J. G.; Olivos-Suarez, A. I.; Gonzalez-Nelson, A.; Osadchii, D.; Nasalevich, M. A.; van der Veen, M. A.; Kapteijn, F.; Sheveleva, A. M.; Veber, S. L.; Fedin, M. V.; Murray, A. T.; Hendon, C. H.; Walsh, A.; Gascon, J., *Chem. Mater.* **2017**, *29*, 8963-8967.
- (29) Kim, M.; Cahill, J. F.; Fei, H.; Prather, K. A.; Cohen, S. M., *J. Am. Chem. Soc.* **2012**, *134*, 18082-18088.
- (30) Cliffe, M. J.; Wan, W.; Zou, X.; Chater, P. A.; Kleppe, A. K.; Tucker, M. G.; Wilhelm, H.; Funnell, N. P.; Coudert, F.-X.; Goodwin, A. L., *Nat. Commun.* **2014**, *5*, 4176.
- (31) Abdala, P. M.; Safonova, O. V.; Wiker, G.; van Beek, W.; Emerich, H.; van Bokhoven, J. A.; Sá, J.; Szlachetko, J.; Nachttegaal, M., *CHIMIA* **2012**, *66*, 699-705.
- (32) Mathon, O.; Beteva, A.; Borrel, J.; Bugnazet, D.; Gatla, S.; Hino, R.; Kantor, I.; Mairs, T.; Munoz, M.; Pasternak, S.; Perrin, F.; Pascarelli, S., *J. Synchrotron Rad.* **2015**, *22*, 1548-1554.
- (33) Plonka, A. M.; Wang, Q.; Gordon, W. O.; Balboa, A.; Troya, D.; Guo, W.; Sharp, C. H.; Senanayake, S. D.; Morris, J. R.; Hill, C. L.; Frenkel, A. I., *J. Am. Chem. Soc.* **2017**, *139*, 599-602.
- (34) Hennig, C.; Ikeda-Ohno, A.; Kraus, W.; Weiss, S.; Pattison, P.; Emerich, H.; Abdala, P. M.; Scheinost, A. C., *Inorg. Chem.* **2013**, *52*, 11734-11743.
- (35) Jakobsen, S.; Gianolio, D.; Wragg, D. S.; Nilsen, M. H.; Emerich, H.; Bordiga, S.; Lamberti, C.; Olsbye, U.; Tilset, M.; Lillerud, K. P., *Phys. Rev. B* **2012**, *86*, 125429.
- (36) Trouselet, F.; Archereau, A.; Boutin, A.; Coudert, F.-X., *J. Phys. Chem. C* **2016**, *120*, 24885-24894.

Insert Table of Contents artwork here



Supporting information

Exact stoichiometry of $\text{Ce}_x\text{Zr}_{6-x}$ cornerstones in mixed-metal UiO-66 MOFs revealed by EXAFS spectroscopy

K.A. Lomachenko^{*,1}, J. Jacobsen², A.L. Bugaev³, C. Atzori⁴, F. Bonino⁴, S. Bordiga⁴, N. Stock² and C. Lamberti^{*,3,5}

¹European Synchrotron Radiation Facility, 71 Avenue des Martyrs, CS 40220, 38043 Grenoble Cedex 9, France

²Institut für Anorganische Chemie, Christian-Albrechts-Universität, Max-Eyth-Straße 2, D 24118 Kiel, Germany

³Smart Materials Research Institute, Southern Federal University, Sladkova 178/24, 344090 Rostov-on-Don, Russia

⁴Department of Chemistry, NIS interdepartmental Center and INSTM Reference Center, University of Turin, Via Quarello 15, 10135 Turin, Italy

⁵Department of Physics, INSTM Reference Center and CrisDi Interdepartmental Centre for Crystallography, University of Turin, Via P. Giuria 1, 10125 Turin Italy

1. Synthesis

Cerium (IV) ammonium nitrate (98 %, $(\text{NH}_4)_2\text{Ce}(\text{NO}_3)_6$, Alfa Aesar), 1,4- benzenedicarboxylic acid (98 %, H_2BDC , Sigma Aldrich), zirconyl nitrate monohydrate ($\text{ZrO}(\text{NO}_3)_2 \cdot \text{H}_2\text{O}$, ABCR), zirconium(IV) chloride (99 %, ZrCl_4 , Sigma Aldrich), N,N-dimethylformamide (99 %, DMF, Grüssing GmbH) and formic acid (100 %, HCOOH , BASF) were used as obtained.

The synthesis of the mixed-metal Ce/Zr-UiO-66 compounds was previously reported by Lammert et al.¹⁻² and this procedure was also used in the current study. The Ce/Zr-UiO-66 compounds were synthesized using Pyrex glass reaction tubes (maximum volume 14 mL). The linker 1,4-benzenedicarboxylic acid (H_2BDC , 127.6 mg) was dissolved in N,N-dimethylformamide (DMF, 3.6 mL) and transferred into the glass reactor. Subsequently the formic acid (HCOOH , 100 %, 1.03 mL) and finally the aqueous solutions of $(\text{NH}_4)_2\text{Ce}(\text{NO}_3)_6$ (0.533 mol/L) and $\text{ZrO}(\text{NO}_3)_2 \cdot \text{H}_2\text{O}$ (0.533 mol/L) were added in the desired stoichiometry (Table S1). The total volume of the two metal salt solutions was always 1.2 mL.

Table S1 Parameters for the synthesis of the pure Ce-UiO-66 and mixed-metal Ce/Zr-UiO-66 compounds.

Sample	Ratio				Ce [μ L]	Zr [μ L]	H ₂ BD C [mg]	DMF [mL]	HCOOH [μ L]
	Ce	Zr	H ₂ BDC	HCOOH					
Ce10	0.6	5.4	7.2	256	120	104	127.6	3.6	1.03
						0			
Ce22	2.0	4.0	7.2	256	400	800	127.6	3.6	1.03
Ce45	4.0	2.0	7.2	256	800	400	127.6	3.6	1.03
Ce84	5.5	0.5	7.2	256	1100	100	127.6	3.6	1.03
Ce-UiO-66	6.0	0.0	7.2	256	1200	0	127.6	3.6	1.03

The glass reactors were heated under stirring for 15 min at 100 °C using an aluminium heating block. After the synthesis the glass reactor was cooled down to room temperature and the precipitate was isolated by centrifugation. The mother liquor was decanted off and the MOF were re-dispersed and centrifuged two times in DMF (2 mL) and three times in acetone (2 mL). Finally, the MOF was dried in air at 70 °C.

Zr-UiO-66 was synthesized following the procedure reported by Cavka et al.³ Zirconium(IV) chloride (530 mg) and 1,4-benzenedicarboxylic acid (H₂BDC, 340 mg) were dissolved in N,N-dimethylformamide (DMF, 20 mL). This mixture was sealed in a steel autoclave and placed in an oven at 120 °C for 24 hours. After the synthesis the solvothermal reactor was cooled down to room temperature and the precipitate was centrifuged. The mother liquor was decanted off and the product was re-dispersed and centrifuged two times in DMF (5 mL) and three times in acetone (5 mL). Finally, the MOF was dried in air at 70 °C.

2. EDX spectroscopy

Ce/Zr ratio of the samples indicated in the samples' designations was determined by the energy-dispersive X-ray (EDX) spectroscopy. The data were recorded on a Philips XL30 FEG microscope for the samples in powder form, collecting EDX spectra in three different points to check the sample homogeneity. Obtained data are summarized in the Table S2.

Table S2 Ce content in the bimetallic CeZr-UiO-66 MOFs determined by EDX spectroscopy measured in three different points

Sample	Ce content, at%				Standard deviation, at %
	(1)	(2)	(3)	Mean	
Ce10	10.17	9.68	9.97	9.94	0.2
Ce22	21.53	21.93	22.51	21.99	0.40
Ce45	44.52	45.65	45.13	45.10	0.46
Ce84	83.65	84.22	83.65	83.84	0.27

3. PXRD

Powder X-ray diffraction (PXRD) measurements of the pure Ce-, pure Zr- and mixed-metal $Zr_{3.54}Ce_{2.46}$ -UiO-66 MOFs desolvated at 180 °C in vacuum were conducted at the high-resolution powder diffraction beamline of the European Synchrotron Radiation Facility (ID22).

For the refinements several ranges measured for the respective sample were summed up to one pattern (10 ranges for Ce and Zr and 9 ranges for the Ce/Zr mixed-metal MOF). The used wavelength was 0.31783 Å. The peak shape function was fitted with a Pseudo Voigt profile and the beamline set-up was modelled using the simple axial model. For the Rietveld refinements, performed up to $2\theta_{\max} = 32^\circ$ ($d_{\min} = 0.577$ Å) using TOPAS software,⁴ the respective published crystal structures of Zr- or Ce-UiO-66 were employed as starting point. In all refinements the cluster occupancy was set to 1 and the occupancy of the linker molecules was freely refined. For the mixed-metal MOF the metal ions were refined independently of each other and their summed occupancy was fixed to one. In all MOFs traces of electron density were observed by Fourier synthesis inside the pores and attributed to residual solvent molecules represented by partially occupied oxygen atoms which were freely refined. Distance restrains were applied for the C-O and C-C bonds and the O-O distance of the carboxylate group. Collected data and results of refinement are shown in Figure S1, Figure S2, Figure S3 and Table S 3. In all samples, all observed Bragg peaks belong to the UiO-66 phase and no crystalline impurity could be detected.

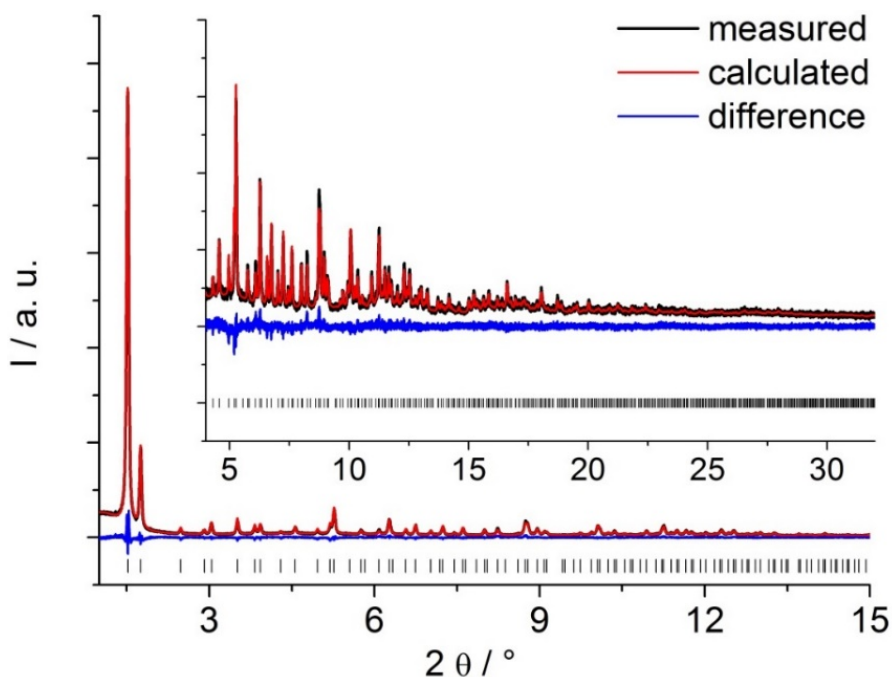


Figure S1 Final Rietveld plot for the refinement of Zr-UiO-66 ($\lambda = 0.31783$ Å). The black line shows the measured data, the red line shows the fit and the blue line is the difference curve. Vertical bars mark the allowed peak positions. The inset shows a magnification at higher angles.

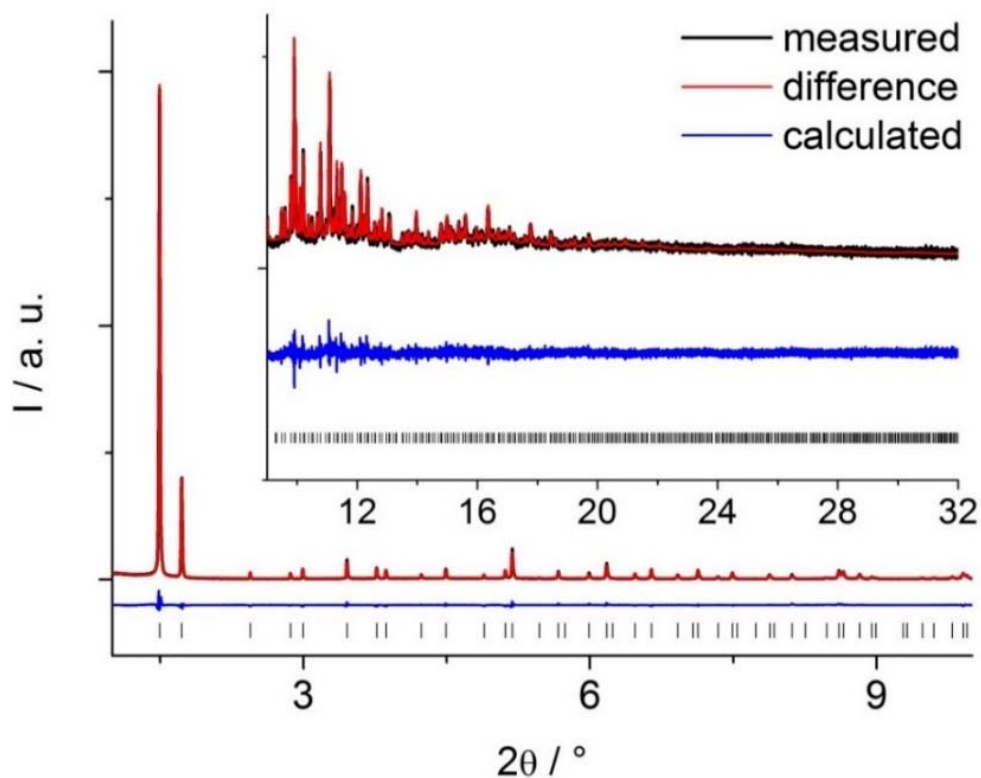


Figure S2 Final Rietveld plot for the refinement of $\text{Zr}_{3.54}\text{Ce}_{2.46}\text{-UiO-66}$ ($\lambda = 0.31783 \text{ \AA}$). The black line shows the measured data, the red line shows the fit and the blue line is the difference curve. Vertical bars mark the allowed peak positions. The inset shows a magnification at higher angles.

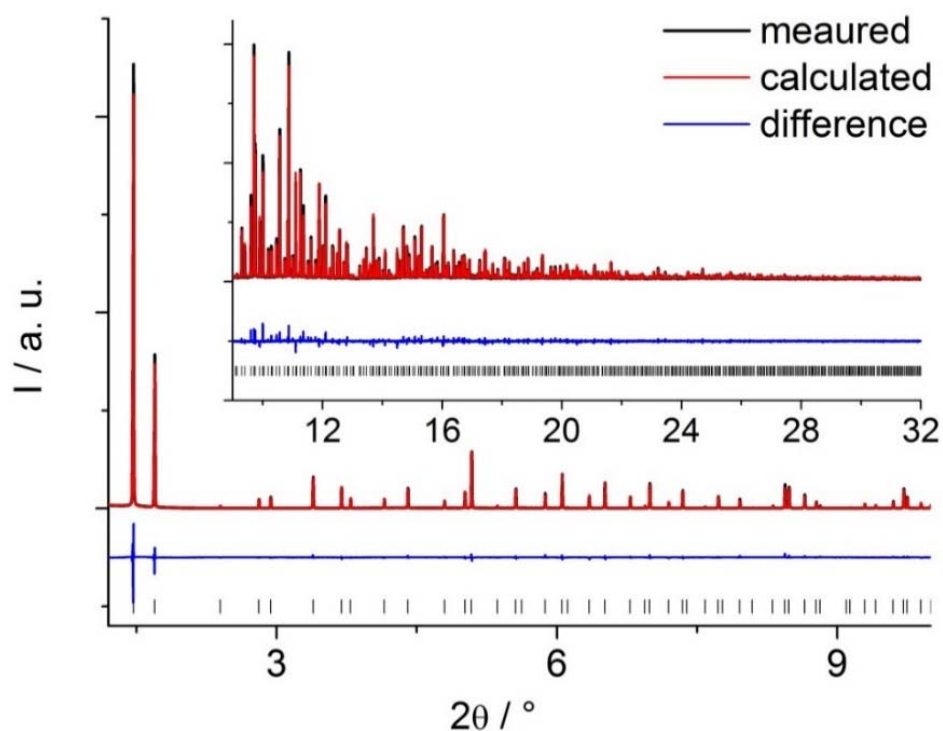


Figure S3 Final Rietveld plot for the refinement of Ce-UiO-66 ($\lambda = 0.31783 \text{ \AA}$). The black line shows the measured data, the red line shows the fit and the blue line is the difference curve. Vertical bars mark the allowed peak positions. The inset shows a magnification at higher angles.

Table S 3 Results of PXRD refinement for pure Ce- and Zr- and mixed-metal Ce/Zr-UiO-66 MOFs

Compound	Zr-UiO-66	Zr _{3.54} Ce _{2.46} -UiO-66	Ce-UiO-66
Crystal system	cubic	cubic	cubic
Space group	<i>Fm-3m</i>	<i>Fm-3m</i>	<i>Fm-3m</i>
$a = b = c$ [Å]	20.7535(2)	21.0652(1)	21.48825(2)
$\alpha = \beta = \gamma$ [°]	90	90	90
V [Å ³]	8938.75(26)	9347.52(14)	9922.09(2)
Metal:linker ratio (ideally 6:6)	6 : 5.5	6 : 5.9	6 : 5.7
Distance restraints	5	5	5
R _{WP} [%]	7.3	8.7	8.5
R _p [%]	5.7	6.3	6.9
R _{Bragg} [%]	2.7	3.0	2.4
GoF	4.9	6.5	7.8
M-M distance [Å] (M= Ce, Zr)	3.51	3.67	3.78

4. XAS

4.1 Experimental

All XAS measurements except for those for Ce10 sample were performed at BM31 beamline⁵ of European Synchrotron Radiation Facility (ESRF, Grenoble, France). The ring was operating in 7/8 multibunch mode with the current between 160 and 200 mA. All the measurements at BM31 were conducted in transmission mode using Si (111) double-crystal monochromator. Three ionization chambers were used for photon detection (30 cm long, 1 bar filling, 1 kV voltage). Gas mixtures used for filling the ionization chambers and resulting absorption values are given in Table S4.

Table S4 Filling the ionization chambers for the XAS experiments reported

Edge	Edge energy, eV	I0 mixture and resulting absorption at the edge	I1,2 mixture and resulting absorption at the edge
Ce L ₃ edge	5723	30% N ₂ in He (18 %)	10% Ar in He (70%)
Zr K-edge	17998	30% Ar in He (15 %)	10 % Kr in Ar (74%)
Ce K-edge	40 443	15% Kr in Ar (15%)	100% Kr (57%)

XAS spectra for Ce10 sample were collected at BM23 beamline⁶ of the ESRF. The experimental setup was similar to the one at BM31, except for the use of Si (311) monochromator for the measurements at Ce K-edge. The effect of higher resolution of Si (311) crystal compared to Si (111) was taken into account during the fitting of the EXAFS spectra of Ce10 sample, as described in the Section 4.4.

All MOFs were measured in the form of self-supporting pellets of 5 mm diameter, pressed using the pressure lower than 500 kgf/cm². The mass of MOF powder for sample preparation was optimized by XAFSmass software.⁷

4.2 XANES

Ce L₃ edge XANES data demonstrate, that Ce in all studied compounds is predominantly in Ce(IV) oxidation state (Figure S4a).

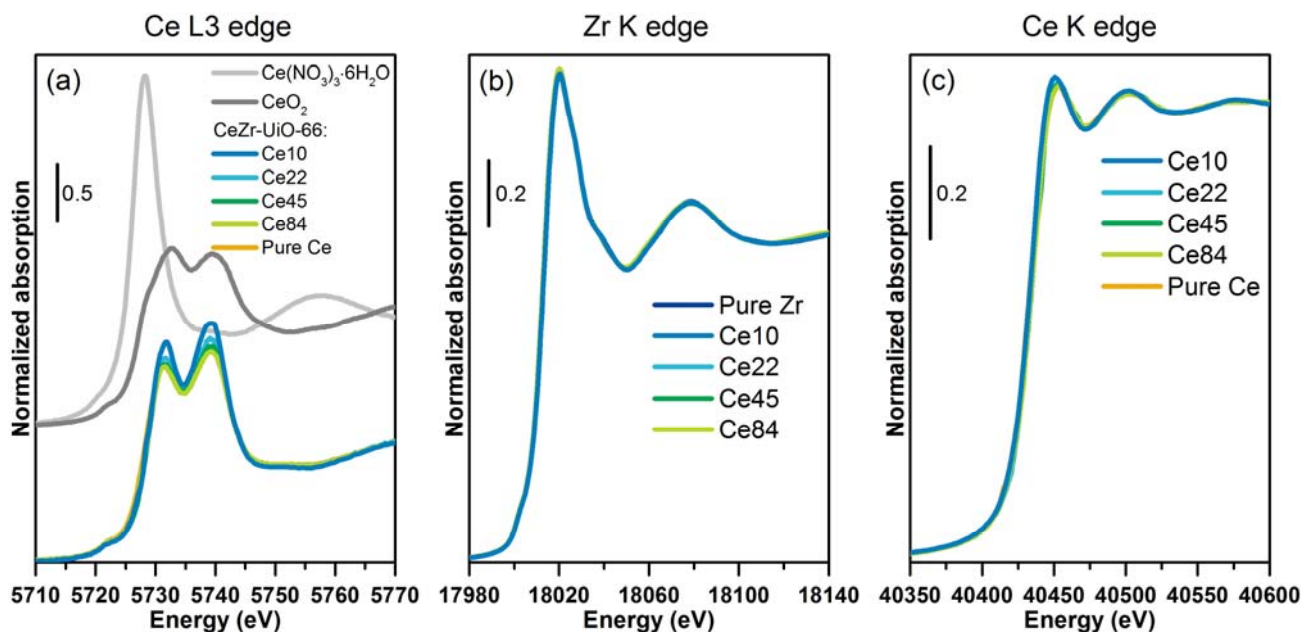


Figure S4 Ce L₃ (a), Zr K and Ce K-edge XANES spectra of bimetallic CeZr-UiO-66 MOFs compared to the spectra of pure Ce- and Zr-UiO-66 and (panel a) to the spectra of reference Ce (III) and Ce(IV) compounds

XANES spectra of pure and bimetallic MOFs are very similar at each of the three absorption edges, which confirms the similarity of local geometry and electronic structure of Zr and Ce centers in these MOFs at different Ce:Zr ratios, indicating that we are dealing with an isomorphous substitution of Ce in Zr sites and that no measurable extra phase is formed. This observation confirms the absence of the extra-phases, including the amorphous ones, generalizing thus the conclusion drawn using the XRD regarding the absence of crystalline extra-phases.

4.3 EXAFS data overview

XAFS data analysis was performed using Athena program for averaging and normalizing data and Artemis code for EXAFS fitting, both codes coming from Demeter package.⁸ The data quality was good, which allowed the EXAFS data collection up to $k=20 \text{ \AA}^{-1}$ at Ce and Zr K-edges for most samples, but in order to compare the data of different samples in the same range, the Fourier transform were performed in the $3.65\text{-}16.8 \text{ \AA}^{-1}$ (Zr K-edge) and $4\text{-}16.8 \text{ \AA}^{-1}$ range (Ce K-edge), limited by signal-to-noise ratio for the samples with the lowest concentration of Ce and Zr (Figure S5).

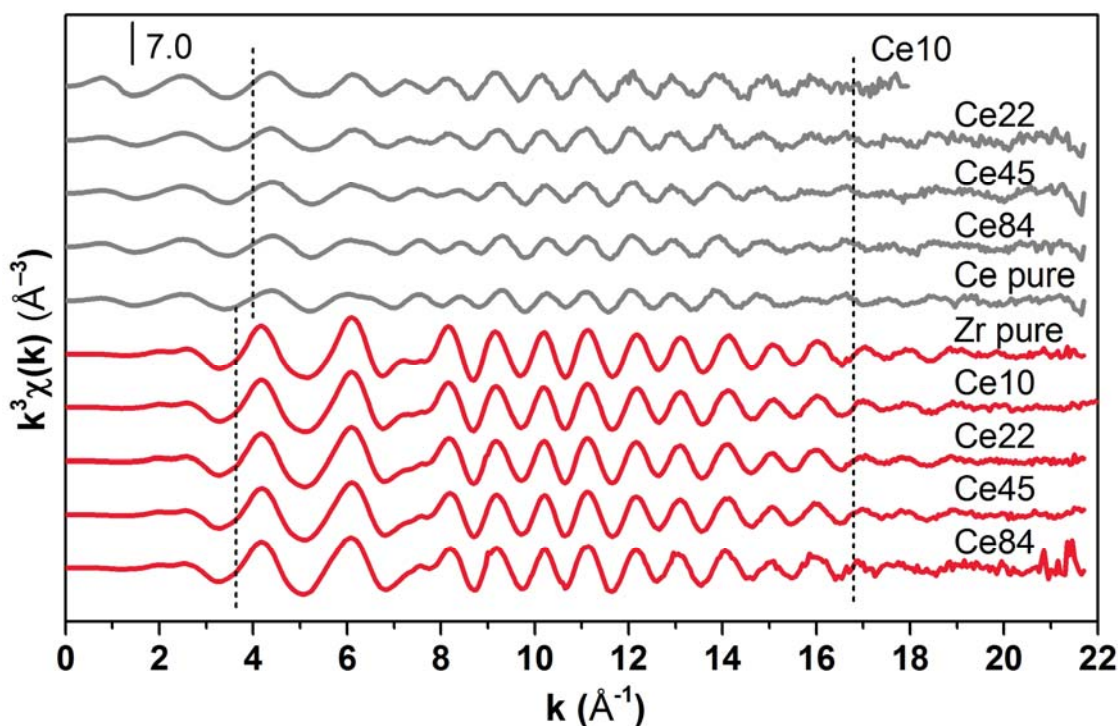


Figure S5 $k^3\chi(k)$ EXAFS data at Ce (gray) and Zr K-edges (red) for pure and bimetallic Ce/Zr-UiO-66 materials. Dashed lines indicate the regions used for the Fourier transform.

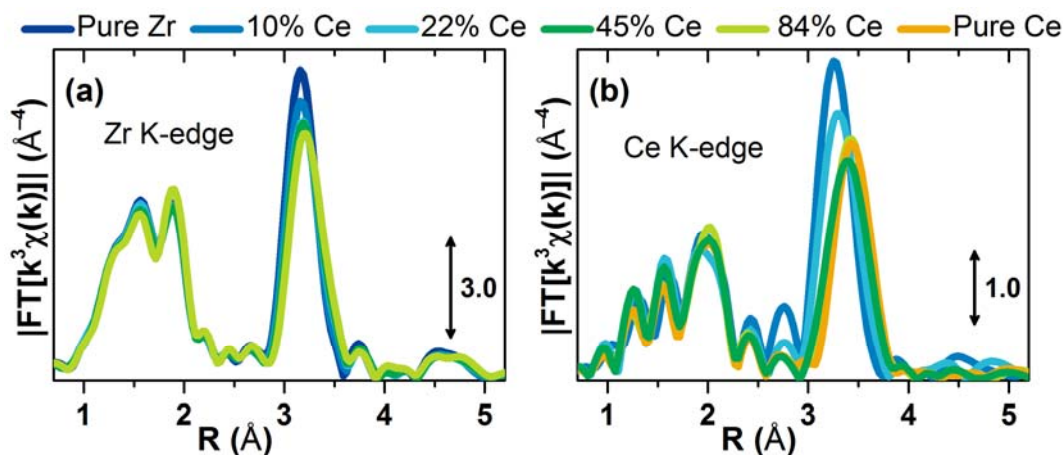


Figure S6 Moduli of the phase-uncorrected Fourier transforms of k^3 -weighted EXAFS data collected at (a) Zr K-edge and (b) Ce K-edge for UiO-66 MOFs with pure Zr-, pure Ce-, and mixed Ce/Zr cornerstones.

k^3 -weighted, Fourier-transformed Zr and Ce K-edge EXAFS data for all MOFs are shown in the Figure S6. Notably, the evolution of the second EXAFS peak is quite different between Zr and Ce K-edges. Indeed, for the case of Zr K-edge, its intensity is at maximum for the pure material. Upon introduction of 22% of Ce the peak decreases significantly and shifts to higher R. However, further increase of Ce fraction in the material has very little effect on both intensity and position of the maximum. Conversely, at the Ce K-edge the Ce–M peak is most intense for the Ce10 sample. Its intensity reaches a minimum for the Ce45 sample, and then stabilizes at an intermediate value for

the MOFs with the highest Ce-content. Gradual shift of the peak to the higher R values indicates that the increase of Ce content in the material leads to an elongation of the average Ce–M distance.

4.4 EXAFS fit parametrization

Structure and composition of cornerstones being the target, the fit was performed in R-space in the region where the signal from M–M scattering is dominant. Therefore, spectra of mixed-metal MOFs were fitted taking only M–M scattering paths into account. Initial values for interatomic Zr–Zr and Ce–Ce distances were taken from the refined PXRD data of the pure Zr and Ce MOFs respectively. For Zr–Ce and Ce–Zr paths the same initial distance as for Zr–Zr path was adopted. Based on the qualitative considerations discussed in the main text, degeneracies of the paths were calculated assuming that in the Ce22, Ce45 and Ce84 materials only CeZr₅ and Ce₆ clusters are present, while Ce10 MOF is built with CeZr₅ and Zr₆ ones. In all cases the total coordination number of the absorbing atom (Zr or Ce) was set to 4. Assuming such composition of the MOFs and using the total Ce/Zr ratio provided by EDX for each material, corresponding degeneracies of different M–M scattering paths, fraction of pure cornerstones as well as other parameters were calculated and presented in the Table S5. Notably, substantial deviation of the relative degeneracies of Ce–Ce and Ce–Zr paths from the molar Ce:Zr ratio can be observed for high-Ce materials. This is the case because each Ce₆ cornerstone contributes to the EXAFS data by 24 Ce–Ce scattering paths, in contrast to only four Ce–Zr paths from every CeZr₅ cluster, which leads to a very fast rise of the Ce–Ce contribution to the Ce K-edge EXAFS with the increase of Ce content. Degeneracies of the Ce–Ce and Ce–Zr paths, reported in Table S5 and calculated from purely stoichiometric considerations, were fixed during the EXAFS fitting, being the characteristic fingerprint of the adopted model.

Table S5 Stoichiometric parameters for mixed-metal MOFs calculated under assumption of preferential formation of CeZr₅ cornerstones.

Sample	Ce content, %	Zr content, %	Fraction of pure cornerstones*	Fraction of CeZr ₅ cornerstones	Ratio Ce-Ce/Ce-Zr paths	Degeneracy Ce-Ce path, Ce K-edge	Degeneracy Ce-Zr path, Ce K-edge	Degeneracy Zr-Zr path, Zr K-edge	Degeneracy Zr-Ce path, Zr K-edge
Ce10	10	90	0.4	0.6	0	0	4	3.56**	0.44
Ce22	22	78	0.064	0.936	0.41	1.16	2.84	3.2	0.8
Ce45	45	55	0.34	0.66	3.09	3.02	0.98	3.2	0.8
Ce84	84	16	0.808	0.192	25.25	3.85	0.15	3.2	0.8

* Pure cornerstones are Zr₆ for Ce10 and Ce₆ for Ce22, Ce45 and Ce84

** For Ce10 the Zr-Zr path was split into two, corresponding to Zr-Zr scattering in Zr₆ and CeZr₅ cornerstones. Degeneracy of each of these two sub-paths was set to 1.78 in the fit, proportional to the number of the Zr-Zr paths in the corresponding cornerstone weighted by abundance of the latter.

In order to decrease the number of parameters and increase the stability of the fit, the spectra of the Ce and Zr K-edges for pure Zr- and Ce–UiO-66 and mixed-metal Zr/Ce–UiO-66 MOFs were fitted together, sharing most of the fitting parameters. In particular, common amplitude reduction

factor S_0^2 was used for all the spectra, which is justified by the structural similarity of the studied compounds and confirmed by previously reported data for Zr and Ce K-edges of similar systems.⁹⁻
¹⁰ Then, since XANES spectra at the same edge are very similar for all compounds (Figure S4), only two energy shift parameters were used for the fitting: ΔE_{Ce} and ΔE_{Zr} for Ce and Zr K-edge, respectively. To maintain consistency of the results, the same interatomic distance and Debye Waller (DW) factor were assigned to the Zr–Ce paths at Zr K-edge and Ce–Zr paths at Ce K-edge. Analogously, the Ce–Ce distance and corresponding DW factor were constrained to be equal for Ce–Ce paths in mixed-metal and pure Ce MOFs, since within the adopted model these paths originate in both cases from pure Ce_6 cornerstones. This choice is also justified by the fact that when independent parameters for Ce–Ce distance and DW factor for the pure Ce MOF were introduced in the fit, the obtained values were within the errors from analogous parameters for mixed-metal compounds. Conversely, independent Zr–Zr distance and DW parameters were assigned to the Zr–Zr paths in the Zr_6 and $CeZr_5$ cornerstones. Notably, Zr–Zr contribution in the Ce10 sample was fitted with two different Zr–Zr scattering paths, since both Zr_6 and $CeZr_5$ clusters were expected to be present in the sample.

Since Ce K-edge data for Ce10 sample were measured with Si(311) monochromator in contrast to the Si(111) used for all other samples, a correction to the DW factor for Ce–Ce scattering path of Ce10 was introduced, to account for the higher resolution of the Si(311) crystal and therefore more intense peaks in the EXAFS FT. To estimate the value for the necessary correction, the EXAFS spectrum of pure Ce–UiO-66 was measured using both Si(111) and Si(311) crystals and fitted fixing the S_0^2 and ΔE_{Ce} parameters to the values obtained during the combined fitting of all the spectra except for those of Ce10. Obtained results are presented in the Figure S7.

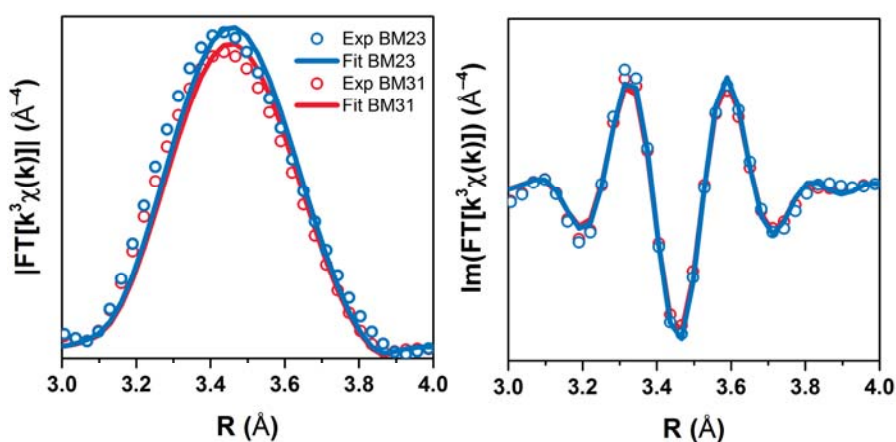


Figure S7 Results of the fitting of the EXAFS spectrum of pure Ce–UiO-66 MOF collected at BM31 and BM23 beamlines with Si (111) and Si (311) monochromators respectively.

While the difference in the obtained Ce–Ce distances was, as expected, negligible, the resulting difference in the DW factors for the two datasets was 0.0002 \AA^2 . This value was therefore used

to correct the DW factor for the Ce10 MOF during the global refinement, introducing the relation (S1)

$$\sigma_{\text{Ce-Zr}}^2(\text{Ce10}) = \sigma_{\text{Ce-Zr}}^2(\text{global}) - 0.0002 (\text{\AA}^2) \quad (\text{S1})$$

4.5 EXAFS fitting results

Under constraints described in the previous section all the parameters were freely varied during the simultaneous fit of all the ten datasets, resulting in the calculation of the global R-factor.

Fit results for all compounds are shown in Figure S8, Figure S9, Figure S10, Figure S11, and Figure S12

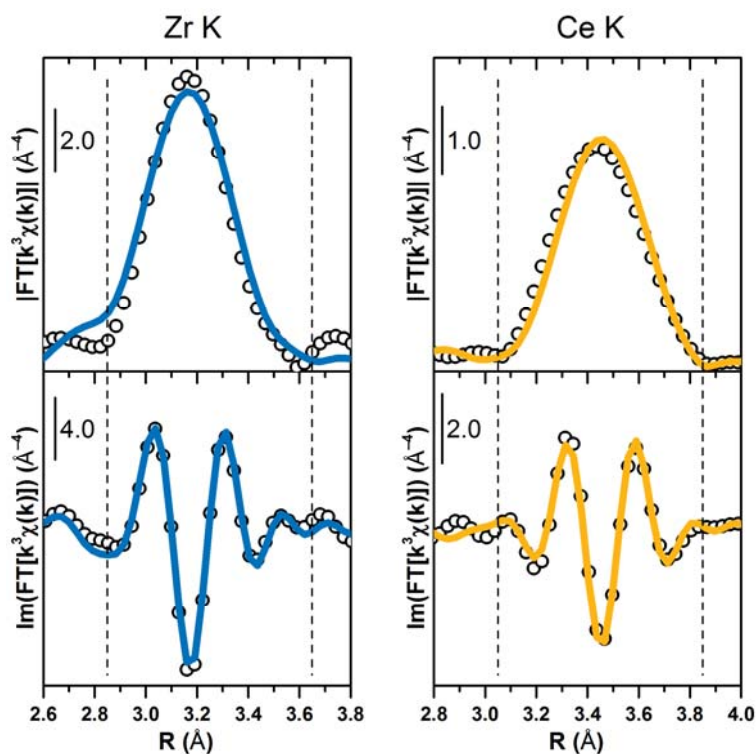


Figure S8 Results of the EXAFS fitting for pure Zr- and Ce-UiO-66 MOFs: experiment (circles) and fit (solid lines).

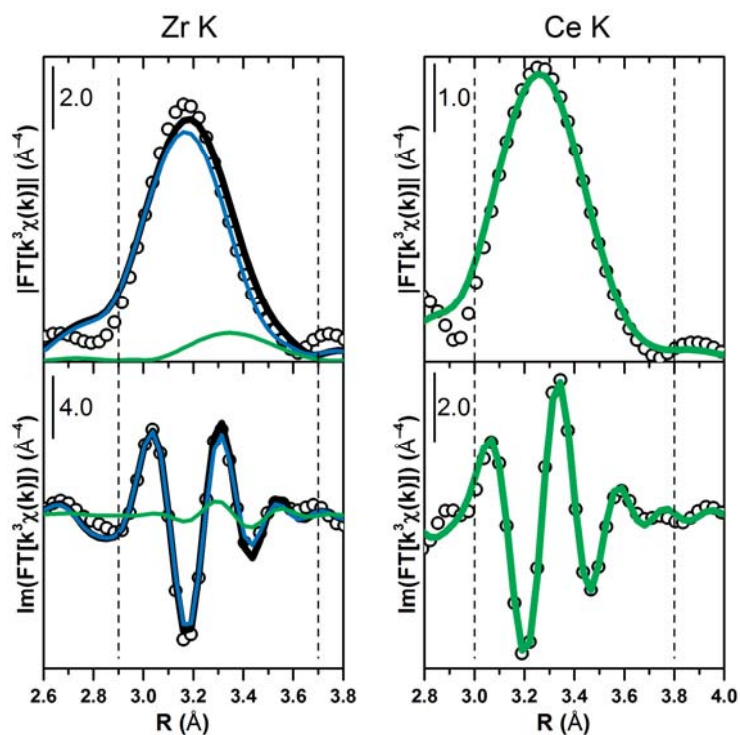


Figure S9 Results of the EXAFS fitting for Ce10 MOF: experiment (circles) and fit (black solid lines). Contribution to the fit from Zr-Zr and Zr-Ce (Ce-Zr) scattering is shown by blue and green lines respectively.

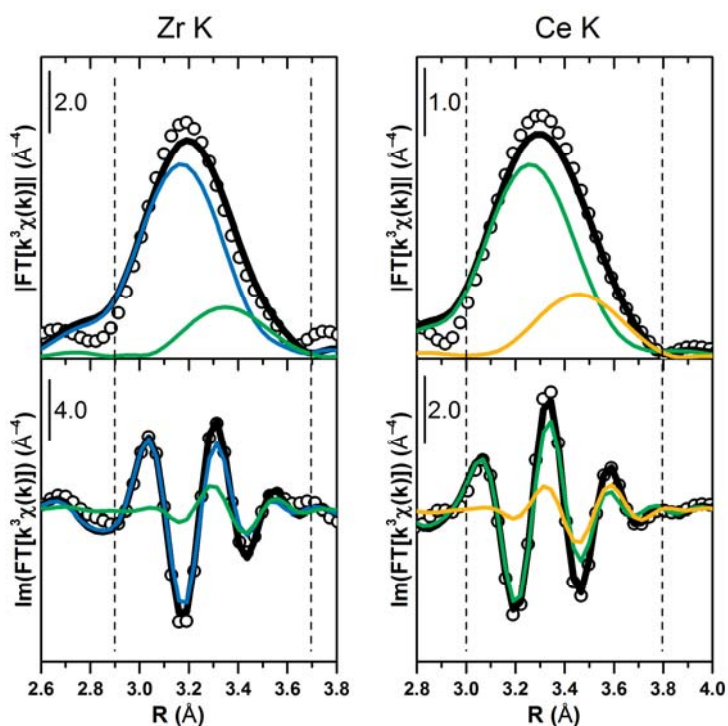


Figure S10 Results of the EXAFS fitting for Ce22 MOF: experiment (circles) and fit (black solid lines). Contribution to the fit from Zr-Zr, Ce-Ce and Zr-Ce (Ce-Zr) scattering is shown by blue, yellow and green lines respectively.

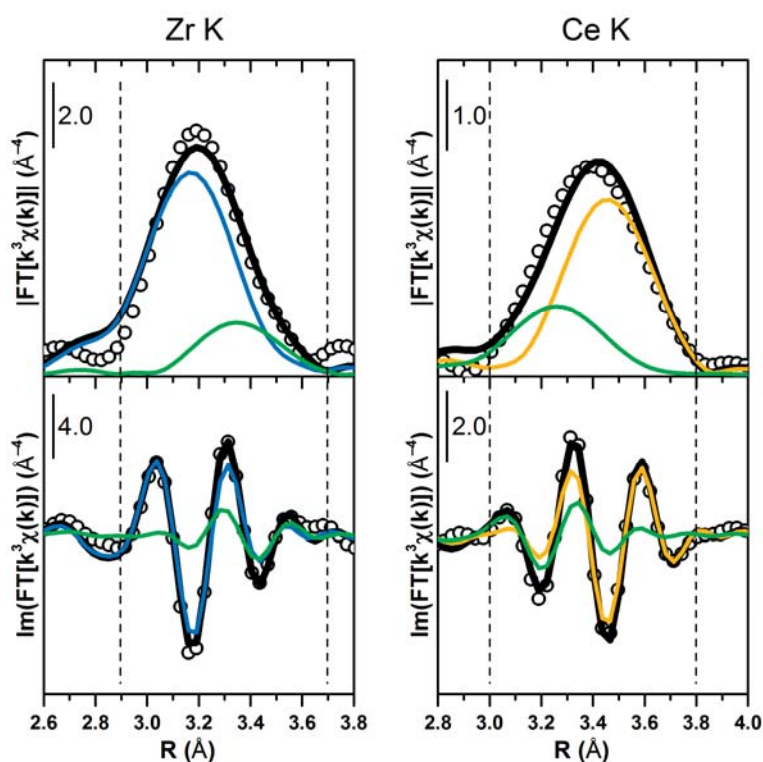


Figure S11 Results of the EXAFS fitting for Ce45 MOF: experiment (circles) and fit (black solid lines). Contribution to the fit from Zr-Zr, Ce-Ce and Zr-Ce (Ce-Zr) scattering is shown by blue, yellow and green lines respectively.

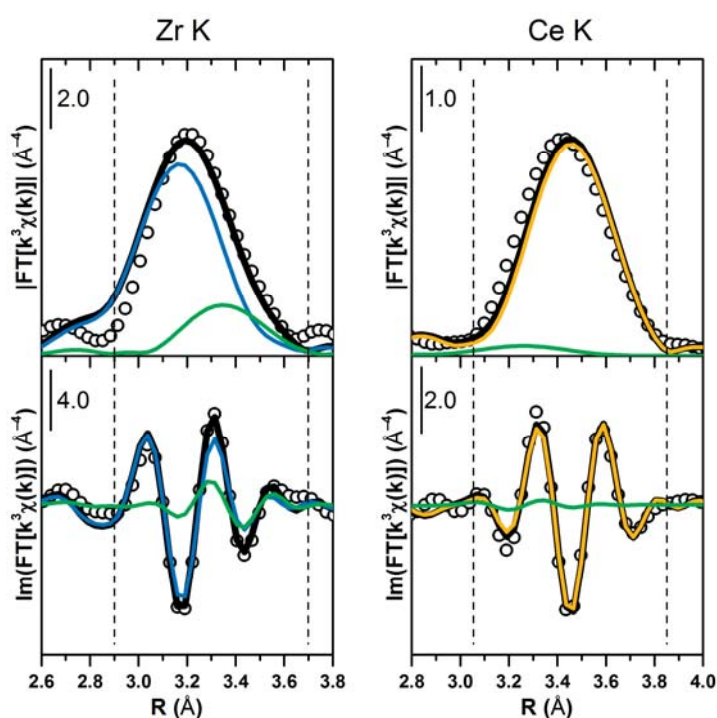


Figure S12 Results of the EXAFS fitting for Ce84 MOF: experiment (circles) and fit (black solid lines). Contribution to the fit from Zr-Zr, Ce-Ce and Zr-Ce (Ce-Zr) scattering is shown by blue, yellow and green lines respectively.

In order to assess the quality of each individual fit, the corresponding R-factors were calculated and presented in the Figure S13. For all the datasets the R-factors are quite low, the highest being 0.021 for the Zr K-edge of Ce84 MOF.

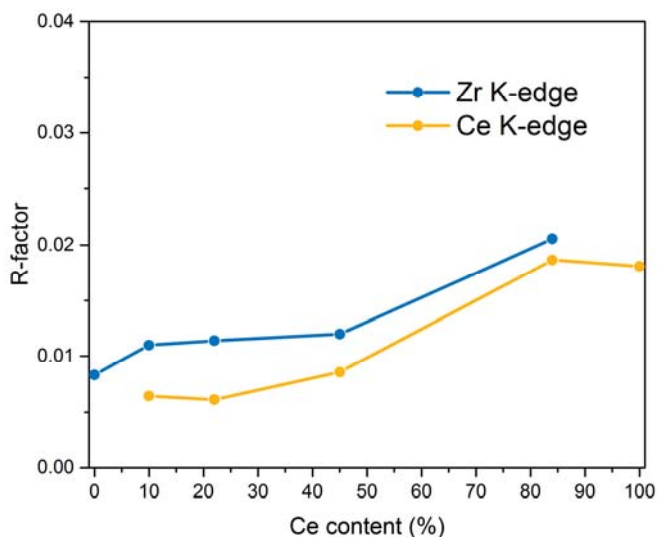


Figure S13 Individual R-factors obtained during the combined refinement of the ten datasets of pure and bimetallic Ce/Zr-UiO-66 MOFs.

5. DFT calculations

Stability of the M_6 cornerstone of UiO-66 MOF with different Ce/Zr ratio was assessed by means of DFT calculations performed in VASP 5.3 code.¹¹⁻¹³ The local environment of the cluster was truncated after the nearest carbons of the linkers, which were terminated by hydrogens to compensate for the unsaturated bonds. For each symmetry non-equivalent model of the bimetallic cluster geometry optimization was performed and the total energy was calculated. PBE exchange-correlation potential was used. The energy cutoff value of 400 eV was taken for the plane-wave basis set. All calculations were performed with one single k-point.

The energy cost of allocating one Ce atom as a part of a mixed cornerstone was calculated using the formula:

$$\Delta E_{\text{Ce}} = \frac{E - E_0}{N_{\text{Ce}}}$$

where E is the energy of the specific cluster, E_0 is the energy of pure Zr cluster and N_{Ce} is the number of Ce atoms in the specific cluster. The choice of such figure of merit was justified by the fact that the amount of Ce in the real MOF is always fixed by the synthesis stoichiometry, and the goal is to find the most energetically favorable way to distribute these Ce atoms among the cornerstones.

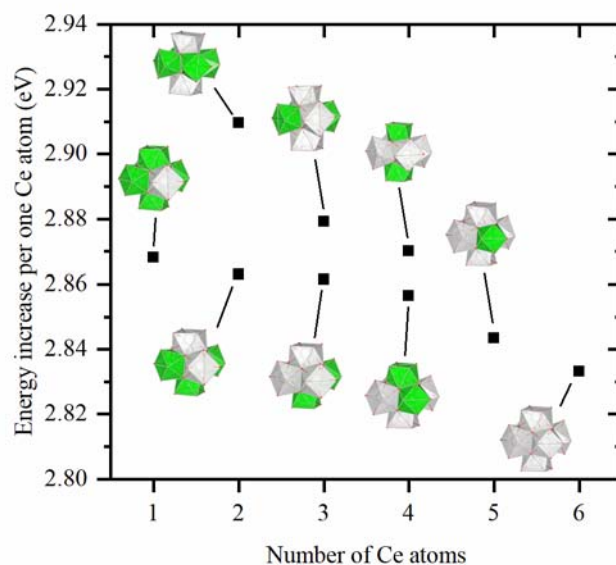


Figure S14 Allocation energies of one Ce atom in different cornerstones compared to the pure Zr_6 cluster

The results are reported in the Figure S14. In agreement with the findings of Trouselet et al,¹⁴ the energies of formation of the bimetallic clusters are positive, making this process energetically unfavorable (at $T = 0$ K and $P = 0$ Pa). The calculations show, that the most energy-efficient way to allocate the given amount of Ce atoms is the formation of Ce_6 cornerstones, that have the lowest energy increase per Ce atom.

Thus, within this computational model, only the Zr_6 and Ce_6 clusters should be expected in the mixed metal UiO-66 MOFs. However, that would lead to the absence of changes in the Ce and Zr K-edge EXAFS spectra of the MOFs with different Ce content. Since it is not the case in the experiment, more complex computational models might be required to properly describe the phenomena that drive the formation of bimetallic MOFs.

References

- (1) Lammert, M.; Wharmby, M. T.; Smolders, S.; Bueken, B.; Lieb, A.; Lomachenko, K. A.; Vos, D. D.; Stock, N., *Chem. Commun.* **2015**, *51*, 12578-12581.
- (2) Lammert, M.; Glißmann, C.; Stock, N., *Dalton Trans.* **2017**, *46*, 2425-2429.
- (3) Cavka, J. H.; Jakobsen, S.; Olsbye, U.; Guillou, N.; Lamberti, C.; Bordiga, S.; Lillerud, K. P., *J. Am. Chem. Soc.* **2008**, *130*, 13850-13851.
- (4) Coelho, A. *Topas Academics 4.2*, Coelho Software: Brisbane, Australia, 2007.
- (5) Abdala, P. M.; Safonova, O. V.; Wiker, G.; van Beek, W.; Emerich, H.; van Bokhoven, J. A.; Sá, J.; Szlachetko, J.; Nachttegaal, M., *CHIMIA* **2012**, *66*, 699-705.
- (6) Mathon, O.; Beteva, A.; Borrel, J.; Bugnazet, D.; Gatla, S.; Hino, R.; Kantor, I.; Mairs, T.; Munoz, M.; Pasternak, S.; Perrin, F.; Pascarelli, S., *J. Synchrotron Rad.* **2015**, *22*, 1548-1554.
- (7) Klementiev, K.; Chernikov, R., *J. Phys.: Conf. Ser.* **2016**, *712*, 012008.
- (8) Ravel, B.; Newville, M., *J. Synchrotron Rad.* **2005**, *12*, 537-541.
- (9) Smolders, S.; Lomachenko, K. A.; Bueken, B.; Struyf, A.; Bugaev, A. L.; Atzori, C.; Stock, N.; Lamberti, C.; Roeffaers, M. B. J.; De Vos, D. E., *ChemPhysChem* **2018**, *19*, 373-378.
- (10) Waitschat, S.; Fröhlich, D.; Reinsch, H.; Terraschke, H.; Lomachenko, K. A.; Lamberti, C.; Kummer, H.; Helling, T.; Baumgartner, M.; Henninger, S.; Stock, N., *Dalton Trans.* **2018**, *47*, 1062-1070.
- (11) Kresse, G.; Furthmüller, J., *Comput. Mater. Sci.* **1996**, *6*, 15-50.
- (12) Kresse, G.; Furthmüller, J., *Phys. Rev. B* **1996**, *54*, 11169-11186.
- (13) Kresse, G.; Joubert, D., *Phys. Rev. B* **1999**, *59*, 1758-1775.
- (14) Trouselet, F.; Archereau, A.; Boutin, A.; Coudert, F.-X., *J. Phys. Chem. C* **2016**, *120*, 24885-24894.

Appendix II

This appendix contains five papers:

Smolders S., Lomachenko K.A., Bueken B., Struyf A., Bugaev A.L., **Atzori C.**, Stock N., Lamberti C., Roeffaers M.B.J., De Vos D.E. “Unravelling the Redox-catalytic Behavior of Ce⁴⁺ Metal-Organic Frameworks by X-ray Absorption Spectroscopy”, *ChemPhysChem*, **2018**, 19, 373-378.

Atzori, C., Shearer, G.C., Maschio, L., Civalleri, B., Bonino, F., Lamberti, C., Svelle, S., Lillerud, K.P., Bordiga, S. “Effect of Benzoic Acid as a Modulator in the Structure of UiO-66: An Experimental and Computational Study”, *J. Phys. Chem. C*, **2017**, 121 (17), 9312-9324

Butova V.V., Budnyk, A.P., Guda, A.A., Lomachenko, K.A., Bugaev, A.L., Soldatov, A.V., Chavan, S.M., Oien-Odegaard, S., Olsbye, O., Lillerud K.P., **Atzori, C.**, Bordiga S., Lamberti C. “Modulator Effect in UiO-66-NDC (1,4-Naphthalenedicarboxylic Acid) Synthesis and Comparison with UiO-67-NDC Isorecticular Metal-Organic Frameworks”, *Cryst. Growth Des.*, **2017**, 2017 (10), 5422-5431

Masala A., Grifasi F., **Atzori C.**, Vitillo J.G., Mino L., Bonino F., Chierotti M.R., Bordiga S. “CO₂ Adsorption Sites in UTSA-16: Multitechnique Approach”, *J. Phys. Chem. C*, **2016**, 120 (22), 12068-12074

Kavoosi, N., Bon, V., Senkovska, I., Krause, S., **Atzori, C.**, Bonino, F., Pallmann, J., Paasch, S., Brunner E., Kaskel, S. “Tailoring adsorption induced phase transitions in the pillared-layer type metal-organic framework DUT-8(Ni)”, *Dalton Trans.*, **2017**, 46 (17), 4685-4695.

These papers concern topics not discussed in the present thesis but also part of my PhD activities.

Special
Issue

Unravelling the Redox-catalytic Behavior of Ce⁴⁺ Metal–Organic Frameworks by X-ray Absorption Spectroscopy

Simon Smolders,^[a] Kirill A. Lomachenko,^[b, c] Bart Bueken,^[a] Arnaud Struyf,^[a] Aram L. Bugaev,^[c, d] Cesare Atzori,^[d] Norbert Stock,^[e] Carlo Lamberti,^[c, d] Maarten B. J. Roeffaers,^[a] and Dirk E. De Vos^{*[a]}

The introduction of Ce⁴⁺ as a structural cation has been shown to be a promising route to redox active metal–organic frameworks (MOFs). However, the mechanism by which these MOFs act as redox catalysts remains unclear. Herein, we present a detailed study of the active site in [Ce₆O₄(OH)₄]-based MOFs such as Ce–UiO-66, involved in the aerobic oxidation of benzyl alcohol, chosen as a model redox reaction. X-ray absorption spectroscopy (XAS) data confirm the reduction of up to one Ce⁴⁺ ion per Ce₆ cluster with a corresponding outwards radial shift due to the larger radius of the Ce³⁺ cation, while not compromising the structural integrity of the framework, as evidenced by powder X-ray diffraction. This unambiguously demonstrates the involvement of the metal node in the catalytic cycle and explains the need for 2,2,6,6-tetramethyl-1-piperidinyloxy (TEMPO) as a redox mediator to bridge the gap between the one-electron oxidation of the Ce⁴⁺/Ce³⁺ couple and the two-electron alcohol oxidation. Finally, an improved catalytic system with Ce–MOF-808 and TEMPO was developed which outperformed all other tested Ce⁴⁺-MOFs.

Metal–organic frameworks (MOFs) are a class of porous crystalline materials constructed from inorganic nodes and organic linkers. Their modularity, high concentration of metal nodes,

well-defined porosity and exceptional surface area make MOFs particularly interesting for catalysis, gas sorption and separation.^[1–3] One of the most studied MOFs is UiO-66 ([M₆O₄(OH)₄(bdc)₆]; bdc = terephthalate; M = Zr⁴⁺, Hf⁴⁺, Ce⁴⁺), a thermally and chemically robust material built up from hexanuclear metal clusters which are 12-fold connected via terephthalate linkers.^[4–7] The catalytic performance of UiO-66, attributed to the Lewis acidic metal nodes, has been investigated numerous times.^[8–12] Among these, Ce–UiO-66 was reported to act as catalyst for the aerobic oxidation of benzyl alcohol.^[13]

Cerium is the cheapest and most abundant rare earth element and has been widely investigated for catalytic applications due to its remarkable redox behavior. It is the only lanthanide with a stable +IV oxidation state due to its vacant f-shell. Ce⁴⁺ is therefore a strong one-electron oxidant and cerium ammonium nitrate has found many applications as stoichiometric oxidant or homogeneous catalyst.^[14,15] CeO₂-containing heterogeneous catalysts are widely applied for the decomposition of NO_x and the oxidation of CO due to the excellent oxygen mobility and oxygen storage capacity of this oxide.^[16–18] Hence, CeO₂ particles are often designed as well-defined nano-objects with a focus on maximizing the reactive surface.^[19,20] Recently, Lammert et al. reported the synthesis of cerium analogues of several Zr-based MOFs, including UiO-66, containing carboxylate-capped [Ce₆O₄(OH)₄]¹²⁺ clusters.^[13,21–24] With respect to bulk CeO₂, the hexanuclear node in the Ce–UiO-66 framework could be considered as the smallest possible CeO₂ unit, with every Ce cation exposed to the micropores of the material.^[25] This expands the catalytic scope of the UiO-66 topology beyond the well-known acid-base activity to include redox reactions, as exemplified by the activity of Ce–UiO-66 in the aerobic oxidation of benzyl alcohol to benzaldehyde.^[13] Higher reaction rates were achieved with Ce–UiO-66 than with an equimolar amount of 15 nm CeO₂ nanoparticles. A redox mediator, TEMPO (2,2,6,6-tetramethyl-1-piperidinyloxy) was employed to couple the one-electron reduction of Ce⁴⁺ to Ce³⁺ with the two-electron alcohol oxidation.^[13,26]

The interest in Ce MOFs is mainly driven by their potential redox applicability; unraveling their redox behavior is therefore of great interest. Herein, we study the oxidation state of Ce and the geometry of the hexanuclear cluster in Ce⁴⁺-MOFs before and after reaction with TEMPO and benzyl alcohol, since no experimental evidence for the redox change in Ce–MOFs has been provided to date. For this, Ce–UiO-67 was chosen as catalyst, with 4,4'-biphenyldicarboxylate linkers lining the pores. The resulting large pores ensure that reaction

[a] S. Smolders, Dr. B. Bueken, A. Struyf, Prof. M. B. J. Roeffaers, Prof. D. E. De Vos
Centre for Surface Chemistry and Catalysis
Department of Microbial and Molecular Systems (M2S)
KU Leuven, Celestijnenlaan 200F P.O. box 2461
3001 Leuven (Belgium)
E-mail: dirk.devos@kuleuven.be

[b] Dr. K. A. Lomachenko
European Synchrotron Radiation Facility
71 avenue des Martyrs, CS 40220
38043 Grenoble Cedex 9 (France)

[c] Dr. K. A. Lomachenko, A. L. Bugaev, Prof. C. Lamberti
The Smart Materials Research Centre
Southern Federal University, Sladkova 174/28
344090 Rostov-on-Don (Russia)

[d] A. L. Bugaev, C. Atzori, Prof. C. Lamberti
Department of Chemistry, NIS and INSTM Reference Center
University of Turin, Via P. Giuria 7, 10125 Turin (Italy)

[e] Prof. N. Stock
Institut für Anorganische Chemie, Christian-Albrechts-Universität, Max-Eyth
Straße 2, 24118 Kiel (Germany)

Supporting Information and the ORCID identification number(s) for the author(s) of this article can be found under <https://doi.org/10.1002/cphc.201700967>.

An invited contribution to a Special Issue on Reactions in Confined Spaces

can take place in the crystal bulk and not only on the outer surface of the MOF-particles, thereby greatly increasing the number of active sites. The microenvironment around the catalytically active Ce cluster in Ce-UiO-67 is also identical to the one in the previously studied Ce-UiO-66. Ce-UiO-67 was subjected to a solution of 7.5 equiv. TEMPO and 50 equiv. benzyl alcohol in acetonitrile under inert atmosphere to reduce Ce to its +III oxidation state, while avoiding rapid reoxidation to Ce^{4+} .

X-ray absorption near edge structure (XANES) at the Ce L_3 - and Ce K-edge was performed to assess the average oxidation state of Ce throughout the whole structure (Figure 1). This type of analysis is very reliable, since XANES features of both Ce L_3 - and Ce K-edges are known to be mostly dependent on the average oxidation state of Ce atoms, being much less affected by the variations of local geometry. At the Ce L_3 -edge the shape of the spectrum changes dramatically upon transition from Ce^{3+} to Ce^{4+} : while a very sharp single peak is characteristic for the former, the white line of the latter consists of two well-separated maxima of much lower intensity. Spectral features at the Ce K-edge are significantly broader but Ce^{3+} and Ce^{4+} can still be easily distinguished because the edge energy for Ce^{3+} is around 5 eV lower than for Ce^{4+} . The relative concentration of Ce^{3+} in Ce-UiO-67 exposed to the TEMPO/benzyl alcohol mixture (Ce-UiO-67-red) was determined by making a linear combination of a Ce^{3+} -reference, $\text{Ce}(\text{NO}_3)_3 \cdot 6\text{H}_2\text{O}$, and a Ce^{4+} -MOF reference, Ce-UiO-66.^[13] No measurable Ce^{3+} was present before reaction (Figure S1) but after reduction by the TEMPO/benzyl alcohol mixture, the fraction of reduced Ce was calculated to be $19.4 \pm 0.2\%$ and $16.9 \pm 0.2\%$ at the Ce L_3 and the Ce K-edge, respectively (Figure 1, Table S1; the reported errors are of statistical origin; the intrinsic error associated to such XANES analyses is in the order of 5%).^[27] The best-fit curves are able to remarkably reproduce the experimental data, which is confirmed by the low R-factors (0.0013 at Ce L_3 and 0.0001 at Ce K-edge). The calculated Ce^{3+} -fraction corresponds to an average of approximately one Ce^{3+} ion per hexanuclear cluster (16.7%). This clearly demonstrates that Ce^{4+} -MOFs can accommodate valence

changes in the hexanuclear cluster, and hence catalyze redox reactions through the reduction of Ce^{4+} cations. The presence of on average one Ce^{3+} per cluster suggests a structural change that inhibits the reduction of a second cation. Investigating this modification cannot be done from powder X-ray diffraction (PXRD) data because such changes in the cluster are too subtle to accurately determine for porous materials filled with disordered solvent molecules.^[5] PXRD however confirmed the conservation of the long-range order in Ce-UiO-67-red (Figure S4).

The exact nature of the active site was therefore studied via extended X-ray absorption fine structure (EXAFS) of Ce-UiO-67-red and compared to the reference Ce-UiO-66, measured at the Ce K-edge (Figure 2a). The amplitude of the EXAFS oscillations was significantly damped compared to the reference, which resulted in lower intensity of the Ce-Ce peak in the Fourier transform (FT) (Figure 2b). To model the observed changes, a fit was carried out in the 3.0–3.9 Å region because the lower-R region had to be excluded due to the very strong contribution of the atomic X-ray absorption fine structure signal which interfered with the Ce-O first shell peaks.^[28,29] As a result, the FT shape at low R values is extremely sensitive to background subtraction parameters, which makes precise quantitative analysis very difficult. Conversely, the intensity and position of the Ce-Ce peak were virtually unaffected upon variation of the background spline, which made it a much more reliable indicator.

The EXAFS fit of the reference Ce-UiO-66 compound resulted in a perfect agreement with the geometry of unperturbed cluster with a Ce-Ce coordination number $N_{\text{Ce}} = 4$ (R-factor of 0.0063). The Ce-Ce distances agreed with the previously reported Ce-UiO-66 structure within 0.01 Å and meaningful values were obtained for both the Debye-Waller (DW) parameter ($\sigma_{\text{Ce1}}^2 = 0.006 \text{ \AA}^2$) and amplitude reduction factor ($S_0^2 = 0.98$).^[13] The Ce-Ce peak of Ce-UiO-67-red was however significantly dampened so several models were tested to investigate the origin of the intensity decrease.

First, a fit with fixed N_{Ce} and S_0^2 , obtained from Ce-UiO-66, was performed to test whether the reduced intensity is due to

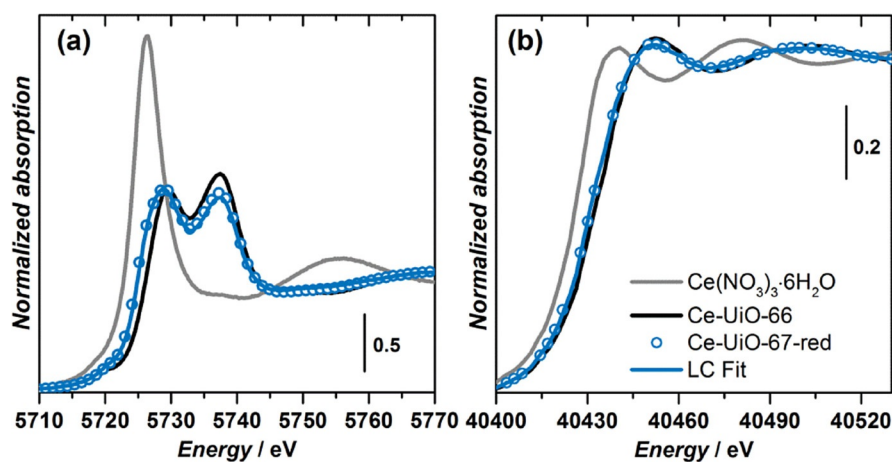


Figure 1. Experimental Ce L_3 -edge (a) and Ce K-edge (b) XANES spectra of Ce-UiO-67-red; results of linear combination fitting performed using the spectra of Ce-UiO-66 and Ce^{3+} nitrate as standards.

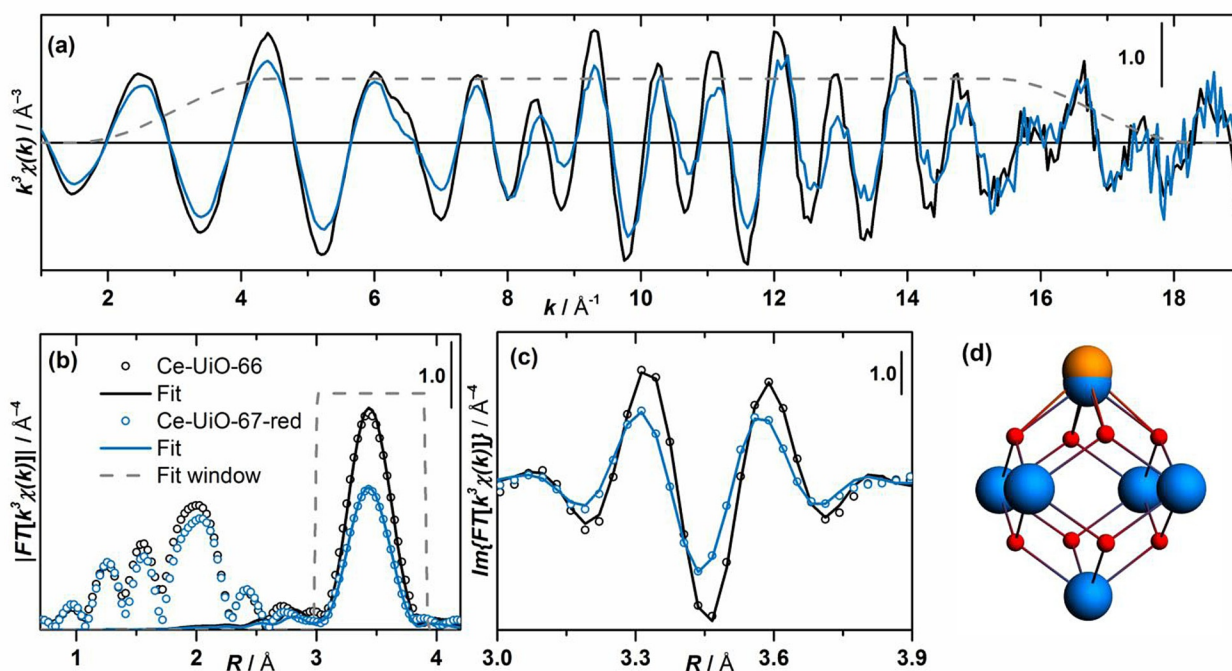


Figure 2. k^3 -weighted phase-uncorrected Ce K-edge EXAFS with the Fourier-transform window function (a) and its moduli (b) and imaginary parts (c) for Ce-UiO-66 and Ce-UiO-67-red together with their corresponding fits. For Ce-UiO-67-red the results of the Fit 4 are shown. The range in the panel (c) corresponds to the fitting window (3.0–3.9 Å) shown in the panel (b). Panel (d) schematically illustrates the distortion of the Ce-UiO-67-red cornerstone suggested by Fit 3 (color code: O—red, Ce—blue, perturbed Ce—orange).

an increased uniform (static or dynamic) disorder, which would be reflected by a higher DW value. As expected, the fit resulted in a higher DW factor ($\sigma_{\text{Ce1}}^2 = 0.0075 \text{ \AA}^2$), but the corresponding large R-factor (0.0310) indicated that the observed damping cannot be explained by a uniform increase of disorder (Fit 1 in Table 1). To simulate anisotropic disorder, expected due to the presence of a Ce^{3+} inside the Ce_6 -octahedron, one Ce atom was translated along the octahedron diagonal (Figure 2d). This implies that the 12 Ce–Ce edges of the octahedron are no longer equivalent, but split into 4 long ones and 8 short ones. This model is parametrized in the EXAFS fit by introducing two different Ce–Ce distances with coordination numbers fixed to $N_{\text{Ce1}} = 2.67$ and $N_{\text{Ce2}} = 1.33$. Both DW factors

$\sigma_{\text{Ce1}}^2 = \sigma_{\text{Ce2}}^2$ were fixed to the value obtained from Ce-UiO-66. As expected, the fit resulted in two significantly different Ce–Ce distances, causing the decrease of the EXAFS peak. The R-factor (0.0301) remained however virtually unchanged, which indicated that the quality of the fit was not improved (Fit 2 in Table 1). Repeating this fit with free DW parameters resulted in a strongly decreased R-factor (0.0041) indicating a nearly perfect mathematical fit (Fit 3 in Table 1). However, careful examination of the obtained parameters reveals that, while a short Ce–Ce path was not significantly perturbed, the second path was elongated by 0.3 Å and its DW factor increased to $\sigma_{\text{Ce2}}^2 = 0.014 \text{ \AA}^2$, which led to an important decrease of the longer path contribution to the examined spectral region. Such numbers

are a clear indication that the fitted peak mainly originates from a single Ce–Ce path with a distance close to the reference and a degeneracy significantly lower than 4. Consequently, in Fit 4, only one Ce–Ce path was considered, but the corresponding coordination number, Ce–Ce distance and DW factor were fitted simultaneously. This resulted in a low R-factor (0.0075), close to the one for the unperturbed Ce-UiO-66, and R_{Ce1} and σ_{Ce1}^2 values that closely match the reference ones. The obtained coordination number ($N_{\text{Ce}} = 2.58$) is very close to the theoretical value of 2.67, which corresponds to the situation where upon interaction with TEMPO

Table 1. Fitting parameters for the Ce K-edge EXAFS spectra of Ce-UiO-66 and Ce-UiO-67-red.

	Ce-UiO-66		Ce-UiO-67-red		
		Fit 1	Fit 2	Fit 3	Fit 4
Fit number	-	Fit 1	Fit 2	Fit 3	Fit 4
Fitting parameters	4	3	3	5	4
S_0^2	0.98 ± 0.13	0.98	0.98	0.98	0.98
$\Delta E / \text{eV}$	-2 ± 1	0 ± 2	2 ± 2	-1 ± 2	0 ± 1
N_{Ce1}	4	4	2.67	2.67	2.58 ± 0.37
$R_{\text{Ce1}} / \text{\AA}$	3.779 ± 0.005	3.771 ± 0.009	3.755 ± 0.009	3.765 ± 0.006	3.768 ± 0.005
$\sigma_{\text{Ce1}}^2 / \text{\AA}^2$	0.0059 ± 0.0004	0.0075 ± 0.0003	0.0059	0.0062 ± 0.0002	0.0060 ± 0.0005
N_{Ce2}	-	-	1.33	1.33	-
$R_{\text{Ce2}} / \text{\AA}$	-	-	3.838 ± 0.013	4.078 ± 0.051	-
$\sigma_{\text{Ce2}}^2 / \text{\AA}^2$	-	-	0.0059	0.0144 ± 0.005	-
R-factor	0.0063	0.0310	0.0301	0.0041	0.0075
Fitting range in k: 4.0–16.8 \AA^{-1} ; fitting range in R: 3.0–3.9 \AA ; independent points: 7.22					

one of the Ce atoms is significantly shifted from its original position, so its contribution to the regarded EXAFS spectrum becomes very weak. This conclusion is in agreement with the Ce K-edge and Ce L₃-edge XANES data, which indicate that roughly one Ce atom per cornerstone is reduced to Ce³⁺, which is probably a concomitant effect for the displacement of one Ce atom caused by the reaction with TEMPO and benzyl alcohol. The combined XANES and EXAFS results imply that the originally perfect Ce₆-octahedron is turned into a rigid Ce₅ square pyramid formed by Ce⁴⁺ ions, while the sixth Ce ion gets reduced to Ce³⁺ and lifted above the equatorial plane with an increased disorder of both static and dynamic origin (Figure 2d).

Such an important distortion of the Ce₆-cluster is not unlikely since previous EXAFS and PDF experiments on the analogous Zr₆ cluster in UiO-66 already showed that the cluster can be reversibly distorted to a comparable extent upon external stimuli.^[5,30] A similar distortion was also reported in partially reduced ceria nanoparticles and results from the larger ionic radius of Ce³⁺ (1.03 Å vs. 0.92 Å for Ce⁴⁺).^[31,32]

A reaction mechanism for the Ce-mediated alcohol oxidation is proposed based on the presence of Ce³⁺ upon exposure to reactants under inert atmosphere (Figure 3). First, one Ce⁴⁺ in the cluster oxidizes TEMPO to its oxoammonium cation (step a), being reduced itself to Ce³⁺. The slightly distorted Ce³⁺-containing cluster is then regenerated by molecular oxygen, thereby closing the Ce cycle. The possible reduction of a second Ce ion in the same cluster is implausible based on the XAS data since only 1/6th of the Ce ions were reduced after 7 h under inert atmosphere, while multiple turnovers were observed for Ce-UiO-66 during the same reaction under oxygen.^[13] The oxoammonium cation further reacts with benzyl alcohol to selectively form benzaldehyde while it is reduced to TEMPOH (2,2,6,6-tetramethyl-1-hydroxypiperidine) (step b). The selective oxidation of benzyl alcohol by the oxoammonium cation is often described in literature and the

presence of this cation was already reported previously when the reaction was conducted with Ce-UiO-66 under inert atmosphere; a low conversion of benzyl alcohol as well as the detection of TEMPOH pointed towards the oxoammonium cation as an intermediate.^[13,33–35] A proton is released during the oxidation of benzyl alcohol and it is hypothesized that it protonates a μ₃-O on the cluster to balance the excess negative charge when one Ce⁴⁺ is reduced to Ce³⁺. Charge compensation could also occur through protonation and subsequent detachment of a linker but no evidence for this could be found in the IR spectra (Figure S6). Finally, TEMPOH is swiftly regenerated by molecular oxygen to the initial TEMPO radical (step c), thereby closing the TEMPO cycle. Steps (b) and (c) are known to be much faster than step (a) since numerous catalyst systems involving these two reactions have been described with a much higher rate than reported for Ce-UiO-66.^[26,36,37] Therefore, the overall activity could be increased by improving the oxoammonium formation rate (step a).

The reaction rate of the TEMPO oxidation strongly depends on the accessibility of Ce in the cluster. The pore aperture of Ce⁴⁺-MOFs should therefore be sufficiently large to allow diffusion of TEMPO through their pore network. In addition, there should be open coordination sites available on the cluster to interact with incoming reactants, which directly implies that the (average) number of linkers surrounding each cluster should be lower than the maximum twelve. A clear illustration of the effect of node connectivity on catalytic performance of analogous Zr-MOFs can be found in the work of Farha et al.^[38] Besides UiO-66, which contains 12-connected clusters (in the absence of defects), NU-1000 and MOF-808, bearing, respectively eight-fold and six-fold coordinated clusters, were compared for their catalytic activity in the hydrolysis of dimethyl 4-nitrophenyl phosphate, a nerve-agent simulant. The reported turnover frequencies of 0.004 s⁻¹, 0.09 s⁻¹ and > 1.4 s⁻¹ respectively for UiO-66, NU-1000 and MOF-808, clearly indicate the benefit of low-coordinated clusters on catalytic activity.^[38]

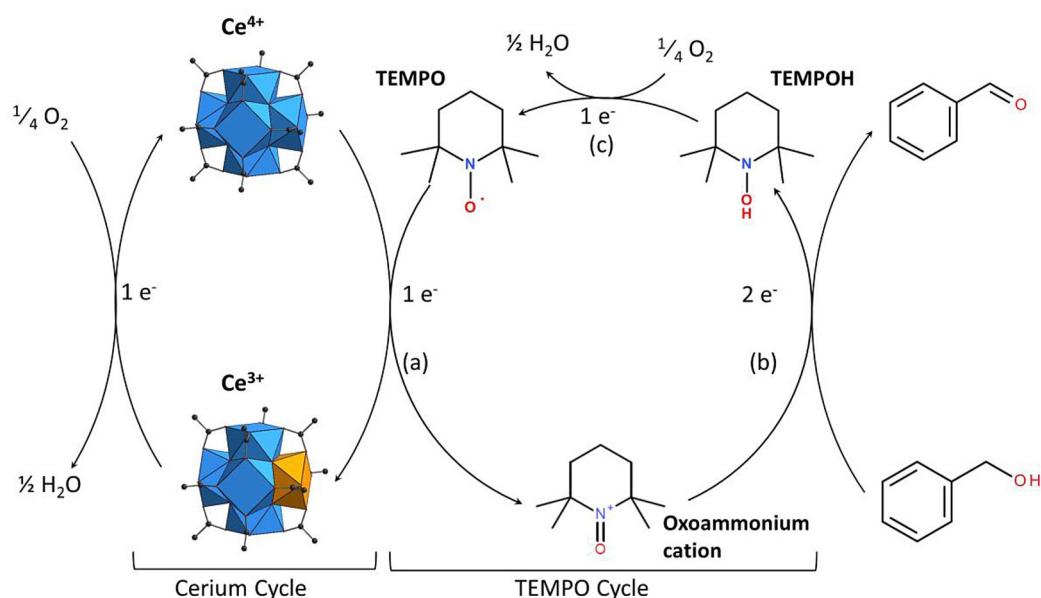


Figure 3. Proposed reaction mechanism for the aerobic TEMPO-mediated oxidation of benzyl alcohol by Ce⁴⁺-MOFs.

While previous work demonstrated the activity of Ce-UiO-66 and Ce-UiO-66-ndc (ndc = 2,6-naphthalenedicarboxylate) in aerobic alcohol oxidations, the reaction rate was limited by pore size and the number of open sites originating from missing linker defects.^[13] Here, we report an improved catalytic activity for the TEMPO-mediated aerobic oxidation of benzyl alcohol by replacing Ce-UiO-66 with Ce-MOF-808 ($[\text{Ce}_6\text{O}_4(\text{OH})_4(\text{btc})_2(\text{OH})_6]$; btc = trimesate), a large-pore MOF with the lowest connectivity of all known MOFs based on the same M_6 -clusters ($M = \text{Zr}, \text{Hf}, \text{Ce}$).^[21,22,39,40]

The activity of Ce-MOF-808 was tested under reaction conditions identical to those of the oxidation of benzyl alcohol by Ce-UiO-66.^[13] The activation procedure of Ce-MOF-808 was adapted to its lower thermal stability, that is, the activation temperature was decreased to 100 °C and vacuum was applied to ensure complete evacuation of the pores.^[22] The resulting Ce-MOF-808 outperformed all previously tested Ce^{4+} -MOFs (Table 2). After seven hours, Ce-MOF-808 converted 97 % of the

Catalyst	Activation temperature [°C]	Conversion [%]
Ce-UiO-66 ^[13]	180	29
Ce-UiO-66-NDC ^[13]	180	80
Ce-MOF-808	100	97

6 bar O_2 , 110 °C, 7 h, CH_3CN , 10 mol% Ce, 30 mol% TEMPO

benzyl alcohol, which is much higher than the previously reported Ce-UiO-66 (29%) and Ce-UiO-66-ndc (80%).^[13] The improved activity is due to the large pore size and low connectivity of Ce-MOF-808: the clusters are 6-fold connected by trimesate linkers. Liquid ^1H NMR of a digested sample revealed the presence of 2 additional coordinating formates leading to four remaining open sites that can act as active sites during reaction (Figure S2). The structural integrity of Ce-MOF-808 during activation and reaction was demonstrated via PXRD (Figure S5) and the heterogeneity of the catalyst was proven by a hot filtration test: after 2 h reaction; Ce-MOF-808 was removed and no further reaction was observed (Figure S7).

In conclusion, the redox behavior of Ce^{4+} -MOFs was investigated using a combined XANES and EXAFS approach, focusing on the Ce oxidation state and the geometry of the active site. One Ce ion could be reduced per cluster, thereby moving slightly away from the center of the cluster. This unambiguously demonstrates the redox activity of Ce-MOFs, paving the way for their further application in redox catalysis. This was exemplified by the development of a catalytic system with Ce-MOF-808 which displayed an increased activity for the aerobic TEMPO-mediated oxidation of benzyl alcohol.

Acknowledgements

S.S., B.B., and D.D.V. gratefully acknowledge the FWO Flanders for funding (Aspirant grant and postdoctoral grant). CL and ALB

acknowledge the Mega-Grant of the Russian Federation Government (14.Y26.31.0001). The XAS experiments were performed on beamline BM31 at the European Synchrotron Radiation Facility (ESRF), Grenoble, France. We are grateful to Michela Brunelli and Hermann Emerich at the ESRF for providing assistance in using beamline BM31.

Conflict of interest

The authors declare no conflict of interest.

Keywords: catalysis · cerium · metal–organic frameworks · redox chemistry · X-ray spectroscopy

- [1] J. Liu, L. Chen, H. Cui, J. Zhang, L. Zhang, C.-Y. Su, *Chem. Soc. Rev.* **2014**, *43*, 6011–6061.
- [2] H. Kim, S. Yang, S. R. Rao, S. Narayanan, E. A. Kapustin, H. Furukawa, A. S. Umans, O. M. Yaghi, E. N. Wang, *Science* **2017**, *356*, 430–434.
- [3] J. R. Li, J. Sculley, H. C. Zhou, *Chem. Rev.* **2012**, *112*, 869–932.
- [4] J. H. Cavka, S. Jakobsen, U. Olsbye, N. Guillou, C. Lamberti, S. Bordiga, K. P. Lillerud, *J. Am. Chem. Soc.* **2008**, *130*, 13850–13851.
- [5] L. Valenzano, B. Civalieri, S. Chavan, S. Bordiga, M. H. Nilsen, S. Jakobsen, K. P. Lillerud, C. Lamberti, *Chem. Mater.* **2011**, *23*, 1700–1718.
- [6] S. Jakobsen, D. Gianolio, D. S. Wragg, M. H. Nilsen, H. Emerich, S. Bordiga, C. Lamberti, U. Olsbye, M. Tilset, K. P. Lillerud, *Phys. Rev. B* **2012**, *86*, 125429.
- [7] T. Montini, M. Melchionna, M. Monai, P. Fornasiero, *Chem. Rev.* **2016**, *116*, 5987–6041.
- [8] F. Vermoortele, R. Ameloot, A. Vimont, C. Serre, D. De Vos, *Chem. Commun.* **2011**, *47*, 1521–1523.
- [9] F. Vermoortele, B. Bueken, G. Le Bars, B. Van de Voorde, M. Vandichel, K. Houthoofd, A. Vimont, M. Daturi, M. Waroquier, V. Van Speybroeck, C. Kirschhock, D. De Vos, *J. Am. Chem. Soc.* **2013**, *135*, 11465–11468.
- [10] F. Vermoortele, M. Vandichel, B. Van De Voorde, R. Ameloot, M. Waroquier, V. Van Speybroeck, D. E. De Vos, *Angew. Chem. Int. Ed.* **2012**, *51*, 4887–4890; *Angew. Chem.* **2012**, *124*, 4971–4974.
- [11] C. Caratelli, J. Hajek, F. G. Cirujano, M. Waroquier, F. X. Llabrés i Xamena, V. Van Speybroeck, *J. Catal.* **2017**, *352*, 401–414.
- [12] G. W. Peterson, S. Y. Moon, G. W. Wagner, M. G. Hall, J. B. Decoste, J. T. Hupp, O. K. Farha, *Inorg. Chem.* **2015**, *54*, 9684–9686.
- [13] M. Lammert, M. T. Wharmby, S. Smolders, B. Bueken, A. Lieb, K. A. Lomachenko, D. De Vos, N. Stock, *Chem. Commun.* **2015**, *51*, 12578–12581.
- [14] V. Nair, A. Deepthi, *Chem. Rev.* **2007**, *107*, 1862–1891.
- [15] V. Sridharan, J. C. Menéndez, *Synthesis* **2010**, *110*, 3805–3849.
- [16] A. Trovarelli, C. de Leitenburg, M. Boaro, G. Dolcetti, *Catal. Today* **1999**, *50*, 353–367.
- [17] Z. Wu, R. Jin, Y. Liu, H. Wang, *Catal. Commun.* **2008**, *9*, 2217–2220.
- [18] S. Carrettin, P. Concepción, A. Corma, J. M. López Nieto, V. F. Puntes, *Angew. Chem. Int. Ed.* **2004**, *43*, 2538–2540; *Angew. Chem.* **2004**, *116*, 2592–2594.
- [19] R. Si, M. Flytzani-Stephanopoulos, *Angew. Chem. Int. Ed.* **2008**, *120*, 2926–2929; *Angew. Chem.* **2008**, *120*, 2968–2970.
- [20] R. Wang, P. A. Crozier, R. Sharma, J. B. Adams, *nanoletters* **2008**, *8*, 962–967.
- [21] M. Lammert, H. Reinsch, C. A. Murray, M. T. Wharmby, H. Terraschke, N. Stock, *Dalton Trans.* **2016**, *45*, 18822–18826.
- [22] M. Lammert, C. Glißmann, H. Reinsch, N. Stock, *Cryst. Growth Des.* **2017**, *17*, 1125–1131.
- [23] M. Lammert, C. Glißmann, N. Stock, *Dalton Trans.* **2017**, *46*, 2425–2429.
- [24] A. C. Dreischarf, M. Lammert, N. Stock, H. Reinsch, *Inorg. Chem.* **2017**, *56*, 2270–2277.
- [25] S. L. Estes, M. R. Antonio, L. Soderholm, *J. Phys. Chem. C* **2016**, *120*, 5810–5818.
- [26] S. S. Kim, H. C. Jung, *Synthesis* **2003**, *14*, 2135–2137.
- [27] S. Bordiga, E. Groppo, G. Agostini, J. A. Van Bokhoven, C. Lamberti, *Chem. Rev.* **2013**, *113*, 1736–1850.

- [28] J. J. Rehr, C. H. Booth, F. Bridges, S. I. Zabinsky, *Phys. Rev. B* **1994**, *49*, 12347–12350.
- [29] D. E. Ramaker, D. C. Koningsberger, *Phys. Chem. Chem. Phys.* **2010**, *12*, 5514–5534.
- [30] A. E. Platero-Prats, A. Mavrandonakis, L. C. Gallington, Y. Liu, J. T. Hupp, O. K. Farha, C. J. Cramer, K. W. Chapman, *J. Am. Chem. Soc.* **2016**, *138*, 4178–4185.
- [31] S. Deshpande, S. Patil, S. V. Kuchibhatla, S. Seal, *Appl. Phys. Lett.* **2005**, *87*, 133133.
- [32] M. Nolan, S. C. Parker, G. W. Watson, *Surf. Sci.* **2005**, *595*, 223–232.
- [33] A. Dijkstra, I. W. C. E. Arends, R. A. Sheldon, *Chem. Commun.* **1999**, *2*, 1591–1592.
- [34] R. A. Sheldon, I. W. C. E. Arends, G. J. Ten Brink, A. Dijkstra, *Acc. Chem. Res.* **2002**, *35*, 774–781.
- [35] A. Badalyan, S. S. Stahl, *Nature* **2016**, *535*, 406–410.
- [36] A. Dijkstra, I. W. C. E. Arends, R. A. Sheldon, *Org. Biomol. Chem.* **2003**, *1*, 3232.
- [37] M. F. Semmelhack, C. R. Schmid, D. A. Cortés, *Tetrahedron Lett.* **1986**, *27*, 1119–1122.
- [38] S. Y. Moon, Y. Liu, J. T. Hupp, O. K. Farha, *Angew. Chem. Int. Ed.* **2015**, *66*, 6795–6799.
- [39] Y. Bai, Y. Dou, L.-H. Xie, W. Rutledge, J.-R. Li, H.-C. Zhou, *Chem. Soc. Rev.* **2016**, *45*, 2327–2367.
- [40] M. J. Cliffe, W. Wan, X. Zou, P. A. Chater, A. K. Kleppe, M. G. Tucker, H. Wilhelm, N. P. Funnell, F.-X. Coudert, A. L. Goodwin, *Nat. Commun.* **2014**, *5*, 4176.

Manuscript received: August 31, 2017

Accepted manuscript online: October 13, 2017

Version of record online: November 15, 2017

Effect of Benzoic Acid as a Modulator in the Structure of UiO-66: An Experimental and Computational Study

Cesare Atzori,[†] Greig C. Shearer,[‡] Lorenzo Maschio,[§] Bartolomeo Civalleri,[§] Francesca Bonino,[†] Carlo Lamberti,^{§,||} Stian Svelle,[‡] Karl Petter Lillerud,[‡] and Silvia Bordiga^{*,†,‡,§,||}

[†]Department of Chemistry, NIS and INSTM Reference Centre, University of Turin, Via Quarello 15, I-10135 Turin, Italy

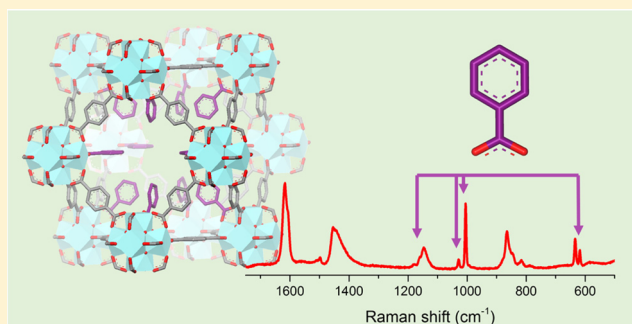
[‡]Department of Chemistry, University of Oslo, P.O. Box 1033, N-0315 Oslo, Norway

[§]Department of Chemistry, NIS and INSTM Reference Centre, University of Turin, Via Giuria 7, I-10125 Turin, Italy

^{||}IRC “Smart Materials”, Southern Federal University, Zorge Street 5, 344090 Rostov-on-Don, Russia

Supporting Information

ABSTRACT: The identification and quantification of defects are undoubtedly thorough challenges in the characterization of “defect-engineered” metal–organic frameworks (MOFs). UiO-66, known for its exceptional stability and defect tolerance, has been a popular target for defect-engineering studies. Herein, we show that synthesizing UiO-66 in the presence of an excess of benzoic acid is a reliable method for obtaining UiO-66 samples with a very high concentration of missing-cluster defects, allowing one to modulate specific properties (i.e., surface area and hydrophobicity). This was elucidated by a multitechnique marriage of experimental and computational methods: a combination of PXRD, dissolution/¹H NMR spectroscopy, and N₂ sorption measurements was used to quantify the defect loading, while vibrational spectroscopies (FTIR and Raman) allowed us to unequivocally identify the defect structure by comparison with DFT-simulated spectra and visual analysis of the computed vibrational modes.



1. INTRODUCTION

Among the numerous classes of porous materials, metal–organic frameworks (MOFs) stand out for their structural and chemical diversity, exhibiting a wide range of well-defined pore size distributions and chemical functionalities.^{1,2} This variety endows MOFs with incredible potential in many areas of technological relevance, e.g., adsorption³ and catalysis,⁴ but their real-world applicability in these areas has thus far been hindered by serious drawbacks, such as poor stability, particularly to moisture.^{5–9} Much attention has therefore been given to relatively stable subclasses of MOFs, e.g., zirconium(IV) MOFs, particularly those with clusters based on a Zr₆ octahedral core.^{10–15} The most widely studied material among these “Zr₆ MOFs” is UiO-66 (Figure 1), in which the Zr₆-oxyhydroxide clusters are 12-fold connected by 1,4-benzenedicarboxylate (BDC, a linear ditopic linker), resulting in a highly symmetric face-centered cubic (fcc) structure.¹²

While UiO-66 is indeed exceptionally thermally, chemically, and mechanically stable, its performance in commonly proposed applications (e.g., adsorption, separation, and catalysis) is limited by its relatively modest porosity and lack of chemical functionality. In recognition of these shortcomings, many researchers have opted to instead focus on isoreticularly expanded and/or functionalized UiO-66 derivatives (e.g., UiO-67, UiO-66-NH₂), which offer improvements in these

areas.^{16–33} However, these derivatives generally harbor two rather significant drawbacks with respect to UiO-66: lower stability^{18,21,23,24,34,35} and higher cost. The bulk of their expense can be attributed to the functionalized and/or extended organic linker(s), many of which are not even commercially available, necessitating the development of in-house synthesis procedures,³⁶ which can take months (or longer) to optimize unless the molecule has already been reported in the literature. It is therefore clear that an alternative approach for tuning the porosity and functionality of UiO-66 (and thus, performance) is desired.

One such alternative approach is “defect engineering”, a term often used as shorthand for the practice of manipulating defects via controlled, synthetic means.^{37–46} This approach has proven to be particularly effective for UiO-66,^{16,37,38,43–72} which is famed for its ability to tolerate an extraordinarily high concentration of defects while retaining much of its stability³⁷ [except for certain cases where the thermal stability has been shown to be heavily compromised⁷³ and one sample (50Benz-HA in ref 49) that was found to have reduced water stability]. We stress that this fascinating trait is not just an academic

Received: January 16, 2017

Revised: April 3, 2017

Published: April 5, 2017

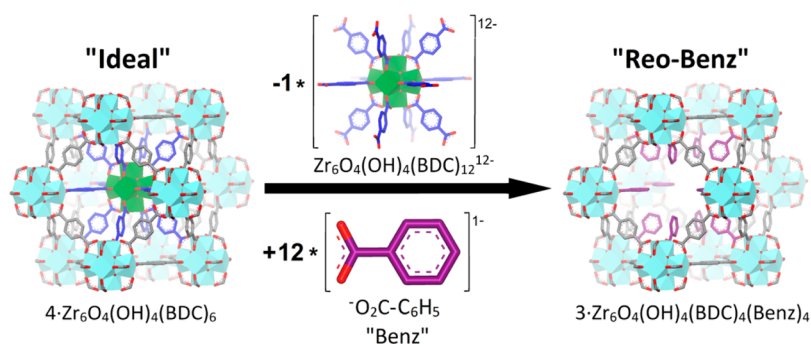


Figure 1. Illustration showing how the structure of a “Reo-Benz” defect differs from that of ideal, defect-free UiO-66. Hydrogen atoms have been omitted for the sake of clarity.

curiosity; many studies have shown that defects significantly enhance UiO-66’s porosity (see refs 37, 38, 43, 44, 46, 48, 49, 53, 58, 59, 61, 73, and 74) and reactivity (see refs 44, 47, 49, 50, 57, 60, and 62), leading to better performances in a wide variety of applications (see refs 38, 48–50, 53, 56–59, 62–67, 75, and 76). Such positive demonstrations have encouraged many researchers to seek out strategies to gain synthetic control over the defects in the UiO-66 framework.

To this end, the most common method is to synthesize UiO-66 in the presence of additives known as “modulators”.^{68,69,77–80} Many types of modulator (e.g., HCl,^{61,63} HF,⁶⁸ NH₄OH,⁷⁹ and amino acids⁶⁹) are known to promote the formation of defects, but monocarboxylic acid “coordination modulators” (e.g., acetic acid, formic acid, benzoic acid, etc.) are the most widely studied and, thus, best understood.^{37,38,46–50,52–55,58,59,77} In recent work,^{37,49} we proved that monocarboxylic acid modulation promotes the formation of “missing-cluster defects” whose charge and coordination deficiencies are compensated by modulator ligands (in their carboxylate form; see benzoate ligands in Figure 1). More importantly, we showed that these defects can massively enhance the porosity and reactivity of the material^{49,73} and that new, otherwise elusive functionalities can be incorporated by postsynthetically exchanging the defect-compensating ligands.⁴⁹

Another important (albeit less striking) aspect of our systematic investigations is that they have enabled us to objectively compare different monocarboxylic acid modulators for their propensity for introducing defects to the UiO-66 framework, a property which we hereafter refer to as their “defect-inducing potency”. On the basis of such comparisons, we have identified trifluoroacetic acid³⁷ and benzoic acid⁴⁹ as the most potent modulators we have investigated thus far, and have ascribed their effectiveness to a combination of acidity,³⁷ solubility,⁴⁹ and steric⁴⁹ effects. While the defect-inducing potency of the two modulators are roughly equivalent, we now harbor a strong preference toward benzoic acid for the following reasons: (1) Trifluoroacetic acid (a strong acid) readily catalyzes the hydrolysis of DMF during UiO-66 synthesis, generating formic acid which then goes on to act as a modulator in its own right, resulting in a material with defects compensated by a combination of trifluoroacetate and formate ligands.³⁷ This increases the complexity and heterogeneity of the material in a manner that is probably not entirely reproducible, and is much less of an issue when benzoic acid (a much weaker acid) is employed as the modulator.⁴⁹ (2) Trifluoroacetic acid (bp = 72.4 °C) is a relatively volatile molecule that may therefore evaporate from the solution during UiO-66 syntheses. We speculate that this volatilization could

occur to different extents and rates from one synthesis batch to the next, potentially affecting reproducibility, a situation that is completely avoided by using the nonvolatile benzoic acid (bp = 249.2 °C) as the modulator. (3) In our experience, UiO-66 syntheses modulated by trifluoroacetic acid often provide poor yields, a negative outcome which is much less severe when benzoic acid is employed as the modulator. (4) Trifluoroacetic acid-modulated syntheses tend to yield UiO-66 samples with very poorly defined crystal morphology and size,^{37,50} while benzoic acid-modulated syntheses provide reasonably monodisperse octahedral crystals.^{20,49,59,77} (5) Benzoic acid is much cheaper than trifluoroacetic acid.

It is important to keep in mind that all of the findings discussed thus far were backed up by a large amount of convincing experimental evidence, something that we feel is especially vital for defect-engineering pursuits, since disorder is notoriously challenging to characterize. In acknowledgment of this challenge, researchers have sought to develop methods that are able to detect, quantify, and evaluate the nature of the defects in different UiO-66 samples, preferably with routine characterization techniques available in most laboratories. To this end, most research groups (including our own) employ some combination of PXRD (see refs 37, 49, 52, 54, and 73), TGA (see refs 37, 49, 50, 53–55, 58, 61, 68, 69, and 73), dissolution/¹H NMR spectroscopy (see refs 37, 47, 49, 53, 59, and 69), and N₂ adsorption measurements (see refs 37, 38, 47–49, 53, 58, 59, 61, 63, 68, 69, and 73) [sometimes in conjunction with simulations (see refs 37, 49, 61, 67, and 73)]. While indirect, this approach has proven to be valuable for detecting defects and assessing their concentration via simple semiquantitative data analysis methods.^{37,49} Conversely, vibrational spectroscopies (FTIR, Raman) have thus far had only a peripheral, qualitative role for characterizing the defectivity of UiO-66. For example, they have been used to detect the presence of different defect-compensating ligands (i.e., deprotonated modulator molecules^{37,49}) and superfluous hydroxyl groups^{81,82} (also thought to terminate defects in some cases^{57,60,61,65,70–72}) and to indicate defectivity by noting differences between experimental spectra and that simulated from the ideal, defect-free UiO-66 structural model.⁷³ This rather limited use is somewhat surprising given that vibrational spectroscopies are traditionally very well suited to characterize defects,^{83,84} and it was this realization that motivated us to investigate these techniques further herein.

To this end, we synthesized a series of five defective UiO-66 samples, each obtained in the presence of different amounts of benzoic acid (our preferred defect-engineering modulator; see reasons above). All of the samples (given the general name

“ α Benz”, where α is the molar equivalents of benzoic acid used in the synthesis, with respect to ZrCl_4) were then characterized by means of Raman and FTIR spectroscopies, as well as the methods more commonly used for characterizing defects in UiO-66 (PXRD, dissolution/ ^1H NMR, and nitrogen sorption measurements). In accordance with our previous studies,^{37,49} the results show that (1) using benzoic acid as a modulator yields UiO-66 samples with a high concentration of missing-cluster defects with benzoate as the compensating ligand [herein named “Reo-Benz” defects (see Figure 1) due to their RCSR⁸⁵-denoted topology (reo)] and (2) the concentration of these defects systematically increases as increasing amounts of benzoic acid are used in the synthesis. Although we are fully convinced of these conclusions, we speculate that some of the MOF community may still be skeptical due to the indirect manner in which these methods probe defectivity. This potential criticism is opposed by the vibrational spectroscopy results, which, when compared with simulated spectra, provide direct and unequivocal evidence for these conclusions (and those of our previous studies^{37,49}). Perhaps more importantly, this paper demonstrates that vibrational spectroscopies can be a powerful tool for characterizing defects in MOFs, especially when experimental results are compared with spectra simulated from models of proposed defect structures.^{86,87}

2. EXPERIMENTAL SECTION

2.1. Materials Synthesis. **2.1.1. Defective UiO-66 Samples.** The five defective UiO-66 samples (named 10Benz, 20Benz, 30Benz, 40Benz, and 50Benz) were synthesized by the same method, albeit with different amounts of benzoic acid as a modulator (see Table 1). First, the synthesis solutions were

Table 1. Quantities of Benzoic Acid Used in the Synthesis of the Five Defective UiO-66 Samples

sample ^a	amount of benzoic acid used in synthesis
10Benz	8.807 g (72.12 mmol)
20Benz	17.613 g (144.23 mmol)
30Benz	26.420 g (216.34 mmol)
40Benz	35.226 g (288.45 mmol)
50Benz	44.033 g (360.57 mmol)

^aThe names of the samples are derived from the benzoic acid:ZrCl₄ molar ratio in their respective synthesis solutions.

prepared by sequentially adding 1.680 g of ZrCl_4 (7.209 mmol), 0.173 mL of H_2O (9.603 mmol), benzoic acid (quantities given in Table 1), and 1.198 g of 1,4-benzenedicarboxylic acid (H_2BDC , 7.211 mmol) to a 1 L Erlenmeyer flask containing 413.2 mL of warm (ca. 70 °C) N,N' -dimethylformamide (DMF, 5336 mmol) under constant magnetic stirring.

Once the reagents had fully dissolved, the stirring bars were removed and watch glasses were placed over the mouths of the flasks as a loose cover. The covered synthesis solutions were then placed in an oven preheated to 120 °C and were allowed to react over a period of 24 h before applying the purification steps given in section 2.1.3.

2.1.2. “Defect-Free” UiO-66 (Ref.). The “defect-free” UiO-66 sample (Ref.) was synthesized via an optimized version^{37,49} of a procedure originally outlined by Serre and co-workers⁸⁸ and later promoted by us.⁷³ First, the synthesis mixture was prepared by sequentially dissolving 3.781 g of ZrCl_4 (16.22 mmol), 2.865 mL of 35% HCl (32.45 mmol), and 5.391 g of H_2BDC (32.45 mmol) in 97.40 mL of warm (ca. 70 °C) N,N' -

dimethylformamide (DMF, 1258 mmol) under constant magnetic stirring. Once all reagents had fully dissolved, the mixture was transferred to a 200 mL Teflon liner, sealed in a stainless steel autoclave, and placed in an oven preheated to 220 °C. After 24 h of reaction at this temperature, the autoclave was removed from the oven and rapidly cooled by dropping it into a bucket of cold tap water for 30 min before applying the purification steps given in section 2.1.3.

2.1.3. Purification Procedures. After all reactions, the resulting microcrystalline powder precipitates were separated from their synthesis solutions via centrifugation and washed by shaking them overnight in 80 mL of fresh DMF. Three further separation/washing cycles were performed the next day, albeit for a shorter duration (ca. 2 h per wash) before the washed products were separated by centrifugation, dried overnight in an oven set to 60 °C, and ground with a mortar and pestle. The samples were then subjected to a further “activation” procedure to remove the DMF guest molecules from their pores. This was achieved by heating them at 200 °C for 24 h in a conventional oven, a simple treatment which we have found to be very effective for UiO-66.^{37,49} The Ref. sample was subjected to a further heat treatment (dubbed “calcination”), in which unidentified nonvolatile organic impurities³⁷ are removed via a two-step program on a multistep muffle furnace. In the first step, a 5 °C min⁻¹ ramp was used to heat the material from room temperature to 200 °C, at which it was held for 10 min. A 0.5 °C min⁻¹ ramp was then used between 200 and 270 °C, where the temperature was held for 70 h. After calcination, the product was allowed to cool to room temperature naturally.

The activated/calcined samples are not completely empty, as they adsorb a small amount of atmospheric water vapor when allowed to cool to room temperature in air. The theoretical yields of the procedures (discounting adsorbed water) is 2 g for the defective samples and 4.5 g for the defect-free one.

2.2. Experimental Methods. **2.2.1. Powder X-ray Diffraction (PXRD).** Samples were prepared for measurement by dispersing 30 mg of sample on a flat, glass plate PXRD sample holder with a diameter of 2.5 cm. A stretched piece of plastic film was then used to spread, flatten, and hold the sample in position for measurement. The plastic film is evident in the PXRD patterns, appearing as two broad peaks covering 2θ ranges of ca. 20°–22° and 23°–24°.

PXRD patterns (Cu $K\alpha$ radiation, $\lambda = 1.5418 \text{ \AA}$, 2θ range = 2°–50°, time scale = 1, resulting in a d -spacing down to 1.82 Å) were collected in reflectance Bragg–Brentano geometry with a Bruker D8 Discovery diffractometer equipped with a focusing Ge-monochromator and a Bruker LYNXEYE detector.

Values of the relative intensity of the broad peak [$\text{Rel}(I)_{\text{BP}}$] have been extracted from the patterns by fitting with a peak-shaped function (a pseudo-Voigt or a Pearson VII, depending on which one gave the lowest error) and normalizing the area of the fitted peak by dividing by the intensity (measured in the same manner of the broad one) of three key reflections [the (100), (200) and (600)] of UiO-66. A detailed description of this method can be found in section 4 of the Supporting Information of the present paper and in two preceding works.^{37,49}

2.2.2. Dissolution/ ^1H NMR Spectroscopy. Samples were prepared by weighing 20 mg of the MOF sample of interest into an NMR tube and adding 600 μL of 1 M NaOH (in D_2O). The NMR tube was then capped and the contents were mixed by inverting the tube two or three times. The MOF was then left to digest over a period of 24 h before measurement. This

hydroxide-based procedure dissolves only the organic portion of the MOF (linker, modulator, solvent etc.), while the inorganic content is converted into ZrO_2 , which sinks to the bottom of the NMR tube and does not influence the spectra. Liquid 1H NMR spectra were obtained with a Bruker Avance DPX-300 NMR Spectrometer (300 MHz). The relaxation delay (d1) was set to 20 s to improve the reliability of integration and, thus, the accuracy of the molar ratios determined from the results. The number of scans (ns) was 64. Molar ratios were extracted from these spectral data using a procedure reported in section 6 of the the Supporting Information of the present paper and two preceding works.^{37,49}

2.2.3. Nitrogen Sorption Measurements at 77 K. Nitrogen sorption measurements were performed on a BelSorp mini II instrument at 77 K. In each experiment, approximately 50 mg of the sample of interest was weighed into a 9.001 cm³ glass cell. Prior to measurement, guest molecules were removed from the MOF pores via simultaneous vacuum and heat treatment, first for 1 h at 80 °C and then for 2 h at 200 °C. The sample cells were then immersed in a Dewar of liquid nitrogen for the duration of the nitrogen adsorption measurement. BET areas were extracted from the nitrogen adsorption isotherms via the method described in section 5 of the Supporting Information of the present work and in two of our previous papers.^{37,49}

2.2.4. Attenuated Total Reflection Infrared (ATR-IR) Spectroscopy. Loose MOF powder was introduced into a Bruker Vertex70 FTIR spectrometer equipped with a Bruker OPTIK Platinum ATR accessory with a diamond internal reflection element. ATR-IR spectra (2 cm⁻¹ resolution, 256 scans) were then recorded in the 4000–600 cm⁻¹ range and detected with an MCT detector. The spectral intensity was corrected for the change in the effective thickness value as a function of the incident wavelength.

2.2.5. Transmission IR Spectroscopy. Samples were measured in the form of small (ca. 2 cm²), thin, self-supporting wafers, which were prepared by pellet-pressing ca. 30 mg of pure, undiluted MOF powder with a force of ca. 10 kN. In separate experiments, wafers were placed in a home-built airtight quartz cell with mid-IR transparent KBr windows. Before measurement, guest molecules were removed from the MOF pores by attaching the quartz cell to a custom-made vacuum line and applying simultaneous vacuum and heat treatment (1 h at 80 °C and then 2 h at 200 °C). The transmission FTIR spectra were then recorded in the 4000–600 cm⁻¹ range with a Bruker Vertex 70 FTIR spectrometer equipped with a MCT detector (2 cm⁻¹ resolution, 32 scans).

2.2.6. Raman Spectroscopy. Samples were prepared and pretreated in the same manner as for the transmission FTIR measurements, albeit using another type of locally constructed airtight cell featuring a Suprasil quartz cuvette. Raman spectra were recorded over a wavenumber range of 1800–500 cm⁻¹ on a Renishaw inVia Raman microscope spectrometer in back-scattering mode. A 785 nm diode laser was used for the excitation, and the scattered photons were dispersed by a 1200 lines/mm grating monochromator and collected on a CCD camera whose collection optic was set at 20× objective summing up 66 scans with an exposition time of 20 s per step.

2.3. Computational Methods. **2.3.1. Used Models.** Two atomistic models were used for both DFT calculations and isotherm simulations: the crystallographic structure of UiO-66^{12,82} for the defect-free model (named “Ideal”) and a defective benzoate-containing structure (dubbed “Reo-Benz”) that was created by starting from the perfect UiO-66

framework. First, from the primitive unit cell of UiO-66 {114 atoms, $Zr_6O_4(OH)_4[C_6H_4(COO)_2]_6$ } the crystallographic cubic cell was built that corresponds to a 4 times larger supercell (456 atoms). Then, to create the defect, a $Zr_6O_4(OH)_4$ unit was removed along with the carboxylate groups of the neighboring linkers, and finally, the dangling bonds on the aromatic rings were saturated with hydrogen atoms. The resulting structure was comprised of a 414-atom cubic unit cell $\{3Zr_6O_4(OH)_4[C_6H_4(COO)_2]_4[C_6H_5COO]_4\}$ that has 12 benzoic moieties in the defective site, as shown in Figure 1.

2.3.2. DFT Calculations. All calculations were performed by means of the CRYSTAL14 ab initio code.⁸⁹ The hybrid B3LYP^{90,91} method, combined with an all-electron Gaussian basis set, was employed. The basis set consists of the following contractions of Gaussian functions: (8s)-(7631sp)-(621d) for Zr, (8s)-(411sp)-(1d) for O, (6s)-(31sp)-(1d) for C, and (31s)-(1p) for H (see ref 82 for details). All computational parameters were the same as in the previous work of Valenzano et al.,⁸² except for the shrinking factor used in reciprocal space sampling (here raised to 3 from the original value of 2). Both the perfect (Ideal) and defective (Reo-Benz) UiO-66 models were fully relaxed by keeping the symmetry of the systems (24 symmetry operators). The presence of the defect leads to a negligible expansion of the unit cell volume (i.e., less than +0.1%), which is probably due to the well-known rigidity of the UiO-66 framework. Vibrational frequencies were computed at the Γ point on the optimized geometries.⁹² Infrared and Raman intensities were calculated via an entirely analytical procedure based on a linear response.^{93,94} A Lorentzian broadening of 5 cm⁻¹ was adopted for both the infrared and Raman spectra. Vibrational frequencies were shifted by a factor of 0.98 in order to compensate for the well-known DFT overestimation effect.

The choice of the B3LYP functional is justified by consistency with previous works on the UiO-66 crystal. The introduction of empirical dispersion corrections (Grimme’s D3 with three-body contribution) leads to a mild contraction of cell volumes (1.4% for the perfect structure, less than 2% for the defective one), resulting in shifts for the individual frequencies not larger than 10 cm⁻¹. Since the discussion in the following focuses on isolated features of the vibrational spectra relative to the benzoate defect rather than collective modes, we consider the choice of the functional of minor importance.

2.3.3. Isotherm Simulation. Adsorption isotherms were simulated with the “adsorption isotherm” task within the “Sorption Tools” menu in Accelrys Materials Studio version 8.1. The simulations were performed at 77 K, using a geometry-optimized N₂ molecule as the adsorptive and a single, geometry-optimized unit cell of the model structure of interest as the adsorbent. We adopted the Metropolis method and the COMPASS force field. The isotherms were simulated over a pressure range of 0.01–100 kPa, in which 50 fugacity steps were distributed logarithmically in order to increase the number of data points in the steep initial portion of the isotherm. The “Fine” quality setting was used for all simulations. Charges were force field assigned, while electrostatic forces were calculated with the Ewald method. The “atom-based” method was adopted for the calculation of van der Waals forces. No constraints were assigned.

3. RESULTS AND DISCUSSION

Figure 2 illustrates the complete set of PXRD patterns obtained on the full series of samples over a 2θ range of 2° – 35° . All the

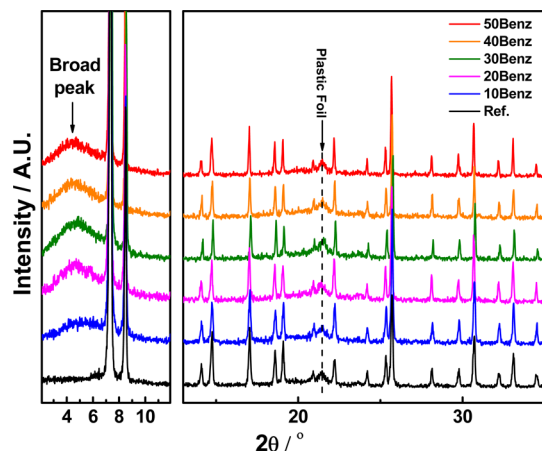


Figure 2. PXRD patterns obtained on the six UiO-66 samples. The same y-scale is applied to both plots.

samples are highly crystalline and with the expected patterns, except for the region preceding the first reflection of the UiO-66 phase. This region is emphasized in the left plot of Figure 2, where it can be seen that a very broad peak (spanning a 2θ range of ca. 2° – 7°) is observed in the PXRD patterns obtained on the samples synthesized in the presence of benzoic acid. In a couple of previous works^{37,49} we unambiguously assigned this “broad peak” to very tiny “nanoregions” of missing cluster defects and showed that the relative intensity of the broad peak [Rel(I)_{BP}] is correlated with the concentration of these defects. The absence of this peak in the pattern obtained on the reference UiO-66 sample (“Ref.,” black line in Figure 2) proves its very low defectivity. In contrast, the broad peak is already clearly present in the pattern obtained on 10Benz, and its intensity (and, thus, the concentration of missing cluster defects) systematically increases in 20Benz and 30Benz, at which point it essentially plateaus. This is more visually and quantitatively evident in Figure 3, where the Rel(I)_{BP} values (calculated via the method outlined in section 4 of the Supporting Information; see Table 2 and Table S1 for

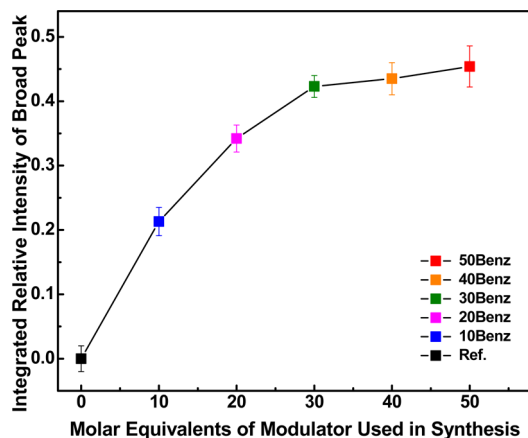


Figure 3. Integrated relative intensity of the broad diffraction peak [Rel(I)_{BP}], (see Table 2 and Table S1) vs the molar equivalents of benzoic acid added to the UiO-66 synthesis mixture.

Table 2. Summary of the Quantitative Experimental Data Extracted from the PXRD, Dissolution/¹H NMR, and Nitrogen Adsorption, Results Obtained on the UiO-66 Samples, and Theoretical Values from the Models (see Figure 1)

sample	Rel(I) _{BP} /error	$\frac{n_{\text{mod.}}}{n_{\text{BDC}}}$	BET area (m ² g ⁻¹)	ref
Ref.	0.000/0.020	0.00	1236	37
10Benz	0.213/0.022	0.34	1252	this work
20Benz	0.342/0.021	0.59	1382	this work
30Benz	0.423/0.017	0.69	1480	this work
40Benz	0.435/0.025	0.78	1494	this work
50Benz	0.454/0.032	0.79	1515	this work

model	Rel(I) _{BP} /error	$\frac{n_{\text{mod.}}}{n_{\text{BDC}}}$	BET area (m ² g ⁻¹) ^a	ref
Ideal	–	0.00 ^b	1241	37
Reo-Benz	–	1.00 ^c	1532	49

^aCalculated from the simulated nitrogen adsorption isotherms (see Figure 6a). ^bThere are no monocarboxylate ligands in the ideal UiO-66 composition, Zr₆O₄(OH)₄(BDC)₆, so $\frac{n_{\text{mod.}}}{n_{\text{BDC}}} = 0$. ^cThe composition of Reo-Benz is Zr₆O₄(OH)₄(BDC)₄(Benz)₄, where “Benz” is benzoate, a monocarboxylate ligand. Thus, $\frac{n_{\text{mod.}}}{n_{\text{BDC}}} = \frac{4}{4} = 1$.

numerical data) are plotted against the molar equivalents of benzoic acid used in the MOF syntheses. These observations suggest that benzoic acid is very effective at creating missing-cluster defects in UiO-66, even at relatively low concentrations.

Liquid ¹H NMR spectroscopy was used to identify and determine the molar ratios between the organic components in the UiO-66 samples. Figure 4 compares the dissolution/¹H

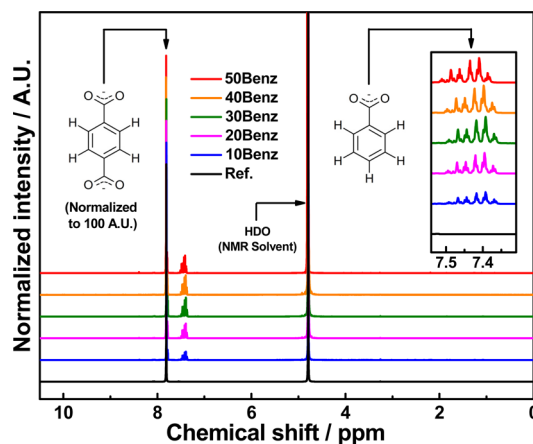


Figure 4. Dissolution/¹H NMR spectra obtained on the six UiO-66 samples.

NMR spectra obtained on all six samples and clearly illustrates the appearance of signals attributed to benzoate in the samples synthesized in the presence of benzoic acid. Since benzoate ligands are thought to terminate the missing cluster defects in these materials, their benzoate content is essentially a measure of their defectivity. However, differences in the intensity of the benzoate signal throughout the series are not particularly apparent upon visual inspection of the spectra, making it difficult to discern qualitative trends in their benzoate content by observation alone.

Regardless, the real strength of the dissolution/¹H NMR is that one can quantify the molar ratios between the organic components in MOF samples by integrating the spectra and

performing simple calculations. Thus, we determined the benzoate/BDC molar ratios $\left(\frac{n_{\text{Benz}}}{n_{\text{BDC}}}\right)$ in our samples, which can be considered as a quantitative descriptor for their benzoate content. Moreover, a very small concentration of formate moieties (originating from the in situ hydrolysis of DMF during the MOF synthesis³⁷) was determined via integration of the faint signal falling at ca. 8.4 ppm, yielding the formate to BDC molar ratio $\left(\frac{n_{\text{Form.}}}{n_{\text{BDC}}}\right)$. This contribution was added to $\frac{n_{\text{Benz}}}{n_{\text{BDC}}}$ to get the “total modulator to BDC molar ratio” $\left(\frac{n_{\text{mod.}}}{n_{\text{BDC}}}\right)$, which is a quantitative descriptor for the amount of monocarboxylate ligands in the samples (and, thus, the concentration of defects in the UiO-66 framework³⁷). These calculations were somewhat complicated by the overlap of the BDC and benzoate signals, as discussed in section 6 of the Supporting Information, where full details of the method are provided.

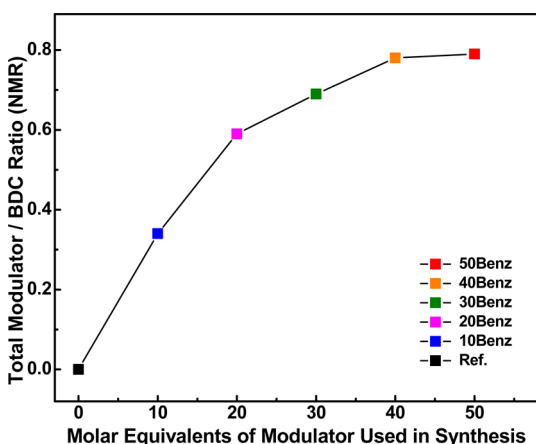


Figure 5. Graph obtained when the total modulator to BDC molar ratios $\left(\frac{n_{\text{mod.}}}{n_{\text{BDC}}}\right)$ (see Table 2 and Table S2 of the Supporting Information) are plotted against the molar equivalents of modulator (benzoic acid) added to the UiO-66 synthesis mixture.

Figure 5 is the plot obtained when the $\frac{n_{\text{mod.}}}{n_{\text{BDC}}}$ values of the six samples (see Table 2 and Table S2 of the Supporting Information for the numerical data) are plotted against the molar equivalents of benzoic acid added to their syntheses. The plot clearly shows that the extent of monocarboxylate incorporation (and, thus, the defectivity of the samples) systematically increases throughout the series but essentially plateaus for the last two samples (40Benz and 50Benz). This again emphasizes the ability of benzoic acid to induce a high level of defectivity to the UiO-66 framework, even when used at relatively low concentrations. If we consider that the Reo-Benz model misses 25% of the clusters (three Zr-bricks instead of four in the unit cell), the 50Benz sample (the most defective material) is missing 19.5% of the clusters.

Nitrogen sorption measurements were used to assess the porosity of all the UiO-66 samples. All the experimentally obtained isotherms are presented in the right plot of Figure 6, while those simulated from the “Ideal” and defective “Reo-Benz” UiO-66 structural models (see Figure 1) are shown in the left plot for comparison. Starting with the simulated isotherms, one can clearly see that the nitrogen uptake capacity of the “Reo-Benz” model (and thus, porosity) is significantly higher than that of ideal UiO-66. This essentially proves that increasing the concentration of missing cluster defects terminated by benzoate ligands should result in an increasingly porous material.

With this in mind, let us turn our attention to the experimentally obtained isotherms shown in the right plot of Figure 6. Before delving into the trends, we feel it is noteworthy to comment on the contour (profile) of the isotherms. For example, the isotherm obtained on the reference UiO-66 sample (Ref.) has a textbook type I profile, featuring a well-defined knee and perfectly flat plateau at higher relative pressures, emphasizing the uniformity of the sample’s micropores. On the other hand, the isotherms obtained on the rest of the samples feature less-well-defined knees and plateaus, as is expected for defective UiO-66 materials with a broader distribution of pore sizes. Nevertheless, these cavities do not appear to enter into the mesoporous size range, as there is no evidence of hysteresis in any of the isotherms, the adsorption and desorption branches of which are perfectly superimposed over the full pressure range.

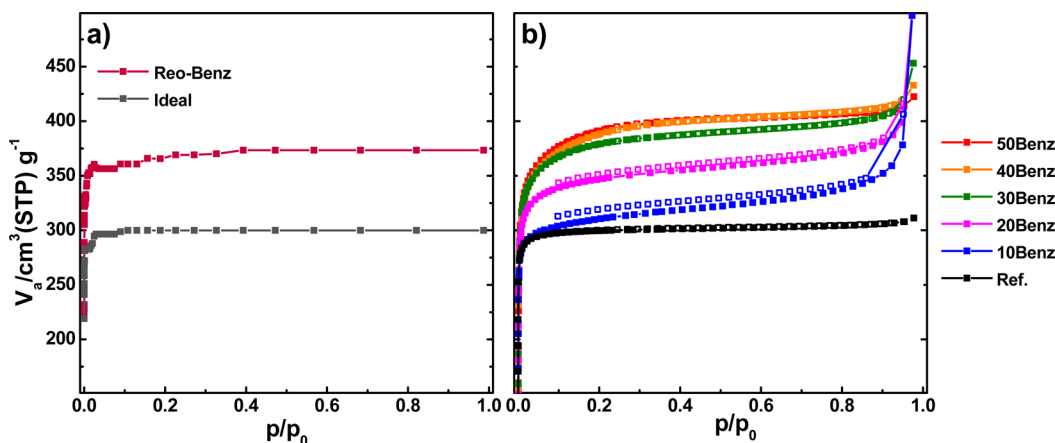


Figure 6. Simulated and experimental nitrogen adsorption isotherms obtained on all UiO-66 samples at 77 K. (a) Simulated isotherms for the Ideal (dark gray) and Reo-Benz (dark red) models. (b) Experimental isotherms; adsorption is depicted by filled squares and desorption by open squares. The same y-scale is applied to both plots.

Of greater relevance to this work is the clear trend that emerges when comparing the nitrogen uptake capacity (and thus, defectivity) of the samples. As one can see, the uptake capacity of the materials systematically increases as the amount of benzoic acid used in the synthesis was increased, eventually plateauing for the last two samples in the series (40Benz and 50Benz). This trend in porosity is quantitatively confirmed by Figure 7, in which the BET areas of the samples (calculated by

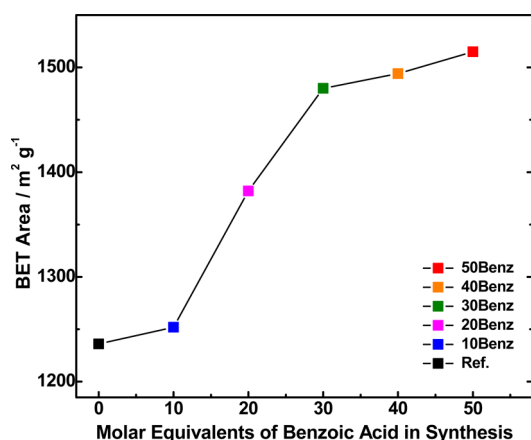


Figure 7. BET areas of the six UiO-66 samples (see also Table 2) plotted against the molar equivalents of modulator (benzoic acid) used in their synthesis.

the method outlined in section 5 of the Supporting Information; see Table 2 for numerical data) are plotted against the molar equivalents of benzoic acid added to their syntheses.

Finally, it is of interest to compare the simulated and experimental data to contextualize our results. For example, one can clearly see that the qualitative (isotherm contour) and quantitative (nitrogen uptake capacity, BET areas) data obtained on the reference material (Ref.) matches very closely with that simulated from the Ideal UiO-66 model, strongly suggesting that the sample is indeed close to defect-free. On the other hand, the data obtained on the three most defective samples (30Benz, 40Benz, and 50Benz) is similar to that simulated from the Reo-Benz model, suggesting that the three samples are extremely defective, which is an especially striking

revelation when one considers that the Reo-Benz model represents an extreme case in which one-quarter of the clusters are missing from the UiO-66 framework.

As was the case for the equivalent plots in previous work,³⁷ the trends observed in Figures 3, 5, and 7 appear to be qualitatively similar, prompting us to explore the relationship between the data plotted therein, $\text{Rel}(I)_{\text{BP}}$, $\frac{n_{\text{mod.}}}{n_{\text{BDC}}}$, and BET area).

To this end, we plotted the $\text{Rel}(I)_{\text{BP}}$ values against the $\frac{n_{\text{mod.}}}{n_{\text{BDC}}}$ and BET area values of the samples (see Table 2 for numerical data), with the results shown in Figure 8.

As one can see from the fitted straight lines and R^2 values of the figure, the data is very well correlated. This makes sense when one considers that all three parameters are all in some way correlated with the concentration of defects in the UiO-66 framework, further validating their branding as “defectivity descriptors” in our previous work.³⁷ As also mentioned in said previous work, only one of the defectivity descriptors [the relative intensity of the broad peak, $\text{Rel}(I)_{\text{BP}}$] is exclusively associated with one type of defect (missing-cluster defects). The fact that the other two descriptors are linearly correlated with $\text{Rel}(I)_{\text{BP}}$ is thus a strong indication that missing-cluster defects (terminated by monocarboxylate ligands, mostly benzoate in these samples) are the predominant defect in the samples under investigation herein. This conclusion is further backed by the similarity between the nitrogen adsorption isotherms obtained on the most defective samples and the isotherm simulated from Reo-Benz, a highly defective UiO-66 structural model in which a quarter of the clusters are missing and compensated by benzoate ligands (see Figure 6 for isotherms and Figure 1 for the structural model).

While the combined evidence from these results points strongly toward the predominance of Reo-Benz-type defects in the samples under investigation herein, the individual methods each detect said defects in a rather indirect manner. We therefore speculate that some of the MOF community may be skeptical of the conclusions drawn from these results (and those of our previous papers^{37,49}). Thus, we employed vibrational spectroscopic techniques (FTIR, Raman, and simulations thereof) to more directly probe the short-range order of these materials.

The O–H and C–H stretching region of the transmission FTIR spectra obtained on the full set of samples after thorough

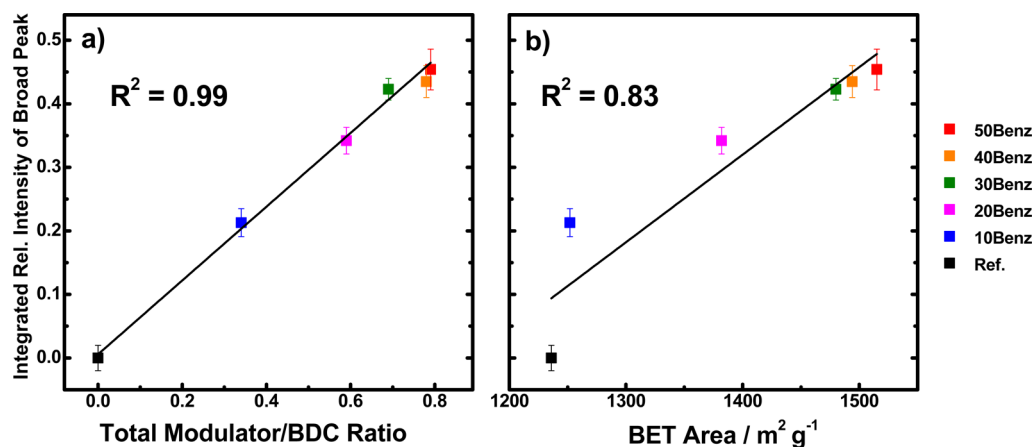


Figure 8. Graphs and linear fits obtained when the relative intensity of the PXR broad peak [$\text{Rel}(I)_{\text{BP}}$] is plotted against (a) the total modulator to BDC ratio ($\frac{n_{\text{mod.}}}{n_{\text{BDC}}}$) and (b) the BET area.

activation (see [Experimental Section](#)) is reported in [Figure 9a](#). As one can see, the spectrum obtained on the Ref. sample is

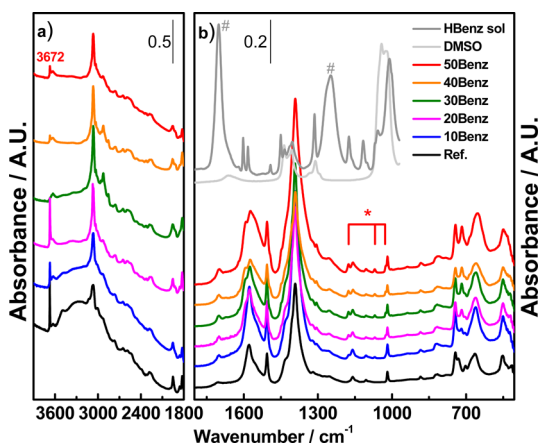


Figure 9. (a) Transmission FTIR spectra obtained for UiO-66 samples activated under dynamic vacuum for 2 h at 200 °C. (b) ATR-IR spectra obtained for the samples in air and for benzoic acid (in DMSO solution) and DMSO are also reported for comparison.

characterized by an intense and sharp band at 3672 cm^{-1} , attributed to the isolated $\mu_3(\text{OH})$ groups on the hydroxylated $\text{Zr}_6\text{O}_4(\text{OH})_4^{12+}$ cluster.^{82,95} Its spectrum also features a broad band centered at 3250 cm^{-1} , which is due to hydrogen-bonded species. The barycenter of this band is rather low in frequency, testifying that the hydrogen bonding is rather strong. The aromatic C–H stretching region of the spectrum features a clear band at 3065 cm^{-1} , which we assign to C–H stretching modes of the BDC linkers.

Moving on to the set of samples made with benzoic acid as modulator, we observe that all the absorptions due to $\nu(\text{OH})$ modes drastically decrease in intensity, both the hydrogen-bonded species (the broad band centered at 3250 cm^{-1}) and the isolated $\mu_3(\text{OH})$ groups at 3672 cm^{-1} (especially in the three most defective samples, 30Benz, 40Benz, and 50Benz). This interesting observation signifies that the samples made with benzoic acid as modulator are more easily activated and dehydroxylated, indicating that they adsorb water less strongly. Indeed, the larger pores of these defective samples may be expected to provide lesser dispersion forces, thus weakening their adsorptive strength for small molecules. Part b of [Figure 9](#) compares the ATR-IR spectra obtained on the full set of samples, which are presented together with ATR-IR spectra obtained on benzoic acid (in DMSO solution) and pure DMSO. The benzoic acid spectrum is included to determine whether the benzoate detected in the samples (see ^1H NMR results in [Figure 4](#)) can simply be attributed to free benzoic acid molecules in the MOF pores. However, it is clear that this is not the case since benzoic acid's most intense signals at 1700 and 1250 cm^{-1} [due to $\nu(\text{C}=\text{O})$ and $\nu(\text{C}-\text{O})$, respectively highlighted by the hashes in [Figure 9b](#)] are only very faintly visible in the spectra obtained on the UiO-66 samples and do not have a clear relationship with the amount of benzoic acid used in their syntheses, as more clearly shown in [Figure S2](#). Instead, they feature bands at 1580 and 1394 cm^{-1} , due to the $\nu_{\text{asym}}(\text{OCO})$ and $\nu_{\text{sym}}(\text{OCO})$ modes of carboxylate groups, respectively. One may have expected to see a trend in which the intensity of these bands follows the amount of benzoic acid used in the synthesis, but this is not the case, since the carboxylate groups are not unique to benzoate (they are also

present in the linker and formate ligands). However, a trend is clearly observed in the intensity of the weak signals falling at 1178, 1070, and 1025 cm^{-1} (each highlighted by the asterisk in [Figure 9b](#)), eventually plateauing in the spectra obtained on 40Benz and 50Benz. An enlarged view of this spectral range is reported in the [Supporting Information](#) ([Figure S1](#)). This trend is very similar to that of the defect descriptors discussed earlier, strongly suggesting that these bands are associated with the presence of defect-compensating benzoate moieties in the UiO-66 framework.

The Raman spectra obtained on the full set of samples (after thorough activation; see the [Experimental Section](#)) are presented in [Figure 10](#), together with those recorded on solid benzoic acid, benzoic acid in DMSO solution, and pure DMSO.

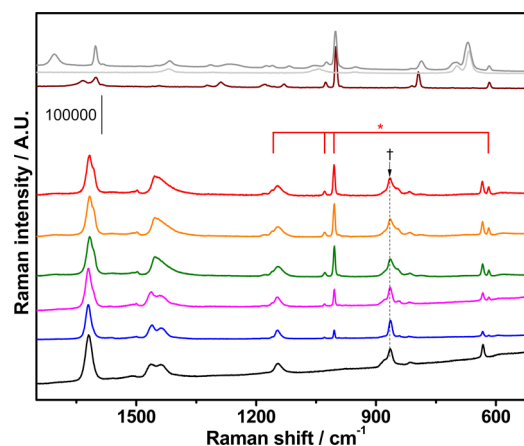


Figure 10. Raman spectra obtained on the full set of samples (activated under dynamic vacuum for 2 h at 200 °C), solid benzoic acid, benzoic acid in DMSO solution, and DMSO. The UiO-66 spectra were normalized to the intensity of the band at 866 cm^{-1} (emphasized with a dagger in the figure). Key: UiO-66-Ref. (black), 10Benz (blue), 20Benz (magenta), 30Benz (green), 40Benz (orange), 50Benz (red), solid benzoic acid (brown), benzoic acid in DMSO (gray), and DMSO (light gray).

As one can see, the Raman spectra of these materials feature many fewer bands than their FTIR counterpart, allowing for an easier identification of specific fingerprints ascribable to the presence of the benzoate ligands. Spectra obtained on benzoic acid (both as a pure solid and as a DMSO solution) have again been included for comparison to determine whether any free benzoic acid (evidenced in previous studies⁷⁷) is present in the MOF pores. To this end, it is clear that benzoic acid was completely removed by washing since key bands [such as the $\nu(\text{C}=\text{O})$ at 1705 cm^{-1} and $\nu(\text{C}-\text{O})$ at 1260 cm^{-1} , among others] are completely absent from the UiO-66 spectra, as more clearly shown in [Figure S2](#). Conversely, new bands (highlighted with an asterisk in the figure) appear at 1161 (shouldering the band at 1147 cm^{-1}), 1029, 1005, and 618 cm^{-1} in the spectra obtained on the benzoic acid-modulated UiO-66 samples, systematically increasing in intensity as the amount of benzoic acid used in the synthesis was increased. Much like the defectivity descriptors discussed throughout this work, the intensity of these bands reaches a plateau in the spectra obtained for 30Benz, 40Benz, and 50Benz, strongly suggesting that these new bands are associated with the presence of defect-compensating benzoate moieties in the UiO-66 framework.

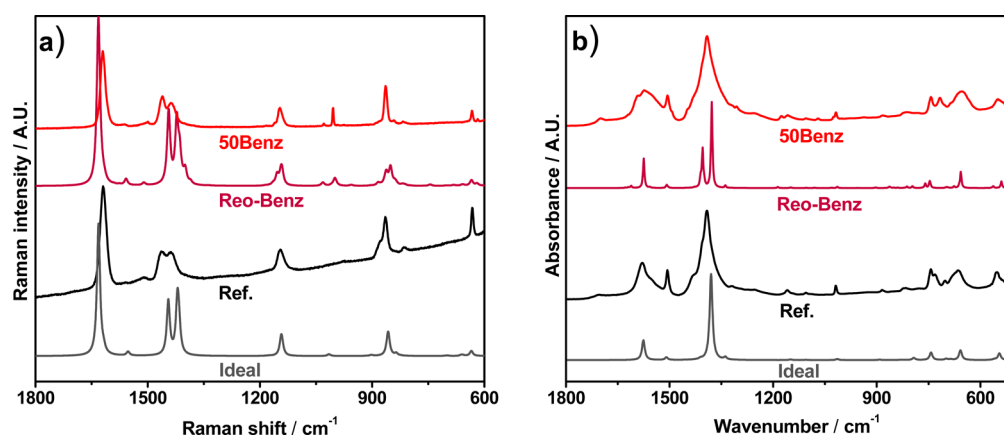


Figure 11. Comparison between simulated (dark gray and dark red) and experimental (black and red) spectra of Ref. (black) and 50Benz MOFs (red) samples with Ideal (dark gray) and Reo-Benz (dark red) models by the means of Raman (a) and IR (b) spectroscopies.

Table 3. Assignment of a Selection of Experimental and Calculated Vibrational Modes Compared for the Perfect “Ideal” and Defective “Reo-Benz” Models^a

experimental		computed		description of the mode
IR	Raman	IR	Raman	
3672	not visible	3812	3812	OH stretching of isolated hydroxyls
3065	not active	3181, 3176	not active	CH stretching in terephthalate and benzoate
3030	not visible	3146, 3139	3146, 3139	CH stretching in benzoate
1700	1705	not calcd	not calcd	C=O stretching of benzoic acid
1580	not visible	1575	1575	OCO asymmetric stretching in carboxylate
not active	1620	not active	1632	C=C stretching of aromatic rings
not detectable	1452, 1434	1445, 1422	1445, 1422	OCO symmetric stretching in carboxylate in-phase
1394	not active	1378	not active	OCO symmetric stretching in carboxylate out-of-phase
1252	1260	not calcd	not calcd	C–O stretching of benzoic acid
1178	not active	1187	not active	in-plane CH bending in benzoates
1158	not active	1150	not active	in-plane CH bending in terephthalates and benzoates
not active	1161	not active	1165	in plane CCH bending in benzoates
not active	1147	not active	1154	terephthalates rings breathing + benzoate rings deformation
1070	not active	1080	not active	in-plane CCH bending in benzoates
1025	1029	1031	1031	benzene ring deformation in benzoates
1019	not active	1014	not active	benzene ring deformation in terephthalates
not active	1005	not active	1001	benzene ring deformation in benzoates
not active	633	not active	634	benzene ring deformation in terephthalates
not active	618	not active	619	benzene ring deformation in benzoates

^aA scaling factor of 0.98 has been adopted in order to correct for the DFT overestimation issue.

In order to assign all these spectroscopic features, a parallel computational study on the perfect “Ideal” UiO-66 framework and on the Reo-Benz defective counterpart (see the [Experimental Section](#) for the details) has been conducted. Parts a and b of [Figure 11](#) compare the experimental data obtained in case of 50Benz UiO-66 sample with the computed ones. Thanks to the possibility to animate each vibrational frequency, the assignments of major bands was possible. [Table 3](#) summarizes the most relevant vibrational features with the corresponding assignment based on the animations visualized for both Raman and IR computed spectra.

At least four signals of the Raman spectra can be unambiguously assigned to the presence of modeled defects: the modes falling at 1029, 1005, and 618 cm^{-1} , present only in the defective samples, are due to the deformation of the benzene rings belonging to benzoate moieties (vibrational modes that are prohibited for symmetry in terephthalates). The 1161 cm^{-1} signal is similarly assigned to a CH bending mode

involving the proton in the para position with respect to the carboxylate in benzoates.

In the IR spectra three very weak signals falling at 1178, 1070, and 1025 cm^{-1} (shoulder) are ascribed in the same way to ring deformations and CH bending modes.

The computed intensity of all these signals with respect to the measured ones is slightly higher, as the Reo-Benz model has been constructed with a molar ratio between benzoates and terephthalates of 1:1, whereas liquid NMR measurements (see [Table 2](#) and [Table S2, Supporting Information](#)) have found only a molar ratio of 0.78:1 for the 50Benz sample. It should be noticed that, as the broadening of the computed spectral signals is arbitrarily set to 5 cm^{-1} , only the integrated intensity should be taken into account.

The $\nu(\text{C-H})$ region (reported only for experimental infrared spectroscopy in [Figure 9a](#)), which shows two different signals belonging to terephthalates and benzoates (falling respectively at 3065 and 3030 cm^{-1}), is again nicely modeled by the DFT calculations.

4. CONCLUSIONS

A systematic and detailed study about the synthetic insertion of missing-cluster defects (via benzoic acid additions) inside the UiO-66 framework has been reported through the present work, together with their characterization with a selection of techniques. While the long-range crystalline order of the original framework has been preserved, as demonstrated by the PXRD patterns, tiny nanoregions where defects order themselves were identified by the growth of a broad symmetry-prohibited diffraction peak, the intensity of which is strongly correlated with the number of introduced defects.

The true concentration of Reo-Benz defects has been accurately measured with dissolution liquid $^1\text{H}/\text{NMR}$ spectroscopy: the outcome reveals that even massive excesses of benzoic acid during synthesis (up to 50 equiv in the 50Benz sample) are only able to insert about 0.78 benzoic moieties per terephthalic ligand: this number is likely to be a plateau, as also 30Benz and 40Benz samples almost reached this value.

Coming to N_2 physisorption measurements, we noticed that defectivity is able to effectively increase the accessible surface area inside the framework by about 30% with respect to the reference sample with a change in the shape of the isotherm, which probably points out differences in the dimensions of the micropores now accessible thanks to the presence of defects. Vibrational spectroscopy (IR and Raman) measurements gave a beautiful set of spectra with a series of signals for which the relative intensity is growing with the concentration of defects; the identity of every vibrational band has been fully assigned with ab initio DFT calculations and the graphical analysis of the vibrational modes. The effectiveness of the constructed atomistic models, representative of both ideal and defective structures, is confirmed by both isotherm simulation and simulated IR and Raman vibrational spectra, which are in nice agreement with experimental results. Nevertheless, in situ IR spectroscopy of vacuum-treated samples pointed out that defective samples are more hydrophobic than their ideal counterpart, a result that is in agreement with the nonpolar nature of benzoate moieties.

This work also demonstrates that these techniques can be used as a “tool-box” to probe the presence and the concentration of dangling benzoate moieties inside the MOF; this approach could potentially be extended to different chemical species (i.e., other monodentate ligands) if they also present a well-defined spectroscopic fingerprint.

Empowered by these results, we presented in the present paper strong evidence of the possibility to include benzoate-decorated defects inside the UiO-66 framework and to specifically characterize them. This “defect-engineering” approach is able to increase the sorptive performance of this material by a significant degree, as discussed in the Introduction, and can be used to tune the properties of these materials for specific applications.

■ ASSOCIATED CONTENT

■ Supporting Information

The Supporting Information is available free of charge on the ACS Publications website at DOI: 10.1021/acs.jpcc.7b00483.

Quantitative data extracted from PXRD and $^1\text{H}/\text{NMR}$ measurements; comparison between vibrational spectra of MOFs and benzoic acid; detailed description of the method used for calculating the relative intensity of the broad PXRD peak, the BET area, and the molar ratios

between linker and modulator from $^1\text{H}/\text{NMR}$ data (PDF)

■ AUTHOR INFORMATION

Corresponding Author

*E-mail: silvia.bordiga@unito.it.

ORCID

Carlo Lamberti: 0000-0001-8004-2312

Silvia Bordiga: 0000-0003-2371-4156

Notes

The authors declare no competing financial interest.

■ ACKNOWLEDGMENTS

The work received financial support from the Research Council of Norway, thanks to the FUTUREFEED project Grant Number 228157. C.A. acknowledges Horizon 2020 ProDIA project (grant agreement No 685727). G.C.S. thanks inGAP Center of Research-based innovation, which receives financial support from the Research Council of Norway under Contract 174893. C.L. acknowledge the Mega-grant of the Russian Federation Government, No. 14.Y26.31.0001. The computational work was performed on the Abel Cluster, owned by the University of Oslo and the Norwegian Metacenter for High Performance Computing (NOTUR) and operated by the Department for Research Computing at USIT, the University of Oslo IT Department (<http://www.hpc.uio.no/>).

■ REFERENCES

- (1) Furukawa, H.; Cordova, K. E.; O’Keeffe, M.; Yaghi, O. M. The Chemistry and Applications of Metal-Organic Frameworks. *Science* **2013**, *341*, 1230444.
- (2) Kaskel, S. The Chemistry of Metal–Organic Frameworks: Synthesis. In *Characterization, and Applications*; Kaskel, S., Ed.; John Wiley & Sons: Weinheim, 2016.
- (3) Sumida, K.; Rogow, D. L.; Mason, J. A.; McDonald, T. M.; Bloch, E. D.; Herm, Z. R.; Bae, T.-H. H.; Long, J. R. Carbon Dioxide Capture in Metal-Organic Frameworks. *Chem. Rev.* **2012**, *112*, 724–781.
- (4) Corma, A.; García, H.; Llabrés i Xamena, F. X. Engineering Metal Organic Frameworks for Heterogeneous Catalysis. *Chem. Rev.* **2010**, *110*, 4606–4655.
- (5) Kaye, S. S.; Dailly, A.; Yaghi, O. M.; Long, J. R. Impact of Preparation and Handling on the Hydrogen Storage Properties of $\text{Zn}_4\text{O}(1,4\text{-benzenedicarboxylate})_3$ (MOF-5). *J. Am. Chem. Soc.* **2007**, *129*, 14176–14177.
- (6) Tan, K.; Nijem, N.; Canepa, P.; Gong, Q.; Li, J.; Thonhauser, T.; Chabal, Y. J. Stability and Hydrolyzation of Metal Organic Frameworks with Paddle-Wheel SBUs upon Hydration. *Chem. Mater.* **2012**, *24*, 3153–3167.
- (7) Saha, D.; Deng, S. Structural Stability of Metal Organic Framework MOF-177. *J. Phys. Chem. Lett.* **2010**, *1*, 73–78.
- (8) Lu, P.; Wu, Y.; Kang, H.; Wei, H.; Liu, H.; Fang, M. What Can pKa and NBO Charges of the Ligands Tell Us about the Water and Thermal Stability of Metal Organic Frameworks? *J. Mater. Chem. A* **2014**, *2*, 16250–16267.
- (9) Bosch, M.; Zhang, M.; Zhou, H.-C. Increasing the Stability of Metal-Organic Frameworks. *Adv. Chem.* **2014**, *2014*, 1–8.
- (10) Kalidindi, S. B.; Nayak, S.; Briggs, M. E.; Jansat, S.; Katsoulidis, A. P.; Miller, G. J.; Warren, J. E.; Antypov, D.; Corà, F.; Slater, B.; et al. Chemical and Structural Stability of Zirconium-Based Metal-Organic Frameworks with Large Three-Dimensional Pores by Linker Engineering. *Angew. Chem., Int. Ed.* **2015**, *54*, 221–226.
- (11) Wang, B.; Lv, X. L.; Feng, D.; Xie, L. H.; Zhang, J.; Li, M.; Xie, Y.; Li, J. R.; Zhou, H. C. Highly Stable Zr(IV)-Based Metal-Organic Frameworks for the Detection and Removal of Antibiotics and Organic Explosives in Water. *J. Am. Chem. Soc.* **2016**, *138*, 6204–6216.

- (12) Cavka, J. H.; Jakobsen, S.; Olsbye, U.; Guillou, N.; Lamberti, C.; Bordiga, S.; Lillerud, K. P. A New Zirconium Inorganic Building Brick Forming Metal Organic Frameworks with Exceptional Stability. *J. Am. Chem. Soc.* **2008**, *130*, 13850–13851.
- (13) Schaate, A.; Roy, P.; Preuße, T.; Lohmeier, S. J.; Godt, A.; Behrens, P. Porous Interpenetrated Zirconium-Organic Frameworks (PIZOFs): A Chemically Versatile Family of Metal-Organic Frameworks. *Chem. - Eur. J.* **2011**, *17*, 9320–9325.
- (14) Wang, R.; Wang, Z.; Xu, Y.; Dai, F.; Zhang, L.; Sun, D. Porous Zirconium Metal–Organic Framework Constructed from 2D → 3D Interpenetration Based on a 3,6-Connected kgd Net. *Inorg. Chem.* **2014**, *53*, 7086–7088.
- (15) Ma, J.; Wong-Foy, A. G.; Matzger, A. J. The Role of Modulators in Controlling Layer Spacings in a Tritopic Linker Based Zirconium 2D Microporous Coordination Polymer. *Inorg. Chem.* **2015**, *54*, 4591–4593.
- (16) Kandiah, M.; Nilsen, M. H.; Usseglio, S.; Jakobsen, S.; Olsbye, U.; Tilset, M.; Larabi, C.; Quadrelli, E. A.; Bonino, F.; Lillerud, K. P. Synthesis and Stability of Tagged UiO-66 Zr-MOFs. *Chem. Mater.* **2010**, *22*, 6632–6640.
- (17) Cavka, J. H.; Grande, C. A.; Mondino, G.; Blom, R. High Pressure Adsorption of CO₂ and CH₄ on Zr-MOFs. *Ind. Eng. Chem. Res.* **2014**, *53*, 15500–15507.
- (18) Øien-Ødegaard, S.; Bouchevreau, B.; Hylland, K.; Wu, L.; Blom, R.; Grande, C.; Olsbye, U.; Tilset, M.; Lillerud, K. P. UiO-67-Type Metal-Organic Frameworks with Enhanced Water Stability and Methane Adsorption Capacity. *Inorg. Chem.* **2016**, *55*, 1986–1991.
- (19) Yee, K. K.; Reimer, N.; Liu, J.; Cheng, S. Y.; Yiu, S. M.; Weber, J.; Stock, N.; Xu, Z. Effective Mercury Sorption by Thiol-Laced Metal-Organic Frameworks: In Strong Acid and the Vapor Phase. *J. Am. Chem. Soc.* **2013**, *135*, 7795–7798.
- (20) Pullen, S.; Fei, H.; Orthaber, A.; Cohen, S. M.; Ott, S. Enhanced Photochemical Hydrogen Production by a Molecular Diiron Catalyst Incorporated into a Metal-Organic Framework. *J. Am. Chem. Soc.* **2013**, *135*, 16997–17003.
- (21) Biswas, S.; Zhang, J.; Li, Z.; Liu, Y.-Y.; Grzywa, M.; Sun, L.; Volkmer, D.; Van Der Voort, P. Enhanced Selectivity of CO₂ over CH₄ in Sulphonate-, Carboxylate- and Iodo-Functionalized UiO-66 Frameworks. *Dalton Trans.* **2013**, *42*, 4730.
- (22) Huang, Y.; Qin, W.; Li, Z.; Li, Y. Enhanced Stability and CO₂ Affinity of a UiO-66 Type Metal-Organic Framework Decorated with Dimethyl Groups. *Dalton Trans.* **2012**, *41*, 9283–9285.
- (23) Biswas, S.; Van Der Voort, P. A General Strategy for the Synthesis of Functionalised UiO-66 Frameworks: Characterisation, Stability and CO₂ Adsorption Properties. *Eur. J. Inorg. Chem.* **2013**, *2013*, 2154–2160.
- (24) Lin Foo, M.; Horike, S.; Fukushima, T.; Hijikata, Y.; Kubota, Y.; Takata, M.; Kitagawa, S. Ligand-Based Solid Solution Approach to Stabilisation of Sulphonic Acid Groups in Porous Coordination Polymer Zr₆O₄(OH)₄(BDC)₆ (UiO-66). *Dalton Trans.* **2012**, *41*, 13791–13794.
- (25) Fei, H.; Cohen, S. M. Metalation of a Thiocatechol-Functionalized Zr(IV)-Based Metal-Organic Framework for Selective C-H Functionalization. *J. Am. Chem. Soc.* **2015**, *137*, 2191–2194.
- (26) Jasuja, H.; Zang, J.; Sholl, D. S.; Walton, K. S. Rational Tuning of Water Vapor and CO₂ Adsorption in Highly Stable Zr-Based MOFs. *J. Phys. Chem. C* **2012**, *116*, 23526–23532.
- (27) Fei, H.; Shin, J.; Meng, Y. S.; Adelhardt, M.; Sutter, J.; Meyer, K.; Cohen, S. M. Reusable Oxidation Catalysis Using Metal-Monocatecholato Species in a Robust Metal-Organic Framework. *J. Am. Chem. Soc.* **2014**, *136*, 4965–4973.
- (28) Nickerl, G.; Senkowska, I.; Kaskel, S. Tetrazine Functionalized Zirconium MOF as Optical Sensor for Oxidizing Gases. *Chem. Commun.* **2015**, *51*, 2280–2282.
- (29) Yang, Q.; Vaesen, S.; Ragon, F.; Wiersum, A. D.; Wu, D.; Lago, A.; Devic, T.; Martineau, C.; Taulelle, F.; Llewellyn, P. L.; et al. A Water Stable Metal-Organic Framework with Optimal Features for CO₂ Capture. *Angew. Chem., Int. Ed.* **2013**, *52*, 10316–10320.
- (30) Xydias, P.; Spanopoulos, I.; Klontzas, E.; Froudakis, G. E.; Trikalitis, P. N. Drastic Enhancement of the CO₂ Adsorption Properties in Sulfone-Functionalized Zr- and Hf-UiO-67 MOFs with Hierarchical Mesopores. *Inorg. Chem.* **2014**, *53*, 679–681.
- (31) Chavan, S.; Vitillo, J. G.; Uddin, M. J.; Bonino, F.; Lamberti, C.; Groppo, E.; Lillerud, K.-P.; Bordiga, S. Functionalization of UiO-66 Metal–Organic Framework and Highly Cross-Linked Polystyrene with Cr(CO)₃: In Situ Formation, Stability, and Photoreactivity. *Chem. Mater.* **2010**, *22*, 4602–4611.
- (32) Øien, S.; Agostini, G.; Svelle, S.; Borfecchia, E.; Lomachenko, K. A.; Mino, L.; Gallo, E.; Bordiga, S.; Olsbye, U.; Lillerud, K. P. Probing Reactive Platinum Sites in UiO-67 Zirconium Metal–Organic Frameworks. *Chem. Mater.* **2015**, *27*, 1042–1056.
- (33) Ragon, F.; Campo, B.; Yang, Q.; Martineau, C.; Wiersum, A. D.; Lago, A.; Guillerm, V.; Hemsley, C.; Eubank, J. F.; Vishnuvarthan, M.; et al. Acid-Functionalized UiO-66(Zr) MOFs and Their Evolution after Intra-Framework Cross-Linking: Structural Features and Sorption Properties. *J. Mater. Chem. A* **2015**, *3*, 3294–3309.
- (34) Chavan, S. M.; Shearer, G. C.; Svelle, S.; Olsbye, U.; Bonino, F.; Ethiraj, J.; Lillerud, K. P.; Bordiga, S. Synthesis and Characterization of Amine-Functionalized Mixed-Ligand Metal – Organic Frameworks of UiO-66 Topology. *Inorg. Chem.* **2014**, *53*, 9509–9515.
- (35) DeCoste, J. B.; Peterson, G. W.; Jasuja, H.; Glover, T. G.; Huang, Y.; Walton, K. S. Stability and Degradation Mechanisms of Metal-Organic Frameworks Containing the Zr₆O₄(OH)₄ Secondary Building Unit. *J. Mater. Chem. A* **2013**, *1*, 5642–5650.
- (36) Hylland, K.; Øien-Ødegaard, S.; Lillerud, K.; Tilset, M. Efficient, Scalable Syntheses of Linker Molecules for Metal-Organic Frameworks. *Synlett* **2015**, *26*, 1480–1485.
- (37) Shearer, G. C.; Chavan, S.; Bordiga, S.; Svelle, S.; Olsbye, U.; Lillerud, K. P. Defect Engineering: Tuning the Porosity and Composition of the Metal-Organic Framework UiO-66 via Modulated Synthesis. *Chem. Mater.* **2016**, *28*, 3749–3761.
- (38) Liang, W.; Coghlan, C. J.; Ragon, F.; Rubio-Martinez, M.; D'Alessandro, D. M.; Babarao, R. Defect Engineering of UiO-66 for CO₂ and H₂O Uptake – a Combined Experimental and Simulation Study. *Dalton Trans.* **2016**, *45*, 4496–4500.
- (39) Fang, Z.; Bueken, B.; De Vos, D. E.; Fischer, R. A. Defect-Engineered Metal-Organic Frameworks. *Angew. Chem., Int. Ed.* **2015**, *54*, 7234–7254.
- (40) Wu, D.; Yan, W.; Xu, H.; Zhang, E.; Li, Q. Defect Engineering of Mn-Based MOFs with Rod-Shaped Building Units by Organic Linker Fragmentation. *Inorg. Chim. Acta* **2017**, *460*, 93–98.
- (41) Kozachuk, O.; Luz, L.; Llabrés i Xamena, F. X.; Noei, H.; Kauer, M.; Albada, H. B.; Bloch, E. D.; Marler, B.; Wang, Y.; Muhler, M.; et al. Multifunctional, Defect-Engineered Metal-Organic Frameworks with Ruthenium Centers: Sorption and Catalytic Properties. *Angew. Chem., Int. Ed.* **2014**, *53*, 7058–7062.
- (42) Jiang, Z. R.; Wang, H.; Hu, Y.; Lu, J.; Jiang, H. L. Polar Group and Defect Engineering in a Metal-Organic Framework: Synergistic Promotion of Carbon Dioxide Sorption and Conversion. *ChemSusChem* **2015**, *8*, 878–885.
- (43) DeStefano, M. R.; Islamoglu, T.; Garibay, S. J.; Hupp, J. T.; Farha, O. K. Room Temperature Synthesis of UiO-66 and the Thermal Modulation of Densities of Defect Sites. *Chem. Mater.* **2017**, *29*, 1357–1361.
- (44) Dissegna, S.; Hardian, R.; Epp, K.; Kieslich, G.; Coulet, M.-V.; Llewellyn, P.; Fischer, R. A. Using Water Adsorption Measurements To Access the Chemistry of Defects in the Metal–Organic Framework UiO-66. *CrystEngComm* **2017**, in press, DOI: [10.1039/C7CE00224F](https://doi.org/10.1039/C7CE00224F).
- (45) Takashima, Y.; Sato, Y.; Tsuruoka, T.; Akamatsu, K. Unusual Colorimetric Change for Alkane Solvents with a Porous Coordination Framework. *Inorg. Chem.* **2016**, *55*, 11617–11620.
- (46) Cai, G.; Jiang, H.-L. A Modulator-Induced Defect-Formation Strategy to Hierarchically Porous Metal-Organic Frameworks with High Stability. *Angew. Chem.* **2017**, *129*, 578–582.
- (47) Gutov, O. V.; Hevia, M. G.; Escudero-Adán, E. C.; Shafir, A. Metal-Organic Framework (MOF) Defects under Control: Insights

into the Missing Linker Sites and Their Implication in the Reactivity of Zirconium-Based Frameworks. *Inorg. Chem.* **2015**, *54*, 8396–8400.

(48) Wu, H.; Chua, Y. S.; Krungleviciute, V.; Tyagi, M.; Chen, P.; Yildirim, T.; Zhou, W. Unusual and Highly Tunable Missing-Linker Defects in Zirconium Metal-Organic Framework UiO-66 and Their Important Effects on Gas Adsorption. *J. Am. Chem. Soc.* **2013**, *135*, 10525–10532.

(49) Shearer, G. C.; Vitillo, J. G.; Bordiga, S.; Svelle, S.; Olsbye, U.; Lillerud, K. P. Functionalizing the Defects: Postsynthetic Ligand Exchange in the Metal Organic Framework UiO-66. *Chem. Mater.* **2016**, *28*, 7190–7193.

(50) Vermoortele, F.; Bueken, B.; Le Bars, G.; Van De Voorde, B.; Vandichel, M.; Houthoofd, K.; Vimont, A.; Daturi, M.; Waroquier, M.; Van Speybroeck, V.; et al. Synthesis Modulation as a Tool to Increase the Catalytic Activity of Metal-Organic Frameworks: The Unique Case of UiO-66(Zr). *J. Am. Chem. Soc.* **2013**, *135*, 11465–11468.

(51) Vandichel, M.; Hajek, J.; Vermoortele, F.; Waroquier, M.; De Vos, D. E.; Van Speybroeck, V. Active Site Engineering in UiO-66 Type Metal-organic Frameworks by Intentional Creation of Defects: A Theoretical Rationalization. *CrystEngComm* **2015**, *17*, 395–406.

(52) Cliffe, M. J.; Wan, W.; Zou, X.; Chater, P. a.; Kleppe, A. K.; Tucker, M. G.; Wilhelm, H.; Funnell, N. P.; Coudert, F.-X.; Goodwin, A. L. Correlated Defect Nanoregions in a Metal-Organic Framework. *Nat. Commun.* **2014**, *5*, 4176.

(53) Taylor, J. M.; Dekura, S.; Ikeda, R.; Kitagawa, H. Defect Control to Enhance Proton Conductivity in a Metal-Organic Framework. *Chem. Mater.* **2015**, *27*, 2286–2289.

(54) Cliffe, M. J.; Hill, J. A.; Murray, C. A.; Coudert, F.-X.; Goodwin, A. L. Defect-Dependent Colossal Negative Thermal Expansion in UiO-66(Hf) Metal-organic Framework. *Phys. Chem. Chem. Phys.* **2015**, *17*, 11586–11592.

(55) Van de Voorde, B.; Stassen, I.; Bueken, B.; Vermoortele, F.; De Vos, D.; Ameloot, R.; Tan, J.-C.; Bennett, T. D. Improving the Mechanical Stability of Zirconium-Based Metal-organic Frameworks by Incorporation of Acidic Modulators. *J. Mater. Chem. A* **2015**, *3*, 1737–1742.

(56) Ren, J.; Langmi, H. W.; Musyoka, N. M.; Mathe, M.; Kang, X.; Liao, S. Tuning Defects to Facilitate Hydrogen Storage in Core-Shell MIL-101(Cr)@UiO-66(Zr) Nanocrystals. *Mater. Today Proc.* **2015**, *2*, 3964–3972.

(57) Yang, D.; Odoh, S. O.; Borycz, J.; Wang, T. C.; Farha, O. K.; Hupp, J. T.; Cramer, C. J.; Gagliardi, L.; Gates, B. C. Tuning Zr₆ Metal-Organic Framework (MOF) Nodes as Catalyst Supports: Site Densities and Electron-Donor Properties Influence Molecular Iridium Complexes as Ethylene Conversion Catalysts. *ACS Catal.* **2016**, *6*, 235–247.

(58) Li, B.; Zhu, X.; Hu, K.; Li, Y.; Feng, J.; Shi, J.; Gu, J. Defect Creation in Metal-Organic Frameworks for Rapid and Controllable Decontamination of Roxarsone from Aqueous Solution. *J. Hazard. Mater.* **2016**, *302*, 57–64.

(59) Wang, K.; Li, C.; Liang, Y.; Han, T.; Huang, H.; Yang, Q.; Liu, D.; Zhong, C. Rational Construction of Defects in a Metal-Organic Framework for Highly Efficient Adsorption and Separation of Dyes. *Chem. Eng. J.* **2016**, *289*, 486–493.

(60) Yang, D.; Bernales, V.; Islamoglu, T.; Farha, O. K.; Hupp, J. T.; Cramer, C. J.; Gagliardi, L.; Gates, B. C. Tuning the Surface Chemistry of Metal Organic Framework Nodes: Proton Topology of the Metal-Oxide-Like Zr₆ Nodes of UiO-66 and NU-1000. *J. Am. Chem. Soc.* **2016**, *138*, 15189–15196.

(61) Katz, M. J.; Brown, Z. J.; Colón, Y. J.; Siu, P. W.; Scheidt, K. A.; Snurr, R. Q.; Hupp, J. T.; Farha, O. K. A Facile Synthesis of UiO-66, UiO-67 and Their Derivatives. *Chem. Commun.* **2013**, *49*, 9449–9451.

(62) DeCoste, J. B.; Demasky, T. J.; Katz, M. J.; Farha, O. K.; Hupp, J. T. A UiO-66 Analogue with Uncoordinated Carboxylic Acids for the Broad-Spectrum Removal of Toxic Chemicals. *New J. Chem.* **2015**, *39*, 2396–2399.

(63) Song, J. Y.; Ahmed, I.; Seo, P. W.; Jhung, S. H. UiO-66-Type Metal-Organic Framework with Free Carboxylic Acid: Versatile

Adsorbents via H-Bond for Both Aqueous and Nonaqueous Phases. *ACS Appl. Mater. Interfaces* **2016**, *8*, 27394–27402.

(64) Vermoortele, F.; Vandichel, M.; Van De Voorde, B.; Ameloot, R.; Waroquier, M.; Van Speybroeck, V.; De Vos, D. E. Electronic Effects of Linker Substitution on Lewis Acid Catalysis with Metal-Organic Frameworks. *Angew. Chem., Int. Ed.* **2012**, *51*, 4887–4890.

(65) Katz, M. J.; Klet, R. C.; Moon, S.-Y.; Mondloch, J. E.; Hupp, J. T.; Farha, O. K. One Step Backward Is Two Steps Forward: Enhancing the Hydrolysis Rate of UiO-66 by Decreasing [OH⁻]. *ACS Catal.* **2015**, *5*, 4637–4642.

(66) Nasalevich, M.; Hendon, C.; Santaclara, J. G.; Svane, K.; van der Linden, B.; Veber, S.; Fedin, M.; van der Veen, M.; Kapteijn, F.; Walsh, A.; et al. Electronic Origins of Photocatalytic Activity in d⁰ Metal Organic Frameworks. *Sci. Rep.* **2016**, *6*, 23676.

(67) Ghosh, P.; Colón, Y. J.; Snurr, R. Q. Water Adsorption in UiO-66: The Importance of Defects. *Chem. Commun.* **2014**, *50*, 11329–11331.

(68) Han, Y.; Liu, M.; Li, K.; Zuo, Y.; Wei, Y.; Xu, S.; Zhang, G.; Song, C.; Zhang, Z. C.; Guo, X. Facile Synthesis of Morphology- and Size-Controlled Zirconium Metal-Organic Framework UiO-66: The Role of Hydrofluoric Acid in Crystallization. *CrystEngComm* **2015**, *17*, 6434–6440.

(69) Gutov, O. V.; Molina, S.; Escudero-Adán, E. C.; Shafrir, A. Modulation by Amino Acids: Toward Superior Control in the Synthesis of Zirconium Metal-Organic Frameworks. *Chem. - Eur. J.* **2016**, *22*, 13582–13587.

(70) Trickett, C. A.; Gagnon, K. J.; Lee, S.; Gándara, F.; Bürgi, H. B.; Yaghi, O. M. Definitive Molecular Level Characterization of Defects in UiO-66 Crystals. *Angew. Chem., Int. Ed.* **2015**, *54*, 11162–11167.

(71) Øien, S.; Wragg, D.; Reinsch, H.; Svelle, S.; Bordiga, S.; Lamberti, C.; Lillerud, K. P. Detailed Structure Analysis of Atomic Positions and Defects in Zirconium Metal-Organic Frameworks. *Cryst. Growth Des.* **2014**, *14*, 5370–5372.

(72) Ling, S.; Slater, B. Dynamic Acidity in Defective UiO-66. *Chem. Sci.* **2016**, *7*, 4706–4712.

(73) Shearer, G. C.; Chavan, S.; Ethiraj, J.; Vitillo, J. G.; Svelle, S.; Olsbye, U.; Lamberti, C.; Bordiga, S.; Lillerud, K. P. Tuned to Perfection: Ironing out the Defects in Metal-Organic Framework UiO-66. *Chem. Mater.* **2014**, *26*, 4068–4071.

(74) Thornton, A. W.; Babarao, R.; Jain, A.; Trouselet, F.; Coudert, F.-X. Defects in Metal-organic Frameworks: A Compromise between Adsorption and Stability? *Dalton Trans.* **2016**, *45*, 4352–4359.

(75) Howarth, A. J.; Liu, Y.; Hupp, J. T.; Farha, O. K. Metal-organic Frameworks for Applications in Remediation of Oxyanion/cation-Contaminated Water. *CrystEngComm* **2015**, *17*, 7245–7253.

(76) Rogge, S. M. J.; Wieme, J.; Vanduyhuys, L.; Vandenbrande, S.; Maurin, G.; Verstraelen, T.; Waroquier, M.; Van Speybroeck, V. Thermodynamic Insight in the High-Pressure Behavior of UiO-66: Effect of Linker Defects and Linker Expansion. *Chem. Mater.* **2016**, *28*, 5721–5732.

(77) Schaate, A.; Roy, P.; Godt, A.; Lippke, J.; Waltz, F.; Wiebcke, M.; Behrens, P. Modulated Synthesis of Zr-Based Metal-Organic Frameworks: From Nano to Single Crystals. *Chem. - Eur. J.* **2011**, *17*, 6643–6651.

(78) Ragon, F.; Horcajada, P.; Chevreau, H.; Hwang, Y. K.; Lee, U. H.; Miller, S. R.; Devic, T.; Chang, J. S.; Serre, C. In Situ Energy-Dispersive X-Ray Diffraction for the Synthesis Optimization and Scale-up of the Porous Zirconium Terephthalate UiO-66. *Inorg. Chem.* **2014**, *53*, 2491–2500.

(79) Abid, H. R.; Ang, H. M.; Wang, S. Effects of Ammonium Hydroxide on the Structure and Gas Adsorption of Nanosized Zr-MOFs (UiO-66). *Nanoscale* **2012**, *4*, 3089–3094.

(80) Marshall, R. J.; Hobday, C. L.; Murphie, C. F.; Griffin, S. L.; Morrison, C. A.; Moggach, S. A.; Forgan, R. S. Amino Acids as Highly Efficient Modulators for Single Crystals of Zirconium and Hafnium Metal-organic Frameworks. *J. Mater. Chem. A* **2016**, *4*, 6955–6963.

(81) Shearer, G. C.; Forselv, S.; Chavan, S.; Bordiga, S.; Mathisen, K.; Bjorgen, M.; Svelle, S.; Lillerud, K. P. In Situ Infrared Spectroscopic and Gravimetric Characterisation of the Solvent Removal and

Dehydroxylation of the Metal Organic Frameworks UiO-66 and UiO-67. *Top. Catal.* **2013**, *56*, 770–782.

(82) Valenzano, L.; Civalleri, B.; Chavan, S.; Bordiga, S.; Nilsen, M. H.; Jakobsen, S.; Lillerud, K. P.; Lamberti, C. Disclosing the Complex Structure of UiO-66 Metal Organic Framework: A Synergic Combination of Experiment and Theory. *Chem. Mater.* **2011**, *23*, 1700–1718.

(83) Lamberti, C.; Zecchina, A.; Groppo, E.; Bordiga, S. Probing the Surfaces of Heterogeneous Catalysts by in Situ IR Spectroscopy. *Chem. Soc. Rev.* **2010**, *39*, 4951.

(84) Bordiga, S.; Lamberti, C.; Bonino, F.; Travert, A.; Thibault-Starzyk, F. Probing Zeolites by Vibrational Spectroscopies. *Chem. Soc. Rev.* **2015**, *44*, 7262–7341.

(85) O'Keeffe, M.; Peskov, M. A.; Ramsden, S. J.; Yaghi, O. M. The Reticular Chemistry Structure Resource (RCSR) Database Of, and Symbols For, Crystal Nets. *Acc. Chem. Res.* **2008**, *41*, 1782–1789.

(86) Bonino, F.; Lamberti, C.; Chavan, S. M.; Vitillo, J. G.; Bordiga, S. Characterization of MOFs. 1. Combined Vibrational and Electronic Spectroscopies. In *Metal Organic Frameworks as Heterogeneous Catalysts*; Llabrés i Xamena, F., Gascon, J., Eds.; RSC Catalysis Series; Royal Society of Chemistry: Cambridge, 2013; pp 76–142.

(87) Bonino, F.; Lamberti, C.; Bordiga, S. IR and Raman Spectroscopies Probing MOFs Structure, Defectivity, and Reactivity. In *The Chemistry of Metal–Organic Frameworks: Synthesis, Characterization, and Applications*; Kaskel, S., Ed.; John Wiley & Sons: Weinheim, 2016; pp 657–690.

(88) Bárcia, P. S.; Guimarães, D.; Mendes, P. A. P.; Silva, J. A. C.; Guillerm, V.; Chevreau, H.; Serre, C.; Rodrigues, A. E. Reverse Shape Selectivity in the Adsorption of Hexane and Xylene Isomers in MOF UiO-66. *Microporous Mesoporous Mater.* **2011**, *139*, 67–73.

(89) Dovesi, R.; Orlando, R.; Erba, A.; Zicovich-Wilson, C. M.; Civalleri, B.; Casassa, S.; Maschio, L.; Ferrabone, M.; De La Pierre, M.; D'Arco, P.; et al. CRYSTAL14: A Program for the *Ab Initio* Investigation of Crystalline Solids. *Int. J. Quantum Chem.* **2014**, *114*, 1287–1317.

(90) Becke, A. D. Density-Functional Thermochemistry. III. The Role of Exact Exchange. *J. Chem. Phys.* **1993**, *98*, 5648–5652.

(91) Lee, C.; Yang, W.; Parr, R. G. Development of the Colle-Salvetti Correlation-Energy Formula into a Functional of the Electron Density. *Phys. Rev. B: Condens. Matter Mater. Phys.* **1988**, *37*, 785–789.

(92) Pascale, F.; Zicovich-Wilson, C. M.; López Gejo, F.; Civalleri, B.; Orlando, R.; Dovesi, R. The Calculation of the Vibrational Frequencies of Crystalline Compounds and Its Implementation in the CRYSTAL Code. *J. Comput. Chem.* **2004**, *25*, 888–897.

(93) Maschio, L.; Kirtman, B.; Rérat, M.; Orlando, R.; Dovesi, R. *Ab Initio* Analytical Raman Intensities for Periodic Systems through a Coupled Perturbed Hartree-Fock/Kohn-Sham Method in an Atomic Orbital Basis. II. Validation and Comparison with Experiments. *J. Chem. Phys.* **2013**, *139*, 164102.

(94) Maschio, L.; Kirtman, B.; Rérat, M.; Orlando, R.; Dovesi, R. *Ab Initio* Analytical Raman Intensities for Periodic Systems through a Coupled Perturbed Hartree-Fock/Kohn-Sham Method in an Atomic Orbital Basis. I. Theory. *J. Chem. Phys.* **2013**, *139*, 164101.

(95) Chavan, S.; Vitillo, J. G.; Gianolio, D.; Zavorotynska, O.; Civalleri, B.; Jakobsen, S.; Nilsen, M. H.; Valenzano, L.; Lamberti, C.; Lillerud, K. P.; et al. H₂ Storage in Isostructural UiO-67 and UiO-66 MOFs. *Phys. Chem. Chem. Phys.* **2012**, *14*, 1614–1626.

Modulator Effect in UiO-66-NDC (1,4-Naphthalenedicarboxylic Acid) Synthesis and Comparison with UiO-67-NDC Isoreticular Metal–Organic Frameworks

Vera V. Butova,^{*,†} Andriy P. Budnyk,[†] Alexander A. Guda,[†] Kirill A. Lomachenko,^{†,‡,§} Aram L. Bugaev,^{†,§} Alexander V. Soldatov,[†] Sachin M. Chavan,^{||} Sigurd Øien-Ødegaard,^{||} Unni Olsbye,^{||} Karl Petter Lillerud,^{||} Cesare Atzori,[§] Silvia Bordiga,^{§,||} and Carlo Lamberti^{*,†,⊥}

[†]International Research Center “Smart Materials”, Southern Federal University, 5 Zorge str., Rostov-on-Don, 344090, Russia

[‡]European Synchrotron Radiation Facility, 71 avenue des Martyrs, CS 40220, Grenoble Cedex 9, 38043 France

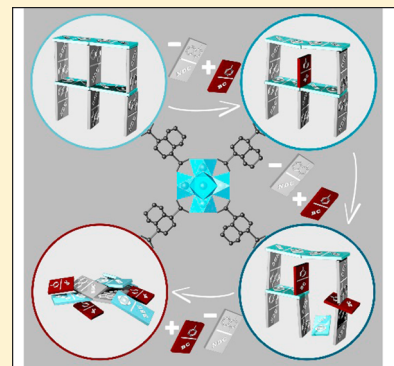
[§]Department of Chemistry, NIS Interdepartmental Center, INSTM Reference Center, University of Turin, Via P. Quarello 15, I-10135 Turin, Italy

^{||}Department of Chemistry, University of Oslo, N-0371 Oslo, Norway

[⊥]Department of Chemistry, CrisDi Interdepartmental Center, INSTM Reference Center, University of Turin, Via P. Giuria 7, I-10125 Turin, Italy

S Supporting Information

ABSTRACT: A zirconium metal–organic framework with UiO-66 topology was synthesized using a 1,4-naphthalenedicarboxylic acid (NDC) linker (UiO-66-NDC). From synchrotron powder X-ray diffraction (PXRD), we found that the naphthalene rings of the NDC linker are out of (*a,c*)-plane equilibrium by 30°, similar to the situation found by single crystal XRD for the benzene rings in UiO-67 (*Cryst. Growth Des.* 2014, 14, 5370). Different fractions of the benzene-carboxylic (BC) acid modulator versus NDC were used to tune structural properties of the final product. The modulator increases both the crystal size and the surface area of the product, but reduces its thermal stability owing to insertion of defects: missing linkers and missing $Zr_6(OH)_4O_4$ clusters. This study proves that the defect density (fraction of BC incorporation) can be tuned in UiO-66-NDC materials up to almost 50%. At that stage, the crystal is characterized also by a high density of missing $Zr_6(OH)_4O_4$ inorganic cornerstones. Notwithstanding such structural defectivity, even the most defective material is stable after thermal activation at 200 °C (able to fully remove the solvent) and in water conditions, opening possibilities for application in the fields of catalysis and molecule sorption.



1. INTRODUCTION

Metal–organic frameworks (MOFs)^{1,2} are a new class of porous materials with high surface area attracting attention due to their numerous potential applications for selective gas absorption³ and storage,^{4–6} catalysis,^{7–11} biomedicine,^{12,13} and others.^{14–18} One of the major reasons for their success in so many fields is the high flexibility in their structure and composition as they consist of metal–oxygen clusters (or secondary building units, SBUs) connected by organic molecules (linkers). In 2008 (and successive works), the Lillerud group reported a new family of zirconium-based MOFs, namely, UiO-66,67,68 (UiO stands for University of Oslo) with unprecedented thermal, chemical, and mechanical stability,^{19–31} that have found a wide range of applications.^{32–36} It has even been foreseen that the all-gas-phase synthesis of UiO-66 through modulated atomic layer deposition could enable implementations in microelectronics.³⁴ The prototype member of this family is UiO-66, with 1,4-benzene-dicarboxylate (BDC) as a linker and $Zr_6O_4(OH)_4$ as the SBU, that

transforms into Zr_6O_6 upon solvent removal.^{21–23} The framework is preserved up to 400 °C in air and possess a high surface area of 1236 m²/g.³⁷ In 2014 Shearer et al. reported that various synthesis methods can be used to tune the BDC incorporation in the framework, influencing both the surface area and the thermal stability of UiO-66.²⁴

In 2009 the “coordination modulator” concept was introduced by Tsuruoka et al. for capping reagents, who used carboxylic acids to regulate the rate of framework extension and crystal growth.³⁸ Later, other groups reported that addition of modulators to the synthesis of HKUST-1 results in formation of bigger crystals.^{39,40} A similar approach was further adopted for synthesis of UiO-66-type MOFs, reaching a higher surface area and better catalytic activity with respect to unmodulated UiO-66.^{41,42} Schaate et al.⁴³ employed benzoic and acetic acids

Received: June 25, 2017

Revised: July 25, 2017

Published: July 31, 2017

Table 1. Molar Composition of the Reagents and Average Size ($\langle L \rangle$) of the Resulting UiO-66-NDC Crystals after 24 h of Synthesis^a

sample name	ZrCl ₄ , mol	1,4NDC, mol	H ₂ O, mol	BC, mol	DMF, mol	$\langle L \rangle$, nm	surface area (m ² g ⁻¹)		pore volume (mm ³ g ⁻¹)
							BET	Langmuir	
0BC	1	1	3	0	300	80	448	593	221
10BC	1	1	3	10	300	150	575	696	260
60BC	1	1	3	60	300	800	693	840	319
100BC	1	1	3	100	300	NP			

^aComparable results have been obtained for the 96 h synthesis. Also reported in the last four columns are the surface area and the pore volume obtained from N₂ adsorption isotherms applying both BET and Langmuir methods (vide infra section 3.2). Pore volumes were calculated at $P/P_0 = 0.5$ and taking into account the density of liquid N₂ at 77 K.^{52,53} NP = no precipitate.

as modulators for synthesis of UiO-66 and other UiO-type structures.

The control of the defect chemistry in MOFs, in particular, for UiO-66, has been investigated in order to achieve better performances in many applications. This approach has been named “defect engineering” as a shorthand for the ability to manipulate defects by a synthetic and controlled way. Many authors have recently shown with their works several fascinating ways to achieve this kind of defect control.^{16,24,29,31,32,35,37,42,44–49}

On the other hand, Garibay et al.,⁵⁰ following a slightly modified procedure from ref 19, obtained a MOF with UiO-66 topology replacing BDC linkers with 1,4-naphthalenedicarboxylic acid (1,4-NDC). Because of structural similarity, it is labeled hereafter as UiO-66-NDC. The replacement of the linker opens new possibilities such as an increased affinity toward postsynthesis π -functionalization on the naphthalene rings.²⁰ Starting reagents were ZrCl₄, 1,4-NDC, and *N,N*-dimethylformamide (DMF) with a molar ratio 1:1:143. No modulator was used in that synthesis.⁵⁰ Similarly, Huang et al.⁵¹ employed 2,5-dimethylterephthalic acid (2,5-BDC-(CH₃)₂) in order to synthesize UiO-66-(CH₃)₂, a material that has shown enhanced chemical stability toward water adsorption and an improved performance in CO₂ adsorption with respect to the plain UiO-66.

In the present work, we further modified the synthesis technique and investigated how benzene-carboxylic (BC) acid, acting as a modulator, affects UiO-66-NDC properties. For the first time, we refined the influence of the BC/NDC ratio on the formation of UiO-66-NDC phase (Table 1).

2. EXPERIMENTAL AND METHODS

2.1. MOF Synthesis. The chemicals ZrCl₄, 1,4-NDC, BC acid, and DMF were purchased from Alfa Aesar and used without further purification. Deionized (DI) water (18 M Ω cm) was obtained from a Simplicity UV ultrapure water system. In a typical procedure, ZrCl₄ (0.250 g) was dissolved in 25 mL of DMF in a conical flask, and 57.9 μ L of DI water was added. Then, a respective amount of BC, as reported in Table 1, was poured into the flask with ZrCl₄ solution, and 1,4-NDC (0.232 g) was added. After complete dissolution of the reagents, the flask was sealed and placed into the preheated oven at 120 °C for 24 h. In this way, we obtained three samples labeled with respect to an added amount of BC: 0BC (without BC acid), 10BC, and 60BC with 10 and 60 equiv of BC acid, respectively (Table 1). The synthesis performed using 100 equiv of BC resulted in no precipitate even after 96 h at 120 °C. Also for the other molar compositions (0BC, 10BC, and 60BC) the synthesis was duplicated increasing the heating time at 120 °C to 96 h. In those cases, there was no significant difference in the XRD profiles and in the product yield, indicating that 24 h is sufficient to complete the synthesis. For comparison, a standard UiO-66 was obtained under the same conditions using BDC as a linker but without a BC modulator.

2.2. Characterization Techniques. Diffraction patterns were measured in 0.7 mm rotating glass capillaries at the European Synchrotron Radiation Facility (ESRF), beamline BM01B⁵⁴ (successively moved to BM31) for 0BC, 10BC, and 60BC samples, and for the standard UiO-66 for comparison. Twenty diffraction patterns were measured for each sample with a CMOS-Dexela 2D detector and averaged before the analysis. Wavelength of the incoming beam, $\lambda = 0.505235(5)$ Å, and sample-to-detector distance were calibrated using LaB₆ and silicon powder standards. The adopted experimental setup allowed us to cover the 1.4–40.0° 2θ range, which corresponds to the Q-range from 0.30 to 8.51 Å⁻¹ and to a *d*-spacing ranging from 20.68 down to 0.74 Å. Subsequent averaging and integration were carried out using the PyFAI software.⁵⁵ Profile analysis was performed using Jana2006 software.⁵⁶ Framework stability of 0BC–60BC series was further checked by laboratory powder X-ray diffraction (PXRD) collected in the 30–500 °C temperature interval, with an X-ray powder diffraction system ARL X'TRA (Thermo Scientific) using Cu–K α radiation.

An ultrahigh resolution scanning electron microscope of Hitachi SU8230 type was used to obtain high resolution images of the material. The sample was mounted on a carbon tape prior to the measurement. The surface area and porosity were determined by BET and Langmuir methods from nitrogen physisorption isotherms obtained (at 77 K) on an accelerated surface area and porosimetry analyzer ASAP 2020 (Micromeritics). The sample was activated at 200 °C for 24 h in a dynamic vacuum before the measurement. Pore volumes were calculated at $P/P_0 = 0.5$ and taking into account the density of liquid N₂ at 77 K.^{52,53}

Adsorption isotherms were simulated with the “adsorption isotherm” task within the “Sorption Tools” menu in BIOVIA Materials Studio version 2017r2. The simulations were performed at 77 K, using a geometry optimized N₂ molecule as the adsorptive and a single, geometry-optimized unit cell of the model structure of interest as the adsorbent. We adopted the Metropolis method and the COMPASS force field. The isotherms were simulated over a pressure range of 0.01–100 kPa, in which 50 fugacity steps were distributed logarithmically in order to increase the number of data points in the steep initial portion of the isotherm. The “Fine” quality setting was used for all simulations. Charges were force field assigned, while electrostatic forces were calculated with the Ewald method. The “atom-based” method was adopted for the calculation of van der Waals forces. No constraints were assigned.

Zirconium K-edge X-ray absorption near edge structure (XANES) and extended X-ray absorption fine structure (EXAFS) spectra were measured using a Rigaku R-XAS spectrometer installed in the “Smart Materials” center of the Southern Federal University, Russia. Bremsstrahlung was produced by an X-ray tube with a fixed water-cooled W anode operating at 30 kV and 70 mA. A white beam was monochromatized by a Johansson-type Si(620) crystal with an energy resolution of around 15 eV at 18 keV. The samples in powder form were pressed into pellets of 18 mm in diameter. The mass of the samples was optimized to obtain the best signal-to-noise ratio in EXAFS spectra. Measurements were performed at room temperature in transmission mode using a single scintillation counter as a detector.

Total acquisition time per sample was around 3.5 h. Subsequent data treatment was carried out in Athena code of Demeter package.⁵⁷

The Raman spectra were collected on inVia Raman microscope (Renishaw) on the samples in air with 785 nm laser of 0.05% power, and 20× objective. Reported spectra are the average of 30 acquisitions performed on three different points (10 each) on the sample.

Prior to NMR measurement samples were calcined in air at 200 °C for 24 h to remove solvent and physisorbed modulator. Samples were prepared by weighing 20 mg of MOF into a centrifuge tube. A 1 mL solution of 1 M NaOH in D₂O was then added to the tube. Upon addition of the digestion medium, the centrifuge tubes were capped and stacked on IKA KS260 instrument for 30 min before leaving the samples to digest over a period of 24 h. This OH⁻ based procedure dissolves only the organic portion of the MOF (linker, modulator, solvent, etc.), while the inorganic component precipitate as zirconium dioxide. The precipitate was separated by centrifugation at 3000 rpm for 30 min and the 600 μL of top solution was sampled in NMR. Liquid ¹H NMR spectra were recorded with a Bruker Avance DPX-400 NMR spectrometer (300 MHz). The relaxation delay (d1) was set to 20 s to ensure that reliable integrals were obtained, allowing for the relative concentrations of the molecular components to be accurately determined. The number of scans was 64.

3. RESULTS AND DISCUSSION

3.1. PXRD Synchrotron Radiation Data Refinement: Comparison between 0BC and standard UiO-66. Rietveld refinement of PXRD data collected at the BM01B beamline of the ESRF synchrotron on UiO-66-NDC (0BC) sample confirms that it is isorecticular to UiO-66. Being compared, the patterns show very little difference in shape and intensity of the reflections, although they show a little shift toward lower 2θ due to a small increase of the lattice parameter (from $a = 20.7582(4)$ to $20.851(1)$ Å, corresponding to $\Delta a \approx +0.093$ Å, $\Delta a/a = +0.45\%$, see Figure 1 and Table 2 and Table 3). The increased value of lattice constant in UiO-66-NDC is related to the stress created by extra benzene rings of the 1,4-NDC molecules in comparison with the standard BDC ligands.

The Rietveld refinement of the UiO-66 MOF was performed in the $Fm\bar{3}m$ space group (No. 225) using as a starting model the structure refined in the original manuscript of Cavka et al.¹⁹

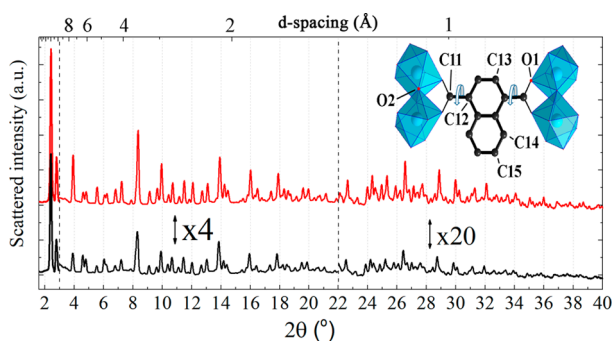


Figure 1. Background corrected PXRD patterns of UiO-66 (red) and UiO-66-NDC-0BC (black) samples obtained using synchrotron irradiation: $\lambda = 0.505235(5)$ Å. To better appreciate the higher 2θ angle data, the patterns have been multiplied by a factor 4 and 20 in the 3–22° and 22–40° 2θ -intervals, respectively. The model in the top right corner depicts connection of a linker with two SBU in UiO-66-NDC structure. Blue polyhedra represent zirconium coordinated by oxygen ions, while the carbon atoms of the linker are represented by black spheres; σ -bonds are denoted by white flat arrows. Also reported are the labels used in the refinement to discriminate among crystallographic independent carbon and oxygen atoms, see Table 2 and Table 3.

(that combined PXRD and Zr K-edge EXAFS data) and fixing to unit the occupancy factors of all atoms, see Table 2. Because of the high symmetry of the space group, the structure contains only one independent zirconium atom, two independent oxygen atoms (O2 being the μ -3-O atom of the inorganic cornerstone and O1 belonging to the carboxylate unit of the linker), and three carbon atoms of the BDC linker (C11, C12, and C13; C14 and C15 are present only in NDC linker); see inset in Figure 1 and Table 2.^{19,21,25} A quite large isotropic atomic displacement parameter was found for C13 ($U_{\text{iso}} = 0.077(5)$ Å²) with respect to that of C11 and C12 atoms. This could be interpreted as a small twisting of the benzene ring of the BDC linker around the σ -bonds between C11 and C12. Such twisting would not affect the time averaging of the electron density of C11 and C12, being on the rotation axis, while that of C13 would result in a clearly anisotropic atomic displacement, which is difficult to clearly show from PXRD data. Another possible explanation would be that the benzene ring of the BDC linker would have an out of plane equilibrium position. If this would be the case, the C13 atom should have a y -coordinate different from zero, half of the occupancy and double degeneration for symmetry reasons. This is indeed the situation found by the recent single crystal synchrotron radiation X-ray diffraction reported by Øien et al.²⁵ As the C13 atom is quite close to the rotation axis, such a twisting effect (if present) is relatively small, and we are unable to confirm or discard the result of Øien et al.²⁵ from our PXRD data. As the refinement obtained with the simpler model reported in the original work of Cavka et al.¹⁹ was able to properly reproduce the experimental PXRD pattern, we decided to keep this higher symmetry model. The comparison between observed, calculated, and difference (black, red, and blue line, respectively) PXRD patterns has been reported in Figure 2a.

The same strategy adopted to refine the data of UiO-66-NDC-0BC succeeded in locating Zr, O1, O2, C11, C12, C13 in reasonable positions with physically meaningful U_{iso} parameters, but failed in locating C14 and C15 with y fixed to 0. Indeed, when we tried to refine the corresponding occupancy factors, they resulted to almost null values. We then adopted the model reported by Øien et al.,²⁵ removing the constraints on the y ordinate of C13, C14, and C15 atoms. To guarantee stability to the refinement, we applied soft constraints to the C12, C13, C14, and C15 atoms to stay on the same plane. Soft constraints have also been adopted on all C=C distances between aromatic carbons (around 1.4 Å) and between C11 and C12 (around 1.5 Å, single-bond distance). The refinement stability further improved by adding a soft constrain on the O1–C11–O1 angle around 126°, that defines the connection between the linker and the inorganic cornerstone.

The occupancy factors of the atoms of the inorganic cornerstone have been fixed to unit, while those of the atoms of the NDC linkers were fixed to 0.87 according to the thermogravimetric analysis (TGA) data (see below Figure 9). The result of the refinement is reported in Table 3, the structure of the NDC linker is reported in Figure 3, while the comparison between observed, calculated, and difference (black, red and blue line, respectively) PXRD patterns can be appreciated in Figure 2b.

Repeating the last refinement fixing to unit we obtained results fully compatible with those presented here, as the atomic coordinates for all atoms are equivalent in both refinements within less than 2 estimated standard deviations

Table 2. Atomic Parameters Resulting from the Rietveld Refinement of the UiO-66 in the $Fm\bar{3}m$ Space Group (No. 225): Fractional Coordinates (x, y, z); Isotropic Atomic Displacement Parameters (U_{iso}), Occupancy Factors, Site Degeneration and Number of Atoms in the Unit Cell^a

atom	x	y	z	U_{iso} (\AA^2)	occupancy factor	site	no. of atoms/unit cell
Zr	0.1198(1)	0	0	0.0116(4)	1.000	24e	24
O1	0.1750(3)	0	0.0919(3)	0.022(2)	1.000	96j	96
O2	0.0555(3)	$-x$	$-x$	0.018(3)	1.000	32f	32
C11	0.1467(4)	0	$-x$	0.035(5)	1.000	48h	48
C12	0.2044(5)	0	x	0.065(7)	1.000	48h	48
C13	0.2686(6)	0	0.1772(6)	0.077(5)	1.000	96j	96

^aTo compare with the previous refinement,¹⁹ please consider that $U_{\text{iso}} = B_{\text{eq}}/(8\pi^2)$. Values of R_{wp} and R_p parameters are 0.86 and 0.82, respectively, and reduced $\chi^2 = 2.13$ for 40 variables. The refined cell parameter is $a = 20.7582(4)$ \AA [$V = 8944.8(6)$ \AA^3]. See the inset in Figure 1 for the atom labeling.

Table 3. Atomic Parameters Resulting from the Rietveld Refinement of the UiO-66-NDC-0BC MOF in the $Fm\bar{3}m$ Space Group (No. 225): Fractional Coordinates (x, y, z), Isotropic Atomic Displacement Parameters (U_{iso}), Occupancy Factors, Site Degeneration and Number of Atoms in the Unit Cell^a

atom	x	y	z	U_{iso} (\AA^2)	occupancy factor	site	atoms/unit cell
Zr	0.1176(1)	0	0	0.0129(8)	1.00	24e	24
O1	0.1699(3)	0	0.0903(3)	0.022(2)	1.00	96j	96
O2	0.0641(4)	$-x$	$-x$	0.056(5)	1.00	32f	32
C11	0.1504(2)	0	$-x$	0.003(4)	0.87	48h	41.76
C12	0.2012(2)	0	x	0.043(7)	0.87	48h	41.76
C13	0.2603(3)	0.0280(5)	0.1890(3)	0.023(6)	0.435	192i	83.52
C14	0.2724(5)	0.056(1)	0.1296(4)	0.24(3) ^b	0.217	192i	41.76
C15	0.3317(7)	0.084(2)	0.1174(6)	0.36(5) ^b	0.217	192i	41.76

^aValues of R_{wp} and R_p parameters are 0.76 and 0.81, respectively, and reduced $\chi^2 = 1.55$ for 45 variables. The refined cell parameter is $a = 20.851(1)$ \AA [$V = 9065(1)$ \AA^3]. See the inset in Figure 1 for the atom labeling. The occupancy factors of the atoms of the inorganic cornerstone have been fixed to unit, while those of the atoms of the NDC linkers were fixed to 0.87 according to the TGA data (see below Figure 9). The refined structure has been deposited in the CCDC data base with number 1553924. ^bAn unique U_{iso} parameter for C14 and C15 atoms was set proportional to the distance from the rotational axis.

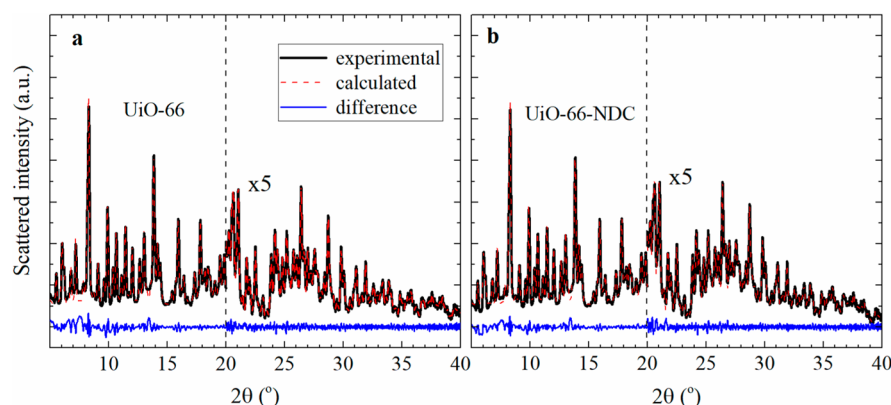


Figure 2. Panel (a): Observed (black line), calculated (red line), and difference (blue line) PXRD patterns for the UiO-66 MOF: $\lambda = 0.505235(5)$ \AA . Panel (b): as panel (a) for the UiO-66-NDC-(or 0BC) MOF. The quantitative results of the two Rietveld refinements are reported in Table 2 and Table 3, respectively.

(esd). The simulated pattern still resulted in a good agreement with the experimental one, but the all the U_{iso} of the carbon atoms slightly increased, and the fit goodness factors worsen by about 5% with respect to the results reported in Table 3. We consequently decided to consider as final refinement that obtained by fixing the occupancies of the atoms of the NDC linkers to 0.87. See section S1 and Table S1 of the Supporting Information for a more detailed comparison between the two refinements.

For symmetry reasons four equivalent values of the φ angle are available: $\varphi = +30, -30, +150,$ and -150 ; for graphical

reasons, only the $\varphi = +30$ case has been represented in Figure 3a. From this picture, it becomes evident why the first refinement, performed fixing $y = 0$ for the C13, C14, and C15, resulted in locating only C13, with a larger U_{iso} parameter with respect to that of C11 and C12 atoms. Indeed, if we label as C13', C14', and C15' the carbon atoms of the NDC linker corresponding to the $\varphi = -30$ solution, then the relative distances of the symmetry equivalent atoms are 1.21, 2.42, and 3.63 \AA for $d(\text{C11}-\text{C11}')$, $d(\text{C12}-\text{C12}')$, and $d(\text{C13}-\text{C13}')$, respectively. This implies that only the couple of C13 and C13' have some electron density on the $y = 0$ plane, while C14, C14',

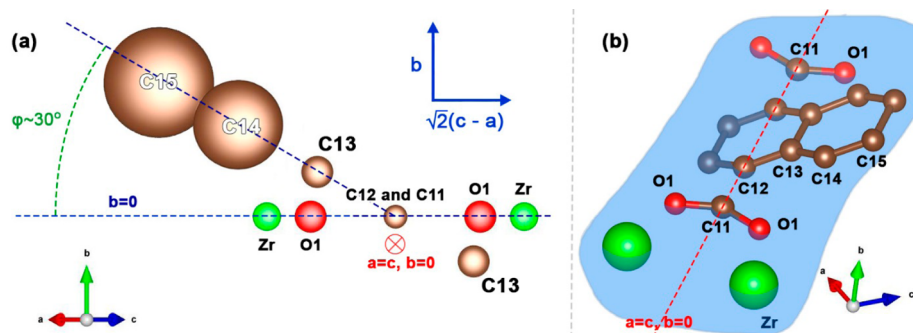


Figure 3. Panel (a) View from the (101) direction of the atoms of the NDC linker as optimized in the refinement reported in Table 3. For each atom, the radius of the spheres is defined by the corresponding $(U_{\text{iso}})^{1/2}$ value. For symmetry reasons four equivalent values of the φ angle are available: $\varphi = +30, -30, +150,$ and -150 (only the first solution is here represented). Panel (b): analogous representation of the same optimized structure reported from a tilted view. In this case the sphere radii correspond to the atomic radii and do not consider the thermal motion. In both parts, the three-dimensional visualization of crystal structure was performed using the VESTA code.⁵⁸

and C15 and C15' are too far from that plane. The optimized U_{iso} parameters (Table 3) exhibit the following trend: C11 < C12 < C13 < C14, C15. This observation suggests a small twisting of the NDC rings around the equilibrium position ($\varphi = +30, -30, +150,$ or -150).

Summarizing, our synchrotron radiation PXRD study confirmed that UiO-66-NDC (0BC) sample is isoreticular to UiO-66 and evidenced that the NDC ligand adopts a tilted position of $\varphi = 30^\circ$, a value that is indeed comparable to the torsion angles found in molecular structures of naphthyl carboxylates and carboxylic acids, which is usually a 10–40° interval.^{59–63}

For the standard UiO-66 analogue, the BDC ligands are free to occupy the high symmetry position ($\varphi = 0^\circ$), see Figure 4a. Conversely, using the more bulky NDC ligands, in the UiO-66-NDC framework there is a steric conflict between the naphthyl groups of two adjacent linkers (Figure 4b), that forces carboxylate and naphthyl groups of the same linker to be out of plane. The torsional angle optimized in the present PXRD refinement ($\varphi = 30^\circ$, see Table 3) is stabilized by the optimization of an attractive interaction between a σ orbital of a C–H group and the π orbital of two naphthyl groups in two adjacent linkers (Figure 4c). It is worth noticing that this tilting effect is even more pronounced in the case of the UiO-67 analogue ($\varphi = 36^\circ$),²⁸ where the φ value confirms the tendency of binaphthyl to have high torsion angles, due to intramolecular interactions, see Figure 4d. It is finally worth considering that neutron powder diffraction would have been a much more suitable technique to obtain a more accurate location the linker atoms than PXRD (in which scattering is dominated by the Zr atoms);⁶⁴ however, the much larger sample amount requested (from some milligrams to few grams) and the need to use deuterated linkers in the synthesis prevented the use of such strategy. Notwithstanding this evidence, the accuracy of our synchrotron radiation PXRD study is sufficient to evidence the tilted position of the ligand.

3.2. Crystal Size and Textural Properties. The materials crystallize in intergrown crystals (shown in Figure 5) which are too small ($<1 \mu\text{m}$) for structure determination by single crystal diffraction. From the SEM images it emerges that a higher amount of BC leads to the formation of larger crystals with better defined morphology. The average size increases from 80, through 150 up to 800 nm for 0BC, 10BC, and 60BC, respectively. Without addition of BC intergrown aggregates of very small crystals are observed, and the shape of 0BC crystals

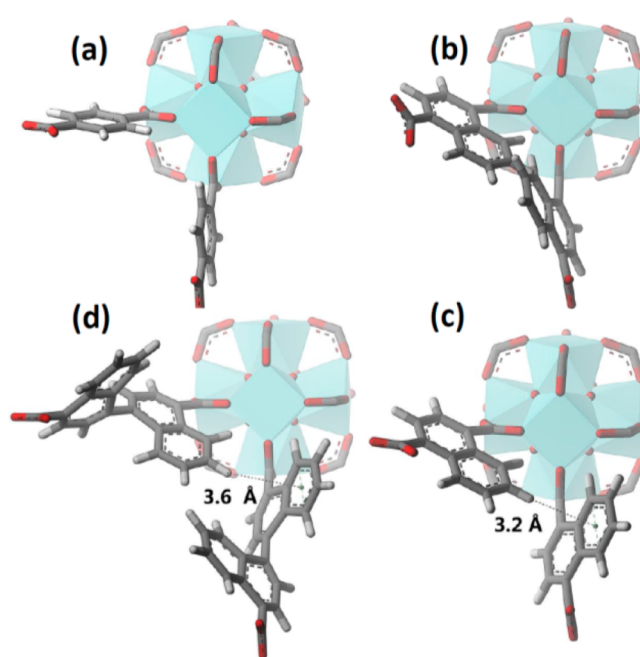


Figure 4. Graphical representation of the inorganic $\text{Zr}_6(\text{OH})_4\text{O}_4$ SBU with two adjacent linkers in some different UiO-66- and UiO-67-type structures. Panel (a) Standard UiO-66 (BDC ligand), from single crystal XRD refinement ($\varphi \approx 0^\circ$).²⁵ Panel (b): picture showing the overlap between adjacent NDC ligands in the case of a too small value of the torsional angle φ for UiO-66-NDC. Panel (c): UiO-66-NDC, optimized from PXRD ($\varphi = 30^\circ$), this work. Panel (d): UiO-67-BN (3,3'-dimethylbiphenyl and 1,1'-binaphthyl linker scaffolds), from single crystal XRD refinement ($\varphi = 36^\circ$).²⁸

is not well established (Figure 5a). On the contrary, addition of 10 or 60 equiv of BC results in well-defined octahedral crystals (Figure 5b,c). It is also evident from the images that one crystal is formed on the facet of another.

PXRD patterns of UiO-66-NDC structure with variation of modulator content are shown in Figure 6. The intensities of PXRD reflections become sharper with an increase of BC amount, evidencing different crystallinity of the samples. Reflections due to planes with similar d -spacing could be best resolved in the 60BC sample. For example, the (315) and (006) reflections in the 8.2–8.5° 2θ region can be distinguished starting from the 0BC sample, but they are becoming fully split only in the 60BC pattern. Moreover, the (339) and (608)

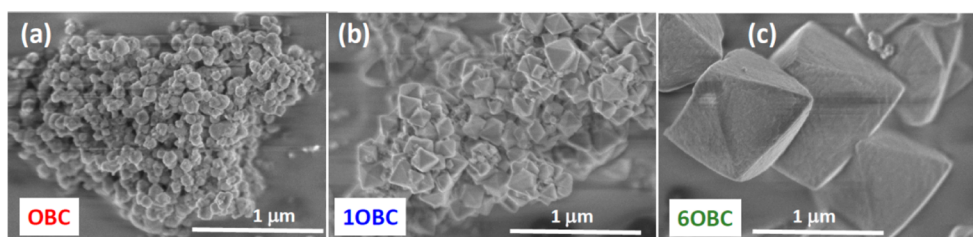


Figure 5. SEM micrographs of 0BC, 10BC, and 60BC samples, panels (a), (b), and (c), respectively. All images were taken with the same magnification.

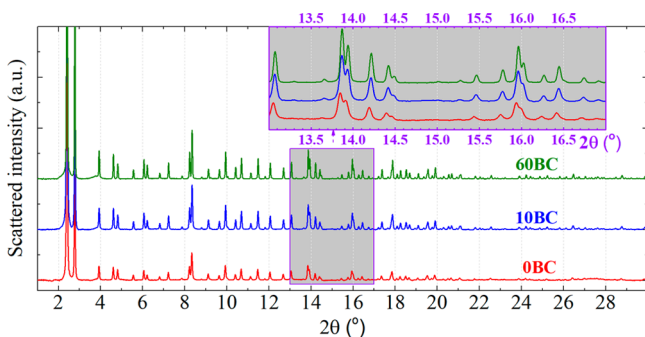


Figure 6. PXRD patterns of UiO-66-NDC samples prepared with different amounts of BC modulator, from bottom to top: 0BC (red), 10BC (blue), and 60BC (olive): $\lambda = 0.505235(5)$ Å. The inset shows a magnification of the 13–17° 2θ region.

reflections, in the 14.0–14.2° 2θ region, and (719) and (828) reflections, in the 16.1–16.3° 2θ region, are merged to a single peak for the 0BC sample, and resolved in the 60BC pattern, which is demonstrated in the inset of Figure 6. The fwhm of (317) reflection at $\sim 10.8^\circ$ decreases from 0.063° for sample synthesized without BC modulator to 0.046° for the 60BC sample. The limiting resolution of the setup obtained for a standard LaB_6 (NIST) sample is 0.042° fwhm for (101) reflection at 10° . Cell parameters decrease from 20.851 Å for the 0BC sample to 20.827 and 20.820 Å for 10BC and 60BC, respectively, as determined by Rietveld refinement of the XRD patterns. This means that the progressive addition of modulator decreases the stress created by the use of 1,4-NDC linkers instead of the standard BDC for the UiO-66 synthesis, resulting in $a = 20.7582(4)$ Å, see Table 2.

3.3. N₂ Adsorption Isotherms. For the UiO-66, 67, and 68 family of MOFs, the increase of crystal size with addition of modulator was previously described⁴³ and can be explained by the fact that zirconium ions form a complex salt with BC. The presence of BC in the synthesis batch changes the reaction mechanism, because all active sites around Zr^{4+} ions became occupied with BC molecules. In such a situation, any linker molecule can interact with zirconium ion only via exchange reaction. This fact decreases the rate of nucleation in solution and, therefore, results in bigger crystals. It should be mentioned that another process could also take place. If concentration of a monobasic acid in solution is much higher than that of a linker, an exchange reaction might be suppressed. As the result, a portion of SBUs will keep molecules of modulator coordinated to the metal ion instead of being available for the coordination of linker since monobasic acids can contact zirconium in one SBU only (while linker molecules can connect two adjacent SBUs, compare panels (a) and (b) of Figure 7).

Depending on the number of vacancies this feature may increase the surface area and the pore volume and reduce

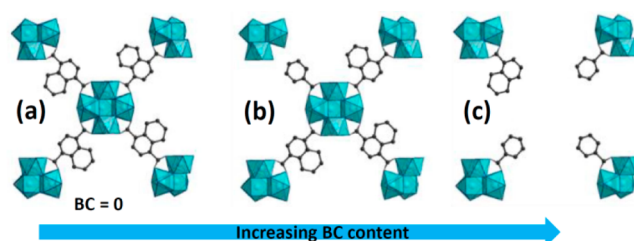


Figure 7. Qualitative scheme of defect formation in synthesis with increasing amount of BC acid. (a) Perfect case (absence of BC acid). (b) Formation of little pores (small amount of BC acid). (c) Formation of big pores, with missing clusters (large amount of BC acid).

stability of the material, as demonstrated by Shearer et al.²⁴ where the linker vacancies were tuned by acting on the synthesis temperature and on the ZrCl_4/BDC ratio. Linker vacancies may yield to Zr ions characterized by two coordination vacancies, thus representing surface Lewis acid centers of potential catalytic interest.^{8–10} When the BC/NDC ratio is high it may be possible that some $\text{Zr}_6\text{O}_4(\text{OH})_4$ cornerstones are missing: this happens when most of the adjacent ones are capped by BC units, as schematically shown in Figure 7c. Finally, by further increasing the BC/NDC ratio (see the 100BC case in Table 1), most of the 12 connections of the SBU are capped by BC, preventing the crystallization process.

The presence of an increasing density of cornerstone vacancies upon increasing the BC content in the synthesis (hypothesized in Figure 7) is confirmed by the N₂ adsorption isotherms reported in Figure 8a (scattered curves), that clearly show that the adsorption plateau appears at significantly higher $\text{cm}^3 \text{g}^{-1}$ STP values moving from 0BC to 10BC and 60BC. The consequent Barrett–Joyner–Halenda⁶⁵ (BJH) pore size distribution is shown in Figure 8b,c as determined from adsorption and desorption isotherms, respectively.⁶⁶ All samples exhibit a similar sorption profile, and the isotherms can be attributed to the type I (IUPAC classification), which is typical for microporous materials. Specific surface area calculated by Brunauer–Emmett–Teller (BET)⁶⁷ and Langmuir⁶⁸ models increases with amount of BC, and the same occurs for the pore volumes (Table 1), supporting the defective models schematized in Figure 7b,c: see the distribution of nanopores in the 2–3 nm region (Figure 8b,c). For microporous materials the region of the isotherm near to $P/P_0 = 1$ is usually ascribed to adsorption in cavities between the crystallites of material. Respectively to what is observed in Figure 8a, the isotherm of 10BC sample demonstrates the highest adsorption, while that of 60BC has no evident increment. This situation is well illustrated by the SEM image shown in Figure 5c, showing well separated big crystals, leaving

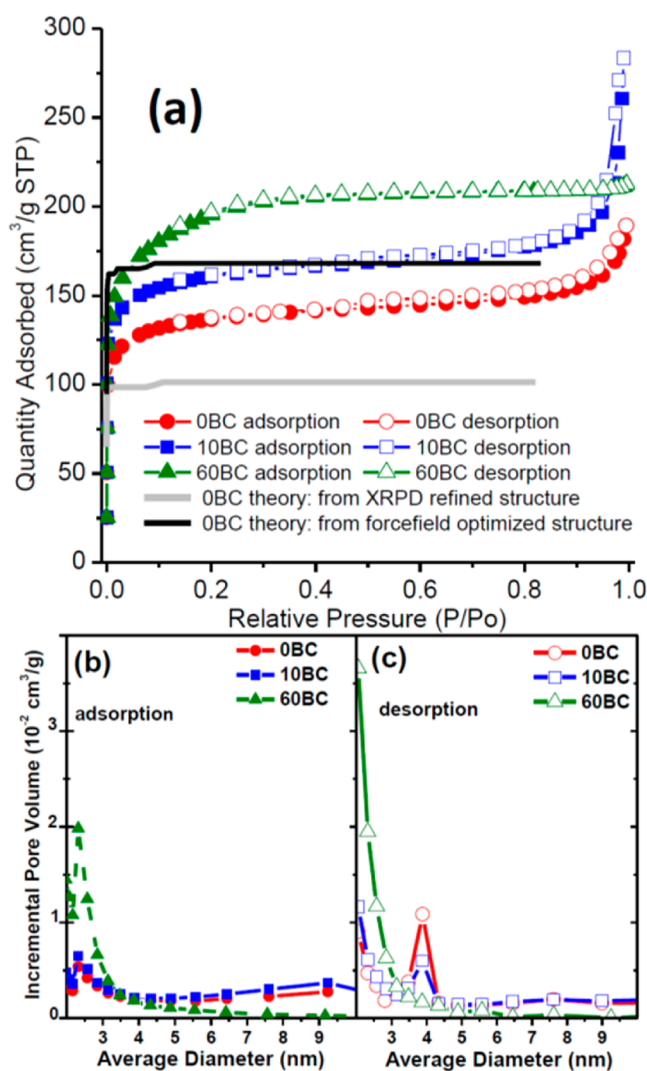


Figure 8. Panel (a): N_2 physisorption isotherms of 0BC (circles), 10BC (squares), and 60BC (triangles) samples. The filled and open symbols represent the adsorption and desorption branches, respectively. Also reported are the theoretical adsorption curves calculated on the structures obtained from PXRD refinement (gray line) and from a subsequent force field optimization (black curve). Panel (b): BJH adsorption pore distribution obtained from the N_2 physisorption isotherms reported in part (a). Panel (c) as panel (b) from the desorption isotherms.

almost no cavities between them. In the case of the 0BC sample (Figure 5a), the smaller crystallites exhibit a more dense packing in comparison to the 10BC sample (Figure 5b), which leaves no significant free volume between the crystallites.

The presence of the cornerstone vacancies (hypothesized in Figure 7c) in the 60BC sample is further confirmed by the edge jump of the Zr K-edge study reported in Section S3 of the Supporting Information (see Figure S2a) and quantified it to about 15%. The EXAFS data analysis (Figure S2b–d) confirms the similarity of the SBU in the 0BC and 60BC materials compared to a standard UiO-66 material. This testifies that the local environment of Zr is the same in all samples and corresponds to that of the standard UiO-66 sample.^{19,21} Coming back to the diffraction data (Figure 6), the absence of the forbidden reflections^{24,29,31,37} in the small angle region implies the absence of long-range order in the structural defects.

Of interest are the full line curves in Figure 8a, reporting the simulated adsorption isotherms for the framework optimized by PXRD refinement (gray curve) and after a successive force field optimization of the structure (black curve, see above Section 2.2 for details). The UiO-66-NDC framework, considered as a rigid entity is not able to justify the N_2 uptake measured in the experiment (gray full curve). This uptake increases significantly when the structure is allowed to relax (black full curve). This simulation shows the flexibility of the rotation of the NDC ligands around the torsional φ angle and justifies the high U_{iso} parameters obtained in the Rietveld refinement for C14 and C15 atoms, see Table 3.

3.4. Thermal Stability by TGA and PXRD. It is now well established that the UiO-66 framework is incredibly tolerant to a high concentration of defects. The initial evidence for this came in the form of TGA data presented in a paper by Valenzano et al.²¹ Therein, the authors demonstrated that the magnitude of the decomposition weight loss step was significantly less than that theoretically expected by the idealized chemical equation $[Zr_6O_6(BDC)_6] \rightarrow 6 ZrO_2$. The TGA of all samples are reported in Figure 9 by rescaling the

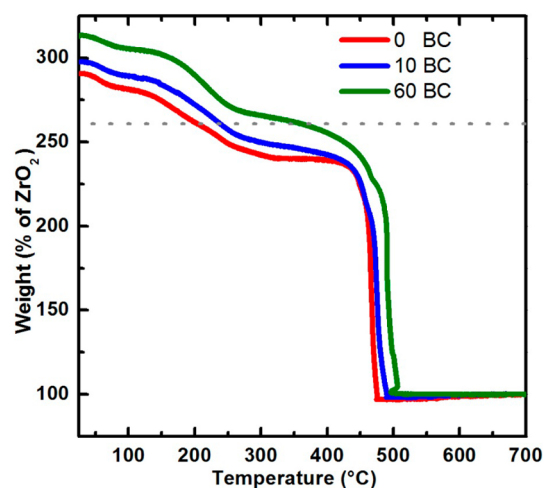


Figure 9. TGA plots showing the thermal degradation of 0BC, 10BC, and 60BC samples renormalized referring the remaining weight at high temperature (ZrO_2) as 100%. Under this convention, the weight of a desolvated UiO-66 free of defects should be 161% (see dotted gray line).

weight at the end of the process to 100% and attributing it to the pure ZrO_2 phase (nonscaled TGA curves are reported in Figure S3). The theoretical weight loss from the burning of the organic linkers are in the case of defect-free 1,4-NDC 161% based on ZrO_2 , and this weight is indicated as a dotted line in Figure 9. The sample made without modulator, 0BC, has a weight loss upon combustion that corresponds to 13% missing linkers. On these basis, we fixed to 0.87 the occupancy factor of the atoms of the NDC linker in the Rietveld refinement of 0BC, see Section 3.1, Table 3. The samples made with benzoic acid as a modulator demonstrate a larger and less sharp weight loss. This is probably due to “missing cluster defects” (Figure 7c), as it is known from a parallel study on UiO-66, that are promoted by modulated synthesis.^{31,41} This evidence, confirmed by the Zr K-edge jump in the XAS experiment (see Supporting Information, Figure S2a), underlines that the formation of missing SBUs (Figure 7b,c) is more effective at higher BC content. The framework breakdown temperature

follows the trend (60BC < 10BC < 0BC) as evidenced by the extend of the stability plateau (250–450 °C interval) and as clearly observed in the temperature dependent PXRD pattern collected after heat treatment in air at 200, 300, 400, and 500 °C for 12 h (Figure 10). Samples 0BC and 10BC preserve their

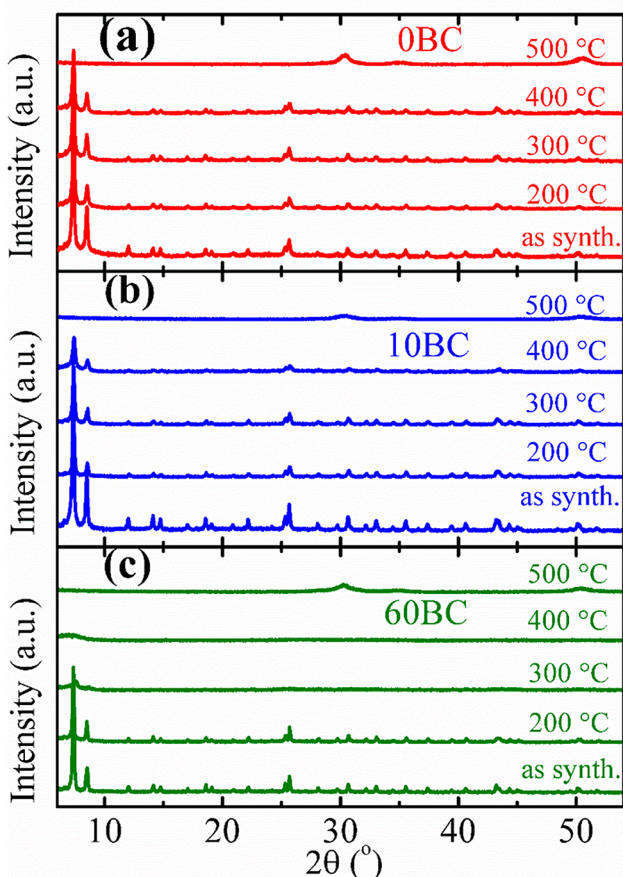


Figure 10. PXRD patterns of 0BC, 10BC, 60BC samples recorded at room temperature after thermal treatment in air, panels (a) to (c), respectively. From bottom to top: as synthesized and heat treatment 200 °C, 300 °C, 400 °C, 500 °C for 12 h. In the adopted ordinate scale, the intensity of the low 2θ reflections are cut for graphical reasons. Patterns have been collected with Cu $K\alpha$ radiation ($\lambda = 1.5406 \text{ \AA}$).

initial structure up to 400 °C. However, at this temperature partial decomposition of the structure of 10BC sample can be observed (see widening of the reflexes in Figure 10b). Sample 60BC maintained crystallinity up to 200 °C only (Figure 10c), while at 300 and 400 °C broad XRD peaks indicate the loss of long-range order. All samples collapsed at 500 °C into ZrO_2 . However, even the most temperature unstable 60BC sample could be activated for potential applications (solvent removal) without losing its initial structure.

Because of possible technologic application (i.e., sorption and catalysis) of the material, water stability tests were performed. All samples preserved their crystal structure after contact with water at room temperature for 24 h and subsequent activation at 200 °C for 12 h (see Supporting Information, Figure S1).

3.5. Incorporation of BC Modulator in the Framework Determined by Dissolution- ^1H NMR and Raman. As deeply described in the works of Shearer et al.,^{29,31,37} the

dissolution- ^1H NMR technique allows researchers to identify and quantify the organic components of an MOF (e.g., linker, modulator, or pore-filling solvent) dissolving the MOF in a deuterated digestion medium and successive liquid ^1H NMR spectroscopy. Figure 11a reports the liquid ^1H NMR spectra of

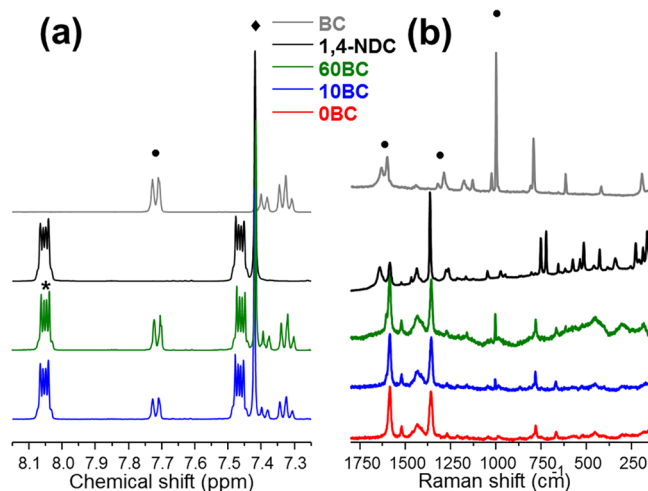


Figure 11. Part (a): Dissolution ^1H NMR spectra obtained on the BC-modulated UiO-66-NDC MOFs. Also reported for comparison are the reference spectra of 1,4-NDC linker and BC modulator (black and gray curve, respectively). All spectra except BC are normalized to the peak 7.4 ppm shown by \blacklozenge . The \bullet and $*$ show the peaks around 7.70 and 8.05 ppm used to calculate the BC to 1,4-NDC ratio. MOF samples were activated 200 °C for 24 h in air prior NMR measurement. Part (b) Raman spectra of 0BC, 10BC, 60BC samples, collected with $\lambda = 785 \text{ nm}$. For comparison, also reported is the spectrum of BC and 1,4-NDC (collected with $\lambda = 514$ and 785 nm, respectively). In the BC spectrum, marker bands of $\nu(\text{C}=\text{O})$ and $\nu(\text{C}-\text{O})$ of the carboxylic acid are underlined by the \bullet symbol, together with the most intense Raman band due to the ring deformation at 1005 cm^{-1} . In both parts spectra were vertically shifted for clarity.

10BC and 60BC, compared with those measured on 1,4-NDC linker and BC modulator. The quantitative integration of the area of the specific NMR peaks in the 7.75–7.65 and 8.10–8.00 ppm regions for the BC and 1,4-NDC, respectively, resulted in a BC/1,4-NDC ratio of 0.28 and 0.47 for 10BC and 60BC samples, respectively.

This result is qualitatively confirmed by Raman spectroscopy (Figure 11b), where the most intense Raman band of the BC modulator (corresponding to a ring deformation mode at 1005 cm^{-1}) is absent in the 0BC sample and progressively increases from 10BC to 60BC. A complete spectroscopic (IR and Raman) characterization of the vibrational properties of linkers and modulators used in the synthesis of modified versions of UiO-66, supported by periodic density functional theory (DFT) calculations, has recently been reported by Atzori et al.,³¹ and we refer to that work for a complete assignment of the bands present in Figure 11b. Moreover, it is clear that benzoic acid was completely removed by the adopted washing procedure, since key bands (such as the $\nu(\text{C}=\text{O})$ and $\nu(\text{C}-\text{O})$) evidenced by the \bullet symbol) are completely absent from the UiO-66 spectra.

4. CONCLUSIONS

Summarizing, UiO-66-NDC was synthesized using a solvothermal method in DMF. PXRD refinement of synchrotron radiation data highlighted that the naphthalene rings of the

NDC linker is out of (*a,c*)-plane equilibrium by 30°, adopting a geometry that maximizes the attractive interaction between a σ orbital of a C–H group and the π orbital of two naphthyl groups in two adjacent linkers. The influence of the BC modulator agent was investigated changing the BC/NDC linker fraction from 0 to 60. No nucleation was observed for BC/NDC = 100. A larger amounts of BC results in formation of bigger octahedral crystals of UiO-66-NDC (due to decrease of crystal growth kinetics) characterized by an increased specific surface area (due to formation of more defects in the lattice). For all crystalline samples PXRD and EXAFS confirmed the target structure on both long- and short-range order grounds. TGA and PXRD analyses revealed a decrease of thermal stability with an increase of modulator amount: the presence of both linker and SBU defects is the origin of the loss of stability, the latter being more important at higher BC content. Remarkably, all samples prepared with and without modulator are stable in water even after reactivation. Thus, UiO-66-NDC, and its defective derivatives synthesized upon increasing the BC/NDC ratio, are sufficiently stable to be fully desolvated and represent good candidates for further functionalization with active catalytic centers for reactions running in gas or in liquid phases up to 200 °C.

■ ASSOCIATED CONTENT

Supporting Information

The Supporting Information is available free of charge on the ACS Publications website at DOI: [10.1021/acs.cgd.7b00892](https://doi.org/10.1021/acs.cgd.7b00892).

Further details on the alternative Rietveld Refinement of the UiO-66-NDC-0BC MOF fixing the occupancy of the linker atoms to unit, on the PXRD diffractograms testifying the water stability of the materials, the Zr K-edge XANES and EXAFS study and the as collected TGA curves (PDF)

Accession Codes

CCDC 1553924 contains the supplementary crystallographic data for this paper. These data can be obtained free of charge via www.ccdc.cam.ac.uk/data_request/cif, or by emailing data_request@ccdc.cam.ac.uk, or by contacting The Cambridge Crystallographic Data Centre, 12 Union Road, Cambridge CB2 1EZ, UK; fax: +44 1223 336033.

■ AUTHOR INFORMATION

Corresponding Authors

*(V.V.B.) E-mail: vbutova@sfedu.ru.

*(C.L.) E-mail: carlo.lamberti@unito.it.

ORCID

Kirill A. Lomachenko: 0000-0003-0238-1719

Aram L. Bugaev: 0000-0001-8273-2560

Unni Olsbye: 0000-0003-3693-2857

Silvia Bordiga: 0000-0003-2371-4156

Carlo Lamberti: 0000-0001-8004-2312

Notes

The authors declare no competing financial interest.

■ ACKNOWLEDGMENTS

V.V.B., A.P.B., A.A.G., K.A.L., A.L.B., A.V.S., and C.L. acknowledge Mega-Grant of Ministry of Education and Science of the Russian Federation (14.Y26.31.0001) for funding the research. A.A.G. acknowledges the grant of the President of Russia for young scientists MK-7300.2016.2. We are indebted

to Vladimir Dmitriev, Herman Emerich, Wouter van Beek, and Michela Brunelli for the friendly and competent support during the experiment performed at the BM01B (now BM31) beamline of the ESRF. We acknowledge the support of Alessandro Damin during the Raman experiments. The authors are grateful to Boris Bouchevreau for helpful discussion.

■ REFERENCES

- (1) Furukawa, H.; Cordova, K. E.; O'Keeffe, M.; Yaghi, O. M. *Science* **2013**, *341*, No. 1230444.
- (2) Kaskel, S.; Ed. *The Chemistry of Metal-Organic Frameworks: Synthesis, Characterization, and Applications*; John Wiley & Sons: Weinheim, 2016.
- (3) Li, J. R.; Kuppler, R. J.; Zhou, H. C. *Chem. Soc. Rev.* **2009**, *38*, 1477–1504.
- (4) Murray, L. J.; Dinca, M.; Long, J. R. *Chem. Soc. Rev.* **2009**, *38*, 1294–1314.
- (5) Farrusseng, D.; Ed. *Metal-Organic Frameworks: Applications from Catalysis to Gas Storage*; Wiley: Weinheim, 2011.
- (6) Sumida, K.; Rogow, D. L.; Mason, J. A.; McDonald, T. M.; Bloch, E. D.; Herm, Z. R.; Bae, T. H.; Long, J. R. *Chem. Rev.* **2012**, *112*, 724–781.
- (7) Ma, L. Q.; Abney, C.; Lin, W. B. *Chem. Soc. Rev.* **2009**, *38*, 1248–1256.
- (8) Corma, A.; Garcia, H.; Llabrés i Xamena, F. *Chem. Rev.* **2010**, *110*, 4606–4655.
- (9) Ranocchiari, M.; van Bokhoven, J. A. *Phys. Chem. Chem. Phys.* **2011**, *13*, 6388–6396.
- (10) Llabrés i Xamena, F. X.; Gascon, J. *Metal Organic Frameworks as Heterogeneous Catalysts*; Royal Society of Chemistry: Cambridge, 2013.
- (11) Chughtai, A. H.; Ahmad, N.; Younus, H. A.; Laypkov, A.; Verpoort, F. *Chem. Soc. Rev.* **2015**, *44*, 6804–6849.
- (12) Horcajada, P.; Gref, R.; Baati, T.; Allan, P. K.; Maurin, G.; Couvreur, P.; Ferey, G.; Morris, R. E.; Serre, C. *Chem. Rev.* **2012**, *112*, 1232–1268.
- (13) He, C. B.; Liu, D. M.; Lin, W. B. *Chem. Rev.* **2015**, *115*, 11079–11108.
- (14) Kitagawa, S.; Kitaura, R.; Noro, S. *Angew. Chem., Int. Ed.* **2004**, *43*, 2334–2375.
- (15) Ferey, G. *Chem. Soc. Rev.* **2008**, *37*, 191–214.
- (16) Fang, Z. L.; Bueken, B.; De Vos, D. E.; Fischer, R. A. *Angew. Chem., Int. Ed.* **2015**, *54*, 7234–7254.
- (17) Furukawa, H.; Muller, U.; Yaghi, O. M. *Angew. Chem., Int. Ed.* **2015**, *54*, 3417–3430.
- (18) Butova, V. V.; Soldatov, M. A.; Guda, A. A.; Lomachenko, K. A.; Lamberti, C. *Russ. Chem. Rev.* **2016**, *85*, 280–307.
- (19) Cavka, J. H.; Jakobsen, S.; Olsbye, U.; Guillou, N.; Lamberti, C.; Bordiga, S.; Lillerud, K. P. *J. Am. Chem. Soc.* **2008**, *130*, 13850–13851.
- (20) Chavan, S.; Vitillo, J. G.; Uddin, M. J.; Bonino, F.; Lamberti, C.; Groppo, E.; Lillerud, K. P.; Bordiga, S. *Chem. Mater.* **2010**, *22*, 4602–4611.
- (21) Valenzano, L.; Civalleri, B.; Chavan, S.; Bordiga, S.; Nilsen, M. H.; Jakobsen, S.; Lillerud, K. P.; Lamberti, C. *Chem. Mater.* **2011**, *23*, 1700–1718.
- (22) Chavan, S.; Vitillo, J. G.; Gianolio, D.; Zavorotynska, O.; Civalleri, B.; Jakobsen, S.; Nilsen, M. H.; Valenzano, L.; Lamberti, C.; Lillerud, K. P.; Bordiga, S. *Phys. Chem. Chem. Phys.* **2012**, *14*, 1614–1626.
- (23) Jakobsen, S.; Gianolio, D.; Wragg, D. S.; Nilsen, M. H.; Emerich, H.; Bordiga, S.; Lamberti, C.; Olsbye, U.; Tilsted, M.; Lillerud, K. P. *Phys. Rev. B: Condens. Matter Mater. Phys.* **2012**, *86*, No. 125429, DOI: [10.1103/PhysRevB.86.125429](https://doi.org/10.1103/PhysRevB.86.125429).
- (24) Shearer, G. C.; Chavan, S.; Ethiraj, J.; Vitillo, J. G.; Svelle, S.; Olsbye, U.; Lamberti, C.; Bordiga, S.; Lillerud, K. P. *Chem. Mater.* **2014**, *26*, 4068–4071.
- (25) Øien, S.; Wragg, D.; Reinsch, H.; Svelle, S.; Bordiga, S.; Lamberti, C.; Lillerud, K. P. *Cryst. Growth Des.* **2014**, *14*, 5370–5372.

- (26) Reinsch, H.; Bueken, B.; Vermoortele, F.; Stassen, I.; Lieb, A.; Lillerud, K. P.; De Vos, D. *CrystEngComm* **2015**, *17*, 4070–4074.
- (27) Øien, S.; Agostini, G.; Svelle, S.; Borfecchia, E.; Lomachenko, K. A.; Mino, L.; Gallo, E.; Bordiga, S.; Olsbye, U.; Lillerud, K. P.; Lamberti, C. *Chem. Mater.* **2015**, *27*, 1042–1056.
- (28) Øien-Ødegaard, S.; Bouchevreau, B.; Hylland, K.; Wu, L.; Blom, R.; Grande, C.; Olsbye, U.; Tilsted, M.; Lillerud, K. P. *Inorg. Chem.* **2016**, *55*, 1986–1991.
- (29) Shearer, G. C.; Vitillo, J. G.; Bordiga, S.; Svelle, S.; Olsbye, U.; Lillerud, K. P. *Chem. Mater.* **2016**, *28*, 7190–7193.
- (30) Braglia, L.; Borfecchia, E.; Maddalena, L.; Oien, S.; Lomachenko, K. A.; Bugaev, A. L.; Bordiga, S.; Soldatov, A. V.; Lillerud, K. P.; Lamberti, C. *Catal. Today* **2017**, *283*, 89–103.
- (31) Atzori, C.; Shearer, G. C.; Maschio, L.; Civalleri, B.; Bonino, F.; Lamberti, C.; Svelle, S.; Lillerud, K. P.; Bordiga, S. *J. Phys. Chem. C* **2017**, *121*, 9312–9324.
- (32) Trickett, C. A.; Gagnon, K. J.; Lee, S.; Gandara, F.; Burgi, H. B.; Yaghi, O. M. *Angew. Chem., Int. Ed.* **2015**, *54*, 11162–11167.
- (33) Goesten, M. G.; de Lange, M. F.; Olivos-Suarez, A. I.; Bavykina, A. V.; Serra-Crespo, P.; Krywka, C.; Bickelhaupt, F. M.; Kapteijn, F.; Gascon, J. *Nat. Commun.* **2016**, *7*, No. 11832.
- (34) Lausund, K. B.; Nilsen, O. *Nat. Commun.* **2016**, *7*, 13578.
- (35) Yang, D.; Bernales, V.; Islamoglu, T.; Farha, O. K.; Hupp, J. T.; Cramer, C. J.; Gagliardi, L.; Gates, B. C. *J. Am. Chem. Soc.* **2016**, *138*, 15189–15196.
- (36) Bai, Y.; Dou, Y. B.; Xie, L. H.; Rutledge, W.; Li, J. R.; Zhou, H. *C. Chem. Soc. Rev.* **2016**, *45*, 2327–2367.
- (37) Shearer, G. C.; Chavan, S.; Bordiga, S.; Svelle, S.; Olsbye, U.; Lillerud, K. P. *Chem. Mater.* **2016**, *28*, 3749–3761.
- (38) Tsuruoka, T.; Furukawa, S.; Takashima, Y.; Yoshida, K.; Isoda, S.; Kitagawa, S. *Angew. Chem., Int. Ed.* **2009**, *48*, 4739–4743.
- (39) Diring, S.; Furukawa, S.; Takashima, Y.; Tsuruoka, T.; Kitagawa, S. *Chem. Mater.* **2010**, *22*, 4531–4538.
- (40) Umemura, A.; Diring, S.; Furukawa, S.; Uehara, H.; Tsuruoka, T.; Kitagawa, S. *J. Am. Chem. Soc.* **2011**, *133*, 15506–15513.
- (41) Vermoortele, F.; Bueken, B.; Le Bars, G.; Van de Voorde, B.; Vandichel, M.; Houthoofd, K.; Vimont, A.; Daturi, M.; Waroquier, M.; Van Speybroeck, V.; Kirschhock, C.; De Vos, D. E. *J. Am. Chem. Soc.* **2013**, *135*, 11465–11468.
- (42) Wu, H.; Chua, Y. S.; Krungleviciute, V.; Tyagi, M.; Chen, P.; Yildirim, T.; Zhou, W. *J. Am. Chem. Soc.* **2013**, *135*, 10525–10532.
- (43) Schaate, A.; Roy, P.; Godt, A.; Lippke, J.; Waltz, F.; Wiebcke, M.; Behrens, P. *Chem. - Eur. J.* **2011**, *17*, 6643–6651.
- (44) Gutov, O. V.; Hevia, M. G.; Escudero-Adan, E. C.; Shafir, A. *Inorg. Chem.* **2015**, *54*, 8396–8400.
- (45) Taylor, J. M.; Dekura, S.; Ikeda, R.; Kitagawa, H. *Chem. Mater.* **2015**, *27*, 2286–2289.
- (46) Gutov, O. V.; Molina, S.; Escudero-Adan, E. C.; Shafir, A. *Chem. - Eur. J.* **2016**, *22*, 13582–13587.
- (47) Liang, W. B.; Coghlan, C. J.; Ragon, F.; Rubio-Martinez, M.; D'Alessandro, D. M.; Babarao, R. *Dalton Trans.* **2016**, *45*, 4496–4500.
- (48) Cai, G. R.; Jiang, H. L. *Angew. Chem., Int. Ed.* **2017**, *56*, 563–567.
- (49) DeStefano, M. R.; Islamoglu, T.; Hupp, J. T.; Farha, O. K.; Garibay, S. J. *Chem. Mater.* **2017**, *29*, 1357–1361.
- (50) Garibay, S. J.; Cohen, S. M. *Chem. Commun.* **2010**, *46*, 7700–7702.
- (51) Huang, Y. T.; Qin, W. P.; Li, Z.; Li, Y. W. *Dalton Trans.* **2012**, *41*, 9283–9285.
- (52) Lowell, S.; Shields, J. E.; Thomas, M. A.; Thommes, M. Mesopore Analysis. In *Characterization of Porous Solids and Powders: Surface Area, Pore Size and Density*; Lowell, S., Shields, J. E., Thomas, M. A., Thommes, M., Eds.; Springer: Netherlands: Dordrecht, 2004; pp 101–128.
- (53) Sing, K. S. W.; Rouquerol, F.; Llewellyn, P.; Rouquerol, J. Chapter 9: Assessment of Microporosity. In *Adsorption by Powders and Porous Solids*, 2nd ed.; Rouquerol, J.; Rouquerol, F.; Llewellyn, P.; Maurin, G.; Sing, K. S. W., Eds.; Academic Press: Oxford, 2014; pp 303–320.
- (54) van Beek, W.; Safonova, O. V.; Wiker, G.; Emerich, H. *Phase Transitions* **2011**, *84*, 726–732.
- (55) Knudsen, E. B.; Sorensen, H. O.; Wright, J. P.; Goret, G.; Kieffer, J. *J. Appl. Crystallogr.* **2013**, *46*, 537–539.
- (56) Petříček, V.; Dušek, M.; Palatinus, L. Z. *Kristallogr. - Cryst. Mater.* **2014**, *229*, 345–352.
- (57) Ravel, B.; Newville, M. J. *Synchrotron Radiat.* **2005**, *12*, 537–541.
- (58) Momma, K.; Izumi, F. *J. Appl. Crystallogr.* **2011**, *44*, 1272–1276.
- (59) Trotter, J. *Acta Crystallogr.* **1960**, *13*, 732–736.
- (60) Derissen, J.; Timmermans, C.; Schoone, J. *Cryst. Struct. Commun.* **1979**, *8*, 533–536.
- (61) Kress, R. B.; Duesler, E. N.; Etter, M. C.; Paul, I. C.; Curtin, D. Y. *J. Am. Chem. Soc.* **1980**, *102*, 7709–7714.
- (62) Fitzgerald, L. J.; Gerkin, R. E. *Acta Crystallogr., Sect. C: Cryst. Struct. Commun.* **1993**, *49*, 1952–1958.
- (63) Jing, L.-H.; Qin, D.-B.; Mao, Z.-H.; Gu, S.-J.; Zhang, H.-X. *Acta Crystallogr., Sect. E: Struct. Rep. Online* **2005**, *61*, o4365–o4366.
- (64) Borfecchia, E.; Gianolio, D.; Agostini, G.; Bordiga, S.; Lamberti, C. Characterization of MOFs. 2. Long and local range order structural determination of MOFs by combining EXAFS and diffraction techniques. In *Metal Organic Frameworks as Heterogeneous Catalysts*; Llabrés i Xamena, F. X.; Gascon, J., Eds.; Royal Society of Chemistry: Cambridge, 2013; pp 143–208.
- (65) Barrett, E. P.; Joyner, L. G.; Halenda, P. P. *J. Am. Chem. Soc.* **1951**, *73*, 373–380.
- (66) Thommes, M.; Kaneko, K.; Neimark, A. V.; Olivier, J. P.; Rodriguez-Reinoso, F.; Rouquerol, J.; Sing, K. S. W. *Pure Appl. Chem.* **2015**, *87*, 1051–1069.
- (67) Brunauer, S.; Emmett, P. H.; Teller, E. *J. Am. Chem. Soc.* **1938**, *60*, 309–319.
- (68) Langmuir, I. *J. Am. Chem. Soc.* **1916**, *38*, 2221–2295.

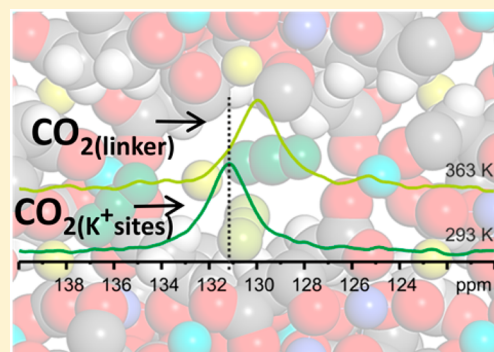
CO₂ Adsorption Sites in UTSA-16: Multitechnique Approach

Alessio Masala, Francesca Grifasi, Cesare Atzori, Jenny G. Vitillo, Lorenzo Mino, Francesca Bonino, Michele R. Chierotti, and Silvia Bordiga*

Department of Chemistry, NIS and INSTM Reference Centres, University of Torino, Via G. Quarelo 15/A, 10135 and Via P. Giuria 7, 10125 Torino, Italy

S Supporting Information

ABSTRACT: The key role of K⁺ counterions in determining the high CO₂ capacity of UTSA-16 has been highlighted thanks to a combined use of in situ infrared and ¹³C solid-state NMR spectroscopies performed in a controlled atmosphere at variable temperature and pressure. A second family of sites, engaged at higher temperature or at higher coverage, was identified in the organic linker. Variable temperature IR measurements of molecular hydrogen at 15 K allowed to further distinguish the K⁺ sites in two families, slightly different in their polarizing ability and indistinguishable on the basis of CO₂ isosteric heat and by using a less sensitive probe than H₂, as CO and N₂.



INTRODUCTION

Porous metal–organic frameworks (MOFs) are a well-known class of crystalline hybrid materials constituted of metal ions (isolated or clustered) bonded through rigid organic linkers that keep high microporosity once the solvent has been completely removed.¹ The tridimensional structure of these materials may be described on the basis of secondary building units (SBU) that characterize the metal cations and the organic linkers, both easily tunable to fulfill specific characteristics required to use them in technologic applications.^{2–6} One of the most interesting properties of porous metal–organic frameworks is their high surface area as well as tunable pore size and pore volume. Thanks to these characteristics, MOFs have been extensively studied for small molecules capture, storage, and separation.^{3,7–9} Within the extraordinary rich library of MOFs, Xiang et al.^{10,11} introduced recently UTSA-16, showing its high performance as adsorbent for carbon dioxide, with a volumetric CO₂ uptake of 160 cm³ cm⁻³ at 1 bar and 298 K.

Recently,¹² UTSA-16 (K₂CO₃(cit)₂, cit = C₆H₄O₇) was characterized by physical chemical techniques, suggesting as main CO₂ adsorption site, the K⁺ counterions. Volumetric data of adsorbed CO₂ at 298 K and 1 bar (4.2 mol kg⁻¹) suggested that CO₂ not only saturates all the K⁺ species present inside the UTSA-16 cavities forming 1:1 adducts, but that there was a consistent fraction of adsorbed CO₂ (approximately 22%) that exceeds and was characterized by an adsorption enthalpy almost coincident with that of the K⁺ cations. The present work aims to highlight the nature of different adsorption sites in UTSA-16 combining solid state NMR of ¹³CO₂ and infrared spectroscopy using different probe molecules (H₂, N₂, and CO) thanks to measurements performed in controlled atmosphere at variable pressures and temperatures.

EXPERIMENTAL SECTION

UTSA-16 was prepared by SINTEF (Oslo-Norway) according to the synthesis described in literature.^{10,11,13} Additional details are reported in section 1 of the Supporting Information. All chemicals were purchased by Sigma-Aldrich. Before any measurement, UTSA-16 was activated under high vacuum for 2 h and then heated up to 363 K overnight. Final vacuum was below 5 × 10⁻⁴ mbar. Carbon dioxide adsorption heat was measured at 303 K, with a Tian-Calvet microcalorimeter (Calvet C80, Setaram, France) connected to a grease-free high-vacuum gas-volumetric glass apparatus (residual p ≈ 10⁻⁴ mbar) equipped with a Ceramicell 0–100 mbar gauge (by Varian). In order to determine both integral heats evolved (–q_{int}) and adsorbed amounts (n_{ads}) a well established stepwise procedure was followed, described in section 2 of the Supporting Information.

Solid-state nuclear magnetic resonance (SSNMR) spectra were recorded on a Bruker Avance II 400 instrument operating at 400.23 and 100.65 MHz for ¹H and ¹³C nuclei, respectively. Zirconia rotors (4 mm o.d., sample volume of 80 μL) were used. Additional details are given in section 3 of the Supporting Information.

CO₂ adsorption isotherms were measured at 273 and 298 K using a commercial volumetric instrument (TriStar II 3020 Micromeritics). The temperature stability was maintained by means of an isothermal water bath. In order to evaluate the isosteric heats of adsorption, CO₂ adsorption isotherms were fitted by a cubic spline function; each calorimetric point

Received: April 1, 2016

Revised: May 12, 2016

Published: May 13, 2016

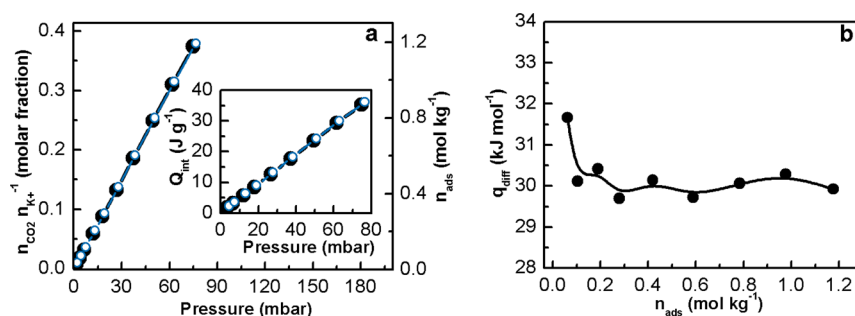


Figure 1. (a): Microcalorimetric first (black) and second (light blue, empty symbols) CO₂ volumetric isotherms (303 K) on UTSA-16. The CO₂ capacity is reported normalized to the number of K⁺ ions (left of y-axis) and to the mass of the sample (right y-axis). The inset illustrates the variation of the integral heat of adsorption (Q_{int}) with respect to the pressure (calorimetric isotherm). (b): CO₂ differential heat of adsorption (q_{diff}) obtained from the data of primary CO₂ isotherm reported in (a).

reported in the inset of Figure 3 was obtained by applying the Clausius–Clapeyron equation defined as

$$q_{\text{st}} = RT^2 \left(\frac{\partial \ln p}{\partial T} \right)_q \quad (1)$$

Plotting the natural logarithm of the pressure (p) as a function of $1/T$, a straight line (isosteric curve) was obtained whose slope is equal to $-q_{\text{st}}/R$ at constant loading (q): this is possible by assuming a Langmuir behavior of the adsorption and applying the Clausius–Clapeyron equation. The isosteric heat of adsorption is obtained by multiplying the slope by the perfect gas constant, as derived from eq 1.

For infrared (IR) measurements, UTSA-16 samples were prepared in form of self-supporting thin pellets. Before gas adsorption, samples were outgassed under high vacuum at 363 K overnight in the cryogenic cell (a closed circuit liquid helium Oxford CCC 1204 cryostat properly modified) allowing infrared investigation of species adsorbed under controlled temperature (between 300 and 15 K) and pressure conditions. Infrared spectra were recorded on a Bruker Equinox 55 FTIR spectrometer (sample compartment modified to accommodate the cryogenic head), 128 interferograms (1 cm⁻¹ resolution) were averaged for each recorded spectrum. H₂ adsorption enthalpy was evaluated by variable temperature IR measurements, following the procedures described in literature^{8,14} and explained in more details in section 4 of Supporting Information.

RESULTS AND DISCUSSION

CO₂ Adsorption by Microcalorimetry. Microcalorimetry was used to obtain a direct measure of CO₂ energetic interaction with UTSA-16 through the measurement of the heat of adsorption.

Figure 1a reports primary (black points and line) and secondary (light blue points and line) CO₂ adsorption isotherms obtained as described in section 2 of the Supporting Information. The adsorption profile suggests the presence of a single specific interaction site that is not saturated at the maximum coverage reached in the experiment (<100 mbar); moreover, the complete coincidence of the two isotherms indicates the total reversibility of the interaction of CO₂ with UTSA-16. In particular, the graph shows that less than 50% of the K⁺ sites are interacting with CO₂ at this equilibrium pressure. Figure 1b illustrates the change in the differential heat of adsorption (q_{diff}) with increasing coverage for the primary adsorption of CO₂ (secondary adsorption is reported in Figure

S1, Supporting Information); we note that the q_{diff} goes from 32 kJ mol⁻¹ at 0.06 mol kg⁻¹ to a constant value of 30 kJ mol⁻¹, over the full range of measurements, suggesting the presence of only one type of adsorption site, characterized by a medium interaction strength.¹⁵ UTSA-16 CO₂ adsorption enthalpy is slightly higher than that reported for MOFs without exposed cations, as UiO-66 and UiO-66-NH₂ (22 and 27 kJ mol⁻¹ respectively, see Table S1 in the Supporting Information).¹⁶ For what concerns the comparison with MOFs having exposed cations, different factors determine the CO₂ adsorption enthalpy like charge/radius ratio, pore dimensions and shielding of the cation by the framework: for instance, the q_{diff} of UTSA-16 is similar to what reported for HKUST-1(Cu)¹⁷ (28.2 kJ mol⁻¹) whereas it is slightly lower than that measured for MIL101(Cr)^{3,18} (44 kJ mol⁻¹) and CPO-27(Mg)¹⁹ (53 kJ mol⁻¹). In a previous paper,¹² reporting the isosteric heat of adsorption and IR data, it was shown that the most energetically favorable adsorption site was due to K⁺ species, which are able to form 1:1 linear adducts with CO₂. The maximum capacity of the K⁺ sites for CO₂ is 3.2 mol kg⁻¹ for a 1:1 adduct. This indicates that for a CO₂ uptake higher than 3.2 mol kg⁻¹ a second adsorption site must be involved. The interest in the nature of this second adsorption site relies in the fact that it is characterized by an adsorption enthalpy only slightly lower than the K⁺ ion.¹²

As described below, NMR data allow to illustrate CO₂ adsorption features in a equilibrium pressure range not explored by microcalorimetry.

Solid State ¹³CO₂ NMR. SSNMR is an element-selective technique which can give new insights on the nature of adsorbed molecules and their interaction with the host surfaces, describing both CO₂ adsorption sites and CO₂ dynamics within the porous structure. Many SSNMR studies were conducted to investigate gas adsorption in zeolites, molecular sieves, or metal catalysts,^{20,21} while only few of them were devoted to MOFs.^{22–24}

¹³CO₂ gas was dosed at different pressures (5, 20, 50, 100, 200, and 600 mbar) at 298 K on activated UTSA-16. A single signal, around 131 ppm, was observed at all CO₂ pressures (see Supporting Information Figure S2). Interestingly, the peak underwent a shift to lower frequencies (of about 1.1 ppm) on increasing the pressure, suggesting the presence of more than one CO₂ species within the MOF, thus more than one adsorption site inside the UTSA-16 cavities. For the samples at 200 and 600 mbar, variable temperature (VT) 293–373 K SSNMR measurements were also performed. These were instrumental to the detection and elucidation of exchange

phenomena among different molecular species of $^{13}\text{CO}_2$ within UTSA-16.

Figure 2 displays the ^{13}C MAS spectra of the sample at 200 mbar recorded at variable temperature (293 to 373 K). The

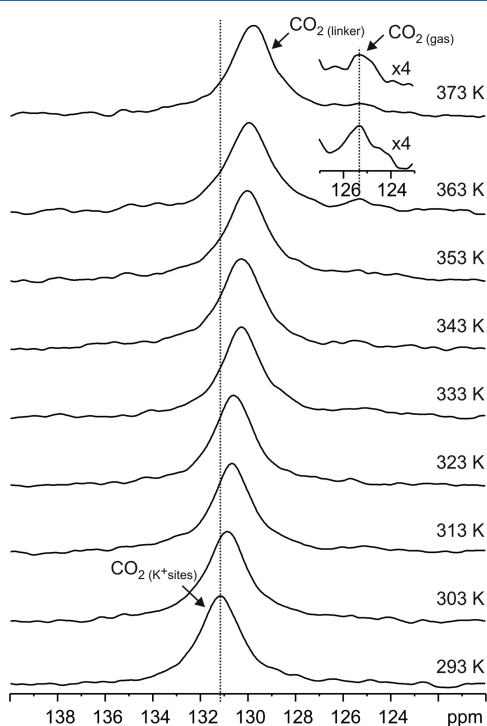


Figure 2. ^{13}C (100.65 MHz) MAS spectra with relevant assignments of $^{13}\text{CO}_2$ -loaded UTSA-16 at 200 mbar in the temperature range from 293 to 373 K recorded with a spinning speed of 12 kHz.

spectrum at 293 K shows a single resonance at 131.2 ppm that can be ascribed to physisorbed CO_2 . This signal shifts toward lower frequency on increasing the temperature. In the spectra at 363 and 373 K, in addition to the main contribution, now shifted to 129.7 ppm, a much weaker contribution at 125.3 ppm appears. The resonance peak at 125.3 ppm is easily assigned to the CO_2 in the gas phase (labeled as $\text{CO}_{2(\text{gas})}$ in Figure 2), while the chemical shift of the main band (from 131.2 to 129.7 ppm) with increasing temperature reflects the dynamical behavior of adsorbed CO_2 . Combining FTIR,¹² microcalorimetric, and SSNMR data, it was possible to assign the contribution at 131.2 ppm (clearly seen at coverage below 100 mbar at 293 K) to CO_2 directly interacting with K^+ (labeled as $\text{CO}_{2(\text{K}^+\text{ sites})}$ in Figure 2), while the signal at 129.7 ppm can be attributed to CO_2 still trapped inside the MOF cages and involved in a slightly weaker interaction probably with the organic linker (labeled as $\text{CO}_{2(\text{linker})}$ in Figure 2), as indicated by the chemical shift with respect to $\text{CO}_{2(\text{gas})}$.

Similar behaviors were already observed for CO and CO_2 loaded on $\text{Cu}_3(\text{BTC})_2$: while the extent of the shift is comparable (~ 1.2 ppm), in those cases the resonance shift was toward lower frequencies.²⁵ This may be due to the difference in adsorption site (Cu vs K^+) and also to the difference in the metal component of the MOF (Cu vs Co with different paramagnetic character).

VT measurements were also performed on the sample with 600 mbar of CO_2 equilibrium pressure (see Supporting Information, Figure S3). In this case, the free CO_2 gas ($\text{CO}_{2(\text{gas})}$) signal (125.3 ppm) becomes well visible at 333 K.

Dynamical data were derived from the chemical shift temperature dependence of the VT ^{13}C NMR spectra for adsorbed CO_2 molecules. The appearance of two distinct features at high temperature attributed, respectively, to CO_2 molecules in the gas phase ($\text{CO}_{2(\text{gas})}$) and to those adsorbed in the MOF, indicating a slow exchange in the NMR time scale between adsorbed molecules and the gas phase under equilibrium conditions, without change of the total number of molecules. However, owing to the low signal intensity, the fraction of $\text{CO}_{2(\text{gas})}$ cannot be estimated from the spectra,²⁵ so that it is not possible to obtain an enthalpy of activation for the exchange between these two CO_2 species. On the other hand, the temperature dependence of the signal related to CO_2 molecules adsorbed in the MOF reflected a fast exchange process, compared to that of the NMR time scale, between the strongly adsorbed molecules ($\text{CO}_{2(\text{K}^+\text{ sites})}$; $\delta \sim 131$ ppm) and those more weakly adsorbed ($\text{CO}_{2(\text{linker})}$; $\delta \sim 130$ ppm). This observation leads to a determination of the exchange energy between $\text{CO}_{2(\text{K}^+\text{ sites})}$ and $\text{CO}_{2(\text{linker})}$ by using eq 2 which allows the occupation number of the molecules adsorbed on K^+ sites to be calculated by considering the averaged shift due to the fast exchange between the molecules on K^+ sites and on the linker.

$$\delta(T)_{\text{measured}} = (1 - P_{(\text{K}^+\text{ sites})})\delta_{(\text{linker})} + P_{(\text{K}^+\text{ sites})}\delta_{(\text{K}^+\text{ sites})} \quad (2)$$

$\delta_{(\text{linker})}$ was extrapolated from the peak shift shown in Figure 2 to infinite temperature. In a similar way the measured low temperature values for $\delta_{(\text{K}^+\text{ sites})}$ were extrapolated with an error of 3 ppm. By using $P(T)_{\text{adsorbed}}$ and assuming an Arrhenius plot (see Supporting Information, Figure S4) a calorimetric quantification of the exchange phenomena between $\text{CO}_{2(\text{K}^+\text{ sites})}$ and $\text{CO}_{2(\text{linker})}$ is then given by eq 2, from which an activation enthalpy of 6.3–9.3 kJ mol^{-1} (local motions in the MOFs; $\text{CO}_2(\text{K}^+\text{ sites}) \leftrightarrow \text{CO}_2(\text{linker})$) can be derived.

While magic angle spinning (MAS) spectra distinguished three types of CO_2 species, static spectra highlighted the dynamics of the processes through the analysis of the signal line shapes, as previously reported in the case of CO_2 adsorbed on $\text{Mg}_2(\text{dobdc})$.¹⁸ The VT static ^{13}C NMR spectra are reported in Figure S5 (see Supporting Information). All spectra were characterized by a single very broad peak and no relevant changes were observed when the temperature was increased. The hump-like pattern of the static spectra (fwhm ~ 12 kHz compared to fast rotating $\text{CO}_{2(\text{gas})}$, fwhm < 1 kHz) provides direct evidence of a strong interaction between CO_2 and the MOF matrix. This implies a drastic reduction of the CO_2 motional freedom. Furthermore, the difference in line shapes from that typical of the CSA (chemical shift anisotropy) interaction suggests an intermediate motional regime of the $\text{CO}_{2(\text{K}^+\text{ sites})}$ on the binding sites characterized by disordered reorientational motion.^{22–24}

Volumetric CO_2 Adsorption Measurements and Isosteric Heat of Adsorption. In order to validate the presence of a second adsorption site within UTSA-16, isosteric heat of CO_2 adsorption (Figure 3, inset) was calculated from the volumetric isotherms at 273 and 298 K until CO_2 loadings of 4.2 mol kg^{-1} , extending the pressure range described in a previous work.¹²

To briefly comment the isotherm curves which were widely discussed in our previous work,¹² it is possible to denote that the isotherm at 273 K reaches a maximum value (4.9 mol kg^{-1}) very close to the uptake calculated from the total volume of UTSA-16 pores, which was attested to 5.6 mol kg^{-1} .

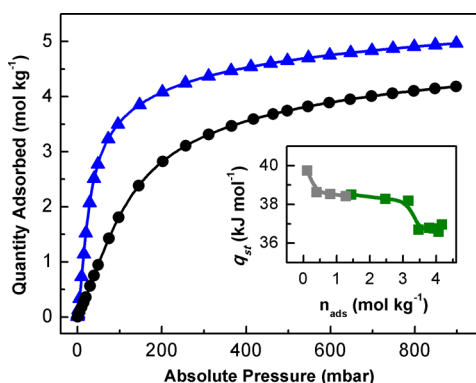


Figure 3. CO₂ volumetric isotherms on UTSA-16 at 273 K (▲, blue points), and 298 K (●, black points) measured until 1 bar. Continuous lines represent the cubic spline fits computed on the experimental points. On the inset, the isosteric heat of CO₂ adsorption (q_{st} , green points) as a function of loading. The first five points of this trend (■, gray points) belong to ref 12 and they have been calculated with three isotherms at 273, 298, and 313 K.

In our previous work, a constant value ($q_{st} = 38 \text{ kJ mol}^{-1}$) of CO₂ isosteric heat of adsorption (q_{st}) was calculated for a coverage range of 0.4–3.2 mol kg⁻¹, where the saturation of K⁺ sites by carbon dioxide is not reached yet.¹² Reducing the number of isotherms involved in the calculation from three to two, it was possible to extend the coverage range well above the K⁺ saturation point at 3.2 mol kg⁻¹ and so to allow to estimate the isosteric heat associated with the adsorption of CO₂ over a second minor site, as shown in the inset of Figure 3: the first part of the trend below K⁺ saturation is related to the interaction of CO₂ with K⁺ sites as suggested by the isosteric heat value of 38 kJ mol⁻¹ coinciding with the literature;^{12,26} when the saturation of K⁺ sites is reached, the isosteric curve steps down of 1 kJ mol⁻¹ approaching an average value of 37 kJ mol⁻¹. This second constant trend confirms the results of NMR, indicating the presence of a second adsorption site other than K⁺ cations. As already discussed in our previous work,¹² the isosteric heat of CO₂ adsorption calculated for UTSA-16 is one of the best among MOFs with exposed cations. Also when compared to MOFs with higher q_{st} , such as Mg₂(dobdc)²⁷ (47 kJ mol⁻¹) or Ni₂(dobdc)²⁸ (42 kJ mol⁻¹), the q_{st} of UTSA-16 does not drop down after saturation of the exposed cations. This can be related to the presence of tight pores ($3.3 \times 5.4 \text{ \AA}^2$)¹⁰ in UTSA-16 that promote the interaction of CO₂ with secondary adsorption sites other than potassium. An attempt to explain the nature of this site will be addressed by infrared spectroscopy.

VT-IR of Probe Molecules on UTSA-16. The nature of the second adsorption site in UTSA-16 was investigated by VT-IR spectroscopy by studying the adsorption of three probe molecules: H₂, N₂, and CO. Most relevant results are reported in Figure 4a–c.

VT-IR method allows to deduce, besides the information normally obtained from IR at constant T , the enthalpy of adsorption for very specific surface sites (see Supporting Information).^{7,8,29}

Molecular hydrogen is one of the most attractive probe molecule for many reasons:^{30,31} (i) the presence of a single bond between the two H–H atoms makes this molecule very sensitive to any surface heterogeneity, as even small perturbations originate shifts of the $\nu(\text{HH})$, larger than those observed in case of probe molecules characterized by multiple

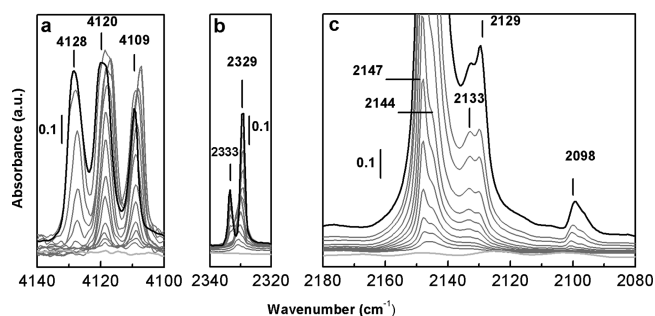


Figure 4. Background subtracted IR spectra of (a) H₂, (b) N₂, and (c) CO adsorbed on UTSA-16 at 15 K for H₂ and 60 K for N₂ or CO. Black lines correspond to the spectra collected in the presence of 0.1 mbar of H₂, 0.2 mbar of N₂, and CO equilibrium pressures, respectively. Light gray lines correspond to the spectra collected after outgassing overnight in a dynamic vacuum. Gray lines: intermediate coverage.

bonds (i.e., N₂ or CO); (ii) $\nu(\text{H–H})$ mode is IR-inactive implying that every signal observed in the IR is related to the perturbations caused by the interaction of the probe with the surface sites; (iii) the small kinetic diameter (2.89 Å)³² of this molecule allows to investigate in detail both cavities and surface active sites; and (iv) because of its amphoteric character, H₂ is able to test both acidic and basic surface sites.

A known amount of hydrogen (20 mbar) was dosed on the activated sample at 250 K and a series of spectra were collected while cooling until 15 K (1 spectrum each 5 K). The set of spectra recorded lowering the temperature are reported in the Supporting Information and were used to evaluate the adsorption enthalpy.

Figure 4a shows background subtracted spectra in the $\nu(\text{H–H})$ region collected during outgassing at 15 K. For the sake of clarity we will describe the spectra starting from low to high coverage. At low equilibrium pressure, two main bands appear at 4109 and 4119 cm⁻¹ and grow in parallel ($\Delta\nu = -52$ and -42 cm^{-1} , respectively, in respect to ν -para-H₂ expected at 4161 cm⁻¹). Both values are compatible with the formation of side-on H₂ adducts with K⁺ sites, on the basis of results reported for K-FER³³ or K-ZSM-5³⁴ ($\Delta\nu = -50$ and -49 cm^{-1} , respectively) but in this case surprisingly sharp bands are observed (fwhm = 4 cm⁻¹). At higher coverage a further band appears at 4128 cm⁻¹ ($\Delta\nu = -33 \text{ cm}^{-1}$) and becomes the most intense component at maximum H₂ loading (bold dark gray curve in Figure 4a). The last spectrum shows small changes in intensity ratio and maxima positions in respect to the medium coverage, suggesting that hydrogen, packing inside the small cavities of UTSA-16, undergoes some rearrangements in order to accommodate new incoming molecules. The frequency separation observed in case of the main doublet ($\Delta\nu = 11 \text{ cm}^{-1}$) is compatible with the co-presence of ortho and para-H₂ but, in this case, upon decreasing the temperature, a change in the intensity ratio would have been expected after a waiting time of 15 h. In fact, it is known that para-H₂ (associated with the highest frequency component) is more stable at low temperature, with respect to the less stable ortho-H₂ adduct.⁸ Conversely, the intensity of the two peaks is constant since their appearance at 90 K (Figure S6a black line) also after a long waiting time. An alternative explanation can be given, implying the presence of two slightly different K⁺–H₂ adducts arising from a difference in the orientation of H₂ (as already described in other MOFs),⁷ or assuming two different K⁺ sites

(K_1^+ and K_2^+). Finally, the peak at 4128 cm^{-1} is easily associated with H_2 perturbed by the oxygen atoms of the citrate organic linkers of UTSA-16, in line to what previously was observed in case of H_2 adsorbed inside microporous materials.^{7,8,33,35} Thanks to the peak sharpness, an evaluation of H_2 adsorption enthalpy was obtained by the analysis of VT-IR spectra recorded in the 90 to 15 K temperature range. Following the procedure previously described^{8,14} three values of H_2 adsorption enthalpy have been calculated (standard linear fits reported in Figure S7, S8, and S9 of the Supporting Information) and presented in Table 1. The presence of

Table 1. Summary of the Most Relevant Properties Obtained from VT-IR of Adsorbed H_2 for the Different UTSA-16 Active Sites^a

UTSA-16	$\nu(H-H)$ (cm^{-1})	$-\Delta\nu(H-H)$ (cm^{-1})	T_{onset} (K)	$-\Delta H_0$ (kJ mol^{-1})
K_1^+ site	4109	52	90	9 ± 1
K_2^+ site	4119	42	90	8 ± 1
linker site	4128	33	70	3 ± 1

^a $\nu(H-H)$ indicates the frequency of H_2 vibration when interacting with the specific site; $-\Delta\nu(H-H)$ indicates the red-shift from para- H_2 vibration (4161 cm^{-1}); T_{onset} is the highest temperature at which the signal first appears; $-\Delta H_0$ represent the enthalpy of H_2 adsorption for that precise site.

multiple interaction sites is in full agreement with what was suggested by $^{13}\text{CO}_2$ NMR measurements and CO_2 isosteric heat (see previous section). A graphic illustration of possible interaction sites for H_2 in UTSA-16 is shown in Figure 5.

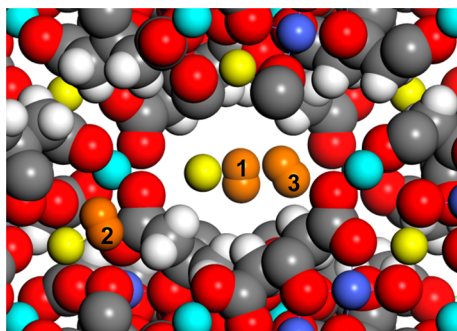


Figure 5. Structure of UTSA-16 as in refs 10 and 11 assuming the presence of extra-framework K^+ atoms (yellow, center of the pore). Water molecules and $-OH$ groups have been omitted. The elements have been reported according to the following color code: carbon (gray), structural hydrogen (white), oxygen (red), cobalt (light blue for tetrahedral Co^{2+} , violet for octahedral Co^{2+}), potassium (yellow), and adsorbed hydrogen (orange). (1) H_2/K_1^+ , (2) H_2/K_2^+ , and (3) H_2/linker .

The stronger interaction between H_2 and UTSA-16 was detected, as expected, for the 1:1 adduction of H_2 with potassium with an enthalpy of adsorption of 9 kJ mol^{-1} for K_1^+ ($T_{\text{onset}} = 90\text{ K}$) and 8 kJ mol^{-1} for K_2^+ site. This value is in line with what obtained for K-ZSMS by Otero Areán et al.³³ (8.9 kJ mol^{-1}) and slightly lower with respect to MOFs containing transition metals which show the highest H_2 enthalpy of adsorption up to 13 kJ mol^{-1} .^{7,29}

The rearrangement seen in the IR spectra at higher loadings can be explained by a redistribution of the H_2 molecules which tend to condensate at higher coverage and low temperature.

The presence of an adsorption site related to the organic linker is definitely proven with H_2 and its signal is detected already at 70 K and 20 mbar of H_2 equilibrium pressure; the enthalpy of adsorption of this linker site is 3 kJ mol^{-1} .

A similar experiment was performed using N_2 as probe. N_2 vibrational mode, as for H_2 , becomes IR active only after polarization by the surface. Because of the larger strength of the $N\equiv N$ bond (945 vs 436 kJ mol^{-1} of H_2),^{36,37} this molecule is less perturbed than H_2 after interaction with the surface. N_2 (40 mbar) was dosed on UTSA-16 at 150 K and then cooled down to 60 K, as shown in Figure S6b of the Supporting Information. The first spectrum was collected at 140 K and showed a maximum at 2330 cm^{-1} . At higher coverage (reached at lower temperature), two signals at 2329 and 2333 cm^{-1} grow at the expenses of the original band at 2330 cm^{-1} . The low intensity of all the components is due to the fact that the observed frequencies are only slightly shifted in respect to the unperturbed molecule (2321 cm^{-1} is the frequency observed in case of N_2 adsorbed at 240 K on silicalite).³⁸ Figure 4b reports the sequence of spectra collected upon lowering the nitrogen equilibrium pressure at 60 K. The two maxima at 2329 and 2333 cm^{-1} decrease in intensity and, at lower coverage, a single component at 2330 cm^{-1} is clearly visible. The evolution of the spectra suggests the formation of more than one adduct between K^+ species and N_2 , with possible rearrangement of the local structure of the adducts. This could justify the appearance of a band associated with adsorbed N_2 at the highest frequencies (most perturbed) only at medium-high coverage.

Carbon monoxide is a probe largely employed for the characterization of different surface features such as alkaline metal cations, transition metal cations, or Lewis acidic centers.³¹ It is commonly used to study microporous materials like zeolites with exchanged alkali-metals^{39,40} or MOFs.^{31,41–44}

CO was sent over UTSA-16 with an equilibrium pressure of 40 mbar at 60 K, that is a temperature lower than what is normally used for this kind of measurements (77 K),³¹ in order to increase the coverage of this weak base and the number of active sites probed. Spectra reported in Figure 4c were plotted following the degassing of CO from the material. The single main band at 2147 cm^{-1} reassembles the formation of 1:1 adduct of CO with K^+ cation (K_1^+ site), with the molecule attaching the site in end-on configuration; the corresponding band related to ^{13}CO is observed at 2098 cm^{-1} . Together with the signal at 2147 cm^{-1} , a red-shifted shoulder at 2144 cm^{-1} indicates the interaction of CO with a different K^+ site (K_2^+ site), as already seen by sending H_2 on the surface. At lower frequencies, a double peak is present: the signal at 2133 cm^{-1} is relative to the less typical interaction of CO with K_2^+ through the side of oxygen,⁴⁵ while the red-shifted component of this feature (2129 cm^{-1}) might be relative to CO interacting by the oxygen with a second K^+ (K_1^+ site). An alternative explanation to these bands can be postulated on the basis of the work reported by Otero Areán et al.⁴⁵ for CO adsorption in K-ZSM-5 who conceives the shoulder at 2144 cm^{-1} as due to the formation of a dual cation site complex where CO bridges two different K^+ sites. This bridging configuration of the CO molecule can take place only if the two adjacent K^+ sites lie at a distance of $7\text{--}9\text{ \AA}$.^{46–48} No significant shift was noted while degassing CO from the material.

CONCLUSIONS

A detailed study on UTSA-16 metal–organic framework was performed by means of different physical-chemical techniques

to elucidate adsorptive properties toward small probe molecules. On our previous work,¹² the role of major active site in UTSA-16 was explained through the adsorption of CO₂, remarking a strong interaction toward K⁺ cation present in the structure. Considering a formula unit such as K₂CO₃(cit)₂ (cit = C₆H₄O₇) and a pore volume of 0.32 cm³ g⁻¹, we estimated a saturation coverage for K⁺ sites at 3.2 mol kg⁻¹. The isotherm at 298 K and 1 bar reported in ref 12 indicates a maximum CO₂ uptake of 4.2 mol kg⁻¹, 22% over the K⁺ saturation limit. This fact points to the presence of another adsorption site other than potassium.

A multitechnique approach based on solid-state NMR, CO₂ isosteric heat evaluated until 1 bar, and the exploration of UTSA-16 surface by means of FTIR coupled with different probes allowed us to identify the presence of three adsorptions sites: two related to K⁺ sites and one to the organic linker.

Microcalorimetric measurements quantified, in the low pressure range (below 100 mbar of equilibrium pressure), the presence of a single medium strength adsorption site (30.1 kJ mol⁻¹) assigned to CO₂ interacting with K⁺ cations located inside the UTSA-16 channels. Conversely, solid-state NMR exploring a wider range of equilibrium pressure (to 600 mbar) was able to distinguish two different species of CO₂ molecules inside the MOF: CO₂(K⁺ site) adsorbed on the K⁺ adsorbing sites and CO₂(linker) relative to a weaker interaction of CO₂ with the organic linker of the MOF. NMR results were in line with isosteric heat of CO₂ adsorption evaluated until 1 bar, that distinguished two families of sites with very close affinity for CO₂, 38 and 37 kJ mol⁻¹.

Moreover, the use of different small molecular probes coupled with IR spectroscopy shed light over the presence of two different adsorption sites, both related to K⁺ sites. In particular, H₂ dosages at low temperature (15 K) allowed to identify two distinct K⁺ species (labeled as K₁⁺ and K₂⁺ sites) characterized by a H₂ adsorption enthalpy of 9 kJ mol⁻¹ and 8 kJ mol⁻¹, respectively. Moreover, as already found in other MOFs, organic linkers represent a further adsorption site characterized by a lower interaction energy (3 kJ mol⁻¹ in case of H₂). The existence of two distinct K⁺ sites was also confirmed by IR data obtained in case of CO adsorption (maximum at 2147 cm⁻¹, associated with K₁⁺ site and maximum at 2144 cm⁻¹ to K₂⁺ site).

■ ASSOCIATED CONTENT

● Supporting Information

The Supporting Information is available free of charge on the ACS Publications website at DOI: 10.1021/acs.jpcc.6b03333.

Microcalorimetry (Figure S1); zero-coverage differential heat of CO₂ adsorption ($-\Delta H$) for some selected MOFs (Table S1); ¹³C (100.65 MHz) SSNMR spectra of CO₂-loaded UTSA-16 at different equilibrium pressure or at different temperature recorded with a spinning speed of 12 kHz (Figure S2 and S3); dependence of $\ln(P_{(K^+ \text{ sites})})$ on the reciprocal temperature (1000/K) for the sample at 200 mbar (Figure S4); ¹³C (100.65 MHz) static spectra of ¹³CO₂-loaded UTSA-16 at 200 mbar in the temperature range from 293 to 353 K (Figure S5); VTIR spectra of H₂ and of N₂ adsorbed on UTSA-16 (Figure S6); van't Hoff plot (Figure S7, S8, and S9) (PDF)

■ AUTHOR INFORMATION

Corresponding Author

*E-mail: silvia.bordiga@unito.it; Tel:0039 011 6708373.

Notes

The authors declare no competing financial interest.

■ ACKNOWLEDGMENTS

The research leading to these results has received funding from the European Union Seventh Framework Programme (FP72007–2013) under Grant Agreement 608534 (MATESA project). We also would like to acknowledge Dr. Carlos Grande and the SINTEF group for providing UTSA-16 MOF.


■ REFERENCES

- (1) Yaghi, O. M.; O'Keeffe, M.; Ockwig, N. W.; Chae, H. K.; Eddaoudi, M.; Kim, J. Reticular Synthesis and the Design of New Materials. *Nature* **2003**, *423*, 705–714.
- (2) Furukawa, H.; Cordova, K. E.; O'Keeffe, M.; Yaghi, O. M. The Chemistry and Applications of Metal-Organic Frameworks. *Science* **2013**, *341*, 974–986.
- (3) Sumida, K.; Rogow, D. L.; Mason, J. A.; McDonald, T. M.; Bloch, E. D.; Herm, Z. R.; Bae, T. H.; Long, J. R. Carbon Dioxide Capture in Metal-Organic Frameworks. *Chem. Rev.* **2012**, *112*, 724–781.
- (4) Vitillo, J. G. Magnesium-Based Systems for Carbon Dioxide Capture, Storage and Recycling: From Leaves to Synthetic Nanostructured Materials. *RSC Adv.* **2015**, *5*, 36192–36239.
- (5) Furukawa, H.; Ko, N.; Go, Y. B.; Aratani, N.; Choi, S. B.; Choi, E.; Yazaydin, A. O.; Snurr, R. Q.; O'Keeffe, M.; Kim, J.; et al. Ultrahigh Porosity in Metal-Organic Frameworks. *Science* **2010**, *329*, 424–428.
- (6) Deng, H. X.; Grunder, S.; Cordova, K. E.; Valente, C.; Furukawa, H.; Hmadeh, M.; Gandara, F.; Whalley, A. C.; Liu, Z.; Asahina, S.; et al. Large-Pore Apertures in a Series of Metal-Organic Frameworks. *Science* **2012**, *336*, 1018–1023.
- (7) Vitillo, J. G.; Regli, L.; Chavan, S.; Ricchiardi, G.; Spoto, G.; Dietzel, P. D. C.; Bordiga, S.; Zecchina, A. Role of Exposed Metal Sites in Hydrogen Storage in MOFs. *J. Am. Chem. Soc.* **2008**, *130*, 8386–8396.
- (8) Chavan, S. M.; Zavorotynska, O.; Lamberti, C.; Bordiga, S. H₂ Interaction with Divalent Cations in Isostructural MOFs: A Key Study for Variable Temperature Infrared Spectroscopy. *Dalton Trans.* **2013**, *42*, 12586–12595.
- (9) Fracaroli, A. M.; Furukawa, H.; Suzuki, M.; Dodd, M.; Okajima, S.; Gandara, F.; Reimer, J. A.; Yaghi, O. M. Metal-Organic Frameworks with Precisely Designed Interior for Carbon Dioxide Capture in the Presence of Water. *J. Am. Chem. Soc.* **2014**, *136*, 8863–8866.
- (10) Xiang, S. C.; He, Y. B.; Zhang, Z. J.; Wu, H.; Zhou, W.; Krishna, R.; Chen, B. L. Microporous Metal-Organic Framework with Potential for Carbon Dioxide Capture at Ambient Conditions. *Nat. Commun.* **2012**, *3*, 954–962.
- (11) Xiang, S. C.; Wu, X. T.; Zhang, J. J.; Fu, R. B.; Hu, S. M.; Zhang, X. D. A 3D Canted Antiferromagnetic Porous Metal-Organic Framework with Anatase Topology through Assembly of an Analogue of Polyoxometalate. *J. Am. Chem. Soc.* **2005**, *127*, 16352–16353.
- (12) Masala, A.; Vitillo, J. G.; Bonino, F.; Manzoli, M.; Grande, C. A.; Bordiga, S. New Insights into UTSA-16. *Phys. Chem. Chem. Phys.* **2016**, *18*, 220–227.
- (13) Grande, C. A.; Agueda, V. I.; Spjelkavik, A.; Blom, R. An Efficient Recipe for Formulation of Metal-Organic Frameworks. *Chem. Eng. Sci.* **2015**, *124*, 154–158.
- (14) Bonino, F.; Lamberti, C.; Chavan, S.; Vitillo, J. G.; Bordiga, S. Characterization of MOFs. In *Metal Organic Frameworks as Heterogeneous Catalysts*; Xamena, F., Gascon, J., Eds.; Royal Soc Chemistry: Cambridge, 2013; pp 76–142.
- (15) Bolis, V. Fundamentals in Adsorption at the Solid-Gas Interface. Concepts and Thermodynamics. In *Calorimetry and Thermal Methods in Catalysis*; Auroux, A., Ed.; Springer Berlin Heidelberg: Berlin, 2013; Vol. 154, pp 3–50.

- (16) Ethiraj, J.; Albanese, E.; Civalleri, B.; Vitillo, J. G.; Bonino, F.; Chavan, S.; Shearer, G. C.; Lillerud, K. P.; Bordiga, S. Carbon Dioxide Adsorption in Amine-Functionalized Mixed-Ligand Metal-Organic Frameworks of Uio-66 Topology. *ChemSusChem* **2014**, *7*, 3382–3388.
- (17) Grajciar, L.; Wiersum, A. D.; Llewellyn, P. L.; Chang, J. S.; Nachtigall, P. Understanding CO₂ Adsorption in CuBTC MOF: Comparing Combined DFT-Ab Initio Calculations with Microcalorimetry Experiments. *J. Phys. Chem. C* **2011**, *115*, 17925–17933.
- (18) Llewellyn, P. L.; Bourrelly, S.; Serre, C.; Vimont, A.; Daturi, M.; Hamon, L.; De Weireld, G.; Chang, J. S.; Hong, D. Y.; Hwang, Y. K.; et al. High Uptakes of CO₂ and CH₄ in Mesoporous Metal-Organic Frameworks MIL-100 and MIL-101. *Langmuir* **2008**, *24*, 7245–7250.
- (19) Bernini, M. C.; Blanco, A. A. G.; Villarroel-Rocha, J.; Fairen-Jimenez, D.; Sapag, K.; Ramirez-Pastor, A. J.; Narda, G. E. Tuning the Target Composition of Amine-Grafted CPO-27-Mg for Capture of CO₂ under Post-Combustion and Air Filtering Conditions: A Combined Experimental and Computational Study. *Dalton Trans.* **2015**, *44*, 18970–18982.
- (20) Sprang, T.; Boddenberg, B. Coadsorption of Xenon and Carbon-Monoxide in Cadmium-Exchanged Zeolite-Y Studied with Xe-129 Nmr-Spectroscopy. *J. Chem. Soc., Faraday Trans.* **1995**, *91*, 555–558.
- (21) Koch, M.; Brunner, E.; Pfeifer, H.; Zscherpel, D. Low-Temperature C-13 NMR Investigations on Carbon-Monoxide Hydrogen-Bonded to Bronsted Acid Sites in H-Y Zeolites. *Chem. Phys. Lett.* **1994**, *228*, 501–505.
- (22) Klein, N.; Herzog, C.; Sabo, M.; Senkovska, I.; Getzschmann, J.; Paasch, S.; Lohe, M. R.; Brunner, E.; Kaskel, S. Monitoring Adsorption-Induced Switching by Xe-129 NMR Spectroscopy in a New Metal-Organic Framework Ni₂(2,6-ndc)₂(dabco). *Phys. Chem. Chem. Phys.* **2010**, *12*, 11778–11784.
- (23) Hoffmann, H. C.; Assfour, B.; Epperlein, F.; Klein, N.; Paasch, S.; Senkovska, I.; Kaskel, S.; Seifert, G.; Brunner, E. High-Pressure in Situ Xe-129 NMR Spectroscopy and Computer Simulations of Breathing Transitions in the Metal-Organic Framework Ni₂(2,6-ndc)₂(dabco) (Dut-8(Ni)). *J. Am. Chem. Soc.* **2011**, *133*, 8681–8690.
- (24) Kong, X. Q.; Scott, E.; Ding, W.; Mason, J. A.; Long, J. R.; Reimer, J. A. CO₂ Dynamics in a Metal-Organic Framework with Open Metal Sites. *J. Am. Chem. Soc.* **2012**, *134*, 14341–14344.
- (25) Gul-E-Noor, F.; Mendt, M.; Michel, D.; Poppl, A.; Krautscheid, H.; Haase, J.; Bertmer, M. Adsorption of Small Molecules on Cu₃(Btc)₂ and Cu₃-Xzn_x(Btc)₂ Metal-Organic Frameworks (MOF) as Studied by Solid-State NMR. *J. Phys. Chem. C* **2013**, *117*, 7703–7712.
- (26) Zukal, A.; Pawlesa, J.; Cejka, J. Isothermic Heats of Adsorption of Carbon Dioxide on Zeolite MCM-22 Modified by Alkali Metal Cations. *Adsorption* **2009**, *15*, 264–270.
- (27) Caskey, S. R.; Wong-Foy, A. G.; Matzger, A. J. Dramatic Tuning of Carbon Dioxide Uptake Via Metal Substitution in a Coordination Polymer with Cylindrical Pores. *J. Am. Chem. Soc.* **2008**, *130*, 10870–10871.
- (28) Dietzel, P. D. C.; Johnsen, R. E.; Fjellvag, H.; Bordiga, S.; Groppo, E.; Chavan, S.; Blom, R. Adsorption Properties and Structure of CO₂ Adsorbed on Open Coordination Sites of Metal-Organic Framework Ni₂(dhtp) from Gas Adsorption, IR Spectroscopy and X-Ray Diffraction. *Chem. Commun.* **2008**, 5125–5127.
- (29) Sumida, K.; Stuck, D.; Mino, L.; Chai, J. D.; Bloch, E. D.; Zavorotynska, O.; Murray, L. J.; Dinca, M.; Chavan, S.; Bordiga, S.; et al. Impact of Metal and Anion Substitutions on the Hydrogen Storage Properties of M-BTT Metal-Organic Frameworks. *J. Am. Chem. Soc.* **2013**, *135*, 1083–1091.
- (30) Kazansky, V. B. Drift Spectra of Adsorbed Dihydrogen as a Molecular Probe for Alkaline Metal Ions in Faujasites. *J. Mol. Catal. A: Chem.* **1999**, *141*, 83–94.
- (31) Lamberti, C.; Zecchina, A.; Groppo, E.; Bordiga, S. Probing the Surfaces of Heterogeneous Catalysts by in Situ IR Spectroscopy. *Chem. Soc. Rev.* **2010**, *39*, 4951–5001.
- (32) Breck, W. D. *Zeolite Molecular Sieves*; John Wiley & Sons, Inc.: New York, 1974.
- (33) Arean, C. O.; Palomino, G. T.; Garrone, E.; Nachtigallova, D.; Nachtigall, P. Combined Theoretical and FTIR Spectroscopic Studies on Hydrogen Adsorption on the Zeolites Na-FER and K-FER. *J. Phys. Chem. B* **2006**, *110*, 395–402.
- (34) Arean, C. O.; Delgado, M. R.; Palomino, G. T.; Rubio, M. T.; Tsyganenko, N. M.; Tsyganenko, A. A.; Garrone, E. Thermodynamic Studies on Hydrogen Adsorption on the Zeolites Na-ZSM-5 and K-ZSM-5. *Microporous Mesoporous Mater.* **2005**, *80*, 247–252.
- (35) Zecchina, A.; Bordiga, S.; Vitillo, J. G.; Ricchiardi, G.; Lamberti, C.; Spoto, G.; Bjorgen, M.; Lillerud, K. P. Liquid Hydrogen in Protonic Chabazite. *J. Am. Chem. Soc.* **2005**, *127*, 6361–6366.
- (36) Vedeneyev, V. I.; Gurchik, L. V.; Kondrat'yev, V. N.; Medvedev, V. A.; Frankevich, Y. L. *Bond Energies, Ionization Potentials and Electron Affinities*; St. Martin's Press: New York, 1962.
- (37) Herzberg, G.; Monfils, A. The Dissociation Energies of H₂, HD and D₂ Molecules. *J. Mol. Spectrosc.* **1961**, *5*, 482.
- (38) Zecchina, A.; Arean, C. O.; Palomino, G. T.; Geobaldo, F.; Lamberti, C.; Spoto, G.; Bordiga, S. The Vibrational Spectroscopy of H₂, N₂, CO and NO Adsorbed on the Titanosilicate Molecular Sieve Ets-10. *Phys. Chem. Chem. Phys.* **1999**, *1*, 1649–1657.
- (39) Arean, C. O.; Tsyganenko, A. A.; Platero, E. E.; Garrone, E.; Zecchina, A. Two Coordination Modes of CO in Zeolites: A Temperature-Dependent Equilibrium. *Angew. Chem., Int. Ed.* **1998**, *37*, 3161–3163.
- (40) Zecchina, A.; Bordiga, S.; Lamberti, C.; Spoto, G.; Carnelli, L.; Arean, C. O. Low-Temperature Fourier-Transform Infrared Study of the Interaction of CO with Cations in Alkali-Metal Exchanged ZSM-5 Zeolites. *J. Phys. Chem.* **1994**, *98*, 9577–9582.
- (41) Vimont, A.; Thibault-Starzyk, F.; Daturi, M. Analysing and Understanding the Active Site by IR Spectroscopy. *Chem. Soc. Rev.* **2010**, *39*, 4928–4950.
- (42) Valenzano, L.; Civalleri, B.; Chavan, S.; Palomino, G. T.; Arean, C. O.; Bordiga, S. Computational and Experimental Studies on the Adsorption of CO, N₂, and CO₂ on Mg-MOF-74. *J. Phys. Chem. C* **2010**, *114*, 11185–11191.
- (43) Cavka, J. H.; Jakobsen, S.; Olsbye, U.; Guillou, N.; Lamberti, C.; Bordiga, S.; Lillerud, K. P. A New Zirconium Inorganic Building Brick Forming Metal Organic Frameworks with Exceptional Stability. *J. Am. Chem. Soc.* **2008**, *130*, 13850–13851.
- (44) Bordiga, S.; Regli, L.; Bonino, F.; Groppo, E.; Lamberti, C.; Xiao, B.; Wheatley, P. S.; Morris, R. E.; Zecchina, A. Adsorption Properties of HKUST-1 toward Hydrogen and Other Small Molecules Monitored by IR. *Phys. Chem. Chem. Phys.* **2007**, *9*, 2676–2685.
- (45) Arean, C. O.; Delgado, M. R.; Frolich, K.; Bulanek, R.; Pulido, A.; Bibiloni, G. F.; Nachtigall, P. Computational and Fourier Transform Infrared Spectroscopic Studies on Carbon Monoxide Adsorption on the Zeolites Na-ZSM-5 and K-ZSM-5: Evidence of Dual-Cation Sites. *J. Phys. Chem. C* **2008**, *112*, 4658–4666.
- (46) Garrone, E.; Bulanek, R.; Frolich, K.; Arean, C. O.; Delgado, M. R.; Palomino, G. T.; Nachtigallova, D.; Nachtigall, P. Single and Dual Cation Sites in Zeolites: Theoretical Calculations and FTIR Spectroscopic Studies on CO Adsorption on K-FER. *J. Phys. Chem. B* **2006**, *110*, 22542–22550.
- (47) Nachtigall, P.; Delgado, M. R.; Frolich, K.; Bulanek, R.; Palomino, G. T.; Bauca, C. L.; Arean, C. O. Periodic Density Functional and FTIR Spectroscopic Studies on CO Adsorption on the Zeolite Na-FER. *Microporous Mesoporous Mater.* **2007**, *106*, 162–173.
- (48) Nachtigall, P.; Delgado, M. R.; Nachtigallova, D.; Arean, C. O. The Nature of Cationic Adsorption Sites in Alkaline Zeolites-Single, Dual and Multiple Cation Sites. *Phys. Chem. Chem. Phys.* **2012**, *14*, 1552–1569.

Cite this: *Dalton Trans.*, 2017, **46**, 4685

Tailoring adsorption induced phase transitions in the pillared-layer type metal–organic framework DUT-8(Ni)[†]

Negar Kavooosi,^a Volodymyr Bon,^a Irena Senkowska,^a ^a Simon Krause,^a Cesare Atzori,^b Francesca Bonino,^b Julia Pallmann,^c Silvia Paasch,^c Eike Brunner^c and Stefan Kaskel^{*a}

Tailoring the characteristics of gating transitions in the porous network, Ni₂(ndc)₂dabco (ndc = 2,6-naphthalenedicarboxylate, dabco = 1,4-diazabicyclo[2.2.2]octane), also termed DUT-8(Ni) (DUT = Dresden University of Technology), was achieved by systematically adjusting the critical synthesis parameters. The impact of the starting composition and solvent mixtures in the synthesis was found to critically affect the guest-response properties of the obtained materials. A comprehensive set of physical characterization methods, namely thermal analysis, ¹H NMR of digested crystals, solid state ¹³C NMR, PXRD, SEM, IR and Raman spectroscopy shows that the crystallite size is a crucial factor, determining the differing characteristics such as “gate pressure” and adsorption capacity in the guest-responsive switching behaviour of DUT-8. Crystallites smaller than 500 nm in size retain the open form after removal of the guest molecules resulting in typical “Type Ia” isotherm, whereas crystallites larger than 1 μm transform into the “closed pore” form and therefore can show a characteristic “gate opening” behaviour during gas adsorption. The particle size distribution of DUT-8(Ni) can be tailored by changing the synthesis conditions and consequently the slope of the isotherm at the “gating step” is affected. The in depth analysis of synthesis conditions and switching behaviour is an important step towards a better understanding of the fundamental principles responsible for guest responsive porosity switching in the solid state.

Received 3rd January 2017,
Accepted 9th March 2017

DOI: 10.1039/c7dt00015d

rsc.li/dalton

Introduction

Structural phase transitions induced by external stimuli such as guest molecules, temperature, electromagnetic irradiation *etc.*, are unique features of flexible metal–organic frameworks, also termed soft porous crystals.^{1–4} Among various kinds of flexibility such as breathing, swelling, ligand flip, sub-network displacement, gating stands out as a pronounced and step-wise transition with an amplitude of cell volume change often by far exceeding any volume changes observed in traditional porous solids.⁵ We therefore address these materials in the following as “switching MOFs” or “gate pressure MOFs”. After

guest removal, “gate pressure MOFs” usually transform into a dense structure that can be reopened by an external stimulus.⁶ Switching between a “porous” and “non-porous” (or dense) states offers tremendous opportunities for the application of these MOFs in gas storage, separation, and sensing.^{7–16} However, there are still numerous open questions in the understanding of “gating” phenomena from both experimental and theoretical points of view.

From the theoretical point of view, various fundamental concepts for understanding the flexible behaviour have been developed, for example: (i) the adsorption-induced deformation can be interpreted as a response of the porous material to an adsorption induced stress; (ii) a rigorous thermodynamic description of the coupled energetics of the crystallographic phase transition(s) and the adsorption isotherms of the different polymorphs within the osmotic ensemble.^{17,18}

The synthesis rules and procedures for the targeted synthesis of “gate pressure” materials and control over the “gate pressure” are a crucial issue for any application. In the case of layered MOFs such as ELM-11 (ELM – Elastic Layered Material), the first “gate pressure MOF” discovered, extensive investigations focused on the adsorption induced transitions

^aDepartment of Inorganic Chemistry, Technische Universität Dresden, Bergstrasse 66, D-01062 Dresden, Germany. E-mail: Stefan.Kaskel@tu-dresden.de

^bDepartment of Chemistry, NIS and INSTM Reference Centre, University of Torino, Via G. Quarello 15, I-10135 and Via P. Giuria 7, I-10125, Torino, Italy

^cDepartment of Bioanalytical Chemistry, Technische Universität Dresden, Bergstrasse 66, D-01062 Dresden, Germany

[†]Electronic supplementary information (ESI) available: Nitrogen and argon physisorption data, theoretical and experimental pore size distribution, PXRD patterns, scanning electron microscopy images, ¹H NMR, FT-IR and TG data. See DOI: 10.1039/c7dt00015d

in the presence of nitrogen, carbon dioxide, *n*-butane, methane, and alcohol vapours.^{6,19–21} Tuning of the “gate pressure” was achieved by varying the metal ions and types of layer-terminating anions.²² The dynamics of the “gating” effect was investigated *in situ* using various gases as guest molecules.²³

Pillared-layer MOFs can be regarded as a second prototypical class of switching MOFs as discovered by Dybtsev,²⁴ but initially only volume changes below 15% were reported in the absence of solvent. However, a complete closing of the framework was not achieved in this case.

A unique member of this family is Ni₂(ndc)₂dabco (ndc – 2,6-naphthalenedicarboxylate, dabco – 1,4-diazabicyclo-[2.2.2]octane), also known as DUT-8(Ni) (DUT = Dresden University of Technology).^{25–30} The highly flexible Ni₂-paddle wheel in combination with the ndc ligand allows complete pore closing after removing the guest molecules to be achieved. Consequently this compound shows the highest cell volume change (>250%) among all pillared layer MOFs and a pronounced “gate opening” effect, initially reported at $p/p_0 = 0.1$ for nitrogen adsorption at 77 K.²⁹ The complex structural diversity of DUT-8(Ni) in the presence of nitrogen, carbon dioxide, ethane, ethylene and *n*-butane was unravelled using *in situ* powder X-ray diffraction (PXRD) at controlled pressure and temperature.²⁶ Characteristic host–guest interactions were detected by applying *in situ* ¹²⁹Xe NMR.³¹

However, recent observations during repeated adsorption/desorption cycling using *n*-butane and InfraSORP technology revealed significant stress built-up upon repeated adsorption caused by grain boundary formation and disintegration of larger crystals.²⁷ Three different types of crystal interfacial surface areas may in principle affect the gating phenomena by adding a kinetic and/or thermodynamic contribution to alter the energetics of switching: (a) the outer surface area (A_o) of a monodomain crystal (surface energy); (b) the interfacial area between two domains (grain boundary or interfacial domain area, A_{id}) with different orientations in one crystal; (c) the interfacial area of a monodomain or multi-domain crystal covered by a second phase (which can also be an amorphous outer layer (A_{oi}), a polymer, or a crystalline shell). For DUT-8, it was shown that an increasing A_{id} causes a shift of the gate opening pressure to higher pressure (equivalent to a higher chemical potential of the guest molecule).²⁷ As we show in this contribution, the gate opening pressure does not reflect a transition at equilibrium, but is kinetically controlled. The concerted pore opening of unit cells can be interpreted as a cooperative lattice movement (soft phonon) propagating throughout the crystal. If adjacent grains have different crystallographic orientations, the interfacial domain area (grain boundary) acts as a phonon propagation barrier and shifts the transition pressure towards the higher chemical potential of the transition inducing guest molecules. However, if the interface between two domains creates gas accessible channels, these defects will act as nucleation centers for the phase transformation. Thus, the number of such defects in a crystal will determine the transition prob-

ability and consequently the gate opening pressure. A mono-domain crystal without grain boundaries in the closed state may be kinetically so severely hindered, that an adsorption induced transition is no longer observed and the crystal remains closed.

The strong influence of domain size on the “gate pressure” was an initial motivation to study the impact of crystal morphology in DUT-8(Ni) in more detail. Another observation triggering our intentions for “gate pressure” tuning came from a report by Lee *et al.* who reported a material with the same structure and composition as for DUT-8(Ni) but described it as a rigid MOF with a clear “Type I” isotherm and no structural transformations during guest removal.³² This material was synthesized using slightly modified synthesis conditions.

Consequently, DUT-8(Ni) is a unique solid, showing either switchable or rigid behaviour depending on the way it is synthesized. So far there are only a few reports describing a synthesis dependent switchability tuning in porous solids.^{9,33–35}

In the following we describe a detailed study on synthesis and pre-treatment parameters affecting “gate pressure” and hysteresis in DUT-8(Ni). In order to elucidate the fundamentals of solid state porosity switching and in the context of the textural characteristics behind them, we have focused on a global analysis using various spectroscopic techniques, scanning electron microscopy, elemental analysis, TG *etc.* and correlated the outcome with gas physisorption results revealing the degree of switchability.

Experimental

Materials

Chemicals and solvents were purchased from Sigma Aldrich and they were used without further purification. Nickel(II) nitrate hexahydrate (99.999%), 2,6-naphthalenedicarboxylic acid (99.0%) and 1,4-diazabicyclo[2.2.2]octane (ReagentPlus®, ≥99%) were handled under an inert atmosphere. *N,N*-Dimethylformamide (99.8%) and methanol (99.8%) were purchased in anhydrous form.

Synthesis

Flexible DUT-8(Ni) (1). The synthesis procedure of DUT-8(Ni) reported in ref. 29 was slightly modified insofar as all chemicals were dissolved separately: Ni(NO₃)₂·6H₂O (0.407 g, 1.40 mmol) in 6 mL DMF, H₂ndc (0.303 g, 1.40 mmol) in 15 mL DMF and dabco (0.100 g, 0.89 mmol) in 9 mL methanol (MeOH). Subsequently the mixture was transferred into a Teflon vessel (50 mL) and heated in an autoclave to 393 K with a heating rate of 4 K min^{−1} and held at that temperature for 48 h. After cooling to room temperature (RT) over 3 hours, the sample was washed several times, first with 30 mL DMF and then with 30 mL ethanol and finally with 30 mL DCM. Afterwards, a washing step with 150 mL of DCM was continued for 3 days. The resulting solid was filtered in an argon flow and activated under dynamic vacuum at 393 K for 4 h. DUT-8 (Ni) crystals have poor heat conductivity, therefore for efficient

activation of the sample it is important to prevent aggregation of the crystals. In order to facilitate the homogeneous heat transfer to all crystallites instantly without solvothermal stress during the desolvation, a flask with a wide flat bottom was used. This method allows for a homogeneous heating of all the crystals without temperature gradients and simultaneous evacuation. Note: a special vacuum safe flask is required for this operation. Evacuation (at 10^{-3} mbar) continued overnight at room temperature. During the activation, the colour of the sample changes from green (open pore phase) to dark yellow (closed pore phase). Finally, the Schlenk tube was purged with argon and transferred into a glove box.

Rigid DUT-8(Ni) (2). The “rigid” form of DUT-8(Ni) was synthesized using a similar procedure as reported by Lee *et al.*³² In a typical synthesis, $\text{Ni}(\text{NO}_3)_2 \cdot 6\text{H}_2\text{O}$ (0.434 g, 1.50 mmol), H_2ndc (0.294 g, 1.36 mmol) and dabco (0.336 g, 3.00 mmol) were mixed and dissolved in 30 mL of DMF using an ultrasonic bath for 10 min. After mixing of all the chemicals, a cloudy suspension was obtained, which is in disagreement with the procedure reported by Lee. A clear solution could not be obtained even after ultrasonication of the cloudy precipitate for 2 hours. The suspension was transferred to a Teflon-lined autoclave, placed into a preheated oven at 408 K and held at that temperature for 72 hours. The resulting material was washed with 30 mL DMF two times and subsequently immersed in 30 mL of dry EtOH for 3 days. The light green powder was filtered off and activated under dynamic vacuum for 5 hours at 443 K. After activation, the colour remained light green. The sample was kept under an inert atmosphere.

Variation of dabco content: series 3. Samples a–d of series 3 were synthesized using the same procedure as described for 2, but utilising varying amounts of dabco. In all the cases, the ratio of $\text{Ni}^{2+}:\text{H}_2\text{ndc}$ 1.1:1 was kept constant (0.434 g $\text{Ni}(\text{NO}_3)_2 \cdot 6\text{H}_2\text{O}$, 0.294 g H_2ndc). The following amounts of dabco were utilised: in 3_a 0.030 g (0.27 mmol), in 3_b 0.058 g (0.52 mmol), in 3_c 0.112 g (1.00 mmol) and in 3_d 0.224 g (2.00 mmol).

Variation of dabco content: series 3'. Samples a–d of series 3' were synthesized using the procedure described for 1. For all the samples, a constant ratio of $\text{Ni}^{2+}:\text{H}_2\text{ndc}$ 1:1 was used (0.407 g $\text{Ni}(\text{NO}_3)_2 \cdot 6\text{H}_2\text{O}$, 0.303 g H_2ndc). The amount of dabco was varied as follows: in 3'_a 0.039 g (0.35 mmol), in 3'_b 0.100 g (0.89 mmol), in 3'_c 0.156 g (1.39 mmol) and in 3'_d 0.336 g (3.00 mmol).

Variation of solvent ratio: series 4. All samples were synthesized using the procedure described for 2, but the ratio of solvents (DMF to MeOH) was varied: in 4_a 29.5 mL DMF and 0.5 mL MeOH, in 4_b 25 mL DMF and 5 mL MeOH, and in 4_c 19 mL DMF and 11 mL MeOH.

Variation of nickel to ligand ratio: series 5. Samples a–b of series 5 were synthesized by the same method used for the preparation of sample 2, but the ratio of Ni^{2+} to other compounds was changed. In both cases, a ratio of $\text{H}_2\text{ndc}:\text{dabco} = 1:2.2$ was used (0.294 g H_2ndc , 0.336 g dabco). In the case of 5_a, 0.394 g (1.35 mmol) of $\text{Ni}(\text{NO}_3)_2 \cdot 6\text{H}_2\text{O}$ and in 5_b, 0.197 g (0.68 mmol) of $\text{Ni}(\text{NO}_3)_2 \cdot 6\text{H}_2\text{O}$ were added.

Variation of nickel content: series 5'. Samples a and b of series 5' were synthesized using the same procedure as described for 1 but the ratio of Ni to other components was changed. In 5'_a, 0.204 g (0.70 mmol) $\text{Ni}(\text{NO}_3)_2 \cdot 6\text{H}_2\text{O}$ and in 5'_b, 0.601 g (2.07 mmol) $\text{Ni}(\text{NO}_3)_2 \cdot 6\text{H}_2\text{O}$ were used and in both cases, the ratio of H_2ndc to dabco was kept constant (0.303 g H_2ndc , 0.1 g dabco).

Powder X-ray diffraction

Powder X-ray diffraction (PXRD) patterns were obtained at room temperature on a STOE STADI P diffractometer using $\text{Cu-K}\alpha_1$ radiation ($\lambda = 1.5405 \text{ \AA}$) and a 2D detector (Mythen, Dectris). All measurements were performed in transmission geometry using a rotating flatbed sample holder, 2θ steps of 0.015° and exposition time of 20 s per step. All activated samples were sealed using a Decathlon aptonia survival blanket (film composition: 4.0% resin, 92.0% polytetrafluoroethylene (PTFE), 4.0% aluminium).

Adsorption

Nitrogen (at 77 K) and argon (at 87 K) physisorption experiments were performed using a BELSORP-max apparatus. A liquid nitrogen bath was used to thermostat the sample at 77 K. Argon physisorption measurements were performed using a special external adsorption cell, mounted on a closed cycle He-cryostat. Measurements were carried out using 25–35 mg of the MOF. For all experiments, nitrogen and argon gases with a purity of 99.999% were used.

Thermogravimetric analyses

Thermogravimetric analyses (TG) were performed in a synthetic air flow in a temperature range from room temperature to 1000 °C with a heating rate of $5 \text{ }^\circ\text{C min}^{-1}$ using a STA 409 PC from NETZSCH Company.

Spectroscopic measurements

DRIFT spectra were measured in the range of 4000–400 cm^{-1} using a VERTEX-70 spectrophotometer (Bruker).

FTIR ATR spectra were collected at 2 cm^{-1} resolution in the 4000–400 cm^{-1} range using a Bruker Alpha instrument equipped with an ATR accessory (diamond crystal) and placed inside the glove box. Raman spectra were recorded on powder samples inserted in a home-made cell with a Suprasil quartz cuvette using a Renishaw inVia Raman microscope spectrometer and an Ar^+ laser emitting at 514 nm. Photons scattered by the sample were dispersed by a 1800 lines per mm grating monochromator and were simultaneously collected using a CCD camera. The collection optic was set at $20\times$. The spectral collection setup consisted of 50 acquisitions, each of 10 s.

Scanning electron microscopy

The SEM images were recorded using a Hitachi Microscope SU8020.

Elemental analysis

CHN analysis was performed on a EuroEA Elemental Analyser. The amount of Ni in the samples was determined by ICP-OES using an Optima 7000 DV instrument.

Nuclear magnetic resonance

Solutions for ^1H NMR were prepared by dissolving the activated samples in a mixture of 1 mL (99.9%) dimethyl sulfoxide- d_6 and 20 μl of DCl (36% solution in D_2O). The spectra were recorded on a Bruker DRX-500 spectrometer. Solid-state ^{13}C NMR experiments were performed using a Bruker AVANCE 300 spectrometer operating at a resonance frequency of 75.5 MHz using a double-resonance 4 mm MAS NMR probe and a sample spinning rate of 12 kHz. Ramped ^1H - ^{13}C cross polarization (CP) and SPINAL proton decoupling during signal acquisition were applied. The chemical shift was referenced with adamantane.

Results and discussion

To identify pivotal parameters responsible for the differences in the switching characteristics of $\text{Ni}_2(\text{ndc})_2(\text{dabco})$ it was essential to reproduce the syntheses of “flexible” and “rigid” materials, in the following denoted as **1** and **2**, respectively. For the synthesis of **1** the amount of dabco was slightly increased²⁹ to improve the yield. When following the reported procedure for the synthesis of “rigid” DUT-8(Ni) (**2**) reported by Lee *et al.*³² the solution became a cloudy suspension after mixing of all the chemicals. This was surprising, since the published procedure reported: “the suspension was treated by ultrasonic radiation to dissolve solid chemicals until a clear solution in green colour is formed”. However, in our hands the precipitate could not be dissolved even after 3 hours of sonication. A reason might be slightly different water contents of solvents or starting materials. The suspension was placed into an oven, which was pre-heated to 408 K beforehand, and kept at that temperature for 3 days. The obtained green precipitate was collected by filtration, washed and activated at 443 K under dynamic vacuum for 5 hours. After activation, samples **1** and **2** were analysed by PXRD, NMR, and nitrogen physisorption.

As expected, the XRD pattern of sample **1** matches the theoretical calculated pattern of DUT-8(Ni) for the closed phase (**cp**) (Fig. 1a) and shows “gate opening” behaviour during the physisorption (Fig. 1b). In contrast, sample **2** shows an XRD pattern typical of the open pore phase (**op**) of DUT-8(Ni) (Fig. 1a) and a “Type Ia” isotherm (Fig. 1b) with a pore volume comparable to that of **1** after “gate opening”. According to the elemental analysis as well as to the ^1H NMR spectra after digestion of the samples, no significant differences in the composition of **1** and **2** could be found (Table S1, Fig. S6 and S7, ESI †).

In addition, we performed TG analysis in synthetic air in order to estimate the thermal stability and metal/organic ratio. Sample **1** shows slightly higher thermal stability than sample **2**

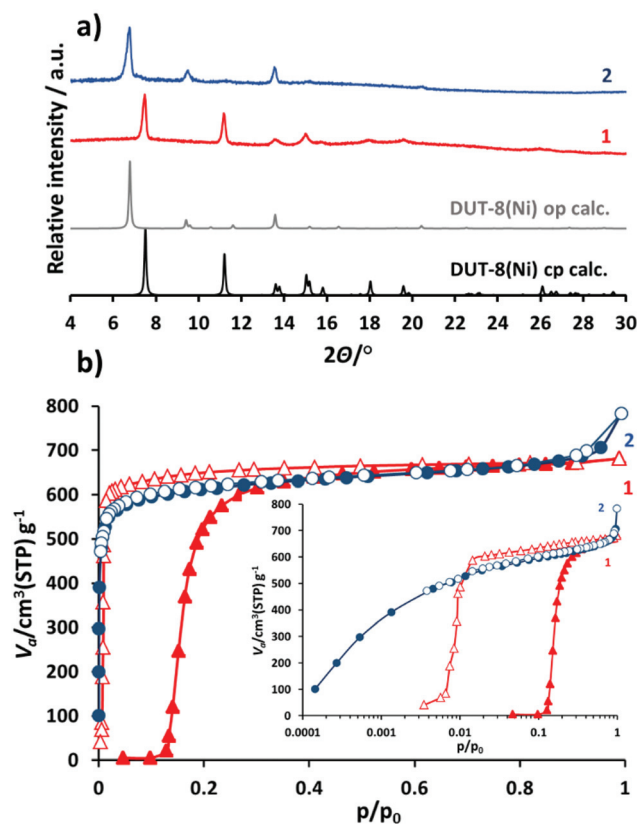


Fig. 1 (a) Calculated and experimental PXRD patterns of activated “flexible” (**1**) and “rigid” (**2**) DUT-8(Ni); (b) nitrogen physisorption experiments at 77 K for DUT-8(Ni) “flexible” (**1**) and “rigid” (**2**) (adsorption – filled symbols, desorption – open symbols), inset: semilogarithmic plot.

and starts to decompose at 380 °C. The decomposition of **2** starts at 340 °C (Fig. S8, ESI †). Decomposition of both samples proceeds in one step. In the case of sample **1** the thermal decomposition is accompanied by the formation of intermediates, which are further oxidized in the temperature range of 500–550 °C, causing an increase of the mass of nearly 4%. The residual mass for samples **1** and **2** is 24.12 and 23.89%, respectively, which is in a good agreement with the calculated value of 22.72%. The PXRD analyses of the residues show phase pure NiO (Fig. S9, ESI †).

Thus, despite the pronounced differences in flexibility, the compositions of **1** and **2** are identical within the limits of errors of the methods. A detailed analysis of defects in a lower concentration level is beyond the scope of this contribution but has been addressed recently using EPR in combination with NO adsorption.²⁵

DRIFT spectra of **1** and **2** are apparently very similar (Fig. 2a). However, the spectrum of rigid compound **2** contains a few additional absorption bands at 1630, 785, and 510 cm^{-1} which are absent in the spectrum of **1**. The first one could correspond to the asymmetric vibration of the carboxylic group.

Therefore, the slight shift of the latter to higher frequencies could be a sign of a different coordination mode of carboxylic

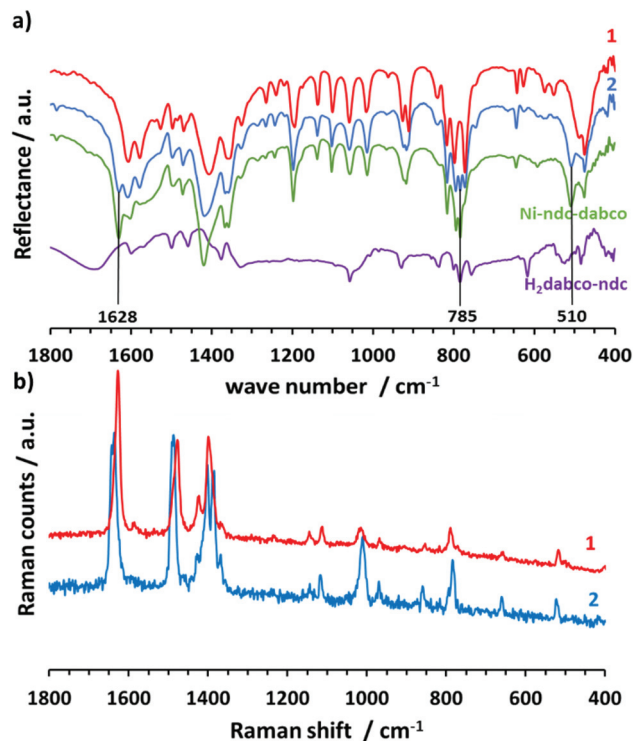


Fig. 2 (a) DRIFT spectra of DUT-8(Ni) “flexible” (1) and “rigid” (2), Ni-ndc-dabco, and (H₂dabco)(ndc) salt; (b) Raman spectra of DUT-8(Ni) “flexible” (1) and “rigid” (2).

groups as could be expected for defective paddle wheels, formed because of rapid crystallization.

The additional absorption band at 785 cm⁻¹ can be assigned to the ν_s N–C3 vibration of the dabco molecule.³⁶

On the other hand, it is known that dabco is able to form salts with naphthoic acid where carboxylate anions are hydrogen bonded to the protonated dabco *via* COO⁻/H–N⁺ hydrogen bonds.³⁷ Indeed, after mixing of H₂ndc (0.294 g, 1.36 mmol) and dabco (0.336 g, 3.0 mmol) in DMF (30 mL), a white crystalline precipitate (H₂dabco)(ndc) is formed. The DRIFT spectrum of the salt contains an absorption band at 785 cm⁻¹, exactly the same wavenumber observed for the additional band of 2 (Fig. 2).

Using the same ratio of components described for 2, if nickel nitrate is added to the H₂ndc–dabco suspension in DMF, a green, cloudy precipitate forms, in the following denoted as “Ni-ndc-dabco”. The DRIFT spectrum of this precipitate contains both the additional absorption bands at 785 and 1630 cm⁻¹ found in the spectrum of 2. This indicates differences in the formation pathways of 1 and 2: for flexible 1 one may assume the direct nucleation of DUT-8(Ni), while the rigid version 2 is formed *via* an intermediate salt. The ATR-IR spectra of 1 and 2 (Fig. S14[†]) confirm, even if less evidently, the presence of these two vibrational fingerprints of the rigid form.

The Raman spectra of 1 and 2 (Fig. 2b) are significantly different. In particular, compound 2 shows: (i) in the

1700–1300 cm⁻¹ range peaks shifted in frequency and with different relative intensities; (ii) in the lower frequency range the intensity of the bands increases at 1010, 784, and 224 cm⁻¹.

Furthermore, solid state ¹³C NMR spectra were recorded on “as made” and “activated” forms of materials 1 and 2 (Fig. 3).

The spectra of the “as made” forms for 1 and 2 are almost identical and contain two signals between 30 and 40 ppm corresponding to the carbon atoms of the dabco ligand and methyl group of DMF. In the range of 135–165 ppm, three sharp signals and one broad signal are observed. These signals are assigned to the five independent carbon atoms in the naphthalene core of the ndc²⁻ linker and C–H group of DMF. The broad signal of the quaternary carbon of the ndc²⁻ located near the metal center is identified in the low field of the NMR spectrum at 260 ppm (inset Fig. 3).²⁸ Activation of the materials leads to a significant change in the ¹³C CP NMR spectra. As has been shown earlier,²⁸ activation of sample 1 leads to the broadening of all signals, belonging to the framework and disappearing of the DMF signals. The broadening of the signals could be explained either by the chemical shift distribution of the carbon atoms in the **cp** phase or more restricted motions of the linkers in the **cp** compared with the **op** phase. The aforementioned chemical shift distribution could be caused by the deformation of the linker molecules as a consequence of structure closing. In the case of 2, removal of the guest molecules from the framework has no influence on the oscillation of the carbon atoms showing no peak broadening or anisotropy. At the same time, a shift of all signals to the high field was observed and can be explained by desolvation of the framework, namely the absence of the ligand–solvent interactions.

It is interesting to note that the signal at *ca.* 260 ppm is considerably broader in the rigid material than in flexible DUT-8(Ni). This might be due to a larger degree of disorder (or

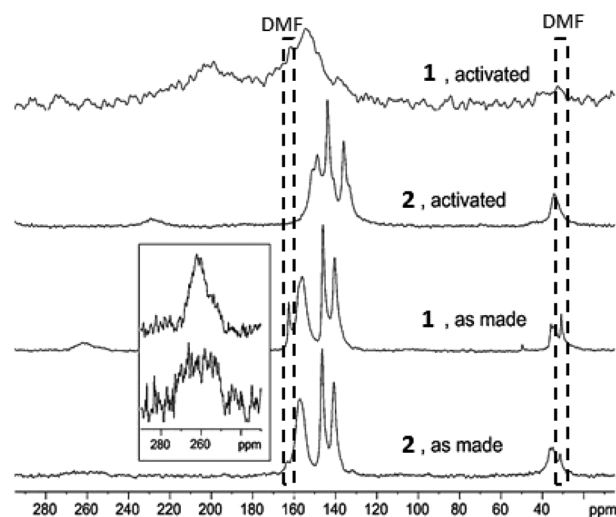


Fig. 3 Solid state ¹³C CP NMR spectra of “as made” and activated forms of 1 and 2.

defects) for rigid DUT-8(Ni) in agreement with EPR spectroscopic studies.²⁵ Thus, the solid state ¹³C NMR spectra show an essential difference between “flexible” **1** and “rigid” **2** DUT-8(Ni) in their activated forms as well as the absence of additional organic species.

Variation of synthesis parameters

The main difference in the synthesis procedure of “flexible” **1** and “rigid” **2** is the molar ratio of the starting compounds and nature of the solvent (or more specifically the solvent ratio) (Table 1). For the synthesis of the flexible version of the framework, a ratio of nickel nitrate, H₂ndc and dabco of 1 : 1 : 0.64 is used, which is very close to the ideal composition of the resulting MOF. As the solvent a DMF/methanol mixture in a volumetric ratio close to 2 : 1 is used. The synthesis protocol of the “rigid” **2** differs by the increased molar amount of dabco up to 2.2 equivalents in the synthesis (Table 1). Moreover, the synthesis is performed in pure DMF at slightly higher temperature.

To find out the critical parameter, which directs the formation of a “flexible” or “rigid” MOF, we studied a wide variety of synthesis parameters such as the molar ratio of the starting materials in the system Ni²⁺/H₂ndc/dabco as well as the solvent mixture composition, starting from the original synthesis procedure for “flexible” **1** and “rigid” **2**.

In the first series, the amount of dabco was varied from 0.20 to 1.47 equivalents (samples **3_a–3_d**), keeping all other synthetic parameters constant according to the synthetic procedure for **2**. In parallel, the syntheses were carried out under the conditions used for **1** and varying the amount of dabco from 0.25 to 2.14 equivalents (samples **3'_a–3'_d**).

If a lower amount of dabco is used than needed for the ideal stoichiometric composition (in the case of samples **3_a**, **3_b** and **3'_a**), the formation of a non-porous coordination polymer

with the composition Ni₃(ndc)₃(DMF)₂(Me₂NH)₂, reported earlier by Du *et al.*,³⁸ was observed (Fig. 4a and c). It shows characteristic reflections at 2θ = 9.22° and 9.57° in the XRD pattern, as well as an additional band at 1666 cm⁻¹ in the FTIR spectrum, which is assigned to the coordination mode of the carboxylic group (Fig. S15 and S16, ESI†).

All the activated samples of series **3** represent a mixture of **cp** and **op** phases. Furthermore, a decreasing intensity of the main reflection of the **cp** phase at 2θ = 7.5° with increasing the dabco content in the synthesis (samples **3_c** and **3_d**) indicates the substantial role of dabco in the formation of the targeted DUT-8(Ni) phase. Higher amounts of dabco lead also to an intensity increase of “fingerprint” absorption bands at 785 and 1630 cm⁻¹ in **3_c** and **3_d**, characteristic of the spectrum of “rigid” DUT-8(Ni) (Fig. S15, ESI†).

Thus, the dabco amount has a crucial role in the synthesis triggering the formation of small amounts of “flexible” DUT-8 (**1**) if utilised in lower concentrations. However, pure “flexible” **1** could not be obtained and very low amounts of dabco utilised in the synthesis caused the formation of a dense phase containing no dabco. In contrast, samples **b** and **c** of series **3'**, synthesized in a DMF : MeOH mixture, are the pure **cp** phase according to the PXRD (Fig. 3) and DRIFT (Fig. S16, ESI†) analyses. Sample **3'_d** shows only a minor impurity of the **op** phase. Thus methanol has an essential influence on the phase formation.

Therefore, in the next step the role of solvent composition was further explored in series **4**. Keeping the Ni²⁺/H₂ndc/dabco ratio constant (1.1 : 1 : 2.2), the MeOH content in DMF was varied from 1.6% to 36% (the MeOH content in the typical synthesis of flexible **1** is 30%).

The PXRD patterns of samples **4_a** and **4_b**, synthesized using only minor amounts of methanol, show exclusively the **op** phase of the MOF. Only if the methanol concentration is higher than 20%, a **cp/op** phase mixture is formed. It is also reflected in the decreasing intensity of the IR absorption bands at 1630 and 785 cm⁻¹ (Fig. S17, ESI†).

Finally, in series **5** and **5'** we could show that the amount of Ni²⁺ does not influence the formation of the expected phases, and independent of the nickel amount utilized (within the investigated range) the resulting crystalline phase is mostly solvent directed (Fig. S1, ESI†). Similar to the results obtained *via* PXRD and SEM techniques, the variation of the nickel amount in the synthesis causes no changes in the DRIFT spectra (Fig. S18, ESI†).

Nitrogen and argon physisorption

One of the main differences between the “flexible” and “rigid” DUT-8(Ni) materials is the response during gas adsorption. First, for investigation of the pore size distribution in MOF **2**, argon physisorption at 87 K was used as is recommended (Fig. S3, ESI†).³⁹ The experimental micropore volume (*V_p*) of 0.97 cm³ g⁻¹ and BET surface area (*S_{BET}*) of 2635 m² g⁻¹ derived from the Ar adsorption isotherm are in perfect agreement with values calculated using Poreblazer from the crystal structure of DUT-8(Ni) (*V_p* = 0.99 cm³ g⁻¹, *S* = 2528 m² g⁻¹). For

Table 1 Synthesis parameters used for tuning DUT-8(Ni) materials^a

	Ni ²⁺	H ₂ ndc	dabco	MeOH, mL	DMF, mL	<i>T</i> , K/sonication time, min
1	1.0	1.0	0.636	9.0	21.0	393/10
2	1.1	1.0	2.206	—	30.0	408/10
3_a	1.1	1.0	0.199	—	30.0	408/10
3_b	1.1	1.0	0.382	—	30.0	408/10
3_c	1.1	1.0	0.735	—	30.0	408/10
3_d	1.1	1.0	1.470	—	30.0	408/10
3'_a	1.0	1.0	0.250	9.0	21.0	393/10
3'_b	1.0	1.0	0.636	9.0	21.0	393/10
3'_c	1.0	1.0	0.993	9.0	21.0	393/10
3'_d	1.0	1.0	2.143	9.0	21.0	393/10
4_a	1.1	1.0	2.206	0.5	29.5	408/10
4_b	1.1	1.0	2.206	5.0	25.0	408/10
4_c	1.1	1.0	2.206	11.0	19.0	408/10
5_a	1.0	1.0	2.206	—	30.0	408/10
5_b	0.5	1.0	2.206	0.0	30.0	408/10
5'_a	0.5	1.0	0.636	9.0	21.0	393/10
5'_b	1.5	1.0	0.636	9.0	21.0	393/10

^a For the starting compounds, the molar ratio normalized to H₂ndc is given.

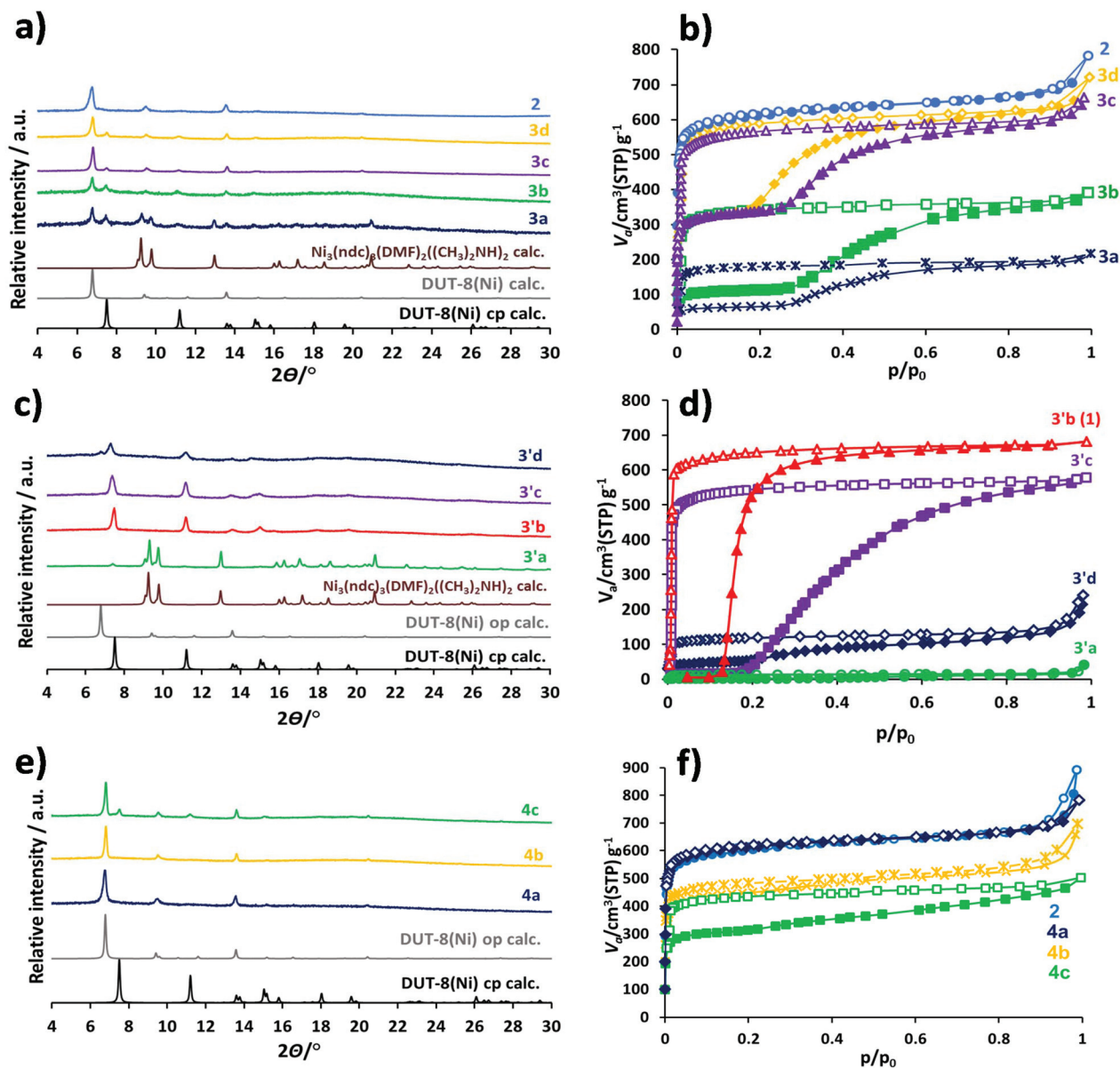


Fig. 4 PXRD patterns of activated samples and nitrogen adsorption isotherms at 77 K for samples 3 and 4.

calculating the pore size distribution NLDFT was applied (zeolite/silica adsorption branch kernel based on a cylindrical pore model). The obtained pore size distribution plot has a maximum at 8.7 Å. This value is 1.1 Å smaller than the value calculated geometrically using Poreblazer software for the DUT-8(Ni) **op** structure (Fig. S4 and S5, ESI†).⁴⁰ The largest included sphere, calculated for the structure, has a diameter of 10.0 Å. Given the limitations of the NLDFT kernels, the pore size calculated from the adsorption isotherm and crystal structure is not in excellent but reasonable agreement. The nitrogen physisorption experiments at 77 K are an ideal technique to distinguish the switchability behaviour of samples prepared under various conditions as the isotherms differ significantly in their slopes but show a comparable total pore volume

(Fig. 1b). We assume that the desorption branch of the isotherm represents the thermodynamic equilibrium of the switching process, as for closing no diffusional activation barrier has to be overcome (Fig. 1b inset). In the case of “flexible” material **1**, this “gate closing” pressure is observed at $p/p_0 = 0.01$, and the structural transformation from **op** to **cp** takes place accompanied by the sharp drop in the nitrogen uptake from $588 \text{ cm}^3 \text{ g}^{-1}$ at $p/p_0 = 0.015$ to $40 \text{ cm}^3 \text{ g}^{-1}$ at $p/p_0 = 0.003$.

In contrast, the desorption branch of **2** matches the adsorption branch without any hysteresis, indicating no structural changes in the sample during physisorption.

The nitrogen adsorption isotherms for samples from series **3** and **3'** reflect the findings from the PXRD analysis. All the samples of series **3** show isotherms characteristic of flexible

MOFs, but are different from typical isotherms usually obtained for “gate pressure” MOFs. In fact, the nitrogen adsorption isotherms of **3_a**–**3_d** are a superposition of the isotherms characteristic of **1** and **2**. Therefore the pore volume, calculated from the nitrogen uptake plateau before “gate opening” can be attributed to the amount of the “rigid” phase in the sample. The ratio between this value and the total pore volume represents the ratio between the amounts of “rigid” and flexible phases and is 35 : 65 for samples **3_a** and **3_b** and 56 : 44 for samples **3_c** and **3_d**.

As expected, sample **3_a** of the composition $\text{Ni}_3(\text{ndc})_3(\text{DMF})_2(\text{Me}_2\text{NH})_2$ has no porosity in its crystal structure and therefore shows nearly no nitrogen uptake (Fig. 4d). Samples **3_b** and **3_c** show “gate opening” behaviour, but slightly different uptakes in saturation.

Further increasing the amount of dabco in the synthesis of **3_d** leads to a significant drop in the total pore volume and changes the isotherm slope in the gate region (Fig. 4d).

Interestingly, the “gate opening” pressure is influenced by the synthetic conditions and is shifted to higher relative pressure from $p/p_0 = 0.13$ for **1** to $p/p_0 = 0.16$ in **3_d** and to $p/p_0 = 0.28$ for samples **3_a**, **3_b**, **3_c** and **3_c**. An interesting observation is that significant differences in the “gate opening” pressure are observed (for example for **3_b** and **3_c**) while the “gate closing” pressure is essentially the same (Fig. S2b, ESI†). These differences are representative of cooperative switching in single crystallites (or agglomerates) within the particle ensemble (see also the Particle size section) and indicate their strong influence on the activation barrier for opening (kinetics) while the closing energetics (equilibrium) are not affected (Fig. S2a and S2b, ESI†). A steep slope at “gate opening” is indicative of a particle ensemble with a relatively uniform activation barrier, while a broadening indicates a broader distribution of activation barriers. Similar phenomena were observed recently by repeated adsorption/desorption of *n*-butane on flexible DUT-8(Ni) and were attributed to the dislocations and lattice strain within the crystallites.²⁷

According to XRD analysis, samples **4_a** and **4_b** (prepared using the reported synthetic procedure for “rigid” DUT-8, but using various DMF : MeOH ratios) present the **op** phase. In sample **4_c** additionally a minor fraction of the **cp** phase is detected. However, the nitrogen adsorption experiments reveal an unexpected adsorption behaviour: an increasing methanol content in the synthesis leads to a gradual decrease of the porosity and total pore volume. Sample **4_c** shows also a broad hysteresis over the whole pressure range (Fig. 4f), indicating the presence of the “flexible” phase.

In contrast, the variation of the amount of Ni^{2+} in the synthesis has only a minor influence on both products, and the nitrogen adsorption isotherm, measured for sample **5_a**, synthesized using the procedure for “flexible” DUT-8(Ni) but with only 50% of Ni^{2+} in the synthesis, reaches the same total pore volume in saturation, but shows a significantly broadened “gate opening” (Fig. S1b, ESI†). The variation of the nickel amount in the procedure for “rigid” DUT-8(Ni) influences only

the total pore volume of the resulting materials **5_a**–**5_b** (Fig. S1d, ESI†), but very little the shape of the isotherm.

Particle size

Recently the influence of crystallite size on adsorption induced phase transitions has been recognized.^{9,33,41} Kitagawa and co-workers reported that downsizing of the twofold interpenetrated frameworks of $\text{Cu}_2(\text{dicarboxylate})_2(\text{amine})$ regulates the structural flexibility and may induce shape-memory effects in coordination frameworks.³³ The downsizing of the ZIF-8 crystallites was shown to suppress ligand flip during adsorption.³⁴ Consequently, an important aspect was to analyze the particle size of the products obtained in the syntheses under varying conditions.

The SEM images of DUT-8(Ni) “flexible” **1** show relatively large crystallites with a size ranging from 20 to 100 μm , which is fully consistent with our previous study (Fig. 5).²⁷ In contrast, the images obtained for DUT-8(Ni) “rigid” **2**, show a particle size magnitude close to the resolution limit of the SEM instrument. In general, the poor electrical conductivity of MOFs is disadvantageous for high-resolution SEM studies. Nevertheless, a rough estimation results in an average particle size of 200–500 nm (Fig. 5).

In samples **3_a** and **3_b**, where an additional non-porous phase of $\text{Ni}_3(\text{ndc})_3(\text{DMF})_2(\text{Me}_2\text{NH})_2$ is observed in PXRD, the SEM images contain besides the typical bricks of DUT-8(Ni) also some spherical particles, which may be attributed to $\text{Ni}_3(\text{ndc})_3(\text{DMF})_2(\text{Me}_2\text{NH})_2$ (Fig. S10, ESI†). The images of **3_a**–**3_d** show a broad particle size distribution for DUT-8(Ni) (Fig. S10, ESI†). Particles larger than 50 μm as well as very small particles (<1 μm) can be observed in the images. This observation is consistent with the results from PXRD and isotherms showing the presence of both the **cp** and **op** phases and 2 steps in the nitrogen adsorption isotherms, if one assumes that only crystals exceeding a critical size may lead to switchability. The broadened “gate pressure” in the isotherms of **3_a**–**3_d**, in this interpretation, can be considered as originat-

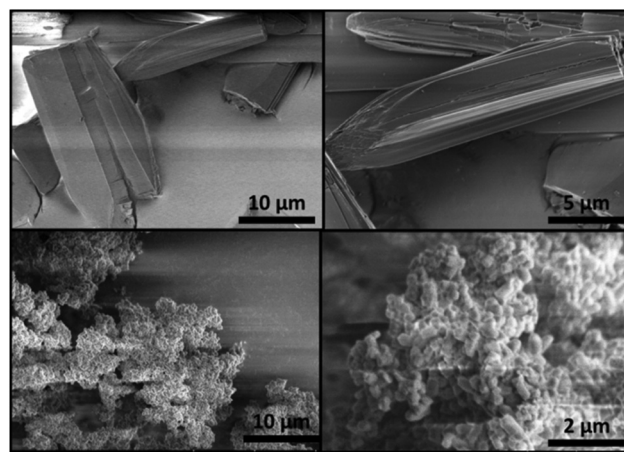


Fig. 5 SEM images: flexible DUT-8(Ni) (**1**) (top) and rigid DUT-8(Ni) (**2**) (bottom).

ing from a broad particle size distribution in these samples. As for many cooperative phenomena, it is reasonable to expect that the activation energy for “gate opening” is related to the crystallite size. In this interpretation, depending on the crystallite size, the crystallites open from **cp** to **op** at different pressures while the closing pressure is not affected. However, this interpretation is oversimplified, since the first guest removal (activation) process causes larger crystals to transform into an intertwined domain structure in which the domain size and the grain boundary energy determine the activation energy. As the solvothermal synthesis results in the formation of the **op** phase, the desolvation procedure is decisive in affecting the microstructure. Due to the huge crystal contraction during solvent removal, larger crystals disintegrate into a complex microstructure with grain boundaries of unknown size creating an interfacial domain area A_{id} as explained above. A uniform microstructure with grains of similar size will afford a steep gate opening characteristic, as the activation energy for switching the microdomains is identical. We expect **op** crystals differing in size to afford differently sized microdomain structures upon desolvation into the **cp** phase, and hence altered activation energies corresponding to the altered gate opening pressures. We hypothesize that grain boundaries act as the nucleation sites for the gating transition as they may act as diffusional entries for the gas. Thus, for smaller crystals fewer grain boundaries and defect statistics could in principle even shift the gate opening pressure so far, that the crystals remain closed in the whole pressure range. This hypothesis could explain the significantly reduced maximum uptake in some samples with an intermediate particle size. If a crystal approaches a certain lower boundary, we can expect a single domain switching mechanism without fracture into microdomains similar to other ferroic size phenomena. Below this critical size only A_o will determine the gate opening pressure. However, crystals varying in size may also differ in point defect concentration and small variations in defect concentration can also change the activation barrier.

In our observations, below a critical size, which for DUT-8 (Ni) we estimate based on this study to be approximately 500 nm, the material does not transform into the closed form by guest removal (activation), and an isotherm typical of rigid microporous materials is observed. The underlying principle for this observation must rely on a thermodynamic stabilization of the **op** vs. **cp** phase as this phenomenon is observed in a vacuum without any gases. A possible explanation relies on the EPR data, and the recently identified high defect concentrations²⁵ could arise from rapid nucleation and growth. In particular, missing ndc^{2-} ligands are expected to reduce the dispersive energetic stabilization of DUT-8(Ni) **cp**. Another potential explanation could be differences in the surface energy related to A_o . However, as A_o is larger for the **op** phase ($\Delta A_o = A_o(\mathbf{op}) - A_o(\mathbf{cp}) > 0$), this explanation would imply that the specific surface energy difference is $\Delta\sigma = \sigma(\mathbf{op}) - \sigma(\mathbf{cp}) < 0$ which is difficult to justify.

Zhang *et al.* proposed an explanation for the thermodynamically controlled crystal-size-dependent structural tran-

sitions in MOFs in the presence of gases. The calculations showed that the suppressed adsorption uptake at the surface of the nanoparticles compared to that at the bulk-like region results in a reduced thermodynamic driving force for the transition in the nanoparticles over the entire range of bulk fluid pressures.³⁴

From an experimental point of view, the overall trend is consistent for all synthesis parameters. In sample series 3', the changes of the amount of dabco also strongly affect the crystallite size. The SEM images of sample 3'_a show block-like overgrown crystallites, which according to XRD should belong to the $Ni_3(ndc)_3(DMF)_2(Me_2NH)_2$ phase (Fig. S11, ESI†). Obviously, the use of methanol in the synthesis creates the best conditions for growing larger crystals. An increased amount of dabco in samples 3'_c and 3'_d leads to a broadening of the particle size distribution as can be directly observed in the images showing crystallites ranging in size from several hundred nanometers to one hundred micrometres. Again, these effects are indirectly reflected in the PXRD results showing mixtures of two phases and nitrogen adsorption isotherms with broadened gating transitions. The gradual increase of the amount of methanol in the mixture in sample series 4 shows a very similar effect. Sample 4_a synthesized with the lowest methanol content consists of crystallites with a maximal size of 500 nm and therefore shows a pure “Type Ia” isotherm and the **op** phase in the PXRD pattern. With increasing the amount of methanol in the synthesis, the particle size distribution is broadened. In sample 4_c the particle size ranges from 500 nm to 10 μm (Fig. S12, ESI†) also reflecting well the nitrogen adsorption and PXRD experiments (Fig. 4e and f). As expected from the isotherms and XRD measurements, varying the amount of nickel in the synthesis does not influence the particle size in samples 5'_a and 5'_b (Fig. S13, ESI†).

Temperature dependent X-ray diffraction study

Kitagawa and co-workers³³ reported that for interpenetrated pillared-layer compound $Cu_2(bdc)_2(bpy)$ ($bdc = 1,4$ -benzenedicarboxylate, $bpy = 4,4'$ -bipyridine) the pore shape could be

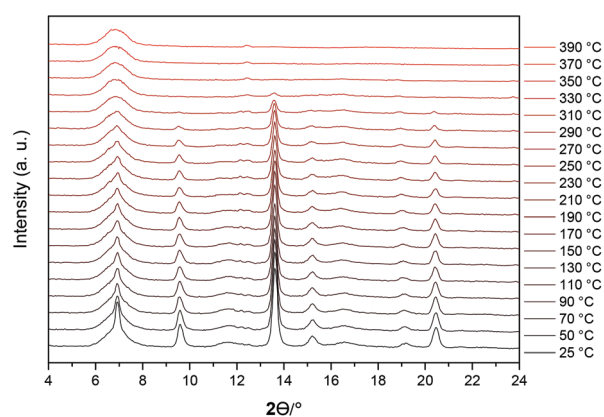


Fig. 6 Temperature dependent X-ray diffraction patterns of **2** heated in a vacuum.

switched from the open to the closed form by heating. Thus, temperature dependent X-ray diffraction experiments were conducted on **2** (Fig. 6 and S19†) to investigate the behavior of DUT-8 during heating. However, the rigid DUT-8 remains in the open form until decomposition and therefore is not temperature responsive.

Conclusions

Significant differences in the synthesis pathway were found to be responsible for the formation of “rigid” and “flexible” DUT-8(Ni) under different synthesis conditions. The high supersaturation in the synthesis of “rigid” DUT-8(Ni) causes the formation of intermediate phases and rapid nucleation, leading to small and defective crystallites showing typical “Type Ia” physisorption isotherms. In contrast, the higher solubility in the crystallization of “flexible” DUT-8(Ni) and slow crystallization cause the formation of large crystals that can undergo a transformation into a closed phase upon desolvation. Samples with crystallites smaller than 500 nm do not show the **op** → **cp** phase transformation and therefore stay in the open form after the guest molecule removal, whereas particles larger than 1 μm can be reversibly transformed into the **cp** phase.

For “flexible” DUT-8(Ni), various synthesis parameters influencing the crystal size can be used to tune the “gate opening” pressure reflecting the activation barrier of the phase transition, while the “gate closing” pressure remains constant.

The reason for a strong effect of the synthesis parameters lies in the differences of the crystallization mechanism: an excess amount of dabco in the synthesis of the “rigid” DUT-8(Ni) is partially consumed by the deprotonation of the H₂ndc ligand resulting in the absence of a metal source and the precipitation of a (H₂dabco)(ndc) salt. In the presence of Ni²⁺ cations, rapid nucleation of the defective DUT-8(Ni) structure proceeds in the formation of a cloudy microcrystalline precipitate. A high concentration of defects in this phase was recently confirmed by EPR in the presence of NO. Additional bands in the IR-spectrum support these findings. Thus particle size and defects are both decisive factors influencing flexibility. In contrast, the use of a stoichiometric ratio of the initial reagents in the crystallization of “flexible” DUT-8(Ni) in a DMF/methanol mixture inhibits complete deprotonation of H₂ndc and therefore slows down the nucleation and crystallization of the target compound. It causes the formation of large crystals (20 to 100 μm). These large crystals undergo a transformation into a closed phase upon desolvation.

An important implication of our findings is that switchable MOFs, especially those showing pronounced volume changes, should always be considered as materials with “history dependent adsorption profiles”, because each transition undergone may cause changes in domain size and defect formation which in turn affects the adsorption behaviour. We believe our findings to be an important step towards a fundamental under-

standing of adsorption induced switching transitions of porous solids.

Acknowledgements

Financial support from the “excellence initiative by German federal and state government” (measure “support the best”) and DFG (FOR 2433) is gratefully acknowledged. V. B. acknowledges the German Federal Ministry of Education and Research (BMBF Project No 05K16OD1) for the financial support. Authors are very grateful to Prof. S. Bordiga for the valuable discussions of the IR and Raman spectra.

References

- 1 S. Horike, S. Shimomura and S. Kitagawa, *Nat. Chem.*, 2009, **1**, 695–704.
- 2 G. Ferey and C. Serre, *Chem. Soc. Rev.*, 2009, **38**, 1380–1399.
- 3 Z. Chang, D.-H. Yang, J. Xu, T.-L. Hu and X.-H. Bu, *Adv. Mater.*, 2015, **27**, 5432–5441.
- 4 F.-X. Coudert, *Chem. Mater.*, 2015, **27**, 1905–1916.
- 5 A. Schneemann, V. Bon, I. Schwedler, I. Senkovska, S. Kaskel and R. A. Fischer, *Chem. Soc. Rev.*, 2014, **43**, 6062–6096.
- 6 A. Kondo, H. Noguchi, S. Ohnishi, H. Kajiro, A. Tohdoh, Y. Hattori, W.-C. Xu, H. Tanaka, H. Kanoh and K. Kaneko, *Nano Lett.*, 2006, **6**, 2581–2584.
- 7 T. R. C. Van Assche, G. V. Baron and J. F. M. Denayer, *Dalton Trans.*, 2016, **45**, 4416–4430.
- 8 T. Song, J. Yu, Y. Cui, Y. Yang and G. Qian, *Dalton Trans.*, 2016, **45**, 4218–4223.
- 9 O. M. Linder-Patton, W. M. Bloch, C. J. Coghlan, K. Sumida, S. Kitagawa, S. Furukawa, C. J. Doonan and C. J. Sumby, *CrystEngComm*, 2016, **18**, 4172–4179.
- 10 M. L. Foo, R. Matsuda, Y. Hijikata, R. Krishna, H. Sato, S. Horike, A. Hori, J. Duan, Y. Sato, Y. Kubota, M. Takata and S. Kitagawa, *J. Am. Chem. Soc.*, 2016, **138**, 3022–3030.
- 11 J. A. Mason, J. Oktawiec, M. K. Taylor, M. R. Hudson, J. Rodriguez, J. E. Bachman, M. I. Gonzalez, A. Cervellino, A. Guagliardi, C. M. Brown, P. L. Llewellyn, N. Masciocchi and J. R. Long, *Nature*, 2015, **527**, 357–361.
- 12 H. Sato, W. Kosaka, R. Matsuda, A. Hori, Y. Hijikata, R. V. Belosludov, S. Sakaki, M. Takata and S. Kitagawa, *Science*, 2014, **343**, 167–170.
- 13 R. Matsuda, *Nature*, 2014, **509**, 434–435.
- 14 P. Serra-Crespo, M. A. van der Veen, E. Gobechiya, K. Houthoofd, Y. Filinchuk, C. E. A. Kirschhock, J. A. Martens, B. F. Sels, D. E. De Vos, F. Kapteijn and J. Gascon, *J. Am. Chem. Soc.*, 2012, **134**, 8314–8317.
- 15 N. Yanai, K. Kitayama, Y. Hijikata, H. Sato, R. Matsuda, Y. Kubota, M. Takata, M. Mizuno, T. Uemura and S. Kitagawa, *Nat. Mater.*, 2011, **10**, 787–793.

- 16 K. Nakagawa, D. Tanaka, S. Horike, S. Shimomura, M. Higuchi and S. Kitagawa, *Chem. Commun.*, 2010, **46**, 4258–4260.
- 17 F.-X. Coudert, A. Boutin, A. H. Fuchs and A. V. Neimark, *J. Phys. Chem. Lett.*, 2013, **4**, 3198–3205.
- 18 H. Tanaka, S. Ohsaki, S. Hiraide, D. Yamamoto, S. Watanabe and M. T. Miyahara, *J. Phys. Chem. C*, 2014, **118**, 8445–8454.
- 19 D. Li and K. Kaneko, *Chem. Phys. Lett.*, 2001, **335**, 50–56.
- 20 V. Bon, I. Senkowska, D. Wallacher, A. Heerwig, N. Klein, I. Zizak, R. Feyerherm, E. Dudzik and S. Kaskel, *Microporous Mesoporous Mater.*, 2014, **188**, 190–195.
- 21 Y. Cheng, H. Kajiro, H. Noguchi, A. Kondo, T. Ohba, Y. Hattori, K. Kaneko and H. Kanoh, *Langmuir*, 2011, **27**, 6905–6909.
- 22 H. Kanoh, A. Kondo, H. Noguchi, H. Kajiro, A. Tohdoh, Y. Hattori, W.-C. Xu, M. Inoue, T. Sugiura, K. Morita, H. Tanaka, T. Ohba and K. Kaneko, *J. Colloid Interface Sci.*, 2009, **334**, 1–7.
- 23 S. Hiraide, H. Tanaka and M. T. Miyahara, *Dalton Trans.*, 2016, **45**, 4193–4202.
- 24 D. N. Dybtsev, H. Chun and K. Kim, *Angew. Chem., Int. Ed.*, 2004, **43**, 5033–5036.
- 25 M. Mendt, F. Gutt, N. Kavosi, V. Bon, I. Senkowska, S. Kaskel and A. Pöpl, *J. Phys. Chem. C*, 2016, **120**, 14246–14259.
- 26 V. Bon, N. Klein, I. Senkowska, A. Heerwig, J. Getzschmann, D. Wallacher, I. Zizak, M. Brzhezinskaya, U. Mueller and S. Kaskel, *Phys. Chem. Chem. Phys.*, 2015, **17**, 17471–17479.
- 27 V. Bon, N. Kavosi, I. Senkowska and S. Kaskel, *ACS Appl. Mater. Interfaces*, 2015, **7**, 22292–22300.
- 28 N. Klein, H. C. Hoffmann, A. Cadiau, J. Getzschmann, M. R. Lohe, S. Paasch, T. Heydenreich, K. Adil, I. Senkowska, E. Brunner and S. Kaskel, *J. Mater. Chem.*, 2012, **22**, 10303–10312.
- 29 N. Klein, C. Herzog, M. Sabo, I. Senkowska, J. Getzschmann, S. Paasch, M. R. Lohe, E. Brunner and S. Kaskel, *Phys. Chem. Chem. Phys.*, 2010, **12**, 11778–11784.
- 30 K. Treppe, S. Schwalbe and G. Seifert, *Phys. Chem. Chem. Phys.*, 2016, **18**, 1348.
- 31 H. C. Hoffmann, B. Assfour, F. Epperlein, N. Klein, S. Paasch, I. Senkowska, S. Kaskel, G. Seifert and E. Brunner, *J. Am. Chem. Soc.*, 2011, **133**, 8681–8690.
- 32 J. Y. Lee, L. Pan, X. Huang, T. J. Emge and J. Li, *Adv. Funct. Mater.*, 2011, **21**, 993–998.
- 33 Y. Sakata, S. Furukawa, M. Kondo, K. Hirai, N. Horike, Y. Takashima, H. Uehara, N. Louvain, M. Meilikhov, T. Tsuruoka, S. Isoda, W. Kosaka, O. Sakata and S. Kitagawa, *Science*, 2013, **339**, 193–196.
- 34 C. Zhang, J. A. Gee, D. S. Sholl and R. P. Lively, *J. Phys. Chem. C*, 2014, **118**, 20727–20733.
- 35 S. Watanabe, S. Ohsaki, T. Hanafusa, K. Takada, H. Tanaka, K. Mae and M. T. Miyahara, *Chem. Eng. J.*, 2017, **313**, 724–733.
- 36 D. A. Guzonas and D. E. Irish, *Can. J. Chem.*, 1988, **66**, 1249–1257.
- 37 A. Jacobs, L. R. Nassimbeni, G. Ramon and B. K. Sebogisi, *CrystEngComm*, 2010, **12**, 3065–3070.
- 38 Y. Du, A. L. Thompson, N. Russell and D. O'Hare, *Dalton Trans.*, 2010, **39**, 3384–3395.
- 39 M. Thommes, K. Kaneko, A. V. Neimark, J. P. Olivier, F. Rodriguez-Reinoso, J. Rouquerol and K. S. W. Sing, *Pure Appl. Chem.*, 2015, **87**, 1051–1069.
- 40 L. Sarkisov and A. Harrison, *Mol. Simul.*, 2011, **37**, 1248–1257.
- 41 S. Tanaka, K. Fujita, Y. Miyake, M. Miyamoto, Y. Hasegawa, T. Makino, S. Van der Perre, J. C. Saint Remi, T. Van Assche, G. V. Baron and J. F. M. Denayer, *J. Phys. Chem. C*, 2015, **119**, 28430–28439.